

Research Article

Observation of Excess Heat by Activated Metal and Deuterium Gas

Tadahiko Mizuno*

Hydrogen Engineering Application and Development Company, Kita 12, Nishi 4, Kita-ku, Sapporo 001-0012, Japan

Abstract

Reports of heat-generating cold fusion reactions in the nickel–hydrogen system have been increasing. The reactions mainly involve nickel with other additive elements. The authors of these reports emphasized the importance of an extremely clean system in the electrolytic tests in which excess heat was generated. Therefore, we attempted to detect excess heat after reducing impurities to a minimum by cleaning the electrode carefully and then fabricating nanoparticles in situ in our test system, without ever exposing them to air. As a result, energy far exceeding input was continuously obtained. In the best results obtained thus far, the output thermal energy is double the input electrical energy, amounting to several hundred watts. The generated thermal energy follows an exponential temperature function. When the reactor temperature is 300°C, the generated energy is 1 kW. An increase of the temperature is expected to greatly increase the output energy. We have recently improved the preparation of the electrode material. This enhanced reproducibility and increased excess heat. The new methods are described in the Appendix.

© 2017 ISCMNS. All rights reserved. ISSN 2227-3123

Keywords: Deuterium gas, Heat generation, Ni metal, Surface activation

1. Introduction

We have aimed to reproduce a long-standing curious phenomenon that occurs in metal–hydrogen systems [1–5]. At first, the reaction was assumed to be a normal nuclear fusion reaction, so confirmation experiments involving neutron detection during the electrolysis of heavy water were conducted [6]. Focus then shifted to analysis of the elements isotopically changed during electrolysis. The generation of heat in the process, which had rarely been observed, became a recurring phenomenon [7–10]. The heat-generating reaction of a nickel–hydrogen system, in particular, has been reported [11–13]. This system, when compared to the initial Pd–D₂ system has been regarded as a null calibration test. The generation of excess heat in reactions involving nickel was observed with additive elements in these reports. However, the authors noted the importance of a very clean system in early electrolysis tests where excess heat was observed. Therefore, in the present work, we eliminated impurities in an attempt to detect excess heat. Specifically, we developed a very simple heat estimation analysis, based on flowing air calorimetry, to confirm excess heat induced by the reaction between hydrogen and a metal. The factors considered are only the amount of air and the temperature difference between the air flowing into and out of the calorimeter. These factors contribute the most to heat analysis

*E-mail: head-mizuno@lake.ocn.ne.jp



Figure 1. Photo of the reactor body. The upper part is the electrode inlet part, on the left is the viewing window, and the gas valve is seen on the right. A heating wire is wrapped around the reactor body center part. The connecting wire and platinum temperature sensor can be seen.

and can easily be used estimate the excess heat. In this paper we describe the excess heat in a simple metal–hydrogen system.

2. Experiment

2.1. Reactor body

The reactor body is a cruciform cylindrical shape as shown in Fig. 1. All parts are connected with metal seal flanges. The upper part of the reactor comprises the heater power inlet, the high-voltage discharge electrode, and a thermocouple. Several platinum temperature measuring elements (Okazaki; Pt AA class $\pm(0.1+0.0017|t|) - 196 \sim 450$) were installed in the reactor. As shown in Fig. 1, there is a Kovar glass window on the left-hand side of the reactor, and a pressure gauge; and a mass spectrometer valve and the gas inlet valve is on the right-hand side. A vacuum evacuation system and a quadrupole gas analysis system are connected to the body.

The reactor is made of SUS 316. Its volume is 2740 cm^3 and its weight is 20.3 kg.

2.2. Reaction material

The inner wall surface of the reactor was covered with two pieces of nickel mesh (99.9%, Ni 200 alloy, 180 mesh, Inada Wire Mesh Co. Ltd.) the wire diameter is 0.055 mm, the total wire length is 896 m, and the surface area is 0.31 m^2 . Each mesh was $300 \times 300 \text{ mm}^2$ and composed of 0.15-mm-diameter wire; the opening size was 180 mesh, and the total weight was 23 g. Figure 2 is a photo of the Ni mesh. The Ni mesh is first degreased with detergent. It is then installed against the wall inside the reactor.

The two meshes were installed in the center of the reactor inner surface. The nickel meshes were unrolled and pressed with a nickel plate (thickness 0.5 mm, width 5 mm, length 500 mm) against the reactor inner surface to ensure contact with the inner wall of the reactor, which is necessary to maintain thermal conduction. Figure 3 shows a view of the mesh and the reactor. The mesh is in tight contact with the inner wall of the reactor. This photo shows the reactor, flange, and mounting hole. A copper gasket can be seen on the flange surface. The Ni mesh in the reactor and body is prepared by cleaning with high temperature pure water for 1 h, and washed with alcohol and acetone.



Figure 2. Nickel mesh as reactant, 30 cm², 200 mesh. This photo shows the two meshes overlapped.

2.3. Inner arrangement of reactor

Figure 4 shows the upper parts of the reactor and cross section of the reactor. Two high-voltage electrodes and one electric power inlet for a small ceramic heater and an inlet for a thermocouple were installed in the reactor as shown in the left-hand side of Fig. 4. In Fig. 4, the electrode on the left-hand inside the reactor, which was for discharge, was a 50-mm-long, 3-mm-diameter palladium tube wound with 200 mm of 1-mm-diameter palladium wire (weight 2.82 g). This electrode was insulated from the reactor body. The gas temperature around the electrode was measured with a stainless-steel-coated K-type thermocouple with a diameter of 1.6 mm and a length of 300 mm. The thermocouple was insulated in a 3-mm-diameter, 100-mm-long alumina tube to prevent it from being affected by the plasma discharge. The other input terminal is for high voltage power supply to the Pd wire wound around the heater. The tip of this terminal leads to the Pd thin wire wound around the heater. A high voltage current is supplied from the terminal to the



Figure 3. View of Ni mesh in the reactor.

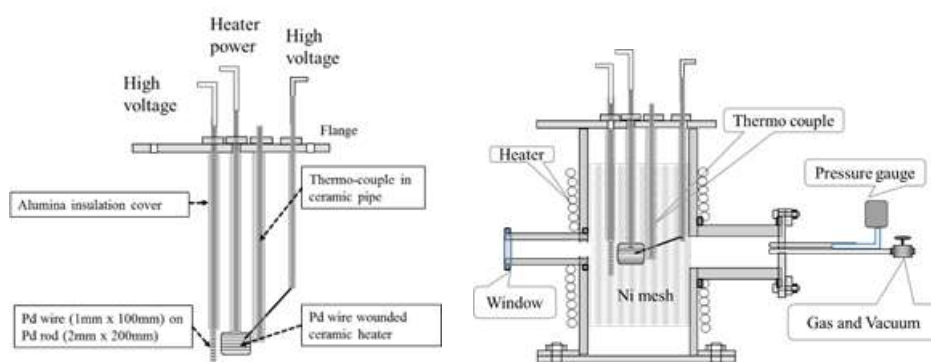


Figure 4. Schematic representation of electrode and cross section of reactor.

Pd fine wire. An aluminum ceramic heater with a maximum temperature of 1000°C was positioned in the reactor's center. The heater was $30 \times 30 \text{ mm}^2$, with a thickness of 2 mm. A K-type thermocouple was positioned near the heater. A palladium wire with a diameter of 0.3 mm length 200 mm, was wound around the heater.

The cross section in Fig. 4 (right-hand side) shows the electrodes inside the reactor, and the internal ceramic heater. It also shows the condition of the nickel mesh. The figure is a conceptual diagram, but it depicts the internal state accurately. In this figure, a heater, valves, and so on are drawn around the reactor body. This is explained below.

Figure 5 shows a photo of the tip of the ceramic heater, Pd fine wire and Pd discharge electrode in the reaction

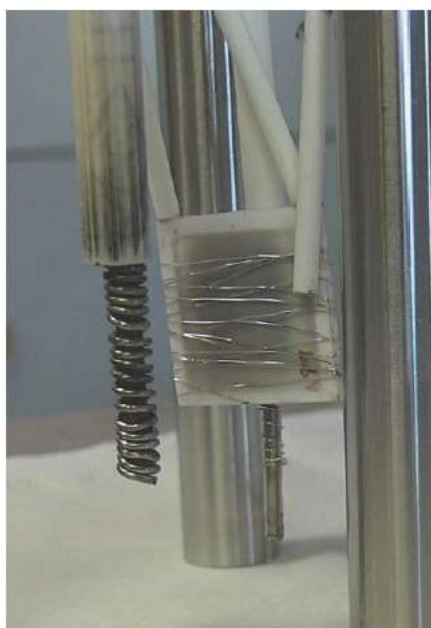


Figure 5. View of the electrode and heater in the reactor.

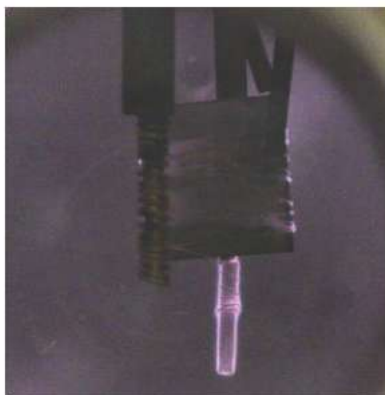


Figure 6. Photo of plasma state when discharging by applying a high voltage to the Pd thin wire on the ceramic heater.

reactor. In the photograph, two thick metal columns are provisional supports are needed while working to attach the electrodes. They are removed when the structure is placed in the reactor body. Pd fine wire is coarse wrapped around the ceramic heater. This heater is heated to evaporate the Pd metal. There is a Pd rod to supply high voltage current under the heater, and a thin wire is wound around it. The ceramic tube on the upper right of the ceramic heater is in contact with the heater. A thermocouple is contained inside this ceramic tube. Two ceramic tubes at the top of the heater are for the power supply to the ceramic heater, with a small copper wire.

2.4. Reactor heater

A 2-m-long heater of stainless sheath was wrapped around the reactor body. Its purpose was to heat the nickel mesh in the reactor. The heater capacity is 100 V, 600 W, with a maximum temperature of 500°C. Six platinum temperature measuring elements were attached to various parts of the reactor. The heater was covered by thick aluminum tape around the heater several times to make the temperature distribution of the reactor uniform, as shown in Fig. 1.

2.5. Preparation of reacting material

The Ni mesh around the inner surface of the reactor is discharged by high voltage of DC current between the wire around the heater electrode and another Pd wire electrode. The reaction gas is 99.9% pure deuterium (Nippon Oxygen).

The electrode preparation treatment procedure is as follows:

- (1) The gas in the reactor is evacuated to several Pa of pressure.
- (2) D₂ gas is supplied to the reactor at several hundred Pa.
- (3) Electric power to the heater around the reactor is supplied at 50 W for 10 h, and the temperature of the reactor reaches around 50°C.
- (4) The gas in the reactor is evacuated to ~40 Pa.
- (5) High voltage is supplied to the wire around the ceramic heater. Plasma is formed. At this stage, if the plasma is difficult to generate you can increase input voltage, but it is better to keep the D₂ gas pressure below 50 Pa. The current becomes stable at ~40 mA. The state of the glow discharge at this time is shown in Fig. 6. Gas is emitted from the heater wound around the ceramic, and the light from the gas can be seen. The part covered

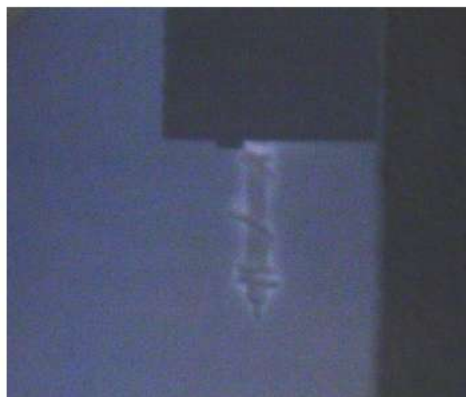


Figure 7. Photo of plasma state in which a high voltage is applied to the Pd thin wire on the ceramic heater.

with the lower pink and violet color plasma is Pd winding which supplies high voltage to the Pd thin wire. It is still covered with same color of plasma and gas which is released from the inside of the reactor.

This discharge is continued for several hours. With this process, the pressure in the reactor increases over time. This is because gases absorbed in the sample and the reactor body are released. If this gas release stops and the pressure does not change, the discharge can be stopped.

Additional procedures are performed:

- (6) When the impurity gas release stops, gas inside the reactor is again evacuated while heating the reactor body.
- (7) New D_2 gas is then supplied at 50 Pa, with 100 W of input power to the reactor heater. When the temperature has stabilized, that is, when it reaches approximately $100^\circ C$, the high voltage current is again supplied to the Pd fine wire around the ceramic heater. Discharge starts at around 500 V. If the glow discharge does not appear, voltage is increased until it appears. The discharge is continued for several hours. Then the pressure in the reactor is increased again.
- (8) The pressure inside the reactor finishes increasing, and when stabilized, the reactor is again evacuated.

During Steps 7 and 8 the reactor temperature is gradually raised up to $350^\circ C$. When residual gas stops coming out from the reactor and the amount of D_2 gas component is large, a light blue discharge appears, as shown in Fig. 7. This is observed at a pressure of less than 5 Pa. When the impurity gas disappears, while keeping the reactor temperature high, the D_2 gas is finally supplied at 500 Pa and the heating of the reactor is stopped. The operator then waits until the temperature drops to room temperature.

When the temperature drops to room temperature, gas is evacuated from the furnace down to 50 Pa or less. Thereafter, a current with a high voltage of 500 V is supplied to the electrode on which the Pd wire is wound around the Pd rod. If discharge is difficult to start, the gas pressure is lowered to about 10 Pa and voltage is raised high. The current at that time is about several 10 mA. This discharge is continued more than several hours.

Since D_2 gas comes out from the Pd rod and wire at the beginning of the discharge, the plasma covers the entire electrode as shown in Fig. 8. After that, when the gas is exhausted from the wire and rod, the whole inside of the reactor emits blue plasma as shown in Fig. 9.

After this processing, the final step is taken. Keeping the pressure intact, electric power is supplied to the ceramic heater, and the ceramic heater temperature is raised to $700\text{--}800^\circ C$. Figure 10 shows a photograph at the time of

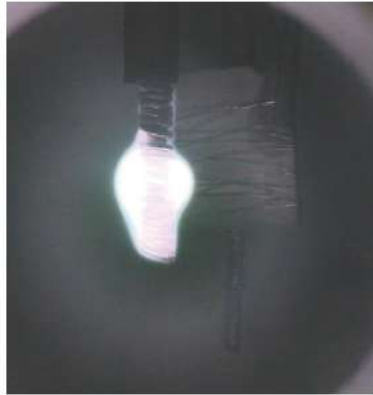


Figure 8. Photo of plasma.

heating by the ceramic heater. The heater shows red incandescence. This state is continued for about 10–20 h, and Pd is deposited on the nickel surface. Doing this produces the conditions needed to generate excess heat.

2.6. Air flow measurement for heat calibration

The same type of reactor is used in the calibration, and is installed as a control for calibration of the heat balance in the enclosure described below. The design, size, weight, and shape of this calibration reactor are exactly the same as the reactor used for testing. The internal reactants are the same nickel, of the same weight, size, dimensions and position. Both are washed and wound the same way. However, excess heat is not produced by the calibration electrode even though deuterium gas is added to the cell, because the nickel material is not processed as described in Section 2.5.

Figure 11 shows the test and calibration reactors. The latter reactor is placed in the calorimeter to obtain test and calibration data, and to demonstrate a heat balance of zero. Both reactors are shown in the photo. These can be tested

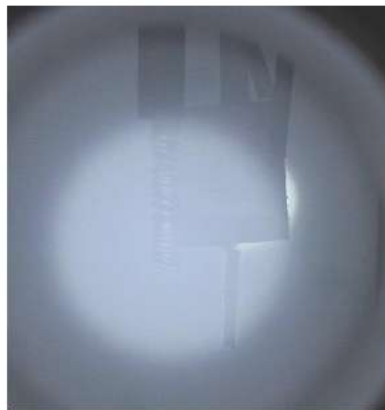


Figure 9. Photo of plasma.

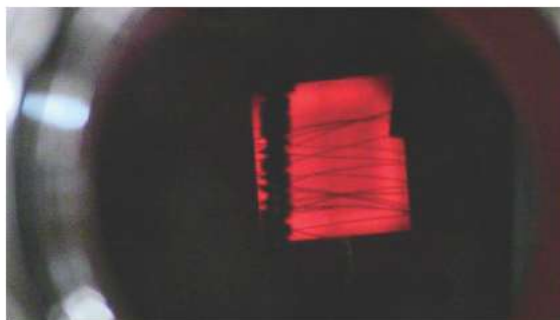


Figure 10. Photo of the ceramic heater.

separately, or at the same time. In this photograph, the calorimeter enclosure is removed. This enclosure will be described below.

The test or calibration reactor were placed in an enclosure, which is an acrylic box (Fig. 12) width 0.4 m, depth of 0.75 m, and height 0.7 m. Air-passage openings of 50-mm-diameter were made at the top and the bottom side of the box. A blower of 12 V, 0.6A, 7.2 W was installed on the top air-passage port. A platinum temperature sensor was positioned in the air outlet pipe of the blower set in the top hole of the box, and another sensor was positioned at the bottom air inlet hole. The blower is made by Sanyo Denki Instruments (San Ace B97, Model 109BM12GC2-1) and it is shown in Fig. 14. The periphery of the air outlet was covered with a paper cylinder having a length of 200 mm, and



Figure 11. Photo of the reactor.



Figure 12. Photo of the acrylic calorimeter enclosure.

the periphery thereof was further wrapped with aluminum foil insulation.

The blower was supplied with 5 W (constant voltage of 12 V, 0.42 A). The voltage and current data of the blower were continuously recorded by a PC. The air flow rate of the blower was calibrated with a digital anemometer (Custom Co. Ltd. CW-60) that shows Fig. 15. The thermoelectric anemometer ranged from 0.2 to 20 m/s, the resolution was 0.1 m/s, and the measurement temperature range was 0–50°C. The temperature of the air outlet and the wind speed were measured continuously by the equipment by the location of the outlet. In this way, the air leaving the blower was sufficiently agitated. An anemometer equipped with an air volume and a thermometer was used to confirm that both the wind speed and temperature were uniform. From the air volume and the air heat capacity, the temperature at the outlet from the box rises by about 0.05° per 1 W power input. Since the resolution of platinum temperature sensor is

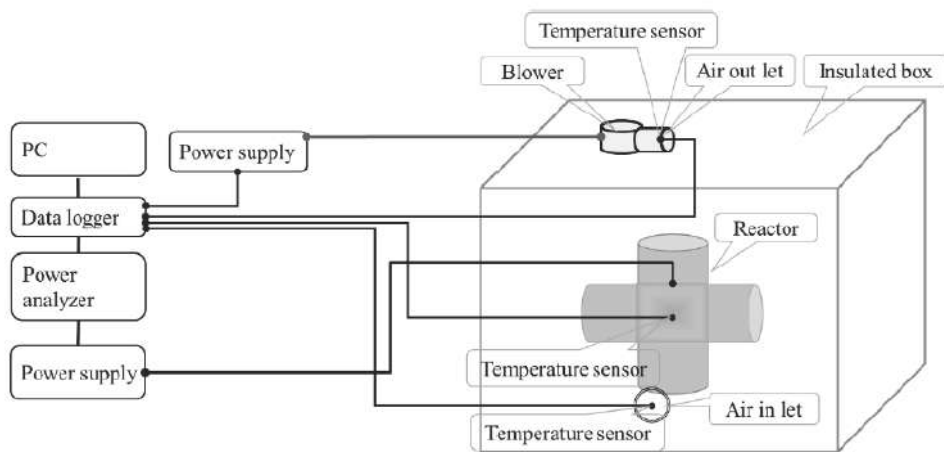


Figure 13. Schematic of measurement system.



Figure 14. Photo of blower.

0.1°, power can be measured to the nearest ~ 2 W.

Figure 13 shows a schematic of measurement system. The test reactor and calibration reactor are set in the center of the enclosure, and the control and the measuring system is shown on the left-hand side.

The rectangles in the lower left of the figure represent the input power supply, the power input analyzer (Yokogawa, PZ 4000), the data logger (Agilent, 34970A), and the PC for data acquisition. A capacitance diaphragm gauge (MKS Co. Ltd.) was used as the reactor's inner gas-pressure gauge. Data from six reactor temperatures, electric power to the test reactor that is processed by the power-meter, electric currents and voltages for the power supply of the blower, and the temperatures of the inlet and the outlet air flows were collected by a data logger and recorded to a PC every 5 s.

The reactor and the calibration reactor are set at the same position in the box. A constant volume of air was flowed from the bottom hole of the box. The air passes through, blowing on both the test reactor and the control reactor. It then goes out through the top hole of the box. The temperature of the inlet air was continuously measured with a platinum temperature sensor. A blower was installed at the upper air outlet port, and another temperature sensor was attached to the outlet hole. This sensor was installed at the air coming out of the blower.

The specific heat of constant pressure air of C_p is hardly affected by temperature. The C_p is described below. It is 1.005 J/g/deg at 273 K and 1.012 J/g/deg at 373 K and 1.026 J/g/deg at 473 K. The temperature of the air under test will be described later in the measurement example. In a typical measurement, the room temperature was 293 K and the maximum temperature of the air outlet was 333 K. In this case, the heat capacity of the warmed air increased by 0.3%. The temperature dependence of the heat capacity of air has a linear relationship with the temperature in the measurement range, and it can be expressed by Eq. (1). The first term and the coefficient of the second term of the equation are constants, and T_{out} is the temperature of the air outlet. These temperatures are continuously measured at both the air inlet and outlet. However, the influence of the factor is 1/10 or less of the measurement error that is



Figure 15. Air volume measurement tool for calibration.

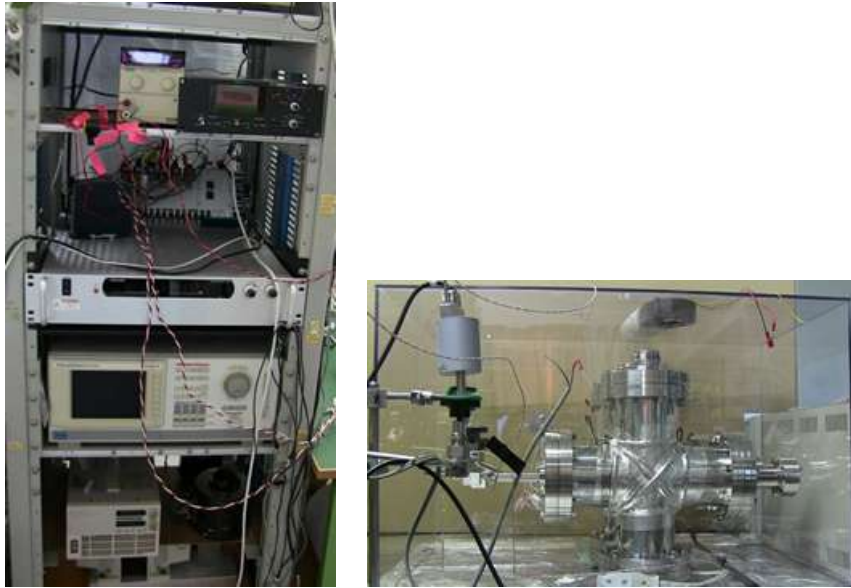


Figure 16. Photo of the measurement system and reactor in the shielding box.

described later.

$$H_c = 0.987 + 0.0000661 \times T_{\text{out}}. \quad (1)$$

The thermal calculations were carried out as follows. The input energy H_{in} was estimated as Eq. (2).

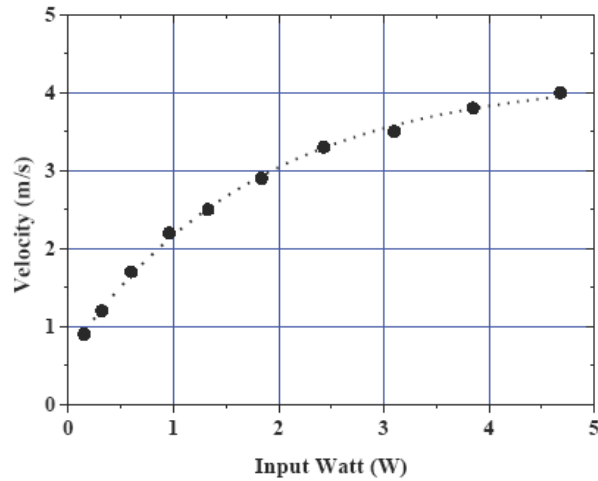


Figure 17. Relationship between the input power and the air velocity of the blower.

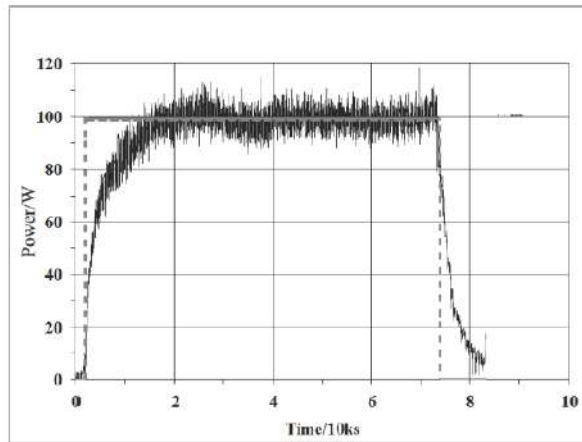


Figure 18. Changes of input and output power obtained reactor before excess heat generation treatment at 100 W of input power.

$$H_{\text{in}} = \sum_0^T \Delta W \times \Delta t, \quad (2)$$

where ΔW is the power at each time and Δt is the data integration time interval (24.47 s). Thermal output energy H_{out} was calculated as Eq. (3).

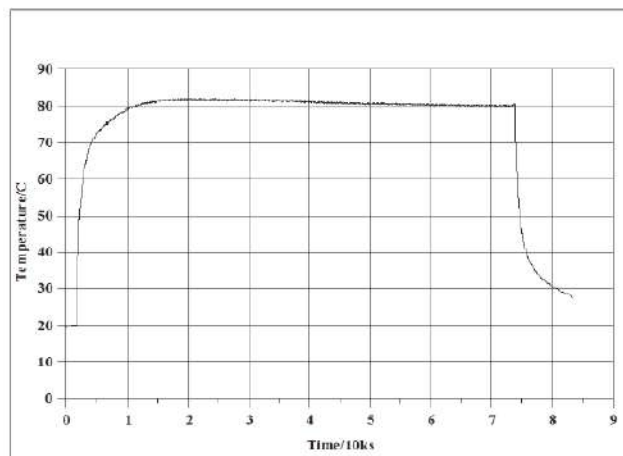


Figure 19. Temperature changes for outside body of reactor center at 100 W of input power before excess heat generation treatment.

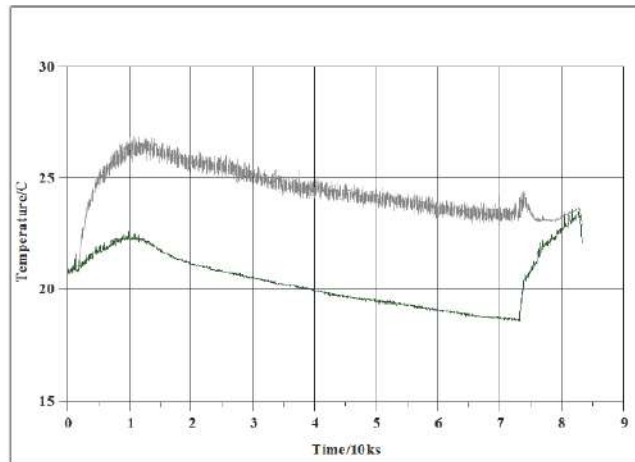


Figure 20. Temperature changes for inlet and outlet of the air at 100 W of input power before excess heat generation treatment.

$$H_{\text{out}} = \sum_0^T \Delta V S \rho H c \Delta t dT, \quad (3)$$

where V is the wind velocity (m/s); S is the area of the air outlet, $8.2 \times 10^{-3} \text{ m}^2$; ρ is the air density, 1.293 kg/m^3 at 273.2 K. This value is numerically presented as Eq. (4).

$$\rho = 3.391 \exp(-T_{\text{out}}/201.26) + 0.41529. \quad (4)$$

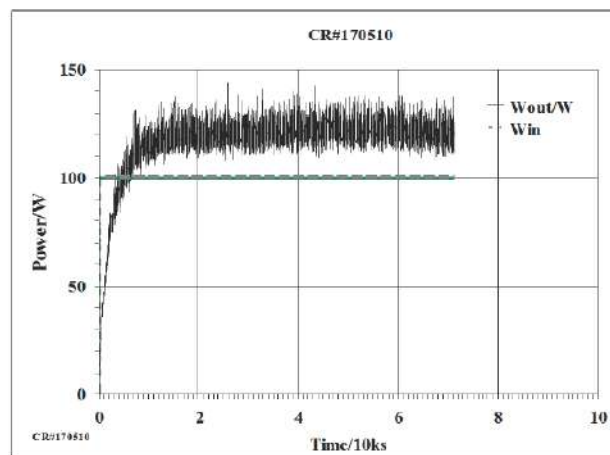


Figure 21. Test results obtained reactor during activation at 100 W of input power.

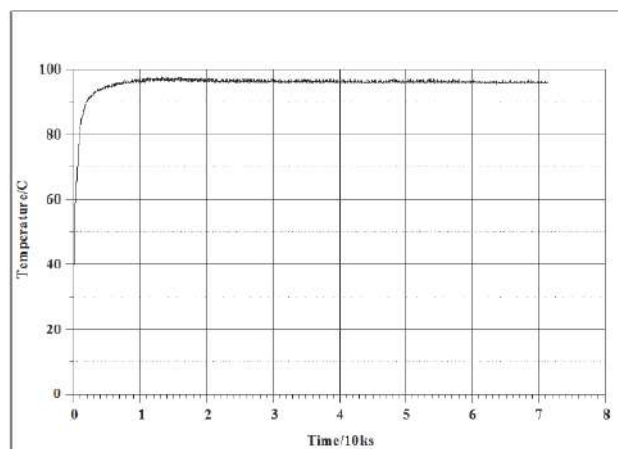


Figure 22. Temperature changes for outside body of reactor center at 100 W of input power during excess heat generation treatment.

The wind velocity at the flow meter was estimated by semi empirical Eq. (5).

$$V = A \exp(-W_b/w) + B, \quad (5)$$

where A is a constant, -3.7 ; $B = 4$; $w = 1.375$; W_b is the blower input (W); and dT is the temperature difference between the air inlet and the outlet, $T_{out} - T_{in}$. In calculating the caloric value of air, the caloric value varies depending on atmospheric pressure and humidity in addition to temperature. The atmospheric pressure was calibrated with a commercially available barometer made by Sunoh company and humidity by a measuring instrument made by Empex company. There was no significant change during the 80 ks measurement period.

Figure 17 shows the relationship between the blower input and the air flow rate obtained from the air volume calibration results. In this figure, the black circle is the measured value, and the dotted line is the approximate expression value obtained measured values and expressed by Eq. (5). Data corresponding to the input power for the blower were also collected during the test. Blower input power was approximately 4–6 W. These results indicate that the heat can theoretically be calculated from the air flow rate, the difference between the temperatures of the air in and the air out, and the air heat capacity. However, we also calibrated the heat balance with the control reactor.

In a usual test, the input power of the blower is 5 W, so the wind speed is 4 m/s. Since the air outlet sectional area is $4.4 \times 10^{-3} \text{ m}^2$, air volume of about $1.6 \times 10^{-2} \text{ m}^3/\text{s}$ passes through the interior of the box. Since the volume of the box is 0.21 m^3 , if the air volume by the blower is 0.03 m^3 , the air in the box is replaced every $\sim 13 \text{ s}$. We confirmed the flow of air using incense smoke. Air entering from the lower air inlet and directly hits the reactor body and then turns to the other side of the reactor. After that, the air rises to the top of the box and exits from the air outlet. We confirmed that the air passes through the entire interior of the box in a few seconds.

3. Results

3.1. Excess heat

The calibration test by control reactor results are shown in Fig. 18. Input power of 100 W was supplied for 2 ks to the control reactor. Output power increased until 20 ks, and then became constant. Input power was stopped at 73 ks and the heat output decreased to 0 W. The D_2 gas pressure in the reactor is 760 Pa. The amount of deuterium gas

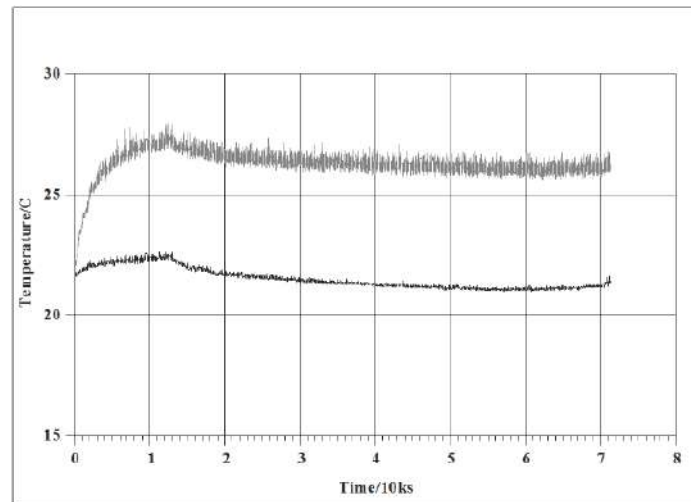


Figure 23. Temperature changes for inlet and outlet of the air at 100 W of input power before excess heat generation treatment.

is calculated as 20 cm^3 at the standard state. After reaching 100 W output, since there is no excess heat, it is almost constant at 100 W. The input was $100 \text{ W} \times 71.46 \text{ ks} = 7.15 \text{ MJ}$, and the output was estimated as 7.05 MJ; thus, the output/input ratio was 0.986. We consider this a reasonable calibration of the control reactor, and we assume the heat unaccounted for was lost by radiation from the box.

Figure 19 shows the change in reactor temperature with input of 100 W to the reactor before excess heat is produced. The temperature is the central temperature outside the reactor body that is shown in Fig. 1. When the room temperature is 21° , at the input of 100 W it reaches 80° Celsius after 10 ks. However, the other parts of the reactor body are lower than this temperature. This temperature is the value of the highest reactor body part.

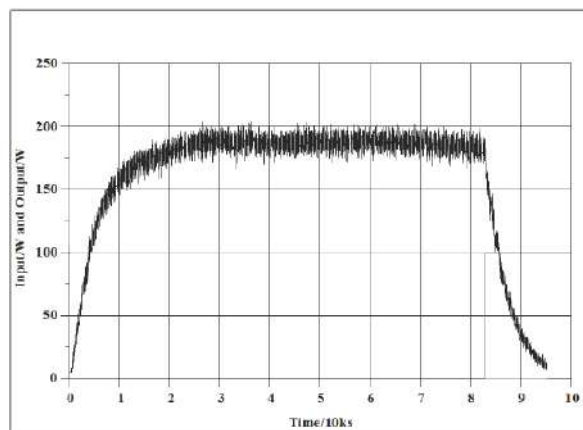


Figure 24. Changes for input and output power for the reactor after treatment of 100 W input.

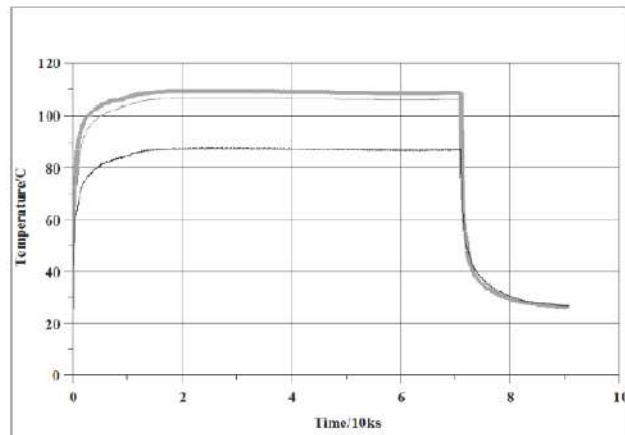


Figure 25. Temperature changes for various position of the outside body of reactor at 100 W of input power after excess heat generation treatment.

Figure 20 shows the temperature changes at the air inlet and outlet during the 100 W calibration. The temperature difference between outlet and inlet reaches 4.5°C at 10 ks after input power is supplied. The inlet temperature is almost the same as the room temperature, which changes by about 5° over the course of one day (i.e. 86 400 s), because there is no air conditioner in the laboratory. The air temperature changes, but the outlet minus inlet temperature difference is nearly constant.

Figure 21 shows the change in power in and power out when 100 W is input to the reactor during the treatment to produce excess heat. The D₂ gas pressure in the reactor was 760 Pa, the same as before (Figs. 18 and 21). Compared to Fig. 18, the output reaches 100 W at 5 ks. This is because excess heat was already being generated, with output of almost 120 W. The input stopped at 70 ks. Thereafter, additional evacuation and discharge processing are performed to increase the amount of excess heat generation.

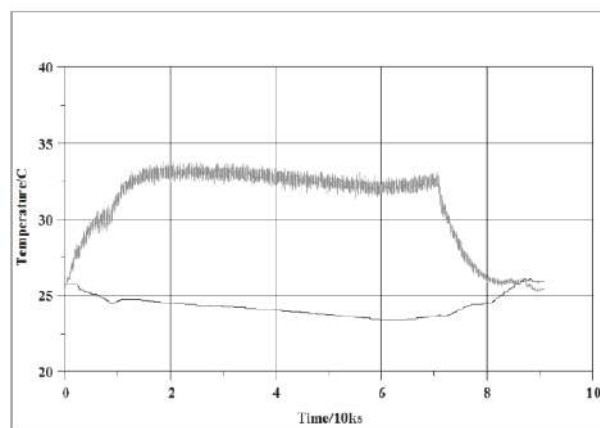


Figure 26. Temperature changes for inlet and outlet of the air at 100 W of input power after excess heat generation treatment.

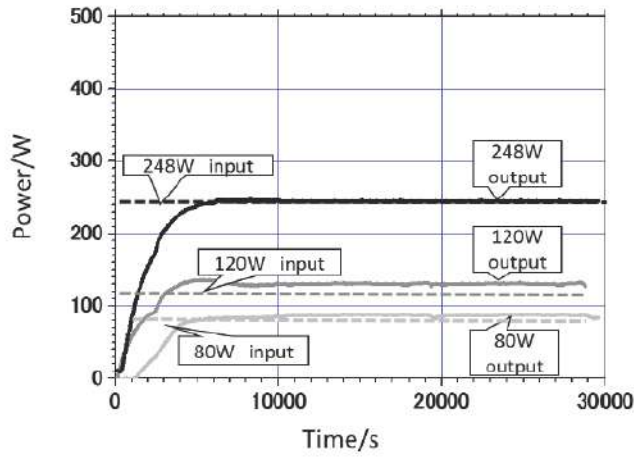


Figure 27. Change in output for calibration reactor.

Figure 22 shows the temperature change of reactor body over time. The temperature is 15°C higher than before the treatment (as shown in Fig. 19).

Figure 23 shows the temperature changes at the air inlet and outlet. The temperature difference between the outlet and inlet reaches 5°C at 10 ks after input power is supplied. The inlet temperature (i.e., room temperature), changes by few degrees during one day, but the outlet minus inlet temperature difference remains constant. The variation of the air inlet temperature is 0.2°C, and the variation of the outlet temperature is about 0.5°C. This is presumably because the amount of excess heat generation varies.

Figure 24 shows the change in power output when input of 100 W to the reactor during after the treatment for excess heat generation. The D₂ gas pressure in the reactor was 760 Pa, the same as before (Figs. 18 and 21). Compared with

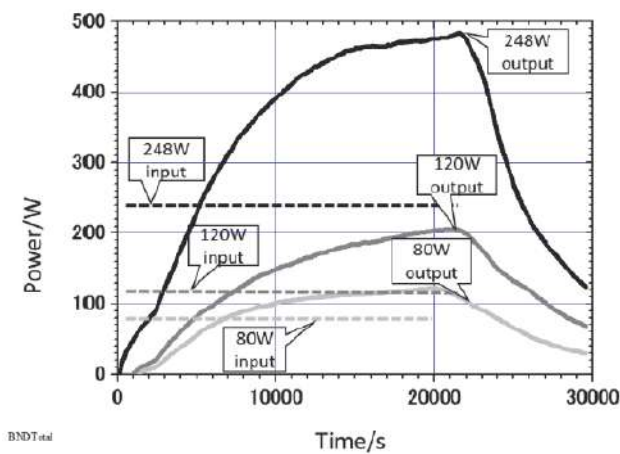


Figure 28. Change in output when input is changed to test reactor.

Fig. 18, the output reaches 100 W at 10 ks. The excess heat was continuously generated, which shows the output power has increased to 180 W. The input power was stopped at 82 ks. The input heat was $100 \text{ W} \times 82.5 \text{ ks} = 8.25 \text{ MJ}$, and the output heat was estimated as 15.19 MJ; thus, the output/input ratio was 1.841.

Figure 25 shows three position of temperature changes for outside body of reactor center and reverse side of the center, and 100 mm from the center of the reactor at 100 W of input power during excess heat generation treatment.

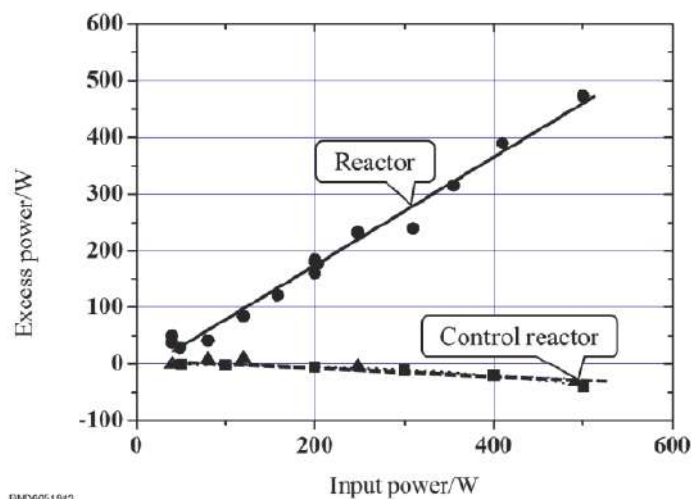
The temperature of the reactor body varies depending on the position. Nickel as a reactant is not present on the entire inner surface of the reactor. As can be seen from Fig. 1, the heater covers only the center portion of the reactor body. Therefore, the temperature varies from place to place in the reactor. The temperature is stable.

Figure 26 shows the temperature changes at the air inlet and outlet. The temperature difference between the outlet and inlet reaches 9°C at 20 ks after input began. The inlet temperature changes by 3°C over the course of 1 day, but the temperature difference between the outlet and inlet is constant. The changing of the air inlet temperature is 0.1°C , and the changing of the outlet temperature is about 0.5°C . This presumes that the amount of excess heat generation is stable.

The calibration test by the control reactor were performed at three input power levels. Figure 27 shows the output power of the control reactor for the input of 80 W, 120 W and 248 W. The output power is confirmed to be the same as input power.

The results of same inputs to the test reactor are shown in Fig. 28. These tests behave differently from the calibration test. The output increases with time. For example, 248 W input is made for 22 ks, the power output reaches 480 W and the Out/In ratio reaches 1.953. The generated power reaches two times input power.

The results of the calibration reactor and the heat generation test by vacuum reactor is shown in Fig. 29. The horizontal axis represents the input power, and the vertical axis represents the value obtained by subtracting the input power from the measured value, that is, the excess power (W_{ex}). The black rectangle mark is the result of the control reactor. As the input increases, the amount of radiation loss due to the temperature rise increases, and the output power becomes lower than the input. As a result, this excess is negative. When there is no deuterium gas (vacuum: indicated by triangle mark) in the reactor indicated by the same results line, the power balance is zero. Given the expected



END06051543

Figure 29. Comparison of several test for various interior reactor conditions.

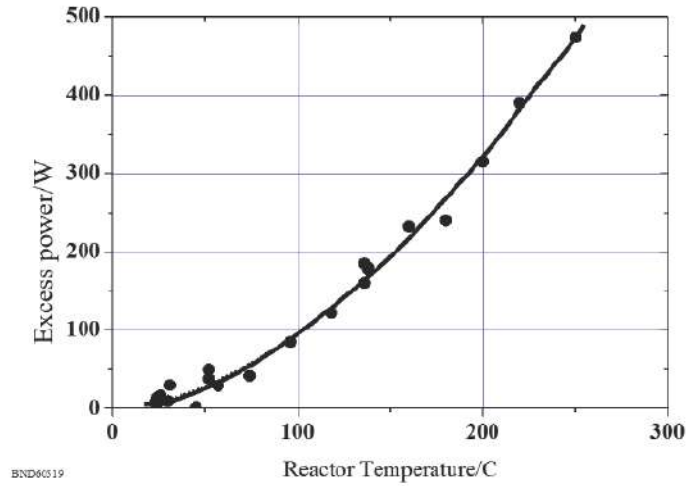


Figure 30. Relationship between excess power and reactor temperature.

losses, a balance of zero indicates slight excess power. This slight excess power is presumed to have been generated by deuterium gas remaining in the reactor. In the excess power generation test indicated by the black circle mark, the reactor body temperature rises as input increases, and as a result, the excess power increases. In this test, excess power is 160 W at 200 W of input power and it increases to 480 W at 500 W of input power.

The relationship between excess power (W_{ex}) and reactor temperature is shown in Fig. 30. The excess power increases with the temperature rise of the reactor. For example, the excess power is 100 W at 100°C, 315 W at 200°C, and 480 W at 250°C. Excess power of 10 W and 20 W was generated even when the reactor was near room temperature.

3.2. Observation of reacting metal

SEM observation of nickel surfaces before and after treatment are shown in Figs. 31 and 32. The surface roughness after processing is remarkable, and its size is not uniform. The particle size was distributed in the range of several tens to 0.001 μm .

The distribution of Pd on the nickel surface after treatment is shown in Fig. 33. In this photograph, it is indicated

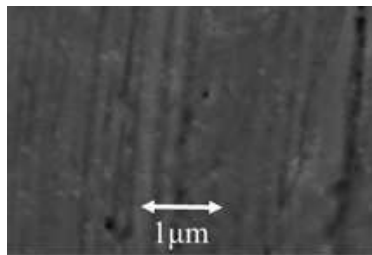


Figure 31. SEM photo of Ni reactant before treatment.

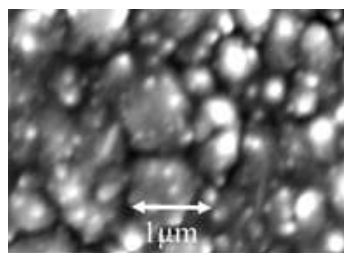


Figure 32. SEM photo of Ni reactant after treatment.

by purple dots. It is almost uniformly distributed. With unprocessed nickel, it is impossible to generate excess heat at all. However, if the surface is covered with particles and further Pd is present on the surface, excess heat is easily generated. The smaller the particles are, and the more Pd is uniformly present, the more the excess heat is generated.

Figure 34 shows the distribution of oxygen after treatment of Ni reacting metal. There is no oxygen observed. When such oxide film, nitride film or carbon are present in large amounts, it is difficult to generate excess heat. Removing impurities completely from reactant metal is one of the important conditions for successful excess heat generation.

Figure 35 shows a SEM image of the nickel mesh after generating 10^9 J of excess heat. Many cracks and peeled parts on the metal surface are observed.

Figure 36 is an enlarged photograph of the sample in Fig. 35. Many granular precipitates are observed on the surface.

Figures 37–39 show the distribution of oxygen, carbon, and nitrogen, respectively. These elements are widely present on the nickel wire surface. In particular, it can be seen that a large amount of carbon is present. It is possible these elements were originally present inside the reactor. However, it is clear that these elements increase on the electrode surface as the excess heat increases.

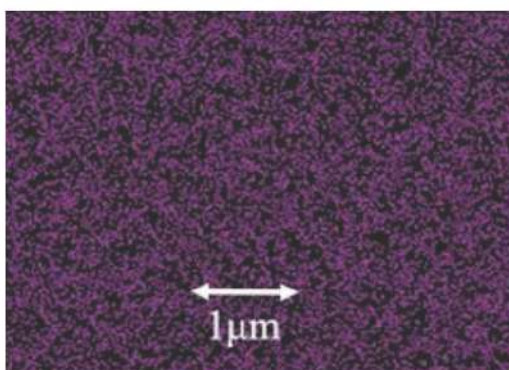


Figure 33. SEM photo of Pd distribution after excess heat generation.

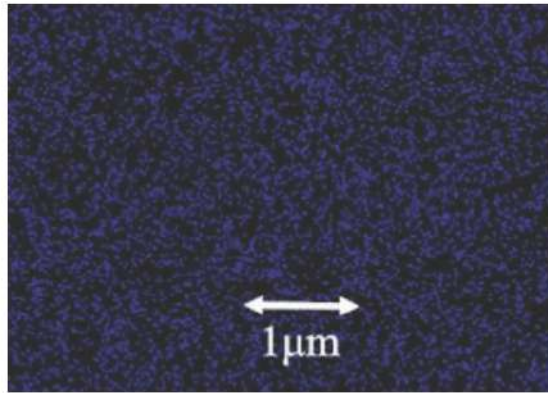


Figure 34. SEM photo of Oxygen distribution after excess heat generation.

4. Discussion

When the temperature of the reactor (T_r) is expressed as the reciprocal of the absolute temperature, as shown in Fig. 40, the excess heat relationship is linear. We speculate that the excess heat would reach the order of kilowatts at $1/T_r = 0.001$, i.e. at T_r of approximately 700°C . We confirmed that the excess heat increases exponentially with reactor temperature. The reaction activation energy E_a was calculated on the basis of the linear region between 100 and 523°C in Fig. 40 to be 0.165 eV/K/atom.

A test with this reactor lasts almost 30 days. Typical excess heat during the time is estimated as 300 W. Total energy is thus $\sim 2.6 \times 10^8$ J. The amount of D_2 used was 20 cm³ STP. Assuming that the reaction is D+D fusion, and assuming that all gases react, the amount of gas required to generate this much energy is approximately 12 cm³ STP. Although this is a very rough calculation, this value coincides with the amount of gas consumed. Granted, this calculation is totally speculation, and there more data is needed to confirm it and to infer the reason for it.

To confirm the anomalous heat generation of the deuterium–metal system, complex thermal factors were narrowed

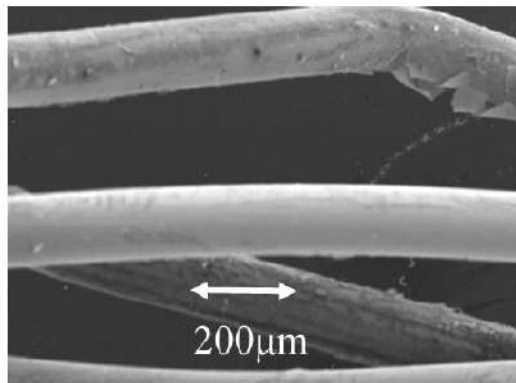


Figure 35. SEM photo of Ni wire after excess heat generation.

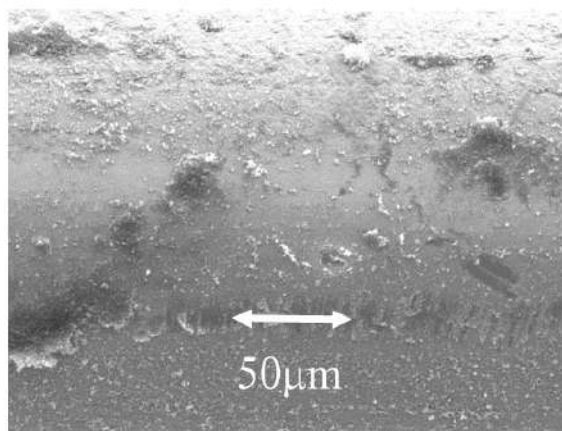


Figure 36. SEM photo enlarged photo 35.

down to two simple factors and analyzed. As a result, we confirmed the occurrence of the anomalous reaction. Factors for thermal analysis are required to change the amount of heat depending on the input power, the amount of flowing air, and the air inlet and outlet temperatures. On the basis of this thermal analysis and the results presented in this work, we presume that the method necessary for anomalous heat generation is as follows:

- (1) Activation of the sample surface to make a fine structure, and addition of surface modification metal.
- (2) Cover the surface with activated deuteride.
- (3) Removal of impurities in the gas.
- (4) Control of the reactor temperature and the deuterium gas pressure.

Activation of the metal surface, that is, removal of the oxide, nitride, and carbide layers, is particularly important. Heating and discharge treatment in deuterium gas is an effective method of activating the metal surface. The use of

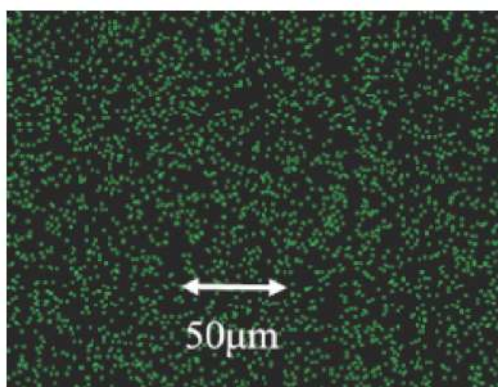


Figure 37. SEM photo of oxygen distribution.

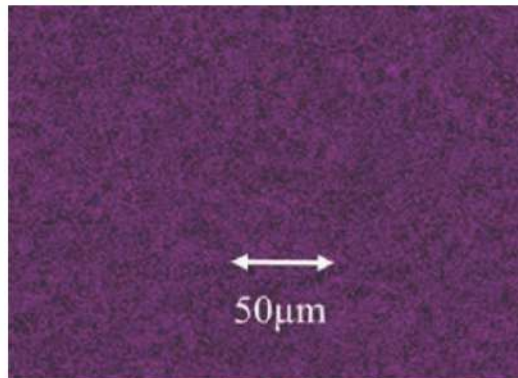


Figure 38. SEM photo of carbon distribution.

highly pure gas and the thorough removal of released gas during the surface treatment are also important. After a reaction metal sample has been fabricated, the activation treatment, where the sample is maintained under a hydrogen gas atmosphere at high temperatures, dissociates deuterium molecules into atomic deuterium on the metal surface, and the amount of dissociated deuterium increases with increasing treatment time. The presence of this atomic deuterium is presumed to be a necessary condition for excess heat. The occurrence of excess heat depends on the temperature, and it is at least on the order of a hundred watts. The excess heat calculated on the basis of the assumption that the reactant was nickel was several 10 W/g and was 1–10 W/cm².

Appendix A

In 2017, we developed a new, simplified method of preparing the electrode material that produces higher heat with better reproducibility. It includes the following steps.

Using 180 mesh nickel.

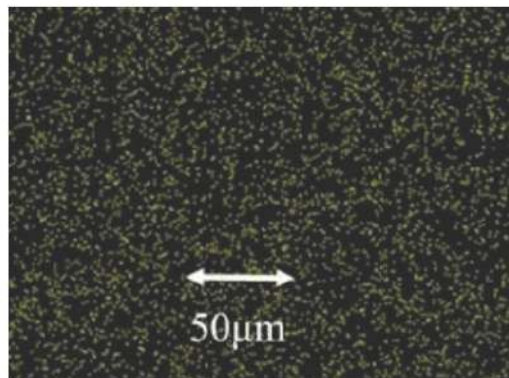


Figure 39. SEM photo of nitrogen distribution.

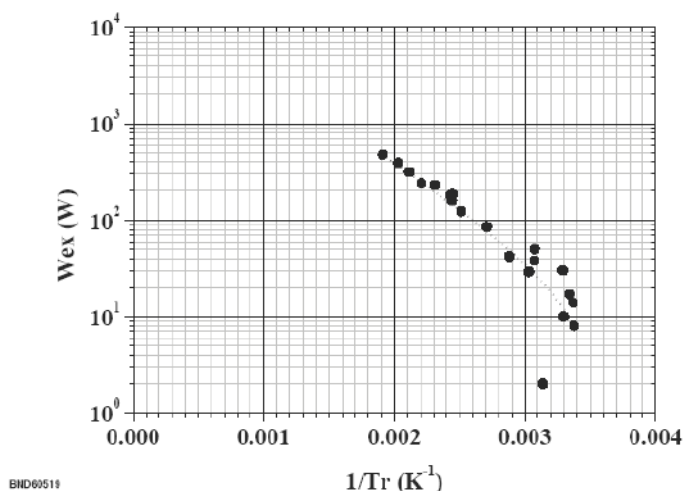


Figure 40. Relationship between excess heat and the inverse of the absolute temperature T_r of the reactor.

- (1) Polish the mesh surface with grade 500 emery paper, and then with grade 1000 paper.
- (2) Wash the surface with hot water. Detergents and the like should be avoided because they may contaminate the surface.
- (3) Rub the surface with pure palladium. The palladium will adhere to the mesh. Alternatively, the palladium can be plated onto the mesh (plating solution: Tanaka Inc., PDMO2LB). This is the key step. In an industrial process, a similar material might be fabricated by some other method such as Nano-sintering.
- (4) Place the mesh in the reactor. Evacuate to degas the mesh.
- (5) Leaving the sample in the vacuum, additional degassing is performed by raising the temperature in stages to 100, 200 and 300°C.
- (6) Introduce D_2 or H_2 gas at 100–700 Pa, and lower the temperature to room temperature to absorb the gas.

We have tested a Pd on a pure Ni surface. We are currently testing with this method. We will describe these results in more detail after enough results have been obtained. In this paper we described only about heat generation. We also analyze neutrons, gamma rays, transmutation, gas analysis and gas isotope analysis. We mainly analyze the correlation between these results and heat. We are preparing to publish a paper on these results.

We believe other metals might be substituted for Pd on Ni, and they might perform better. Pt might be a good candidate.

Acknowledgments

Special thanks are extended to David Nagel for kindly reviewing our manuscript. We also thank Steve Krivit, Dewey Weaver, Hideki Yoshino and Jed Rothwell for support of this study. The author is also grateful for support from the late John O'M Bockris and the late Richard Oriani.

References

- [1] M. Fleischmann, S. Pons and M. Hawkins, *J. Electroanal. Chem.* **261** (1989) 301.

- [2] S. Pons and M. Fleischmann, *J. Electroanal. Chem.* **287** (1990) 293.
- [3] M. Fleischmann and S. Pons, *J. Electroanal. Chem.* **332** (1992) 33.
- [4] M. Fleischmann and S. Pons, *Phys. Lett. A* **176** (1993) 118.
- [5] M. Fleischmann M and S. Pons, *Phys. Lett. A* **187** (1994) 276.
- [6] J.E. Jones, E.P. Palmer, J.B. Czirr, D.L. Decker, G.L. Jensen, J.M. Thorne, S.F. Taylor and L. Rafelski, *Nature* **338** (1989) 737.
- [7] T. Mizuno, T. Akimoto, K. Azumi, M. Kitaichi and K. Kurokawa, *Fusion Technol.* **29** (1996) 385.
- [8] T. Mizuno, T. Ohmori, T. Akimoto and A. Takahashi, *Jpn. J. Appl. Phys.* **39** (2001) 6055.
- [9] T. Mizuno, T. Akimoto, T. Ohmori, A. Takahashi, H. Yamada and H. Numata, *Jpn. J. Appl. Phys.* **40** (2001) L989.
- [10] T. Mizuno, T. Ohmori, K. Kurokawa, T. Akimoto, M. Kitaichi, K. Inoda, K. Azumi, S. Shimokawa and M. Enyo, *Denki Kagaku Oyobi Kogyo Butsuri Kagaku* **64** (1996) 1160 (in Japanese).
- [11] S. Forcardi, R. Habel and F. Piantelli, *Il Nuovo Cimento* **107A** (1) (1994) 163–167.
- [12] S. Forcardi, R. Habel and F. Piantelli, *Il Nuovo Cimento* **111A** (11) (1998) 1233–1242.
- [13] E. Cerron-Zeballos, I. Crotty, D. Hatzifotiadou, J. Lamas Valverde, M.C.S Williams and A. Zichichi, *Nuovo Cimento* **109A** (1996) 1645–1655.



Research Article

Quasiparticles, Collective Excitations and Higher-order Collective Quasi-excitations in Lattice Assisted Nuclear Reactions

Mitchell R. Swartz*

Nanortech Inc., Wellesley Hills, MA 02481, USA

Abstract

Quasiparticles and collective excitations are similar in that they arise de novo from material interactions. They are in need of classification and important because some of them are highly relevant to successful lattice assisted nuclear reactions (LANR). This report reviews this classification along with discussion of their impact on our ability to enable LANR.

© 2017 ISCMNS. All rights reserved. ISSN 2227-3123

Keywords: Coherent excitations, Collective excitations, LANR, Phonons, Quasiparticle

1. Introduction– Overview

Knowledge of collective excitations and quasiparticles and their higher order coherent quasi-excitations helps in understanding the mechanisms occurring in both solid state lattices [1–5] and LANR [6–89]; and why the latter is requisite on the lattice.

Distinguishing quasiparticles from collective excitations and coherent excitations is critical. As a first approximation, these things are closely related. However, upon further examination, distinction between quasiparticles and collective excitations, which can be either coherent or incoherent, give much insight into what they are and their role in successful LANR. Furthermore, recognizing the existence of the higher-order collective quasiexcitations teaches the further relationship(s) of the new particle/object to the real particle/object, offering further exploration of new physics and inventions.

1.1. Quasiparticles

“Quasi” means that something is seemingly or apparently something else that it resembles, but it is not really that thing. Examples in everyday life might include a shadow or one’s reflected mirror image. These are quasi-objects which are the result of something producing something that was not there before.

*Dr. Mitchell R. Swartz ScD, MD, EE, E-mail: nanors@nanortech.com.

So in LANR and material science, quasiparticles are the first group of de novo particles/objects which are created by, and derived from, a real particle or object, or group of them when they interact with extended multibody systems such as a solid metal, or solid plane of glass, or other dielectric. Quasiparticles are induced by an interaction of the original particle/object and the induced quasiparticle, which are closely related things. The quasiparticles are similar to the “parent” real particles that create them, and appear as an “image” or a “reverse image” of the original particle/object that induced them.

The quasiparticle results from the interaction-at-a-distance of the original particle(s) with the surrounding solid polarizable and/or magnetizable material or lattice [1–5]. This follows a change in the material or lattice, sometimes called a “dressing”, in response to the original particle. That word simplifies a highly complex environmental response which having atomic, ionic, orientation, and space charge, polarizations and several types of possible magnetizations.

And there are higher order effects. The end result is a new, real interacting particle/object appearing in space. This quasiparticle can itself react with other particles/objects/masses in space. For example, the changes can impact the particle’s original electric (and magnetic) field(s). They are altered (“dressed”, e.g., by “electric field screening”) and thus, the particle and the environment are each effected by each other and changed. The solid can deform as well as electrically change from the alteration. Simply put, these changes comprise the quasiparticle, which has appeared in space as a response of the multibody stereoconstellation to the object.

Then there comes something new. The quasiparticle exists, and it can behave in a new, possibly anomalous, way.

1.2. Collective excitations

Collective excitations are the second group of de novo particles/objects. Unlike quasiparticles, collective excitations bear no resemblance to the constituent particle(s) of a real system that created them. Nor are collective excitations either the “image” or the “reverse image” of the original particle/object. Instead, collective excitations involve the appearance of an entirely new particle/object that is nothing like the original.

Unlike quasiparticles, a collective excitation involves an entire group, acting together as an aggregate (usually a lattice). Collective comes from the Latin “*collectives*” meaning “gathered together”. They involve simultaneous motion of many physical particles linked together in space.

Collective excitations come from energetic reactions in a group of objects. An example of collective excitations include phonons, magnons, polarons, plasmons and excitons. But the best example may be the case of phonons, that is internal motion of the crystal lattice, itself.

Exactly how they are interconnected determines if the collective is coherent and “in phase” or if they are incoherent. Coherent comes from the Latin “*coherent*” meaning “sticking together”.

1.3. Quasiparticles and collective excitations have real functional roles

The concept of quasiparticles and collective excitations are important to condensed matter physics because they can simplify incredibly complicated quantum mechanical, and macroscopic, many-body problems.

Some critics incorrectly purport without evidence that quasiparticles and coherent and collective excitations are not real. They are quite real and they actually produce many new properties of matter which are quite measurable, such as specific heat, as one example. The heat capacity of a solid crystal has contributions to energy storage from the phonons, and the excitons, and the plasmons, proving they are quite real, and not imaginary.

Furthermore, several of these particles have not been considered previously, and are associated with the metallic lattice [90–114], PdD_x, and the aqueous hydrogen lattice, D₂O [115–128]. Table 1 and Fig. 1 separate these objects/particles into several types, including higher order types, such as quasiparticles of collective excitations. The star (*) next to any name heralds that those quasiparticle/coherent/collective excitations facilitate or are associated with lattice assisted nuclear reactions (called also LENR, LANR, and cold fusion).

2. Background–Lattice Assisted Nuclear Reactions

Lattice assisted nuclear reactions (LANR) [6–89] enable deuterium fusion and perhaps other nuclear reactions and transmutations. The He⁴-heat production manifold is incredibly clean and free of pollution, all toxic emissions, all carbon footprints, all greenhouse gases, and radioactivity, while obviating fossil fuel. The deuterium is plentiful in the oceans. Since 1989, most efforts for robust CF/LANR have failed because of a number of reasons, some which took years to understand, including flawed paradigms, cracked inactive palladium cathodes, contamination (including from ordinary water), improper cell configurations, and especially inadequate loadings (if measured at all).

Table 1. Quasiparticles, collective excitations, and higher-order coherent quasiexcitations.

<p>A. Quasiparticles</p> <ul style="list-style-type: none"> (●) Electric Polaron – electron and its polarization cloud, including surrounding ions (●) Magnetic Polaron – magnetic Moments organized as a magnetic polarization cloud Exciton – bound electron and hole (absence of an electron below the Fermi level) (●) L,D defect – quasiparticle enabling conduction in aqueous systems
<p>B. Collective excitations</p> <ul style="list-style-type: none"> (●) Phonon – collective of mechanical vibrations arising in a lattice Plasmon – collective excitation (quantum) of plasma oscillations (●) Spin-wave magnon – collective excitation of electrons' spin magnetic moments in a lattice
<p>C. Higher order quasiparticle enabling collective excitation or de-excitation</p> <p>Exciton–polaritons, phonon–polaritons, and plasma polaritons</p> <p>Mössbauer-effect couples the entire lattice to a nucleus</p> <ul style="list-style-type: none"> (●) Nanoron – magnetic quasiparticle in magnetized dry preloaded NANOR-type CF/LANR components which produce a second optimal operating point (second pathway) amplifying incremental power gain significantly. (●) Phuson high impedance PHUSOR-type CF/LANR system amplifying incremental power gain significantly. Plasmariton – optical phonon and dressed photon consisting of a plasmon and photon Spinons – observed as quantum spin fluids in Herbertsmithite
<p>(●) Indicates that this plays a role in lattice assisted nuclear reactions.</p>

As always, experiment-derived facts rule. The experimental facts show that LANR research is quite real, and its history shows that it is developing. That development now involves many types of CF/LANR systems. These include the original aqueous electrolytic systems [6–64], which now have a variety of types, ranging from conventional (F+P) [19–22], to electrolytic systems (with solution resistance ranging from conventional to “high impedance” devices in the range of 200,000 Ω or more) [12,13,33–47], to two types of codeposition (JET Energy vs. SPAWAR and Miles) [12,13,49–64]. There are also several nanomaterial systems including preloaded LANR components [65–79], and gas permeation loading [80–82], dual cathode systems [70], ion beam, glow discharge loading cells and other systems [83–87].

They run in both open and closed systems, and driving motors, with on-line monitoring, redundant, high precision, time-resolved semiquantitative calorimetry [13].

Several LANR devices show excess power gains from 25% to many times input electrical power. The preloaded Nanortech nanomaterials show incremental power densities of circa 19 kW/kg [6,73,74].

JET Energy Inc. has shown that some aqueous electrodes, of specific shape, are metamaterials which produce excess heat of a superlative magnitude, successfully driving Stirling engines at the 1–19+ watt excess power level [6,12,13]. In 2003, JET demonstrated a working LANR high impedance PHUSOR-type LANR systems for five days at MIT at ICCF10, producing ~230% excess energy at 1–2 W level [39,6]. Such new LANR technologies, linked helium-4 production [7,11,65], increasing power gains and total energies achieved since 1989, are all paving the way

	Schematic Drawing in Material and LANR Science	Metaphorical Representation
Quasi-particles		
Collective Excitations (Coherent or incoherent)		
Collective Coherent Excitations		 (left – CAM theory shows that a rapid temperature rise in a highly loaded PdD system can initiate catastrophic changes, including deloading and internal deuteron movements)

Figure 1. Schematic and metaphorical quasiparticles and collective excitations. The schematic drawings and the metaphorical representations both show the relationships between quasiparticles and collective excitations and coherent excitations. The first row represents a charged particle and its mirror-image quasiparticle. The second row shows compressional and transverse phonons which are collective excitations. The third row shows catastrophic release of D_2 in suddenly heated, loaded PdD. On the left are graphs and schematic cartoons that attempt to visualize a small portion of a very complex material science stereoconstellation. On the right are the metaphorical representations.

to an important, new, clean form of energy production: LANR.

2.1. LANR/CF is consistent with conventional physics

LANR/CF is consistent with conventional physics, and analysis of the quasiparticles and collective excitations requisite for success demonstrate that. But successful LANR remains very difficult to achieve. The first key for successful LANR is that the PdD_x alloy must be driven, usually electrically, to extremely high loading, until it is filled and

almost saturated like a sponge with water, and near-bursting like an over-filled balloon. The electrode must accept and maintain high loading for excess heat (>90%), for a sufficient incubation time, up to several hundred hours [6,88,89].

Why? Vacancies must drift into the bulk from the surface, energetically facilitated by the loading itself [6,129,130]. The vacancies are the site where the desired reactions occur. The vacancies must be formed, diffuse in, and be filled before the material is destroyed. The additional, difficult to achieve, keys for successful LANR, is that there must be integrity of the loaded alloy. This is a condition which is circumvented to some degree by the codeposition methods, albeit with their limitations [55].

The dynamic control is complicated. As the lattice loads, it swells. Too much swelling yields irreversible failure, just as a burst balloon.

The fuel for LANR is the deuteron. The deuterons are driven onto the surface of the metal by the applied electric field intensity, using electrochemistry [131–134], or by gas pressure applied. They diffuse and are driven into the metal, sometimes being driven into the vacancies, especially by the Catastrophic Active Media (CAM) reactions (described by the CAM theory; discussed below [135,136]).

In LANR, excess heat and He⁴ [7,11,65] are the usual products, and tritium [8–10], charged particles, gamma radiation and the sequelae of neutrons [50, 52–54,66,67] can be sometimes detected.

Melvin Miles of China Lake with Johnson–Matthey Pd rods was the first to show the correlation of heat and He⁴ production. Arata and Zhang reported de novo He⁴ with LANR, including with Zr₂O₄/Pd powder exposed to deuterium gas, but not with hydrogen gas. Les Case using LANR with platinum group metals on carbon catalysts, reported He⁴ production from deuterium gas.

As a result of these findings, but ignoring the intermediates and the impact of the lattice for the moment, the reaction is something like



In most cases, the product is an extraordinary amount of heat. That product is created at above-normal levels of electrical dissipation, called “excess heat”. The LANR-derived “excess energy” begins at high energy, in the excited state of helium, which is obtained from reactions between deuterons within the lattice. That He⁴ excited state is either the first excited state, or one energetically located above it, all at least 20 MeV (20 to ~23+ MeV) above the ground level. This is significant in magnitude and clearly not “low energy”, as often (mis)claimed. As such, purported “low energy nuclear reactions (LENR)” are a misnomer, a paradoxical description of what is actually not observed. Fortunately, they are high energy reactions. An actual LANR sample comprises a population of ~10²⁰–10²² candidate nuclei (among deuterons at ~1:1 ratio) which if active fuses ~10¹² deuterons/s for each 1 W of excess heat produced. The mechanism will be discussed below, with consideration of the CAM and PHUSON coherent excitations, as Eq. (1) is greatly expanded.

2.2. Lattice assisted nuclear reactions may occur at different locations

Three regions are postulated as potential LANR sites. This (called “3RH”) is suggested by existence of three optimum operating point (OOP) manifold groups – known to characterize all LANR systems [33–36,137–143]. It is heralded by, and also consistent with, some experimental data, including our report of (at least) two time constants characterizing “heat after death” (HAD) excess heat [31,43,44]. We previously reported at ICCF10 and thereafter, that the loaded active palladium lattice’s deuteron-loading capacitance is ~64 mmol/V*. The systems’ admittance for the desired excess enthalpy (measured during “heat after death”, also called ‘tardive thermal power (TTP) reactions’), is ~7 pmol/s-V* and that capacitance is dwarfed by the system’s deloading admittance for loss of deuterons during outgassing which follows turning off the electric field intensity, and that is ~15 nmol/s-V*. The kinetics reveals HAD evanescent heat generated by two (or more) sites [43,44]. Most of the sites have TTP which falls off with a time constant of several

minutes, but some of the sites had a time constant of ~ 20 min to hours. This is consistent with vicinal surface and deeper sites, with the longer time constant associated with the deeper location within the lattice.

The three different regions of physical locations distinguished are: Region 1 involves the most superficial portions of the palladium, including surface dendrites and a variety of micro- and nano-particles, that characterize electrodeposited, and codeposited palladium alloys involving and at least several atomic layers. These surface sites, generated via codeposition and conventional LANR produce tritium [8–10,49]. Located deeper in the metal, subsurface Region 2 is the metallic lattice physically located beneath Region 1, existing as a thin rim under the surface in the range of $40 \text{ m}\mu$ to mm. Subsurface sites (Region 2) yield heat and helium production and transmutation products [7,8]. They characterize conventional LANR (“FP”) systems which make excess heat with commensurate helium production in palladium with heavy water, and excess heat with nickel systems in both light and heavy water.

Region 3 represents deeper sites, or spatially, deeper sites in the metallic lattice or palladium-black systems which efficiently yield heat and helium production. Region 3 is less commonly involved in LANR, perhaps only in the very rare reports involving (“paroxysmal”) energy release from larger volumes. It appears to be involved with Arata’s palladium black in dual cathodes and the NANOR-type preloaded LANR components. These three regions have been analyzed. We corrected, and expanded Nagel’s surface monitoring equation [85] to the modified, volume-corrected, multi-site, Excess Power Generation (EPG) equation [36] for use with OOP manifolds [33–143]. The EPG is shown in Eq. (2) is a double summation (or double integral) where the summation is over each of the three regions, and over depth within each region. The area is A . E is energy per reaction and XSE is the excess energy, so dividing it by the time, T yields the excess power, XSP.

$$\text{XSE}/T = \Sigma\Sigma[A * (\text{depth})] * F_{\text{vol}} * [N/(A * \text{depth-sec.})] * F_{\text{theor}} * E = \text{XSP}. \quad (2)$$

Summation occurs over each of the sites (or layers), in the surface, subsurface and deep volume. The first term on the right hand side of the equation is the actual volume involved with active foci, followed by the fractional active palladium sites with defects, etc., as required, within that volume, followed by the reactions per second at each of those sites within that volume, and finally a theoretical term (between 0 and 1).

E is the energy per reaction (circa 24 MeV per fusion reaction from the estimations of Miles, McKubre, and Apicella/Violante [6,7,11, 114], or perhaps 2 MeV less based on the theoretical considerations [161]). F_{vol} is the functional number of the volume of each site (or layer). It could be 1, or less if the nucleus required is blocked from entry (e.g., deuterons blocked by hydrogen). N is the LANR reaction density, or the number of reaction sites per A , by layer. If N are taken as the vacancies, they may vary at the different regions, such as being very high in the codepositionally created volumes.

In the equation, F_{theor} represents several factors that control, or throttle, the coupling of the He^{4*} to the lattice. When it varies from 0 to 1, it can thus handle the Coulomb barrier problem by using several theories and factors [144–166], the most important of which will be discussed below. Some factors might relate to needed loss of the de novo helium-4 generated from the active sites, which might be much higher near the surface region than in the bulk region. Other factors may include magnetic interactions such as have been reported with dry, preloaded NANOR-type systems [79].

If the active sites are taken as vacancies, for normal Pd and some PdD levels, this has been investigated by several means, including discussion of the Fukai state which is the maximal level achievable experimentally, and the “healing” that occurs as the lattice tends to reform from those peak vacancy states [129].

3. Electric Polarization and Electrical Conduction

Electrical polarization is ubiquitous. All materials are characterized by their response to an applied electromagnetic field. The applied electric field intensity, E , results in an electrical conduction within the material, and via the electrical

conduction process (and there may be many), there follows the linked electrical polarization. It is these polarizations (ionic polarization, atomic polarization, orientation polarization, space charge polarization, and domain polarization) which make each material unique.

Electrical conduction and polarization are, and must be, related because any motion of charged particles, and of molecules with distributions of charge, necessarily result in both conduction and subsequent polarization as a result of the motion. As a result, these two aspects of the complex permittivity are also related through the Hilbert space.

There are many types of electric polarizations. Electric polarization is very important because of the many ways it relates to LANR (and so much else). For example, other electrically charged particles also induce polarons, including from deuterons, when they are loaded in the palladium or nickel cathodes

3.1. Role of frequency and E-field intensity

Figure 2 shows the types of electric polarizations that can occur. Notice that fewer types of electrical polarization become available at increasing frequencies. This falloff of contribution occurs because heavier masses cannot keep up with the driving frequency of the applied electric field intensity at higher frequencies.

As Fig. 2 demonstrates, the complex dielectric permittivity is a function of frequency. At low frequencies, the induced (“second-order”) magnetic field can be neglected and so what is important is only the response of material to an applied electric field intensity. That said, it is also important to recognize that the E-field may be quite large locally. Depending on the materials, solutions, and electrodes, if irregularities are present at an electrode, for example spikes on a cathode, and if charge carriers are present in the solution, then the electric field intensity distribution can change dramatically with tens of thousands of volts per centimeter suddenly appearing over, or near, such irregularities.

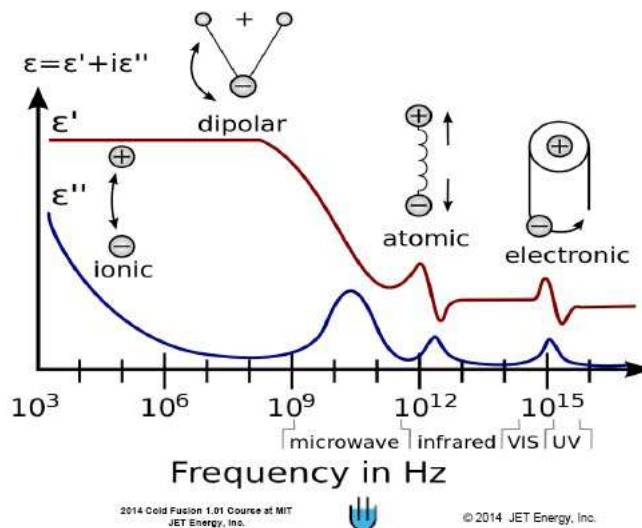


Figure 2. Real (ϵ') and imaginary (ϵ'') parts of the complex dielectric permittivity of a hypothetical material as a function of frequency. Shown are four types of electrical polarization. Each polarisation/conduction has an imaginary contribution, with a peak, (blue curve) adding to the electrical conduction. From von Hippel “Dielectric and Waves” [124].

3.2. Complex relative permittivity

From a mathematical point of view, the electric polarization (κ') is the real part of the complex relative permittivity (κ^*).

$$\kappa^* = \kappa' - j\kappa'' \quad (3)$$

ϵ'_0 is the permittivity of a vacuum. When the permittivity of a material, ϵ is divided by ϵ_0 , the result is κ' which is the relative permittivity. This is called the “dielectric constant”. However the term “dielectric constant” is itself a misnomer because it is not a constant, but changes with, and usually decreases with, frequency. That said, for most materials only electric and ionic polarisation are significant, and therefore the dielectric constants of almost all materials, except ferroelectrics and water/ice (vide infra), are usually in the range of 3–6.

The electrical conductivity of a material is mathematically described by the imaginary part of the complex permittivity and is the product of the electrical conductivity and the angular frequency.

$$\kappa'' = \sigma * \omega. \quad (4)$$

4. Quasiparticles

A quasiparticle generally results from the interaction of a constituent particle with the surrounding solid polarizable or magnetizable material. Several types of quasiparticles are described in this section.

4.1. Electric polaron – Electron and its polarization cloud, including surrounding ions

Perhaps the simplest example of a quasiparticle is the “electron quasiparticle” or “polaron”. A polaron is a quasiparticle which comes about when an electron (and its surrounding electric field) interacts with its surrounding ions, which may be free to move, and then distorts the stereoconstellation of those positive and negative ions around it.

First, the important point here, for this moment regarding polarization (including in water), is that quasiparticles can be induced. For example, if and as the electron moves, the surroundings are perturbed in complex way producing a sort of tunnel through which the electron can move. Attention is again directed to the fact the differences between the real free electron particle, and the one moving through a lattice, driven by an applied electric field, as an electric polaron quasiparticle is created. In the latter, the electron behaves as if it had a different, heavier mass due to exchange and correlation interactions with all the other charged particles, despite their having the same charge and spin.

4.2. Magnetic polaron – Magnetic moments organized as a magnetic polarization cloud

Magnons can be created as two types of quasiparticles and one type of collective excitations. First, one magnetic quasiparticle occurs as the L and S moments (angular magnetic moments of electrons in atoms) couple as J, and as described in quantum chemistry. Thereafter, second, the single magnetic moment is oriented and can magnetically polarize the lattice or environment around it. This is the magnetic equivalent of the electric polaron. However, although the impact on the medium is similar, the interaction forces are much weaker.

4.3. Exciton – Bound electron and hole (absence of an electron below the Fermi level)

What is a “hole”? It is the absence of some material, particle, or object (Fig. 3). Consider a pearl falling into a thick shampoo solution (e.g. from the 1960s Prell shampoo commercial, <https://www.youtube.com/watch?v=9IFsrjoLKq0>).

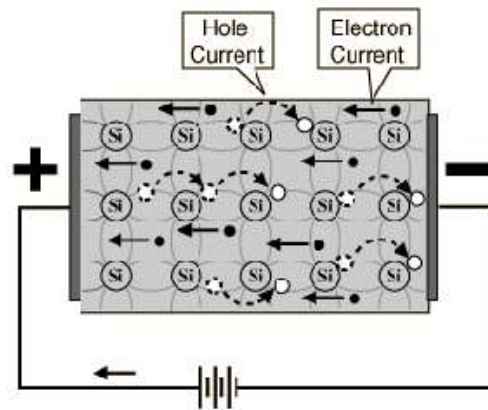


Figure 3. Schematic of the electrical conduction through a semiconductor material driven by a battery. Holes and electrons both contribute to electrical conduction.

The flow analysis can either be based on Eulerian coordinates simply following the flow of the fluid around the pearl (requiring solution of the fluid flow as a $f(x, y, z, t)$, first, and using the convective derivative) OR based on Lagrangian coordinates following the transit through the thick solution (with the location of the pearl as a $f(x, y, z, t)$). The latter is much easier to calculate. In solid state physics, a hole similarly consists of a missing electron from the valence band of the crystal semiconductor. The hole is a quasiparticle in the “reverse image” of an electron, and it can interact electrostatically, much like an electron. That is because the hole is functionally and relatively electrically positive, opposite the charge of the electron. Thus, the hole can interact electrostatically with the electron and even produce a bound state with a measurable binding energy. The interaction creates yet another quasiparticle, the “exciton”, which results from the bound electron and hole and their interactions, together.

4.4. L,D defect – The quasiparticle enabling conduction in aqueous systems and the loading of Pd and Ni

The hydrogen-derived quasiparticle, and particularly relevant here, the deuteron-quasiparticle, must be considered because they each create L- and D-defects in heavy water, and their ferroelectric inscription patterns. This is one of the most important quasiparticles in CF because it is THE origin of the fuel for LANR via the deuteron to He^4 fusion reaction for most aqueous CF/LANR systems, such as the classic F-P system, the codepositional, the high impedance, and PHUSOR[®]-type system. In each of these, the deuteron is driven into the metal by the applied electric field intensity.

In most cases the product is gas evolution, and in successful CF/LANR there is also produced an extraordinary amount of heat and nanoscopic quantities of *de novo* He^4 . Understanding this important quasiparticle begins with the requirement of considering the structure of water and, therefore, ice.

4.4.1. The nano-structure of water – There are two lattices in water and ice

Water is not a gas but has a three-dimensional stereoconstellation, and surprisingly it has both elements of order (the oxygen atoms) and disorder (the protons or deuterons).

Water’s atoms of oxygen and hydrogen (or deuterons) are arranged in structures with definite physical rules and it is best understood as a complicated three-dimensional structure comprised of two lattices. The lattice of the protons

and/or deuterons is located within a second lattice (the oxygen atoms). The most important point is that *there are two lattices* and that the proton lattice is often totally ignored. Much has been learned by studying the protons, their electric dipole moments, and their entropy, which result from their distribution and decoration upon the organized oxygen lattice.

The fact that water has a second proton lattice within it means that water has not only singular properties, but has an incredible impact upon both the properties of materials dissolved within it (including clathrates, hydrates, biological systems, etc.) and the operation of systems using it. Additional complexities occur because the hydrogen in water could be the rarer heavy hydrogen, deuterium, which is the desired fuel in CF/LANR and is used at the 98–99.95% levels in the best CF/LANR systems.

4.4.2. *The organized oxygen lattice*

Water is actually two lattices [115]. First, there is the spatially fixed oxygen lattice, which is a hexagonal lattice (Wurtzite type). It is an ordered lattice and is “decorated” by a second proton lattice, which is disordered in ordinary ice (Ice 1_h).

Deuteron Bond/Hydrogen Bond – Etiology of the Ordered Oxygen Lattice

The origin of the oxygen lattice of water begins with electronegativity of the oxygen atom. That electronegativity creates asymmetry by the displacement of the electron clouds toward the oxygen atom. With that resultant asymmetric redistribution of electronic charge within the water molecule, there then follows the creation of unbalanced (positive) charges at the hydrogens (or deuterons) and negative charges in the form of two “free” (negative) sp^3 lobes surrounding the oxygen nucleus and creating the tetrahedral appearance.

The H-bond process immerses a proton into an electronic cloud of a second neighboring water molecule, creating one hydrogen bond by neutralizing charge. The Coulombic neutralization is large, and on the order of 4.5 kcal/mol (compared to the relatively much less “background thermal energy” which is only $k_B T \approx 0.6$ kcal/mol) making the hydrogen bond thermally stable.

This asymmetric charge redistribution produces both an intramolecular dipole moment, and most importantly can result in a “hydrogen bond” (or “deuteron bond”) by having two (or more) water molecules self-assemble. These hydrogen bonds are ubiquitous, partially due to the low steric requirements of the protons (from the ability to rotate). Then, something wonderful happens.

The water molecules are linked by hydrogen bonds into a complicated tetrahedral system locally and regionally. First, the structure of water and ice on the atomic scale is associated with tetrahedral symmetry from the orientation of the oxygen atom (Fig. 4). Each water molecule is engaged in four hydrogen bonds. In two, the hydrogen atoms are about 1 Å from the origin, whereas the other two hydrogen bonds have hydrogen atoms from neighboring water molecules which are more distant. This difference is critical and creates the electric dipole moment and the proton disorder [115–128].

4.4.3. *The disordered deuteron lattice*

The proton disorder of water’s hydrogen sublattice leads to the unusual electric conduction and polarization properties of water. Most importantly, the proton disorder creates the large dielectric constant of water that enables water to dissolve so many materials. Furthermore, the proton disorder of water/ice contributes to the great heat capacity of water (the ability to absorb heat with a negligible increase in temperature).

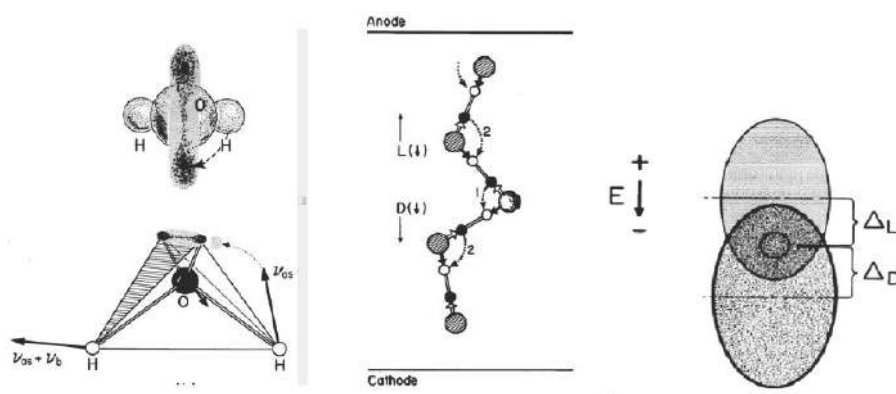


Figure 4. (Left) Water's tetrahedral structure permits intramolecular proton transfer making L and D defects. L- and D-proton defects initially arise from infrared vibrations. Here one such vibration launches a proton from one oxygen electron orbital to another creating the paired defects. (Middle) The diffusion of L, D defects inscribe ferroelectric dipole moments recorded by dielectric spectroscopy. (Right) an applied E-field makes L and D defects move through the lattice and creates drift ellipsoids of leaving the inscribed ferroelectric polarization, from these quasiparticles, onto the aqueous lattice (seen macroscopically).

4.4.4. The macro-structure of water

How is water like ice? In water, only about one-seventh to one quarter of the hydrogen bonds are broken compared to fully frozen ice. This can be quickly shown as follows. Consider the ratio of the heat of fusion (which is what takes ice to water) to the heat of vaporization and fusion and two other terms. The first additional term in the denominator is the 100 calories required to reach 100°C. The second term arises from the fact that ice is not truly a solid (consider the surface during skating) until -30°C, which adds yet another 0.5 cal/g-°C of the material to the denominator. This ratio supports the details and conclusions outlined above, that the only correct conclusion is that the majority of hydrogen bonds in water are intact.

The structure of water appears to be a mixture of Ice 1_h (50%), Ice 2 (30%), and Ice 3 (15%). Probably much more subtle variation exists, and certainly so near any electrode, double layer, and/or energy system. Ice 1_h is the hexagonal form of ordinary ice, ubiquitous on Earth. By contrast, Ice I_c the metastable form characterized by cubic symmetry, and only obtained at high pressure.

4.4.5. Large dielectric constant of water and ice

For most materials the dielectric constants are usually in the range of 2–6. However, for water and Ice 1_h, the arrangement of the molecules permits proton disorder in the sublattice and thus introduces a new method of electric conduction and polarization (Figs. 4–6), and the result is a much larger dielectric constant; a whopping 92 for ice, and 88 for water [115,126–128].

The unusually large dielectric constant (= the real part of the complex permittivity) of water is particularly important because it both distinguishes it from most other materials and because it enables diverse reactions ranging from chemical solvation to free radical reactions, which can then occur by shielding free charge and unpaired electrons, respectively.

It is water/ice's proton disorder and the drift of L,D defects which creates the unusual dielectric properties of water.

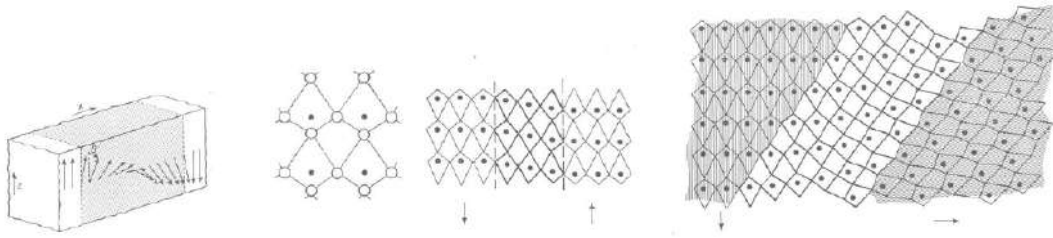


Figure 5. Spin wave magnons can quantum link regionally different domains of magnetic polarization in a lattice. Here they are shown schematically (*above*) as a spin wave; and (*below*) as the domain representations showing the domain shears.

4.4.6. Deuteron disorder and L, D defects

Normally, there is one proton between each pair of oxygen nuclei (Fig. 5), but not always. L and D defects initially arise from infrared vibrations, as suggested by Bjerrum (Fig. 6). A D-defect has two protons between any two oxygen nuclei. An L-defect has none.

Thus, with sufficient background thermal energy there are created many L and D defects throughout the volume of water or ice. Then, the action of an applied electric field intensity to that sample of water/ice results in an electrically induced drift of these intramolecular proton (and deuteron) defects.

4.4.7. Conduction/polarization phenomena – L, D defects quasiparticles and their diffusion

The result of an applied electric field on the L- and D-defects is that the E-field inscribes a series of intramolecular defects into the water lattice (cf. Fig. 4). The inscribed defects create a large electric dipole moment.

Over vast distances, the L- and D-defects migrate in an applied electric field intensity. The normal spheroids of defects distort into field-directed ellipsoids, which are shown. As the defects migrate, they leave trails of proton order which are slowly erased by thermal action. Their movements inscribe into the proton sublattice a generally field directed electric dipole moment, as von Hippel and others at the Laboratory for Insulation Research (MIT) have shown.

It is this inscribed electric dipole moment which creates the large dielectric constant. Those who work with cold fusion and energy conversion systems involving water ought to consider these defects, referred to above, which markedly impact the proton disorder and the characteristics of water and ice.

In heavy water, the small ratio of electrical energy compared to $k_B T$, produces drift ellipsoids of L- and D-deuteron defects. This yields a cathodic “fall” of deuterons, a double layer in front of the electrode surface. The concentration polarization produces very large local electric field intensity, ranging from 10^4 to 10^7 V/cm [131,5]. The double layer is a relaxation response, and not a resonance response. Transfer of deuterons through it can be enhanced by light [42], however.

In summary, the applied electric field intensity causes E-field directed movement of the quasiparticles formed of the defects. The high dielectric constant of water actually results from movements of protons in and through the proton lattice creating a ferroelectric inscription with several important implications.

4.4.8. Dielectric spectroscopy of water/ice

These phenomena are observed and measured by dielectric spectroscopy. Dielectric spectroscopy is the study of a material’s electrical properties as a function of frequency. When water is examined by AC electric fields, from approximately 8×10^{-3} to 10^7 Hz for ice, higher for water. There are resolved several complex dielectric relaxation

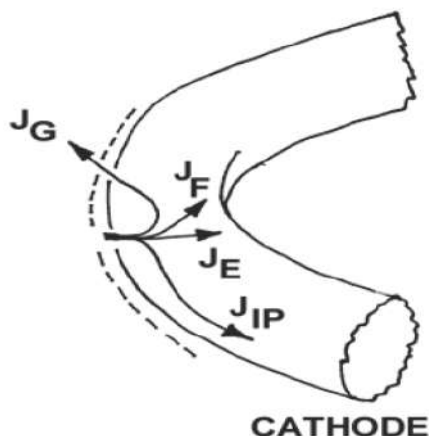


Figure 6. Schematic showing the deuteron flows at a cathodic electrode metal surface. The solution is to the left. At the metal surface, several components of deuteron flux must be considered; entry into the metal (J_E), movement to gas evolution (J_G), and an extremely tiny loss by potential fusion reactions (J_F). J_{IP} is a pathway afforded with a metamaterial [163].

spectra resulting from the proton sublattice and the movements of L- and D-defects (e.g., confer Fig. 6). Even the “purest” Ice 1_h has seven (7) discrete subspectra (not all are seen in Fig. 7). More information is in IE [115] and von Hippel’s texts [126–128].

The largest (“major”) subspectrum (previously, formally called spectrum #3) of water and ice is most related to the classic “dielectric constant.” It does not result from water molecules spinning like tops as is popularly supposed. Also it does not result from rotation of the water molecules, as is also popularly supposed. In fact, it could never

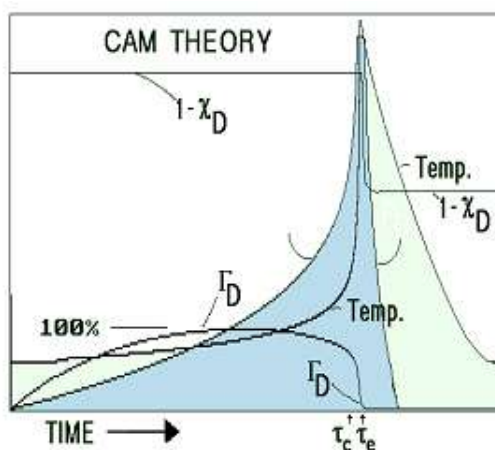


Figure 7. This graph shows the theoretic results of a sudden catastrophic active media (CAM) desaturation of a palladium electrode with respect to deuterons. As the palladium heats up (in positive feedback), the solubility of the D in it decreases, leading to a massive falloff of the fractional saturations (D/(PdD) % defined as Γ_D). This drives the deuterons by the CAM catastrophic desaturation into the vacancies which are the site of the LANR reactions. The time constants, τ_c and τ_e , and the other variables, are discussed further in the original paper [135,136].

result from either because the ratio of the hydrogen bond energy to the thermal energy is so large that the bonds are stable. Simply put, the structure of water and ice are too energetically bonded and energy-expensive to enable the 13.5 kcal/mol required for any such rotation, or the 18 kcal/mol required to rip a water molecule out of an intact lattice.

Hence the high boiling point of water. By contrast, the high dielectric constant of water actually results from movements in the proton sublattice, that result from the electric field-directed movement of defects in the proton sublattice.

5. Collective Excitations

In contrast to quasiparticles, collective excitations result from aggregate behavior (of the lattice, or dielectric, or even plasma) and bear no resemblance in any way to the aggregates components and constituent particles. Some involve motion of many physical particles linked in space, like phonons or plasmons, that are from atomic and electronic motions within the crystal lattice, itself.

How they are connected determines if it is simply incoherent collective, or truly coherent collective excitations.

5.1. Collective excitations – Phonons – Quantizations of mechanical lattice vibrations

The first example of a collective excitation is the phonon. A phonon results from the coherent vibrational motion of the local periodic atoms comprising the crystal lattice. Phonons occur widely because all lattices, in which the energy is invariant under a rigid translation of the entire lattice, must have at least one acoustic mode (sound wave) with resultant collective, coherent, oscillations of the crystal lattice. Unlike fermions, phonons are bosonic quantized lattice vibrations meaning that an arbitrary number of phonons can be excited in each phonon mode.

In successful LANR, there are enough phonons (lattice vibrations) to act coherently, to enable coherent energy transfer (from where the excess heat arises for the just-formed high energy helium excited state to shed $\sim 20+$ MeV to the lattice [6,144–147,149,156–162] as the He^{4*} returns to the He^4 ground state. Hence the “excess heat”. Ergo, it is the lattice – and specifically phonons – that open up the new pathway.

5.2. Collective excitations – Plasmons – collective excitation quantum of plasma oscillations

Plasmons are the quanta of plasma collective oscillations and excitations. They can occur both in lattices and in electron gases and plasmas where all the electrons oscillate synchronously with respect to all counter-ions via Coulomb interactions. Plasmonics goes even further and uses optics and nanoelectronics to make novel devices. However, present plasmonic devices suffer from ohmic loss and electron-core interactions [177].

5.3. Collective excitations – spin-wave magnon in a lattice

Spin wave magnons are quantum magnetic spin waves collectively excited in the crystalline lattice. They exhibit new degrees of freedom as they arise from the interaction of the electrons’ magnetic spin structure (already a quasiparticle) with the crystal lattice within which it sits. The result is the quantum spin wave (Fig. 5) [178,179].

6. Higher Order Quasi-particles of Collective Excitations

Unlike quasiparticles, collective excitations result from the ORGANIZED aggregate behavior within the object (usually a lattice). A coherent collective excitation is one which is united and forms an entire uniform constant phase relationship.

Examples are given in Table 1 and below.

6.1. Quasiparticle avoiding collective excitation – Mössbauer effect

The first example is the Mössbauer effect [167–175] which works by coupling iron nuclei in the crystal lattice by with the iron atoms' electronic s-orbitals. The Mössbauer effect is recoil-free emission and absorption of gamma radiation by a nucleus contained in a solid lattice. Although momentum is conserved, the entire lattice coherently is involved in the excitation and/or de-excitation. In the Mössbauer effect, the lattice as a whole recoils and thus the recoil energy is very well defined with no phonons involved, and thus (inaccurately) called “recoil-free”. Importantly, this leads to very narrow line-widths (with a Q of $\sim 10^{14}$ vs. a laser with a Q circa 10^{10}). This is important to CF/LANR in that it absolutely demonstrates the existence of nuclear coupling to the lattice by demonstrating conclusively that the nucleus is connected to the lattice through the s-orbitals, which do not go to a probability of zero at the nucleus.

6.2. Complete theory of CF/LANR

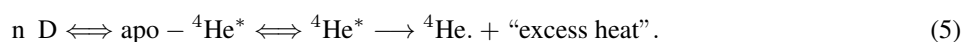
6.2.1. Quasiparticle enabling collective de-excitation

Successful LANR begins with loading of the lattice, the kinetics of which can be described by the quasi-1-dimensional model of loading. LANR, after loading, then has at least two coherent excitation/quasiparticles in its successful action. These sections will describe the pathway to successful activity in LANR. What is described here is a multistep process to LANR.

Then there occurs a coherent excitation involving the catastrophic active media forming deuteron flux and very rapidly filling of the vacancies (CAM theory). Under some circumstances, as discussed by Takahashi, Scott and Talbot Chubb and others, there can occur in the lattice the formation of excited helium 4 (${}^4\text{He}^*$). Finally, in the fourth irreversible step there is the de-excitation through the PHUSON coherent particle [161]. These steps, and the energy levels explain the observations of LANR – including the excess heat, and the lack of significant emissions.

6.2.2. CF/LANR first requires loading

As discussed at ICCF-4, we suggest a series of reversible reactions which lead up to a final irreversible step. The series includes an intermediate state which is called apo- ${}^4\text{He}^*$ (meaning that which occurs before the ${}^4\text{He}^*$ is seen). apo- ${}^4\text{He}^*$ is on the way to becoming the excited helium state, ${}^4\text{He}^*$, located about 22 MeV above the ground state of helium. If the conditions are perfect, ${}^4\text{He}^*$ can then become de novo ${}^4\text{He}$ and heat the lattice, where it appears as “excess heat”. If successful, then in the highly loaded lattice (n D within the Pd, which is ignored in this equation):



Step 1 – (a reversible step) Loading of palladium by deuterons

The LANR reaction begins in the extremely difficult-to-achieve highly loaded Group VIII lattice. There is a critical content of loaded Pd for activity, generally described as a requirement of $>\sim 0.85$ (McKubre, Tanzella and others [6]). Understanding this system requires continuum electromechanics and not electrochemistry.

6.2.3. CF/LANR requires deuteron flux

Deuteron flux is examined here by the quasi-1-dimensional model of loading which shows that conventional “electrolysis” is WRONG and a “red herring”, and is why many have trouble achieving successful LANR. The Q-1-D equations [140,141] show the way to optimal results. These equations explain some of the difficulties $\sim 1989+$ and they DO NOT DEPEND upon equilibrium conditions, and in fact they make successful predictions (both unlike the relatively useless Nernst equation).

Figure 6 shows a metal surface and several components of deuteron flux. They must be considered, including entry into the metal (J_E), movement to gas evolution (J_G), and an extremely tiny loss by potential fusion reactions (J_F). J_{IP} is a pathway afforded by the high impedance spiral PHUSOR-type LANR component (not to be confused with the Phuson).

$$J_D = -B_D \frac{d[D(z, t)]}{dz} - \mu_D [D(z, t)] \frac{d\Phi}{dz}. \quad (6)$$

Equation (6) describes the flow. J_D is the flux of deuterons, B_D is their diffusivity, and μ_D is their electrophoretic mobility. The deuterons can enter the metal forming a binary alloy. Deuterons which enter (load) into the palladium lattice drift from shallow to deeper sites within the palladium, obstructed by ordinary hydrogen at interfaces and grain boundary dislocations. The quasi-1-dimensional model begins with the Navier–Stokes equations which is also used to describe flow for fluids and other materials in continuum electrodynamics [5].

Dividing each flux by the local deuteron concentration yields the first order deuteron flux constants, k_E , k_G , and k_F (cm/s), respectively. They are linked as follows through Gauss' law and integral equations.

$$k_E = \mu_D E - (k_G + k_F). \quad (7)$$

This shows absolutely clearly that LANR can be missed by insufficient loading, contamination (affecting k_E , e.g. by protium), and by the evolution of D_2 gas, which all inhibit the desired reactions. This also shows that the first order deuteron loading rate equation teaches that the deuteron gain by the lattice depends on the applied electric field *MINUS* the loss of deuterons from gas evolution (k_G) and fusion (k_F) (consistent with conservation of mass).

Furthermore, when the deuteron flux equation is modified by the Einstein relation, the first term now has geometric, material factors, and the ratio of two energies (the applied electric energy organizing the deuterons divided by $k_B T$, thermal disorder).

$$k_E = \frac{B_D q V}{L k_B T} - (k_G + k_F). \quad (8)$$

The modified deuteron flux equation reveals how competitive gas evolving reactions destroy the desired reactions, and how the ratio of the applied electric field energy to thermal energy ($k_B T$) are both decisive in successful LANR experiments.

=>In CF/LANR, despite these unimpeachable equations, the mathematics is surprisingly ignored by most, especially those who fail repeatedly. Also usually ignored is the requisite condition of the loaded lattice, how it loads, its variants and noticing that the desired reactions do not occur at robust levels in their absence.

6.2.4. CF/LANR requires CAM-driven deuterons and Anderson focusing

In Pd–D, the key movements on the “road” to successful “cold fusion” (i.e. LANR) begin with the D within the highly loaded Pd. The deuterons are driven by catastrophic desaturation following local temperature increase. This desaturation, and the rise time to produce by positive feedback, are described by the CAM (catastrophic active media) model. Briefly, after loading (Step 1), there can – under some conditions – occur Step 2 which is the CAM-driven filling of vacancies.

Step 2 - (a reversible step) CAM formation of apo- ^4He in hyperloaded Vacancies

In summary, the CAM reactions drive the loaded deuterons to the vacancy sites. Equation (9) notes that Takahashi has denoted that clusters of 4 and 6 may also especially enable these desired reactions.

$$nD[D + D + D + D+?] \iff 4D(H)/TSC \text{ and } 6D(H)/OSC \text{ (Takahashi[149])} \iff \text{apo} - {}^4\text{He}^* \quad (9)$$

The Catastrophic Active Medium (CAM) model [135,136] of LANR considers the deuteron solubility in, and the unusual solubility–temperature relationship with, palladium. The complete model involves the saturation of the Pd by D. This is the expected full amount that can be contained therein, and is a function of temperature. The fractional saturation and its interactions with the phonons and the interstitials and vacancies within the palladium better explain how LANR works. Unlike most metals [91,94] characterized by low solubility (\sim one deuteron per 10,000 metal atoms), the deuteron solubility in palladium is quite large and decreases with temperature. The CAM model first treats the metallic Pd lattice, into which isotopic fuel is loaded, like a vase for the D (emphore, from *amphora*), and follows the changes in partial saturation of the Pd with D.

Second, the model adds in the fact that the Pd is an active medium capable of rapid desorption of deuterons, with recruitment potential of even more deuterons. This can happen in a paroxysmal and catastrophic way with feedback effects. This has a profound impact on increasing deuteron recruitment, which means the increase of heat produces even more suddenly available deuterons by desorption of D from the Pd (positive feedback [135,136]).

Third, the model reflects that the metallic Pd lattice is heterogeneous, and the model considers *all* types of sites in which the inraelectrode deuterons can reside, including deeper traps supplementing the octahedral and tetrahedral sites. Most importantly, the model documents that the loaded Pd is an active medium capable of rapid deuteron desorption and redistribution (shown in Fig. 7 by τ_C), and that there can also be movements into vacancies by Anderson focusing (a solid state effect which focuses D flux into vacancies).

It is the movement of deuterons from throughout the loaded palladium to the active sites that begins the LANR process, and it is augmented by feedback, by phonon-flux coupling, and by the confinement (discussed in the CAM theory from ICCF-4 when the nuclear active site was first introduced). A partial CAM computer model (from ICCF-4) relating the normalized deuteron fugacity, temperature, and the fractional saturation (Fig. 7) shows the relationship of loading, deuterium, and temperature within the cathode. This has been shown to be qualitatively consistent with some experimental observations, as confirmed by Martin Fleischman after ICCF-4.

The model shows that although the deuteron fugacity ($\Theta_{D,Pd}$) (where fugacity is related to the deuteron pressure [131,133]) rises slightly, thereafter the deuteron saturation curve in Fig. 7 falls rapidly for the loaded palladium. There is a 7-fold decrease in deuteron content from 5 to 50°C. Prior to destruction of the lattice through cracks and dislocations and rupture, this desaturation creates an increase in the intrinsic pressure (fugacity) which follows the inraelectrode deuteron flux from redistribution. Because of the fractional saturation-temperature effect, dynamic inversion of $\Gamma_{D,Pd}(t)$ occurs as $\Theta_{D,Pd}(t)$ and temperature reach crescendo levels.

As a result, after sufficient time, the active site (compartment 2) is suddenly and catastrophically “fed deuterons” from the large vicinal volumes of the crystalline palladium lattice (compartment 1), further increasing the likelihood of additional temperature-incrementing reactions. Eventually, however, the crystal lattice is unable to survive intact, and instead the surface energy normally required to prevent the palladium from escaping, becomes insufficient and the reactants continue to move from their normal sites to accumulate in compartment 2 by the catastrophic reactions and thereby maintain close contact for the desired reactions.

The surface energy required to rupture the palladium prevents the escape of the reactants as they continue to accumulate by the catastrophic reactions and thereby maintain close contact for the desired reactions. Positive feedback comes from the catastrophic behavior secondary to the saturation–temperature relationship. However, when the internal pressures are able to exceed the energy needed to create fresh new surfaces in the palladium, leakage then occurs and the sample becomes, at best, locoregionally inactive.

Simply put, there is injection of deuterons into the vacancies by the sudden catastrophic desaturation of highly loaded Pd. That is followed by a quasiparticle which drives the desired reaction by coupling to the lattice.

6.2.5. Band states, Bose–Einstein states



The lattice enables this reversible reaction through internal conversion (Talbot and Scott Chubb [152–155]). The critical reaction proceeds and is described by either Band States and/or Bose–Einstein states, and other interaction models. It is enabled by the collective excitations of phonons. In addition, it is reasonable to assume that conditions may enable formation of $^4\text{He}^*$ if and when there is sufficient activation energy (Cravens, Letts, Swartz) [16,23,24,42].

6.2.6. The Phuson quasiparticle enables coherent collective de-excitation

The coherent means of excitation of the lattice, the Phuson [161], enables LANR by coherent transfer of energy from $^4\text{He}^*$ to the lattice. Understanding LANR from this point of view requires closely studying the PHUSON, which is the coherent “particle” of the PHUSON theory. Simply put, the phusons, coherent excitation objects/particles cooperatively transfer energy from the megavoltage energy of the $^4\text{He}^*$ to the lattice. There results: lattice heating (“excess heat”) and de novo ^4He . As discussed in the original paper, the PHUSON theory has a mechanism which incorporates the observed products, and the energy levels to all those branches. As a result, it succinctly explains the differences in observed outputs, including the observed “excess heat” as T rises. It also explains the different branches observed near room temperature (“LANR”) and at hot fusion temps. The PHUSON theory of LANR has a mechanism which has been, and can be, used to make more reproducible experiments and systems.

Step 3 – (an irreversible step) De-excitation by Phuson to He^4



In this step, there is a critical IRREVERSIBLE (~ 20 MeV) transition that is coherent by PHUSON, enabled by phonons, as Hagelstein has described lossy spin bosons [190–194], and (as will shortly be shown) magnons [77,79].

There are many factors that contribute to increase the likelihood of possible fusion: electrical charging of the cathode to a high negative voltage, the deuteron band structure, Bloch-symmetric Bose–Bloch condensates, plasmon exchange, electron screening, and the increased effective mass of the deuterons due to polarons which occur in the crystalline lattice and other dielectrics used.

The coherent de-exciting PHUSON enables the massive energy loss by way of lossy spin bosons processes involving phonons and (as we have shown at ICCF18) magnons. Hagelstein incorporates the optical phonons in his theory. Swartz at ICCF20 has shown these to also include acoustic phonons [69].

The PHUSON cooperatively transfers energy from the megavoltage energy of the $^4\text{He}^*$ to the lattice in a process which is consistent with conventional physics, and where it appears as “excess heat” [161,162]. The temperature rise occurs as the acoustical and optical phonons become unable to carry off all the momentum and excess energy of the reactions.

Phonon de-excitation modes apparently produce transitional times significant for enabling $^4\text{He}^*$ to ^4He transitions which involving recruitment of sufficient numbers of lattice sites and their associated phonons. After adequate containment time and flux, there is near commensurate amount of excess heat observed in LANR, with the “ash” which is de novo He^4 . This process is the unique feature that allows LANR to occur with energy transfer to the lattice.

Specifically, the PHUSON theory explains why there is a relative absence of strong neutron and gamma ray emissions in LANR. The gamma emission branch from the excited state of $^4\text{He}^*$ is actually spin-forbidden for both hot and cold fusion. However, at higher hot fusion temperatures the restriction is lifted slightly so that some gammas are seen,

and not zero. This spin-forbiddenness of gamma emission is therefore consistent to what is seen for both hot and cold fusion.

The PHUSON theory correctly describes the relative absence of neutrons emissions in LANR. The only nuclear branches available are those whose band gaps are surmountable by the available activation energy (limited by the ambient temperature and incident radiation). The neutron emission branch is more than 1 MeV above the first excited state ($^4\text{He}^*$). Hot fusion has large activation energies available (it is “hot”). LANR does not. In LANR, given the actual much smaller amount of thermal energy, $k_{\text{B}}T$, available for LANR ($\sim 1/25$ eV), absence of adequate activation energy decisively means that that branch is NOT available, as it is for hot fusion. Neutrons are not observed, helium 4 production is in its stead [161,162].

Attention is directed to the fact that the PHUSON theory incorporates the observed products, and the energy levels, which explains the branching ratios based on, and explained by, thermal energies available [161]. It also explains the origin of the excess heat in active LANR systems. The corollary is that the Phuson is a quasiparticle of collective de-excitation observed in high impedance PHUSOR-type CF/LANR systems, and it is quite capable of amplifying incremental power gain significantly.

7. Other Higher Order Systems

Although they are not all related to CF/LANR, some are, and these other higher order systems demonstrate how understanding quasiparticles and collective excitations explain much in physics and material science.

7.1. Quasiparticles of collective excitation – exciton–polaritons, phonon–polaritons, and plasma polaritons

The first example in this higher order categorizations are exciton–polaritons, phonon–polaritons, and plasma–polarons which are quasiparticles of a photon interacting with exciton, phonon, or plasmon, respectively, each arising from collective excitations of a material.

7.2. Quasiparticle of collective excitation – plasmariton – a dressed photon consisting of a plasmon and photon

Another example of a higher order quasiparticle is a plasmariton, which is a photon coupled with both a second optical phonon and a plasmon, a collective excitation.

7.3. Quasiparticle of collective excitation – spinon – quantum spin fluids

Spinons are quasiparticles produced in quantum spin liquids and in rare minerals like Herbertsmithite (Fig. 8) that exhibit magnetic spin liquid states. Herbertsmithite ($\text{ZnCu}_3(\text{OH})_6\text{Cl}_2$, Mohs hardness ~ 3.5 , 3.76 g/cm^3) has that magnetic anomaly beneath its light-green blue color.

Both it, and its synthetic form, have a Kagome lattice structure, named for the Japanese weaving pattern of repeating triangles, and demonstrate a quantum spin “liquid” in that their domains are neither ferromagnet nor antiferromagnet and instead have “constantly fluctuating scattered orientations”. Because of lattice interactions, the magnetic fields are unable to settle into a lowest energy alignment, and must constantly change the direction of their local magnetization. This is confirmed indirectly by neutron scattering.

7.3.1. Coherent quasi-de-excitation – magnetic Phuson (2nd OOP) enables LANR and is a second pathway for de-excitation

There is another coherent de-excitation possible in LANR systems, elicited by an applied magnetic field intensity. Previously, magnetic [15,52,97], and radiofrequency electromagnetic [14] effects have been reported in aqueous LANR

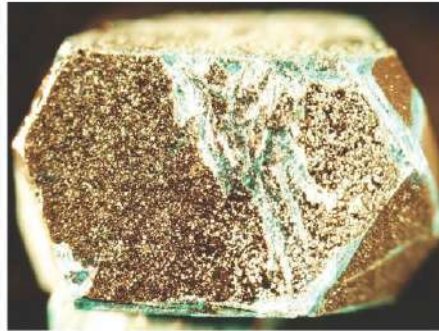


Figure 8. Herbertsmithite containing spinons which demonstrate quantum spin liquids with constantly fluctuating domain magnetic orientation.

systems. In aqueous LANR systems, steady magnetic fields have a small effect which may be inhibitory, especially if perpendicular to the direction of the application of the applied E-field intensity.

Astonishingly, it was discovered that for some magnetic interactions with nanostructured LANR systems [77–79], there is also enhanced improvement of LANR (which occurs at the same time as the applied magnetization and therefore here is called “synchronous”). Also, there is improved LANR excess heat output which also appears later, after the onset of magnetization (since it occurs long after the magnetization when there is no extrinsic magnetic field intensity applied, it is called a “metachronous” effect) and is long-lasting. This was the first evidence of a fractionated high magnetic field intensity producing activation and rejuvenation of nanostructured LANR material, rejuvenating the output to higher levels.

Importantly, as Fig. 9 shows, there results an increase in excess energy gain, and increased incremental power gain, over ordinary LANR. The application of dH/dt created an increase of 4–10 times the peak power gain over conventional LANR with the same system.

The peak power gain of such treated NANOR[®]s (M-NANOR[®]s) ranged from 22 to up to ~80 times input electrical power beyond the ohmic thermal control, as determined by calorimetry.

Pertaining to this paper, there are both synchronous and metachronous impacts after a repeatedly pulsed (“fractionated”) magnetic field intensity, both associated with strong evidence of two (2) OOP manifolds [79]. The second OOP is evidence of a second method/means of coherent de-excitation for successful CF/LANR. The first OOP (as described in the literature in the absence of an applied H-field) is enhanced, and in addition the second OOP makes the entire system make even more excess heat, far beyond that expected in the absence of the H-field, making the system quite improved.

The high intensity fractionated system induces a serious secondary E-field as discussed [79], and is even capable of destroying some circuits.

7.3.2. NANOR[®]-type CF/LANR components

Previously, all LANR systems and the NANOR[®]s had shown a single optimal operating point manifold for excess heat operation, ⁴He production, and other products. Today, that is no longer accurate, or adequate as an engineering principle, because even after a single treatment to a high intensity fractionated magnetic field, there arise two OOP manifolds. The new one is at higher input electrical currents to the NANOR, and is located to the “right” of the conventional LANR OOP.

Although LANR has a first stage mediated by phonons within the loaded lattice, there is a magnetically coerced

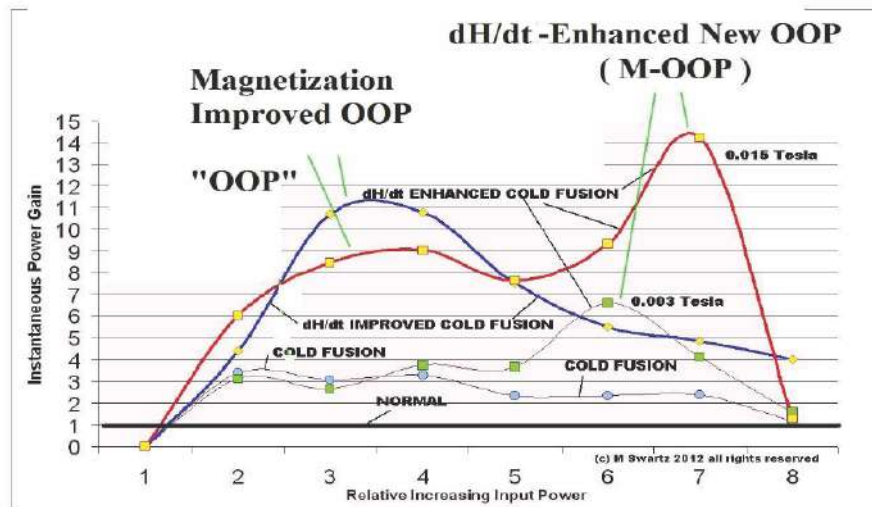


Figure 9. Optical operating point manifolds of LANR, and with and without application of large magnetic field intensities shown against the ohmic control (“normal”). Shown are both synchronous and metachronous results of the applied H-field. A new second (“dH/dt-enhanced) optimal operating point appears (“M-OOP”) appears DURING the application of the field, heralding a new LANR pathway.

second stage, which we believe may be mediated by magnons or interactions of phonons with the magnetization field. Magnetization, alignments of magnetic domains, which are observed in such treated NANOR-type components (called “M-NANORs”; [77,79]).

Figure 10 shows curves which plot the electrical input power, at four different input electrical power levels, and the calorimetric responses of both the ohmic control and the preloaded NANOR[®]-type component. Four complete cycles are shown. The *x*-axis represents time. The *y*-axis on the left-hand side represents electrical input power in watts. The *y*-axis on the right-hand side represents the amount of electrical energy delivered at input, and then released (both the normal electrical dissipation consisting of VI , and the excess heat from CF/LANR).

Those curves (on the right hand side axis) represent time integration to determine total energy. They thus rule out energy storage, chemical sources of the induced heat, possible phase changes, and other sources of possible false positives. The units of this axis are in joules.

The figure shows the input, and the calorimetry, of preloaded NANOR along with that for the ohmic thermal control used to calibrate the system. Those calibration pulses, used for accuracy and precision checks of voltages and currents and time, are also shown. The inputs to the thermal ohmic control, followed by the preloaded NANOR[®]-type component, are shown, as are the calibrated calorimetric outputs for both.

Compare the output for NANOR[®]-type LANR component to the thermal (ohmic) control. As can be seen, this semiquantitative calorimetry, itself calibrated by thermal waveform reconstruction, was consistent with excess heat being produced only during energy transfer to the NANOR[®]-type LANR component. Notice that the active preloaded LANR quantum electronic component clearly shows significant improvement in thermal output compared to a standard ohmic control (a carbon composition resistor). The graph, taken after the MIT IAP January 2012 class, is representative of the NANOR-type of LANR technology, and it shows quite clearly demonstrated over unity thermal output power from the demonstration-power-level NANOR-type cold fusion (LANR) component.

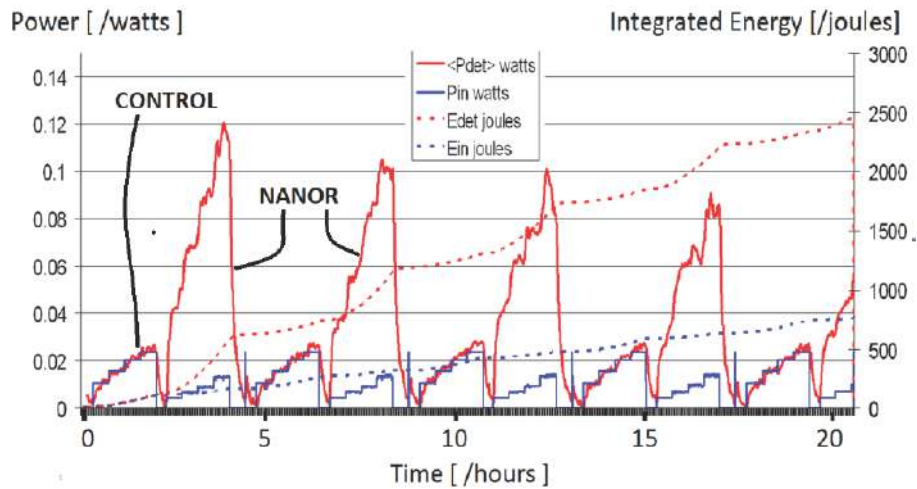


Figure 10. Normal activity of a NANOR[®]-type component – Before magnetic field. The Electrical Power Input and Thermal Power Output of a two terminal NANOR[®]-type component Series 6-33 component, showing the calorimetric response at several input powers, for the ohmic control and the component. “Determined” here means measured using ohmic controls and energy balance. Slightly more than four complete cycles are shown. Notice the exponential fall-off characteristic of such components at the peak output. The electrical input power and energy and output thermal power and heat are shown alternatively both from the ohmic control and the NANOR[®]-type component at several input powers. Note that this component and control was NOT driven in the presence of an applied magnetic field intensity, but only previously had been.

7.3.3. M-NANOR[®]-type CF/LANR components

The proposed Nanoron is a magnetic quasiparticle in magnetized dry preloaded NANOR-type CF/LANR components which produces a second optimal operating point (second pathway) amplifying incremental power gain significantly. Similar to the Spinor, the LANR Nanoron appears to be a potential magnetic quasiparticle picked up initially by the periodic fluctuations in excess heat that had never been seen before. Experimentally, it was also shown later when we were surprised by the two different responses of a NANOR and an M-NANOR. The pre- dH/dt NANOR activity (normal excess heat observed for such active components) is shown in Fig. 10. By contrast, the oscillation of Fig. 11 may reflect the existence of this newly observed magnetic quasiparticle. This appearance is similar to phonons which show their reality through specific heat. Here, this quasiparticle shows its existence through changes in sample activity (like Herbertsmithite does with induced magnetization). Figure 11 shows the input power and output heat flow normalized to input electrical power of a self-contained LANR quantum electronic component AFTER it was magnetically treated [79], and magnetized [77]. Twelve complete cycles are shown. Note the absence of an exponential or linear fall-off of peak activity. Notice that the peak power gain oscillates, never seen in previous unmagnetized NANOR[®]-type components. This experimental run of a M-NANOR[®]-type component was made several hours after a single application sequence of the fractionated magnetic field was delivered. There was no additional H-field applied for this figure. The energy curves are very light, but are there as dotted lines.

There is enhanced improvement of LANR (which is synchronous), and improved LANR which is metachronous and longer-lasting. Notice the exponential falloff of the peak incremental excess power gain in Fig. 10 compared to the unusual behavior in Fig. 11. Specifically, contrast the previous slowly falling response to the more bizarre, not seen before, “oscillation” which occurred after the component was exposed to a dH/dt field) while in the active mode with an applied E field to activate it (Fig. 11).

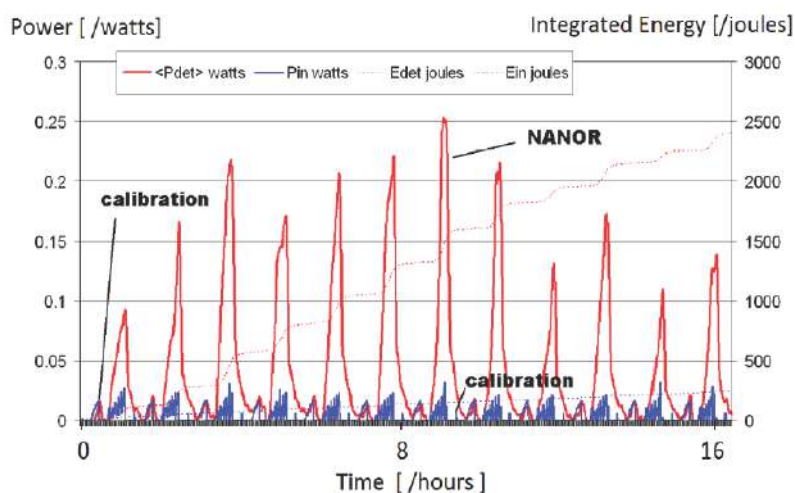


Figure 11. Nanoron – quasiparticle observed as magnetization impact on LANR Activity. Input power and output heat flow normalized to input electrical power of a self-contained LANR quantum electronic component at 124 V peak input voltage.

Specifically, it is important to remember that in Fig. 11, there was no additional H-field applied during the measurements, although a very small, second order H-field is induced in both the components shown in Figs. 10 and 11, by the applied E-field used to activate them.

Similar to the spinon described above, this oscillation of power gain in Fig. 11 may be secondary to a quasiparticle of a coherent de-excitation. We are presently examining an analysis of the force density and homogeneous oscillation frequency using the Maxwell stress tensor [77].

8. Conclusion

Quasiparticles, collective excitations and their higher order quasiparticles of coherent excitations, open up new understanding into material science and engineering. Consider that this brief introduction has not even considered rotons of superfluids, Weyl fermions (Types I and II), dropletions, anyons, and the Bogoliubov quasiparticle from a broken Cooper pair charged electron and hole. There are many more types of quasiparticles, collective excitation and their higher-order particles. They will be examined more, and others sought, in the coming years.

As discussed, from an electrical engineering point of view, quasiparticles, collective excitations and their higher order coherent excitations, discussed here, are also highly relevant to LANR, and in multiple material ways.

Specifically, the L,D-defects, CAM and PHUSON models suggest that quasiparticles and collective excitation have a clear fundamental role in successful CF/LANR. They enable loading of Pd with D, and in that loaded Pd they enable the volumetric redistribution of loaded deuterons followed by high-energy nuclear states returning to their ground state by internal conversion using plasmons, phonons, and sometimes magnons. In summary, these quasiparticles and coherent de-excitations enable successful CF/LANR.

Acknowledgments

The author thanks Gayle Verner and David Nagel for their meticulous help and suggestions for this manuscript. The author acknowledges and thanks Gayle Verner for her very helpful editorial support. This effort was supported by JET

Energy Inc. and the New Energy Foundation. NANOR[®] and PHUSOR[®] are registered trademarks of JET Energy, Incorporated. NANOR[®]-technology, and PHUSOR[®]-technology are protected by U.S. Patents D596724, D413659 and several other patents pending.

References

- [1] A. Von Hippel (Ed.), *Dielectric Materials and Applications*, MIT Press, Cambridge, 1954.
- [2] A. Von Hippel (Ed.), *The Molecular Designing of Materials and Devices*, MIT Press, Cambridge, 1965.
- [3] C. Kittel, *Introduction to Solid State Physics*, 8th Edition, ISBN:978-0-471-41526-8 8th Edition (2004).
- [4] Neil W. Ashcroft and N. David Mermin, *Solid State Physics*, ISBN-13: 978-0030839931, Brooks Cole, 1976.
- [5] J.R. Melcher, *Continuum Electromechanics*, MIT Press, Cambridge, 1981.
- [6] M.R. Swartz, Survey of the observed excess energy and emissions in lattice assisted nuclear reactions, *J. Scientific Exploration* **23** (4) (2009) 419–436.
- [7] M. Miles, R.A. Hollins, B.F. Bush, J.J. Lagowski and R.E. Miles, Correlation of excess power and helium production during D₂O and H₂O electrolysis using palladium cathodes, *J. Electroanal. Chem.* **346** (1993) 99–117; M.H. Miles Trans. and B.F. Bush, Heat and helium measurements in deuterated palladium, *Trans. Fusion Technol.* **26** (1994) 156–159.
- [8] M. Srinivasan et al., Tritium and excess heat generation during electrolysis of aqueous solutions of alkali salts with nickel cathode, *Frontiers of Cold Fusion*, H. Ikegami (Ed.), *Proc. Third Int. Conf. on Cold Fusion*, October 21–25, 1992, Universal Academy Press, Tokyo 123–138.
- [9] F.G. Will, K. Cedzyska and D.C. Linton, Tritium generation in palladium cathodes with high deuterium loading, *Trans. Fusion Technol.* **26** (1994) 209–213.
- [10] F.G. Will, Reproducible tritium generation in electrochemical cells employing palladium cathodes with high deuterium loading, *J. Electroanal. Chem.* **360** (1993) 161–176.
- [11] L.C. Case, Catalytic fusion of deuterium into helium-4, in *The Seventh Int. Conf. on Cold Fusion*, Vancouver, Canada, ENECO Inc., Salt Lake City, UT, 1998.
- [12] M.R. Swartz, C. Haldemann, A. Weinberg and B. Ahern, Possible deuterium loss during excess heat from ordinary water-carbonate electrolyte using nickel, in preparation.
- [13] M.R. Swartz, Excess power gain using high impedance and codepositional LANR devices monitored by calorimetry, heat flow and paired stirling engines, *Proc. ICCF14* 1 (2008) D.J. Nagel and M.E. Melich (Eds.), ISBN: 978-0-578-06694-3, **123** (2010) 123; www.iscmns.org/iccf14/PICCF14a.pdf.
- [14] J. OM. Bockris, R. Sundaresan, D. Letts and Z.S. Minevski, Triggering and structural changes in cold fusion electrodes, *Proc. ICCF4*, Maui, Hawaii, 1993.
- [15] D. Cravens, Factors affecting success rate of heat generation in CF cells, *Proc. ICCF-4*.
- [16] D. Cravens, Letts and P. Hagelstein, Progress on two-laser experiments, *Proc. ICCF15*, 2009, <http://lenr-canr.org/acrobat/Hagelsteinprogresson.pdf>.
- [17] I. Dardik, H. Branover, A. El-Boher, D. Gazit, E. Golbreich, E. Greenspan, A. Kapusta, B. Khachatorov, V. Krakov, S. Lesin, B. Michailovitch, G. Shani and T. Zilov, Intensification of low energy nuclear reactions using superwave excitation, *Proc. 10th Int. Conf. on Cold Fusion*, 2003.
- [18] J. Dash and S. Miguet, Microanalysis of Pd cathodes after electrolysis in aqueous acids, *J. New Energy* **1**(1) (1996) 23.
- [19] M. Fleischmann and S. Pons, Calorimetry of the Pd–D₂O system: from simplicity via complications to simplicity, *Phys. Lett. A* **176** (1993) 118–129.
- [20] M. Fleischmann and S. Pons, Electrochemically induced nuclear fusion of deuterium, *J. Electroanal. Chem.* **261** (erratum, **263**, 187) (1989) 301–308.
- [21] M. Fleischmann and S. Pons, Some comments on the paper analysis of experiments on calorimetry of LiOD/D₂O electrochemical cells, R.H. Wilson et al., *J. Electroanal. Chem.* 332 (1992) 1*, *J. Electroanal. Chem.* **332** (1992) 33–53.
- [22] M. Fleischmann, S. Pons, M. Anderson, L.J. Li and M. Hawkins, Calorimetry of the palladium–deuterium–heavy water system, *Electroanal. Chem.* **287** (1990) 293.
- [23] D. Letts and D. Cravens, Laser stimulation of deuterated palladium: past and present, *Proc. 10th Int. Conf. on Cold Fusion*, 2003.

- [24] D. Letts and P.L. Hagelstein, Stimulation of optical phonons in deuterated palladium, in *ICCF-14 Int. Conf. on Condensed Matter Nucl. Sci.*, 2008, Washington, DC; D. Letts, D. Cravens and P.L. Hagelstein, *Thermal Changes in Palladium Deuteride Induced by Laser Beat Frequencies*, in *Low-Energy Nuclear Reactions*, Sourcebook, J. Marwan and S. Krivit (Eds.), 2008, Oxford University Press, Oxford, D. Letts and D. Cravens, Laser stimulation of deuterated palladium: past and present, in *Tenth Int. Conf. on Cold Fusion*, 2003, Cambridge, MA.
- [25] X.Z. Li et al., The precursor of cold fusion phenomenon in deuterium/solid systems. in anomalous nuclear effects in deuterium/solid systems, *AIP Conf. Proc.* 228, 1990, Brigham Young Univ. Provo, UT, American Institute of Physics, New York.
- [26] F.J. Mayer, J. S. King and J.R. Reitz, Nuclear fusion from crack-generated particle acceleration, *J. Fusion Energy* **9** (1990) 269–271, F.J. Mayer and J.R. Reitz, Nuclear energy release in metals, *Fusion Technol.* **19** (1991) 552.
- [27] McKubre, F. Tanzella, P. Hagelstein, K. Mullican and M. Trevithick, The need for triggering in cold fusion reactions, *Proc. 10th Int. Conf. on Cold Fusion*, 2003.
- [28] G.H. Miley, G. Narne and T. Woo, Use of combined NAA and SIMS analyses for impurity level isotope detection, *J. Radioanal. Nucl. Chem.* **263**(3) (2005) 691–696.
- [29] G.H. Miley and J. Shrestha, Transmutation reactions and associated LENR effects in solids, in *Low-Energy Nuclear Reactions*, Sourcebook, J. Marwan and S. Krivit (Eds.), 2008, Oxford University Press, Oxford.
- [30] Mosier-Boss and S. Szpak, The Pd/nH system: transport processes and development of thermal instabilities, *Il Nuovo Cimento* **112A** (1999) 577–585.
- [31] S. Pons and M. Fleischman, Heat after death, *Proc. ICCF-4*, Maui, EPRI TR104188-V2 2, 8-1 (1994); *Trans. Fusion Technol.* **26**, 4T art 2 (1994) 87.
- [32] M.R. Swartz, C. Haldemann, A. Weinberg and B. Ahern, Possible deuterium loss during CF/LANR using nickel ordinary water, in preparation.
- [33] M.R. Swartz, Consistency of the biphasic nature of excess enthalpy in solid state anomalous phenomena with the quasi-1-dimensional model of isotope loading into a material, *Fusion Technol.* **31** (1997) 63–74.
- [34] M.R. Swartz, Improved electrolytic reactor performance using π -notch system operation and gold anodes, *Trans. American Nuclear Association*, Nashville, Tenn Meeting (ISSN:0003-018X publisher LaGrange, Ill) **78** (1998) 84–85.
- [35] M.R. Swartz, Optimal operating point characteristics of nickel light water experiments, *Proc. ICCF-7* (1998).
- [36] M.R. Swartz, Optimal operating points in active, loaded palladium linked to three distinct physical regions, in *Fourteenth Int. Conf. on Cold Fusion*, 2008, Washington, DC, p. 639.
- [37] M.R. Swartz, Spatial and temporal resolution of three sites characterizing lattice-assisted nuclear reactions, APS 2008; M. Swartz, *Colloquium on LANR in Deuterated Metals Colloquium on LANR at MIT*, August 2007.
- [38] M.R. Swartz, The impact of heavy water (D₂O) on nickel-light water cold fusion systems, *Proc. 9th Int. Conf. on Cold Fusion (Condensed Matter Nuclear Science)*, Beijing, China, Xing Z. Li, May (2002) 335–342.
- [39] M.R. Swartz and G. Verner, Can a Pd/D₂O/Pt device be made portable to demonstrate the optimal operating point, *ICCF-10* (Cambridge, MA), 2003, *Condensed Matter Nuclear Science*, Peter L. Hagelstein, Scott and R. Chubb (Eds.), World Scientific, NJ, ISBN 981-256-564-6 (2006) 45–54.
- [40] M.R. Swartz and G. Verner, Dual ohmic controls improve understanding of “Heat after Death”, *Trans. Amer. Nucl. Soc.* **93** (2005) 891–892, ISSN:0003-018X.
- [41] M.R. Swartz and G. Verner, Excess heat from low electrical conductivity heavy water spiral-wound Pd/D₂O/Pt and Pd/D₂O–PdCl₂/Pt devices, *Condensed Matter Nuclear Science, Proc. ICCF-10*, Peter L. Hagelstein, Scott and R. Chubb (Eds.), World Scientific, NJ, 2006, pp. 29–44; 45–54, ISBN 981-256-564-6.
- [42] M.R. Swartz and G. Verner hotoinduced excess heat from laser-irradiated electrically-polarized palladium cathodes in D₂O, *Condensed Matter Nuclear Science, Proc. ICCF-10* Peter L. Hagelstein, Scott and R. Chubb (Eds.), World Scientific, NJ, 2006, pp. 213–226, ISBN 981-256-564-6.
- [43] M.R. Swartz and G. Verner, Two site of cold fusion reactions viewed by their evanescent tardive thermal power, Abstract *ICCF-11* (2004); M. Swartz, Kinetics and Lumped Parameter Model of Excess Tardive Thermal Power, M. Swartz, APS, 2005.
- [44] M.R. Swartz, Spatial and temporal resolution of three sites characterizing lattice-assisted nuclear reactions, APS 2008; M. Swartz, *Colloquium on LANR in Deuterated Metals Colloquium on LANR at MIT*, August 2007.

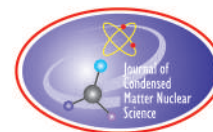
- [45] M.R. Swartz, Gayle Verner and Alan Weinberg, Possible non-thermal near-IR emission linked with excess power gain in high impedance and codeposition Phusor-LANR devices, in *Fourteenth Int. Conf. on Cold Fusion*, 2008, Washington, DC.
- [46] M.R. Swartz, *Trans. Amer. Nucl. Assoc.* **78** (1998) 84–85.
- [47] M.R. Swartz, G. Verner and Alan Weinberg, Non-thermal near-IR emission from high impedance and codeposition LANR devices, *Proc. ICCF14* **1** (2010) 343 ISBN: 978-0-578-06694-3.
- [48] V. Violante, E. Castagna, C. Sibilia, S. Paoloni and F. Sarto, Analysis of mi-hydrate thin film after surface plasmons generation by laser technique, *Proc. 10th Int. Conf. on Cold Fusion* (2003).
- [49] S. Szpak, A. Mosier-Boss, R.D. Boss and J.J. Smith, On the behavior of the Pd/D system: evidence for tritium production, *Fusion Technol.* **33** (1998) 38–51.
- [50] P.A. Mosier-Boss, S. Szpak, F.E. Gordon and L.P.G. Forsley, Use of CR-39 in Pd/D co-deposition experiments, *Euro. P Phys. J.-Appl. Phys.* **40** (2007) 293–303.
- [51] P.A. Mosier-Boss, L. P. Forsley, F.E. Gordon, D. Letts, D. Cravens, M. H. Miles, M. Swartz, J. Dash, F. Tanzella, Hagelstein, M. McKubre and J. Bao, Condensed matter nuclear reaction products observed in Pd/D codeposition experiments, *Current Sci.* **108** (4) (2015) 656. <http://www.currentscience.ac.in/Volumes/108/04/0656.pdf>.
- [52] S. Szpak, A. Mosier-Boss and F.E. Gordon, Further evidence of nuclear reactions in the Pd/D lattice: emission of charged particles, *Naturwissenschaften* **94** (2007) 511–514.
- [53] S. Szpak, A. Mosier-Boss and J.J. Smith, On the behavior of the cathodically polarized Pd/D system: search for emanating radiation *Phys. Letts. A* **210** (1996) 382–390.
- [54] S. Szpak, A. Mosier-Boss and F. Gordon, Further evidence of nuclear reactions in the Pd lattice: emission of charged particles, *Naturwissenschaften* DOI 10.1007 (2007).
- [55] M.R. Swartz, Codeposition of palladium and deuterium, *Fusion Technol.* **32** (1997) 126–130.
- [56] S. Szpak and P.A. Mosier-Boss, On the behavior of the cathodically polarized Pd/D system: a response to vigiers comments *Phys. Letts. A* **221** (1996) 141–143.
- [57] S. Szpak, A. Mosier-Boss and J.J. Smith, Deuterium uptake during Pd–D codeposition, *J. Electroanal. Chem.* **379** (1994) 121–127.
- [58] S. Szpak, A. Mosier-Boss and J.J. Smith, On the behavior of Pd deposited in the presence of evolving deuterium, *J. Electroanal. Chem.* **302** (1991) 255–260.
- [59] S. Szpak, A. Mosier-Boss, C. Young and F.E. Gordon, Evidence of nuclear reactions in the Pd Lattice, *Naturwissenschaften* **92** (2005) 394–397.
- [60] S. Szpak, A. Mosier-Boss, M.H. Miles and M. Fleischmann, Thermal behavior of polarized Pd/D electrodes prepared by co-deposition, *Thermochim. Acta* **410** (2004) 101–107.
- [61] S. Szpak, A. Mosier-Boss, S.R. Scharber and J.J. Smith, Charging of the Pd/nH system: role of the interphase, *J. Electroanal. Chem.* **337** (1992) 147–163.
- [62] S. Szpak, A. Mosier-Boss, S.R. Scharber and J.J. Smith, Cyclic voltammetry of Pd+D codeposition, *J. Electroanal. Chem.* **380** (1995) 1–6.
- [63] S. Szpak, A. Mosier-Boss, C. Young and F.E. Gordon, The effect of an external electric field on surface morphology of co-deposited Pd/D films, *J. Electroanal. Chem.* **580** (2005) 284–290.
- [64] S. Szpak, C.J. Gabriel, J.J. Smith and R.J. Nowak, Electrochemical charging of Pd rods, *J. Electroanal. Chem.* **309** (1991) 273–292.
- [65] Y. Arata and Y.C. Zhang, Observation of anomalous heat release and helium-4 production from highly deuterated fine particles, *Jpn. J. Appl. Phys. Part 2*, **38** (1999) L774.
- [66] M.R. Swartz, Incremental high energy emission from a ZrO₂–PdD nanostructured quantum electronic component CF/LANR, *J. Condensed Matter Nucl. Sci.* **15** (2015) 92. www.iscmns.org/CMNS/JCMNS-Vol15.pdf.
- [67] M.R. Swartz, G. Verner, J. Tolleson, L. Wright, R. Goldbaum, Mosier-Boss and P.L. Hagelstein, Imaging of an active NANOR®-type LANR component using CR-39, *J. Condensed Matter Nucl. Sci.* **15** (2015) 81. www.iscmns.org/CMNS/JCMNS-Vol15.pdf.
- [68] M.R. Swartz, Optical detection of phonon gain distinguishes an active cold fusion/LANR component, *J. Condensed Matter Nucl. Sci.* **20** (2016) 29–53.
- [69] M.R. Swartz and P. Hagelstein, Increased PdD anti-Stokes peaks are correlated with excess heat mode, *Proc. ICCF-20*,

- submitted for publication.
- [70] Y. Arata and Y.C. Zhang, Anomalous production of gaseous ^4He at the inside of DS-cathode during D_2 -electrolysis, *Proc. Jpn. Acad. Ser. B* **75** (1999) 281.
- [71] Y. Arata and Y. Zhang, The establishment of solid nuclear fusion reactor, *J. High Temp. Soc.* **34**(2) (2008) 85.
- [72] M.R. Swartz, P.L. Hagelstein and G. Verner, Impact of electrical avalanche through a ZrO_2 -NiD nanostructured CF/LANR component on its incremental excess power gain, *ICCF-19, J. Condensed Matter Nucl. Sci.* (2016) 19.
- [73] M.R. Swartz, G. Verner, J. Tolleson and P. Hagelstein, Dry reloaded NANOR®-type CF/LANR components, *Current Sci.* **108** (4) (2015) 595. <http://www.currentscience.ac.in/Volumes/108/04/0595.pdf>.
- [74] M.R. Swartz and P.L. Hagelstein, Demonstration of energy gain from a preloaded ZrO_2 -PdD nanostructured CF/LANR quantum electronic device at MIT, *J. Condensed Matter Nucl. Sci.* **13** (2014) 516. www.iscmns.org/CMNS/JCMNS-Vol13.pdf.
- [75] M.R. Swartz, P.L. Hagelstein and G. Verner, Impact of electrical avalanche through a ZrO_2 -NiD nanostructured CF/LANR component on its incremental excess power gain, *ICCF-19*, Padua, Italy, April 16, 2015.
- [76] M.R. Swartz and G. Verner, Energy gain from preloaded ZrO_2 -PdNi-D nanostructured CF/LANR quantum electronic components, *J. Condensed Matter Nucl. Sci.* **13** (2014) 528. www.iscmns.org/CMNS/JCMNS-Vol13.pdf.
- [77] M.R. Swartz, Oscillating excess power gain and coerced magnetic domains in M-NANOR-type CF/LANR components, *J. Condensed Matter Nucl. Sci.* **22** (2017) 38–46.
- [78] M.R. Swartz, Impact of an applied magnetic field on a high impedance dual anode LANR device, *J. Condensed Matter Nucl. Sci.* **4** (2011) 93; 239th American Chemical Society National Meeting and Exposition in San Francisco (2011). www.iscmns.org/CMNS/JCMNS-Vol4.pdf.
- [79] M.R. Swartz, G. Verner, J. Tolleson, L. Wright, R. Goldbaum and P. Hagelstein, Amplification and restoration of energy gain using fractionated magnetic fields on ZrO_2 -PdD nanostructured components, *J. Condensed Matter Nucl. Sci.* **15** (2015) 66. www.iscmns.org/CMNS/JCMNS-Vol15.pdf.
- [80] D. Cravens, M. Swartz and B. Ahern, Condensed matter nuclear reactions with metal particles in gases, *Current Sci.* **108** (4) (2015) 582. <http://www.currentscience.ac.in/Volumes/108/04/0582.pdf>.
- [81] Y. Iwamura, M. Sakano and T. Itoh, Elemental analysis of Pd complexes: effects of D_2 gas permeation, *Jpn. J. Appl. Phys.* A **41** (2002) 4642.
- [82] Y. Iwamura, T. Itoh, N. Yamazaki, J. Kasagi, Y. Terada, T. Ishikawa, D. Sekiba, H. Yonemura and K. Fukutani, Observation of surface distribution of products by X-ray fluorescence spectrometry during D_2 gas permeation through Pd complexes, in *The 12th Int. Conf. on Condensed Matter Nucl. Sci.*, 2005. Yokohama, Japan.
- [83] R. Stringham, Cavitation and fusion, *Tenth Int. Conf. on Cold Fusion*, 2003, Cambridge, MA.
- [84] R. George (personal communication); C. Platt, What if cold fusion is real? *Wired Magazine*, Nov. 1, 1998, <https://www.wired.com/1998/11/coldfusion/>
- [85] D. Nagel, *ICCF13*, Sochi, Russia owners, Materials and Radiations from Low Energy Nuclear Reactions on Surfaces, 2007.
- [86] M.R. Swartz, Noise measurement in cold fusion systems, *J. New Energy* **2**(2) (1997) 56–61.
- [87] J.C. Dickinson, L.C. Jensen, S.C. Langford and R.R. Ryan, Fracto-emission from deuterated titanium: supporting evidence for a fracto-fusion mechanism, *J. Mater. Res.* **5** (1990) 109.
- [88] M.R. Swartz, Atterns of failure in cold fusion experiments, *Proc. 33rd Intersociety Engineering Conf. on Energy Conversion*, IECEC-98-1229, CO, Aug. 1998.
- [89] M.R. Swartz, Atterns of success in research involving low-energy nuclear reactions, *Infinite Energy* **31** (2000) 46–48.
- [90] F.A. Cotton and G. Wilkinson, *Advanced Inorganic Chemistry*, Interscience, NY, 1972.
- [91] C.A. Hampel, *Rare Metal Handbook*, Reinhold, NY, 1954.
- [92] E. Orowan, Surface energy and surface tension in solids and liquids, *Proc. Roy. Soc. Lond. A* **316** (1970) 173–191.
- [93] R.W. Bussard, Virtual-state internal nuclear fusion in metal lattices, *Fusion Technol.* **16** (1989) 231–236.
- [94] C.J. Smithell, *Metals Reference Book*, Butterworths, 1949.
- [95] D.R. Rolison and P.P. Trzaskoma, Morphological differences between hydrogen-loaded and deuterium-loaded palladium as observed by SEM, *J. Electroanal. Chem.* **287** (1990) 287.
- [96] C.R.A. Catlow, Atomic transport in heavily defective solids, *Phill Magazine A* **64** (5) (1991) 1011–1024.
- [97] B.M. Klein and R.E. Cohen, Anharmonicity and the inverse isotope effect in the palladium–hydrogen system, *Phys. Rev. B*

- 45 (21) (1992) 405.
- [98] D.A. Papaconstantopoulos, B.M. Klein, E.N. Economou and L.L. Boyer, Band structure and superconductivity of PdD_x and PdH_x physical Review, **17**, 1 (1977) 141–150.
- [99] A. Pusch, W. Fenzl and J. Peisll, Hydrogen in niobium under pressure, *J. Less-Common Metals* **172–174** (1991) 709–717.
- [100] H.R. Schober and A.M. Stoneham, Diffusion of hydrogen in transition metals, *J. Less-Common Metals*, **172–174** (1991) 538–547.
- [101] H. Teichler, Theory of hydrogen hopping dynamics including hydrogen-lattice correlations, *J. Less-Common Metals* **172–174** (1991) 548–556.
- [102] P. Vargas, L. Miranda, L. Rodriguez, M. Lagos and J. Rogan, Quantum diffusion in transition metals, *J. Less-Common Metals* **172–174** (1991) 557–571.
- [103] E. Wicke and H. Brodowsky, *Hydrogen in Palladium and Palladium Alloys, Hydrogen in Metals II*, G. Alefield and J. Volkl (Eds.), Springer, Berlin, 1978.
- [104] H. Zuchner and T. Rauf, Electrochemical measurements of hydrogen diffusion in intermetallic compound LaNi₅, *J. Less-Common Metals* **172–174** (1991) 611–617.
- [105] R.V. Bucur, Interaction of Hydrogen with the Microstructure in Pd and Pd₇₇Ag₂₃, Cumo Italy, 1991, p. 28.
- [106] G.L. Powell, J.R. Kirkpatrick and J.W. Conant, Surface effects in the reaction of H and D with Pd-macroscopic manifestations, *J. Less-Common Metals* **172–174** (1991) 867–872.
- [107] K.H. Johnson, Jahn–Teller, Symmetry breaking and hydrogen energy in g-PdD cold fusion as storage of the latent heat of water, *Cold Fusion Source Book*, *ibid.* **75** (1994).
- [108] L. DeChiaro, L. Forsley and P.A. Mosier-Boss, Strained layer ferromagnetism in transition metals and its impact upon low energy nuclear reactions, *J. Condensed Matter Nucl. Sci.* 2015.
- [109] J.M. Ok, Y.J. Jo, K. Kim, T. Shishidou, E.S. Choi, H.J. Noh, T. Oguchi, B.I. Min and J.S. Kim, Quantum oscillations of the metallic triangular-lattice antiferromagnet PdCrO₂, *Phys Rev. Lett.* **111**(17) 176405. Epub Oct 25 (2013).
- [110] D.L.R. Santos, P. Venezuela, R.B. Muniz and A.T. Costa, Spin pumping and interlayer exchange coupling through palladium, *Phys. Rev.* **88** B (2013) 054423.
- [111] S. Shimizu, K.S. Sunao, A. Takahashi, T. Hatano, M. Kawasaki, Y. Tokura and Y. Iwasa, Electrically tunable anomalous hall effect in Pt thin films, *Phys. Rev. Lett.* **111** (2013) 216803.
- [112] Y. Sun, J.D. Burton and E.Y. Tsymbal, Electrically driven magnetism on a Pd thin film, *Phys. Rev. B* **81** (2010) 064413.
- [113] S. Shimizu, K.S. Takahashi, T. Hatano, M. Kawasaki, Y. Tokura and Y. Iwasa, Electrically tunable anomalous Hall effect in Pt thin films, *Phys. Rev. Lett.* **111** (2013) 216803.
- [114] M. Apicella, E. Castagna, L. Capobianco, L. DAulerio, G. Mazzitelli, F. Sarto, A. Rosada, E. Santoro, V. Violante, M. McKubre and F. Tanzella, Some recent results at ENEA, *The 12th Int. Conf. on Condensed Matter Nucl. Sci.*, 2005.
- [115] M. Swartz, Dances with protons-ferroelectric inscriptions in water/ice relevant to cold fusion and some energy systems, *Infinite Energy* **44** (2002).
- [116] N. Bjerrum, K. Danske, V. Selskab, *Met.-Fys. Medd.* **27** (1951) 1.
- [117] P. Bridgman, *The Physics of High Pressure*, C. Bell, London, 1949.
- [118] M. Eigen and L. De Maeyer, *Proc. Roy. Soc. (London)* **247** A (1958) 505.
- [119] M. Eigen, L. De Maeyer and H.-Ch. Spatz, *Ber. Bunsen Ges. Phys. Chem.* **68** (1964) 19.
- [120] D. Eisenberg and W. Kauzmann, *The Structure and Properties of Water*, Oxford University Press, New York, 1969.
- [121] N. Fletcher, *The Chemical Physics of Ice*, Cambridge University Press, New York, 1970.
- [122] F. Franks, *Water, a Matrix of Life*, Royal Society of Chemistry, Cambridge, UK.
- [123] B. Kamb, *Ice Polymorphism and the Structure of Water, in Structural Chemistry and Molecular Biology*, A. Rich and N. Davidson (Eds.), a volume dedicated to Linus Pauling by his students, colleagues and friends, W. H. Freeman, San Francisco, 1968, pp. 507–512. Also Structural studies on the high-pressure forms of ice, *Trans. Amer. Cryst. Assoc.* **5** (1969) 61.
- [124] A. von Hippel, *Dielectric Materials and Applications*, MIT Press, Cambridge, USA, 1954.
- [125] A. von Hippel and E.F. Farrell, *Mat. Res. Bull.* **8** (1973) 127.
- [126] A. von Hippel, *Molecular Mechanisms of Conduction and Polarization in Water Vapor, Liquid Water and Ice*, LIR MIT, Cambridge, USA, 1972–1973.
- [127] A. von Hippel, *J. Chem. Phys.* **54** (1971) 145.

- [128] A. von Hippel, D.B. Knoll and W.B. Westphal, Transfer of protons through pure ice 1_h single crystals, *J. Chem. Phys.* **54** (1971) 134, 145.
- [129] M.R. Swartz P.L. Hagelstein, G. Verner and K. Wright, Transient vacancy phase states in palladium following high dose rate electron beam irradiation, *J. New Energy* (2003).
- [130] N. Takanol, T.Kai, K.Shiiki and F.Terasakil, Effect of copious vacancies on magnetism of Pd, *Solid State Commun.* **97** (2) (1996) 153–156.
- [131] J. O'M Bockris and A. Reddy, *Modern Electrochemistry*, Plenum Press, 1970.
- [132] M. Swartz, Kinetics and lumped parameter model of excess tardive thermal power, *APS* (2005).
- [133] H.H. Uhlig, *Corrosion and Corrosion Control*, Wiley, New York, 1971.
- [134] H. Ezaki, M. Morinaga and S. Watanabe, Hydrogen overpotential for transition metals and alloys and its interpretation using an electronic model, *Electrochimica Acta* **38** (1993) 557–564.
- [135] M.R. Swartz, Hydrogen redistribution by catastrophic desorption in select transition metals, *J. New Energy* **1** (4) (1997) 26–33.
- [136] M.R. Swartz, Catastrophic active medium hypothesis of cold fusion, Vol. **4**, *Proc. Fourth Int. Conf. on Cold Fusion*, ibid. (1994).
- [137] M.R. Swartz, Control of low energy nuclear systems through loading and optimal operating points, *ANS/ 2000 Int. Winter Meeting*, Nov. 12–17, 2000, Washington, DC, 2000.
- [138] M.R. Swartz, Generality of optimal operating point behavior in low energy nuclear systems, *J. New Energy* **4**(2) (1999) 218–228.
- [139] M.R. Swartz, Generalized isotopic fuel loading equations, *Cold fusion Source Book, Int. Symposium on Cold Fusion and Advanced Energy systems*, Hal Fox (Ed.), Minsk, Belarus, May 1994.
- [140] M.R. Swartz, Isotopic fuel loading coupled to reactions at an electrode, *Fusion Technol.* **26** (4T) (1994) 74–77.
- [141] M.R. Swartz, Quasi-one-dimensional model of electrochemical loading of isotopic fuel into a metal, *Fusion Technol.* **22** (2) (1992) 296–300.
- [142] R.W. Bass and M. Swartz, Empirical system identification (ESID) and optimal control of lattice assisted nuclear reaction (LANR) devices, *ICCF14*, August 14, 2008.
- [143] M.R. Swartz and L. Forsley. Analysis of superwave-as-transitory-OOP-peak hypothesis, in *ICCF-14 Int. Conf. on Condensed Matter Nuclear Science*, 2008, Washington, DC.
- [144] M. Rabinowitz, Y. Kim, V. Chechin and V. Tsarev, Opposition and support for cold fusion. in *Fourth Int. Conf. on Cold Fusion*, Lahaina, Maui: Electric Power Research Institute 3412 Hillview Ave. alo Alto, CA 94304 (1993) 15–1.
- [145] M. Rabinowitz and D.H. Worledge, An analysis of cold and lukewarm fusion, *Fusion Technol.* **17** (1990) 344.
- [146] M. Rabinowitz, Y.E.Kim, V.A.Chechin and V.A.Tsarev, Opposition and support for 146 cold fusion, 15–1 to 15–12, Vol. 2, *Proc. Fourth Int. Conf. on Cold Fusion*, sponsored by EPRI and the Office of Naval Research, December (1994).
- [147] J. Schwinger, Cold fusion: a hypothesis, *Zeitschrift f. Natur. A* **45** (1990) 756.
- [148] R.A. Rice, G.S. Chulick and Y.E. Kim, Effect of velocity distribution and electron screening on cold fusion, *Proc. ACCF1*, Salt Lake City, 1990, p. 185.
- [149] A. Takahashi and N. Yabuuchi, Study on 4D/TSC condensation motion by non-linear langevin equation, in low-energy nuclear reactions, *Sourcebook*, J. Marwan and S. Krivit (Eds.), 2008, Oxford University Press, Oxford. A. Takahashi, Dynamic mechanism of TSC ##. in *ICCF-14 Int. Conf. on Condensed Matter Nuclear Science*, 2008, Washington, DC.
- [150] H. Hora, J.C. Kelly, J.U. Patel, Mark A. Prelas, G.H. Miley and J.W. Tompkins, Screening in cold fusion derived from D–D reactions, *Phys. Lett. A* **175** (1993) 138–143.
- [151] G. Preparata, *Fusion Technol.* **20** (1991) 82.
- [152] T.A. Chubb and S.R. Chubb, Ion band states: what they are and how they affect cold fusion, *Cold Fusion Source Book*, ibid., 75 (1994).
- [153] S.R. Chubb and T.A. Chubb, The role of hydrogen ion band states in cold fusion, *Trans. Fusion Technol.* **26**(4T) (1994) 414.
- [154] S.R. Chubb and T.A. Chubb. An explanation of cold fusion and cold fusion by-products, based on lattice induced nuclear chemistry. in *Second Annual Conf. on Cold Fusion, The Science of Cold Fusion*, Como, Italy, Societa Italiana di Fisica, Bologna, Italy, 1991.
- [155] T.A. Chubb and S.R. Chubb, Bloch-symmetric fusion in PdD_x, *Fusion Technol.* **17** (1990) 710.

- [156] P.L. Hagelstein, Coherent fusion theory, *J. Fusion Energy* **9** (1990) 451.
- [157] P.L. Hagelstein, Lattice-induced atomic and nuclear reactions, *Proc. Fourth Int. Conf. on Cold Fusion*, sponsored by EPRI and the Office of Naval Research, December 1994.
- [158] P.L. Hagelstein and S. Kaushik, *Neutron Transfer Reactions*, *Proc. ICCF-4*.
- [159] P.L. Hagelstein, Coherent and semi coherent neutron transfer reactions III, *Fusion Technol.* **23** (1993) 353.
- [160] P.L. Hagelstein, I. Chaudhary, M. Melich and R. Johnson, A theoretical formulation for problems in condensed matter nuclear science. in *ICCF-14 Int. Conf. on Condensed Matter Nuclear Science*, 2008, Washington, DC. P.L. Hagelstein and I. Chaudhary, Models relevant to excess heat production in Fleischmann–Pons Experiments, in *Low-Energy Nuclear Reactions Sourcebook*, J. Marwan and S. Krivit (Eds.), 2008, Oxford University Press, Oxford.
- [161] M.R. Swartz, Phonons in nuclear reactions in solids, *Fusion Technol.* **31** (1997) 228–236.
- [162] M.R. Swartz and G. Verner, Bremsstrahlung in hot and cold fusion, *J New Energy* **3** (4) (1999) 90–101.
- [163] M.R. Swartz and G. Verner, Metamaterial function of cathodes producing hydrogen energy and deuteron flux, *Proc. ICCF-14* (2008).
- [164] M.R. Swartz, Deuterium production and light water excess enthalpy experiments using nickel cathodes, *J. New Energy* **1** (3) (1996) 219. www.iscmns.org/FIC/J/JNE1N3.pdf.
- [165] M.R. Swartz, possible deuterium production from light water excess enthalpy experiments using nickel cathodes, *J. New Energy* **3** (1996) 68–80.
- [166] A. Widom and L. Larsen, Ultra low momentum neutron catalyzed nuclear reactions on metallic hydride surfaces, *Euro. Phys. J. C* (2006).
- [167] D.P.E. Dickson and F. Berry, *Mössbauer Spectroscopy*, Cambridge University Press, Cambridge, UK, 1983.
- [168] L. Eyles, Physics of the Mössbauer effect, *Amer. J. Phys.* **33** (10) (1965) 790–802.
- [169] H. Frauenfelder, *The Mössbauer Effect*, W.A. Benjamin, 1962, LCCN 61018181.
- [170] T.C. Gibb, *Principles of Mössbauer Spectroscopy*, Chapman and Hall, London, 1974.
- [171] J. Hesse, Simple arrangement for educational Mössbauer-effect measurements, *Amer. J. Phys.* **41** (1973) 127–129.
- [172] R.L. Mössbauer, Kernresonanzfluoreszenz von Gammastrahlung, in Ir191, *Zeitschrift für Physik A* (in German) **151** (2): 124–143.
- [173] F. Ninio, The forced harmonic oscillator and the zero-phonon transition of the Mössbauer effect, *Amer. J. Phys.* **41** (5) (1973) 648–649.
- [174] U. Gonser, *Mössbauer Spectroscopy*, Springer, NY, 1975.
- [175] G. Vandergrift and B. Fultz, The Mössbauer effect explained, *Amer. J. Phys.* **66** (7) (1998) 593–596.
- [176] T.-H. Han, J.S. Helton, S. Chu, D.G. Nocera, J.A. Rodriguez-Rivera, C. Broholm and Y.S. Lee, Fractionalized excitations in the spin liquid state of a kagome lattice antiferromagnet, *Nature* **492** (2012) 406–410.
- [177] F. Monticone and A. Alu, Metamaterial lasmonic and nanophotonic devices, *Rep. Progr. Phys.* **80** (3) (2017).
- [178] A. Zvyagin, Parametric pumping of the two-dimensional quantum spin liquid, *Phys. Rev. B* **95** (2017) 064428.
- [179] S. Karimi, F. Baboux, F. Perez, C.A. Ullrich, G. Karczewski and T. Wojtowicz, Spin precession and spin waves in a chiral electron gas: beyond Larmors theorem, *Phys. Rev. B* **96** (2017) 045301.



Research Article

Concerning the Problem of Searching for the Optimal Palladium Cathode

M. Tsirlin*[†]

University of Missouri-SKINR, MO 65211-7010, USA

Abstract

This article attempts to describe the processes occurring on the surface of palladium cathodes during their electrolytic electrolysis in electrolyte on the base of heavy water. The discussion is based on the experimental data on which were obtained in Low Energy Nuclear Reactions (LENR) experiments lead for a number of years in Energetics Technology (Israel) (ET). The results of these experiments were presented in detail at the international conferences on cold fusion (ICCF). The main subject of these presentations was the description of experimental techniques and analysis of the results of calorimetric measurements, which in a number of cases indicated anomalous heat release, sometimes very significant, accompanying the process of electrochemical deuteration of Pd cathodes. However, the processes occurring in the cathode material, in particular, its structural transformations occurring during the absorption of deuterium by palladium, in these reports have appeared practically outside of discussion. This article partially fills this gap and, as the author believes, brings some clarity to the problem of searching for “optimal” palladium cathodes from the point of view of the probability of initiation of LENR.

© 2017 ISCMNS. All rights reserved. ISSN 2227-3123

Keywords: Deuterium absorption, Low-energy nuclear reactions, Pd cathodes, Structural and composition changes

1. Introduction

Initial studies of the Low Energy Nuclear Reactions (LENR) phenomenon were carried out in the palladium–deuterium system. Subsequent studies in this direction have revealed a low reproducibility of the effect. The primary task, bearing in mind the low reproducibility of the effect, should be searching for the properties of palladium, which could provide the conditions for its initiation. However, surprisingly little research has been done in this direction. For example, Fleischmann and Pons [1] have indicated that they had used Pd supplied by Johnson–Matthey Company. But by what considerations were guided the authors in choosing this supplier, and what advantages had the metal used by them, have been not specified. Moreover, attempts to detect these properties, undertaken by a number of authors have yielded very insignificant and ambiguous results (see below). As will be seen from the following, the problem posed in this way turns out to be incorrect.

*E-mail: tsirlin.mark@hotmail.com.

[†]Retired.

In a few attempts of this kind, attention was paid to the various physical and structural properties of the original Pd, which used as a cathode in the electrochemical process [2–8].

Similar studies have also been carried out at ET for a number of years. In the course of these studies, it was established that during electrolytic deuteration, a number of processes occur on the surface of the palladium cathode, due to the various causes. Wherein, the metal undergoes complex structural transformations, and the cathode surface significantly changes its relief, and elementary and phase compositions. Some of these processes, as will be shown below, occur very rapidly, starting from the moment of the initial contact of the cathode with the electrolyte.

The result of these studies was the understanding of the variety and complexity of the phenomena occurring on the Pd surface and in the near-surface layer of Pd cathode during its electrolytic deuteration. In addition, the futility of attempts to optimize the properties of the initial Pd with the aim of initiating the LENR became apparent.

2. Experiment and Discussion^a

2.1. Palladium

The main material for the study at ET was Pd, prepared by a group led by Dr. V. Violante (ENEA, Italy) in the framework of joint work ET with ENEA. In addition, the samples of purity 99.5–99.9% obtained from other sources were used, including the metal supplied by Johnson–Matthey. Details of the experimental procedure used in electrolytic experiments performed by ET are described in [9,10]. It is known, that a palladium produced by various manufacturers and certificated as the metal of high purity, contains a number of contaminants. They can be divided into three types: First type (Pt, Ni, Ag, Ir, Rh, and Au) form with Pd unlimited solid solutions, second type (Ti, Zn, Al, B, Ca, Cr, Fe, Si, Mg, and Si) form the intermediate phases with Pd, and of the third type (e.g., Cu) form with Pd the solid solutions of the various structures depending on their concentrations. It is reasonable to assume that impurities of first type are distributed uniformly in the metal. As for impurities of the second and third types, they form inclusions that have different the electrical conductivity and electrochemical properties. As will be seen from the following, the latter circumstance exerts a strong influence on the process of electrochemical deuteration.

A typical surface appearance of the initial palladium after rolling, vacuum annealing and etching in aqua regia is shown in Fig. 1. Thus structure is typical for palladium samples obtained from various sources. Clearly visible the slip twins (Fig. 1a), formed during rolling, and dark spots (Fig. 1b). The latter are usually located along the rolling direction and are the product of the pyrolysis of the lubricant used in the rolling of the foil during the annealing process. Dark spots are an essential element in the structure of the original palladium and play an important role in the process of electrolytic deuteration. As can be seen from the data are shown in Fig. 2 and in Table 1, the main supposed phase components of these spots are complex carbides, sulphides, oxychlorides and silicides of potassium, sodium, calcium and aluminium, as well as silicon carbide. The presence of lines of Pd and Pt in the spectrum is due to the participation of the substrate in the formation of the spectrum.

The presence of carbon in all investigated samples, apparently, due to metallurgical factors. Carbon content defined by EDS method, obviously, overestimated, that may be associated with superposition of the spectral lines M_Z Pd (0.286 eV) and $K_{\alpha}C$ (0.277 eV). The decrease in carbon concentration on the surface of Pd had been observed after metal treatment in glow discharge plasma of deuterium. There are indications that carbon (which, like hydrogen, is an interstitial impurity and occupies octahedral pores in the Pd lattice) reduces the solubility of hydrogen in palladium, and $PdC_{0.1}$ phase suppresses β -PdH formation [11]. Boron additives cause a similar effect.

Carbon, regardless of its origin, plays an important role in the process of electrolytic deuteration of palladium. First of all, it reduces the solubility of hydrogen (deuterium) in the metal. In addition, it leads to the formation of

^aElectrochemical experiments were performed by B. Khachaturov, V. Krakov, A. Shapiro, and T. Zilov.

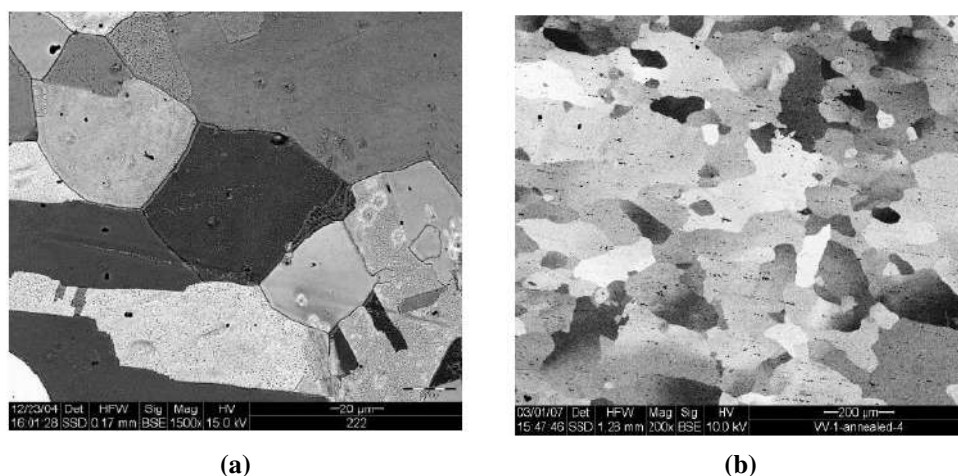


Figure 1. Pd foil after annealing at 850°C and etching in aqua regia, back scattered electrons images. The twins (a) and black spots (b) are seen.

carbide phases of a number of elements - micro-impurities in palladium, for example, silicon, alkaline earth metals, etc. We must also keep in mind the possible interaction of lithium, which exists in the form of various compounds on the surface of palladium, with carbon. The formation of carbide phases on the surface of the cathode is one of the causes of its electrochemical heterogeneity, which plays an important role in the mechanism of deuteration. In this way, micro impurities, forming a micro heterogeneous structure, have a significant effect on the process of electrolytic deuteration [12]. Of course, the mechanism of this influence is different when considering different stages of the process (adsorption, diffusion, recombination, mass transfer, etc.) [13,14].

2.2. Texture

The free energies the faces of Pd (J/m^2) are: (111) – 1.31, (100) – 1.49, (110) – 1.55, and the work functions of these faces are equal (eV) 5.25, 5.11 and 4.87, respectively [15]. Nevertheless, experience shows that the predominant texture of the rolled palladium is (100).

The formation of (100) texture is, apparently, caused by an influence of the impurities (mainly, carbon) at the grain

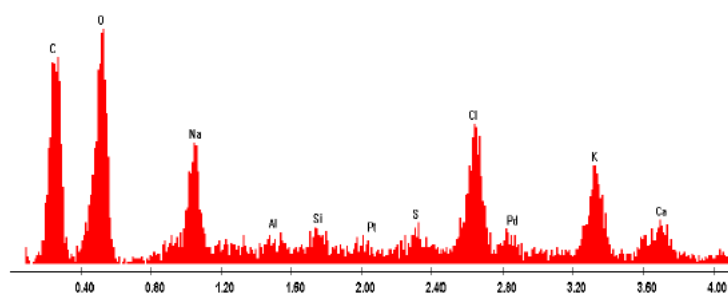


Figure 2. Typical EDS spectrum of the dark spot.

Table 1. The typical composition of the dark spot.

Element	Wt. (%)	At. (%)
C	35.77	52.48
O	26.19	28.84
Na	4.92	3.77
Al	0.43	0.28
Si	1.05	0.66
Pt	0.39	0.04
S	1.44	0.79
Cl	10.68	5.31
Pd	2.55	0.42
K	11.07	4.99
Ca	5.52	2.43
Total	100.00	100.00

boundaries of Pd, which hinder to develop (111) planes parallel to the surface at the rolling procedure. Our experiments on annealing of the rolled Pd in hydrogen convincingly testify to the favor of this assumption. The results of these experiments have shown that the fraction of the texture (111) increases with increasing annealing duration and thus lowering the free energy of the system. Does the texture of the original Pd affect the kinetics of deuterium absorption and (or) to initiating LENR? In [3.5] and other works by the same authors asserted that the texture (100) is the most favorable from the point of view of initiation of LENR. Experimental data are not consistent with this statement. The reasons for this discrepancy are easily understandable. First, besides the texture (100), other orientations, for example (111) and (110), play an important role in initial Pd. The existence of various orientations of grains (and also their sizes!) in the original Pd can be clearly seen in Fig. 3. Secondly, more importantly, during the absorption of deuterium (hydrogen), the intensive processes restructuring of the metal occur, including the reorientation of the grains. This process is especially important in the case of the spinodal decay of the deuterium solid solution in Pd. Finally, the grain boundaries play a much smaller role than the sub-grain ones during the deuterium absorption process. The last two factors will be discussed in more detail below. Therefore, it is not worth to exaggerate the role of the initial palladium texture neither in the processes of adsorption (absorption) of deuterium nor in its initiation of LENR.

It should be noted that deep etching of Pd leads to the formation of the developed microstructures of the type shown in Figure 4, with characteristic prismatic crystals, faceted by the planes (111), very similar to structures spontaneously formed during electrochemical deuteration of Pd. It is clear that such an etching result is due to a decrease in the free energy of the surface. The EBSD method provides valuable information about the orientation of such structural elements, since the X-ray beam in this method falls to the surface at small angles, and the diffraction pattern is formed in a layer several tens of nanometers in thickness. However, the author is not aware of studies of such structures of deep etching of Pd after its electrochemical treatment by this method. Of course, the difficulty of its using it is partly due to the deformation of the metal after the experiment and the formation of an irregular surface.

We used only the X-ray method, in which the depth of formation of the diffraction pattern occurs in a surface layer several microns thick. Therefore, the contribution of surface structures of the type shown in Fig. 4, in the formation of diffraction peaks in this method, is relatively small. The predominant texture (100) of the original palladium samples was detected by us after their standard etching in aqua regia. The textures (111) and (110) have been expressed comparatively weak.

2.3. Grains, mosaic blocks and dislocations

The grain size distributions in some Pd cathodes are shown in Fig. 5. These curves are obtained by using the software “Simagis”, developed by Smart Imaging Technologies. It can be seen that the grain sizes practically do not influence

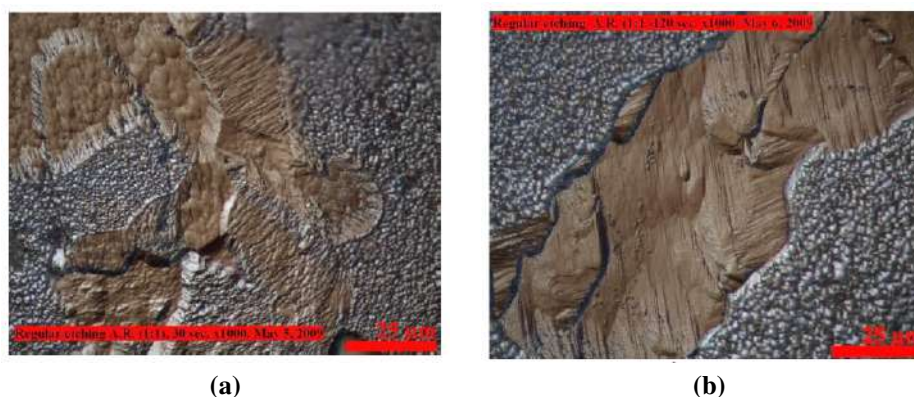


Figure 3. Virgin Pd foils after rolling and annealing at 850°C. Scale bar-25 μm .

the probability of initiation of LENR, and most of the grains have dimensions of $\sim 50 \mu\text{m}$. As noted in [16], such grains are optimal from the point of view of achieving maximum loading.

We measured the sizes of coherent scattering regions (the size of the mosaic blocks) in typical Pd samples by X-ray rocking curve method. They were within the limits of 150–400 nm. Since the boundaries of the blocks of the mosaic are dislocation walls and the latter, it is possible to believe, are traps for absorbed deuterium, it is should be supposed that the grain sizes in themselves do not influence significantly the process absorption, compared to the influence of mosaic blocks' boundaries, bearing in mind that the total length of the latter's approximately three orders of magnitude higher. The typical dislocation density in the Pd sample 64, measured using a transmission electron microscope (JEM 2010) at an accelerating voltage of 200 kV, is $\sim 3\text{--}6 \times 10^{10} \text{ cm}^{-2}$.

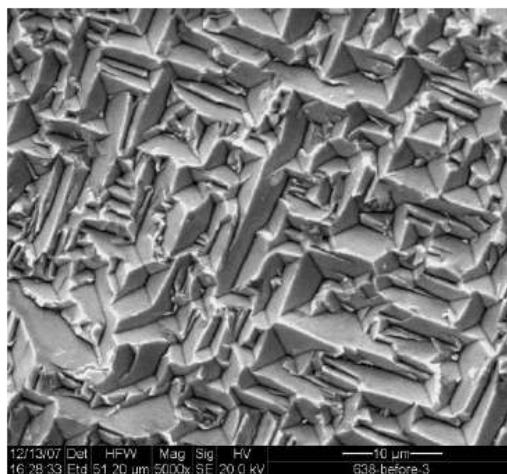


Figure 4. Deep etching reveals the close-packed planes (111) on Pd surface.

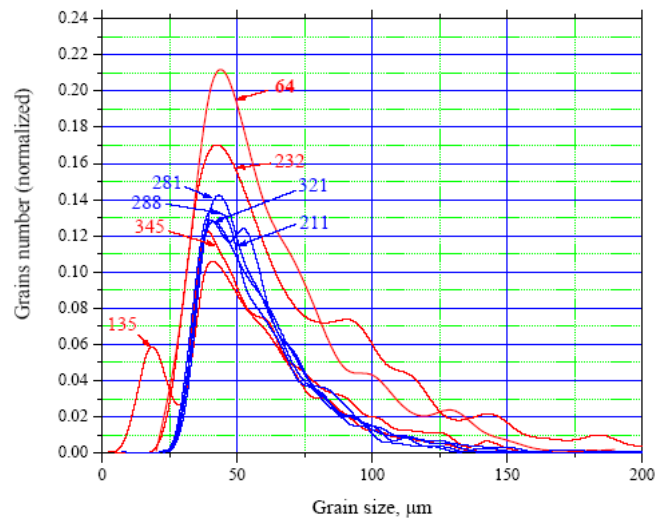


Figure 5. The grain size distribution for some Pd cathodes. The annealing temperature is 870°C, annealing time is 3 h. Red curves – the cathodes showing anomalous heat effect (AHE), blue curves – the cathodes without AHE.

2.4. Spinodal decay

As known [17], the spinodal decay is possible in connection with the system transition into a labile state. This condition is expressed as follows: $(\partial^2\mu/\partial n^2)_{T,P} < 0$. With decreasing this value, the wavelength of the spinodal structures also decreases (Fig. 6). The process is realized by the propagation of a wave of stresses through the sample. The following relaxation of the system gives rise to considerable increasing of the structural heterogeneity. The process is accompanied by so large the increase of defect concentration that their evolution occurs due to the collective effects and formation of the fractal structures. At temperatures below the critical (T_s) at which this condition is fulfilled, the effective coefficient of diffusion, $D(c)$, becomes negative, and the motion of atoms, strictly speaking, can no longer be called diffusion, since it leads to an increase in inhomogeneities. Nevertheless, since Fick's law is formally fulfilled, the diffusion terminology is preserved even at $T < T_s$, and the corresponding atomic transfer for $D(c) < 0$ is known as “upward diffusion”. The system relaxation during the spinodal decomposition is accompanied by growth of its heterogeneity. The process is almost non-activated.

In this way as a result of phase transition of β Pd–D solution ($\beta \rightarrow \beta + \alpha$), for example, due to temporarily reversing the polarity of the electrodes, a specific regular modulated structure is formed, whose morphology is determined by the original texture (100) of Pd.

A surprising effect is the difference in textures of newly formed phases: whereas the β -phase texture remains unchanged (100), that of α -phase becomes (110). The result is a significant increase in the concentration of defects, mainly dislocation walls at the phase boundaries, α/β , and $\beta \leftrightarrow \beta + \alpha$ decay is accompanied by profound rearrangement of Pd–D solid solution, leading to a significant increase in the dislocation density (up to 10^{11} – 10^{12} cm^{-2}).

2.5. Electrochemical heterogeneity of the Pd cathode surface and its consequences

So, the dispersed two-phase structure forms when the spinodal decay of β solid solution Pd–D occurs. It is important for us is the difference of the potentials of these phases in equilibrium with the electrolyte.

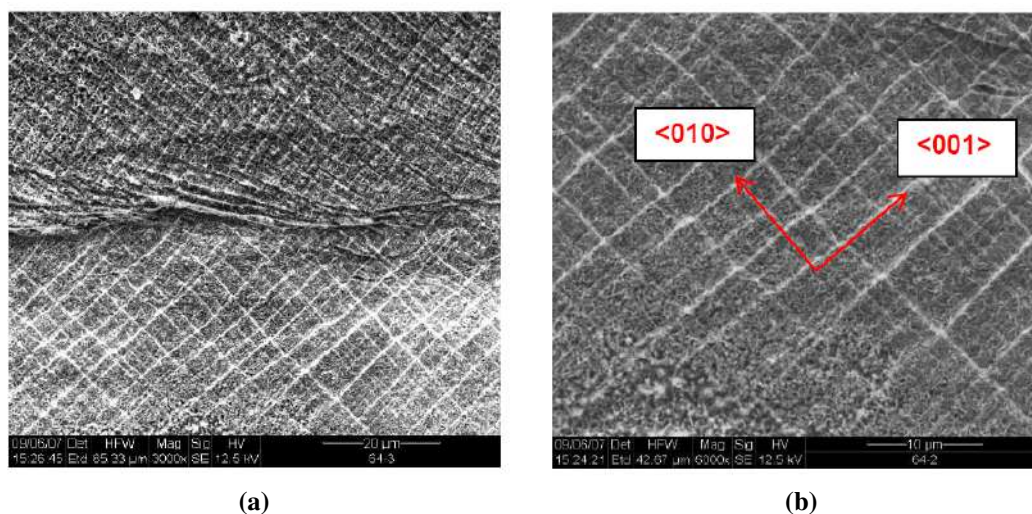


Figure 6. The spinodal decay of β phase (Pd–D solution) and formation of the hierarchical multi-level structures. This extremely heterogeneous structure consists of β and α Pd–D solid solutions. The dislocation walls confine rectangular sub-grains.

According to [18], the open circuit voltages (OCV) of α and β phases relative Pt reference electrode is equal to -0.85 and -1.35 V, respectively. Unfortunately, in the literature, there are no data on the measurement of the electrochemical heterogeneity of the surface of the Pd cathode during its electrochemical deuteration, for example, at the simultaneous presence of α and β phases. At the same time, such in-situ measurements, for example, using the scanning reference electrode technique (SRET), and the scanning Kelvin probe (SKP) [19–23], would make some clarity regarding the details of adsorption, absorption, and surface mass transfer mechanisms of the electrochemical deuteration of Pd. Thus, the scanning Kelvin probe force microscope gives good spatial resolution at direct measurement of the local Volta potential differences resulting from very complicated microstructures. These studies are particularly important since the heterogeneity of the surface of the Pd cathode is its immanent property and decisively influences the mechanism of the process.

The electrochemical heterogeneity of the Pd surface can be caused not only by the spinodal decay of the β Pd–D solution but also by the presence of the other inhomogeneities, for example, the dark spots, the secondary palladium crystals growing in the process of electrolysis with a content of Pt lower than on the rest of the cathode surface, etc. In addition, it must be borne in mind that the original Pd always has foreign, often poorly conducting inclusions, which have a metallurgical origin. We observed various types of similar inclusions, for example, Quartz, silicates, and alkali metal aluminates, etc. It should also be mentioned formation, during the electrolytic process, of the halides, carbonates of the alkaline and alkaline earth metals, localized, as a rule, on the protrusions and facets of newly formed crystals. One should not forget about the presence of Li on the surface of the cathode, which forms solid solutions, inter-metallides and multi-component compounds with the impurities contained in Pd. We detected Li, in particular, in the form of lithium aluminate by the X-ray method. A presence of all these types of micro impurities on the surface, as our experience shows, is almost inevitable, especially when working with open cells.

Thus, the complex elemental and phase compositions of the Pd cathode with heterogeneity of different compositions and sizes, up to submicroscopic ones, create a complex distribution of the electric potential on its surface during the electrochemical process. Finally, a specific contribution to the electrochemical heterogeneity of the surface is introduced by its uneven relief due to the plastic deformation of the metal, because the potentials of the protruding areas

and depressions on the cathode surface are different [24]. Thus, a complex distribution of electrochemical potentials arises on the surface of the Pd during its cathodic polarization, accompanied by the appearance of surface currents and, consequently, surface mass transfer. In this case, relatively non-noble (having a more negative potential relative to the matrix) surface areas, can dissolve in the surface layer of the electrolyte. The reverse process occurs on relatively noble areas. The rates of these processes depend on the magnitude of the local electric fields.

In our experiments, we observed an almost equilibrium “growth” of negative Pd crystals in the form of a truncated semi-octahedron on grains with orientations (100) and (111) – (Figs. 7a and b, respectively) and fast growth of secondary dendritic Pd crystals (Fig. 7c). The growth of dendrites, as a rule, occurs in places of localization of electric fields of high intensity arising at the boundaries of a conducting matrix with non-conducting inclusion. Usually, we observed the growth of such dendrites in places where dark spots were located (Fig. 7c). Often spatially separated dissolution–crystallization processes occupy significant areas of the cathode surface, and in that cases we observe vast surface areas, with characteristic etch structures and mass secondary growth (Fig. 8). A striking similarity is found between the structures of the initial etched palladium (Fig. 4) and the extensive surface sections of the Pd cathode after its electrochemical deuteration (Fig. 8a and c). Figure 8c presents a remarkable picture of the mass crystallization of secondary Pd crystals with a highly developed lace-like structure and an increased content of Pt. It is clear that the description of structures of this kind in terms of their texture does not make sense.

2.6. About selection criteria for Pd cathodes

From what has been said above, it is easy to conclude that the search for properties of the initial Pd that would contribute to the initiation of LENR is meaningless since both the composition of the metal surface and its structure undergo significant and rapid changes immediately after the beginning of the electrochemical process. It must be assumed that this circumstance caused the ineffectiveness of such attempts. Certainly, and our attempts to find correlations between the various physico-chemical and structural characteristics of the original Pd and the probability of nuclear transformations also turned out to be futile.

Let us look at the most popular assumptions about these criteria.

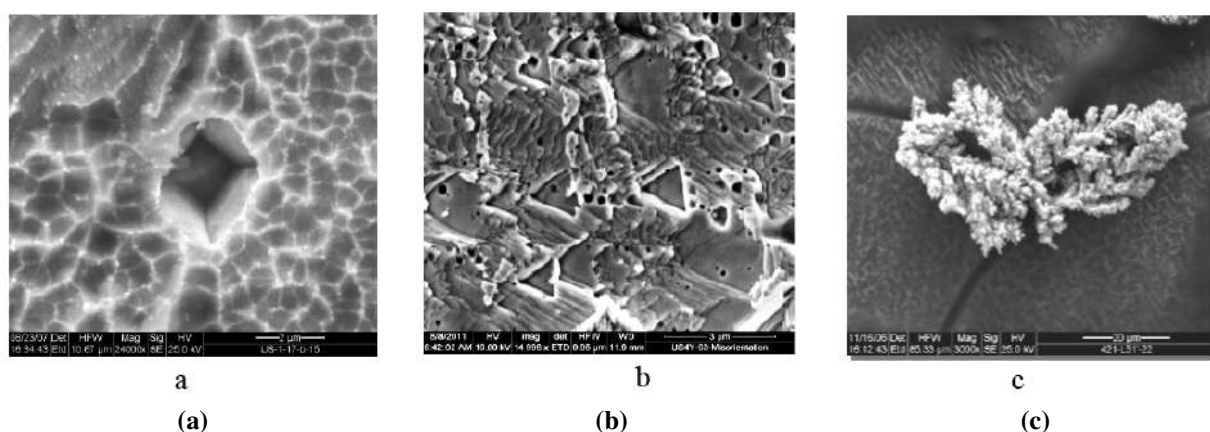


Figure 7. Growth of the negative and the secondary Pd crystals on Pd cathode during electrolytic deuteration; a, b-the negative crystals grown up on the Pd grains of the $\langle 100 \rangle$ and $\langle 111 \rangle$ orientations correspondingly, c – the dendritic secondary Pd crystals grown up on the Pd-dark spot boundary.

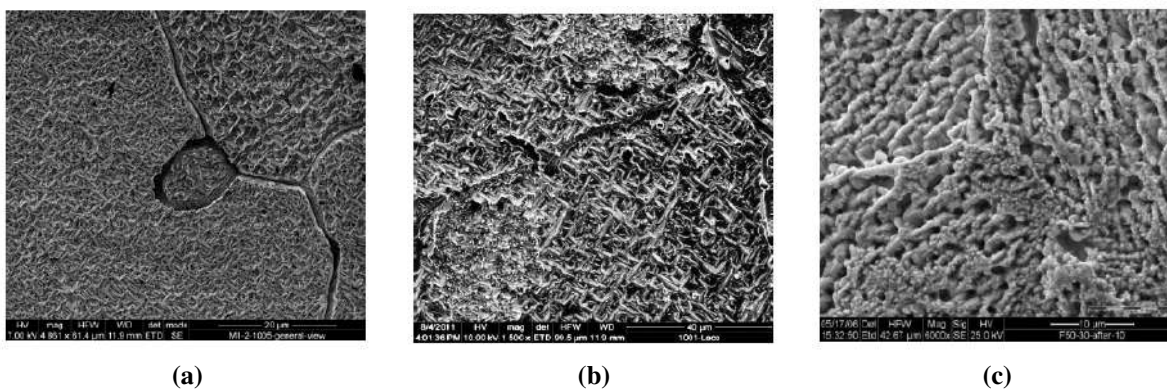


Figure 8. Structural transformations of the cathode surface; a) and b) - apparently, the cathodic regions, undergone the etching process; (compare to the structure shown in Fig. 4, c) a mass crystallization of the secondary Pd crystals (compare to Fig. 7c).

- (a) Common is the assertion that the probability of LENR increases with increasing ratio D/Pd, especially at its values more than 1 [2,25, 26]. Although the D/Pd parameter has an indirect relationship to the search for palladium estimation criteria, its discussion is of great methodological importance. The fact is that the experimental data obtained in different laboratories are contradictory.

Thus, the probability of AHE, according to [26], increases with the increasing in the concentration of deuterium in Pd, and the probability of AHE increases sharply as the loading approach approaches 1. At the same time, in accordance with the data obtained by ET, the effect was observed usually at D / Pd ratio 0.6–0.7, i.e. near the phase boundary of $\alpha + \beta/\beta$. Similar results have been obtained by Storms [12]. From general considerations, it is clear that the probability of the interactions of deuterons, leaving aside the problem of overcoming the Coulomb barrier, does not require extremal high average concentrations of deuterium absorbed in the metal. It is reasonable to assume that a high local concentration of deuterons, say, on dislocation walls, is quite sufficient incentive to initiate their interaction. Anyway, any of known models LENR does not give a reasonable explanation of sharp increase of probability AHE at extremely high loadings which are coming close to 1.

Thus, this problem requires additional theoretical and experimental studies, taking into account other process parameters, for example, the temperature of the cathode and the duration of the incubation period.

- (b) Both characteristics of the initial Pd, namely, texture and grain sizes are very popular as quality parameters of the metal. Supporters of this idea tacitly assume that the loading values play a significant or even dominant role in initiating the LENR (see point a). However, even if we accept the high loading postulate as a prerequisite in initiating LENR, then these parameters cannot play a significant role since radical changes in the surface structure and the formation of a developed sub-grain structure of the metal during its cathodic polarization make their optimization meaningless. From the foregoing, it is also obvious that the statement about the favorable role of the texture (100) as concerning fast loading, and, consequently, the initiation of the LENR effect, does not have any grounds.

As for the influence of the grain size, the foregoing consideration indicates clearly that this parameter does not have any effect on the initiation of the effect and therefore cannot serve as a criterion for Pd pre-selection. First of all, direct experimental data contradict this position (see Fig. 5). The inapplicability of this criterion is obvious, bearing in mind that it is the sub-grain, and not the grain structure, that plays an important role in the absorption of deuterium. In

fact, if we assume that the increase in time of settled life of the absorbed deuterium ions and, therefore, the probability of interaction of their nuclei associated with the concentration of dislocations as traps for deuterium ions, then just the sub-grain structure can be a parameter to optimize the structure of the original Pd.

- (c) In the papers of V. Violante with co-workers (see, e.g. [2,8]) the measurements of the surface energy spectra of the Pd, or a specific state of the surface of the metal, e.g., its roughness, the spectra of the surface plasmons, the form of the power spectral density function, etc., have been suggested as criteria the probability of the LENR. In a view of the aforesaid apparently, that cardinal restructuring of a surface of metal during its electrochemical processing changes a type of the specified spectra right away after the beginnings of experiment and renders impossible to accept such measurements as a way of preliminary selection of cathodes.

It is this circumstance that is the reason why it is impossible in principle to develop criteria for estimating the initial Pd in view of achieving the reproducibility of the LENR effect.

3. Conclusions

The foregoing considerations lead us to a conclusion that there are no properties of the original Pd, the optimization of which could trigger the LENR mechanism automatically due to the high stochasticity of the electrochemical system. Therefore, we have to reformulate the problem. First, it is necessary to achieve reproducibility of the experiment. That is, to exclude, or at least minimize the influence of uncontrolled parameters. The main factor that introduces uncontrollable disturbances into the system is the presence of micro-impurities in Pd. Therefore, the first step in overcoming the low reproducibility of the experiment is the use of high-purity metal. Here we can see an obvious analogy with the beginning of the semiconductor era. An essential flaw in this analogy is the absence of the working theory of LENR. The existence of such a theory would radically change the formulation of the problem, namely, instead of improving reproducibility, the task would be a programmable launch of LENR.

The difficulty in obtaining pure Pd is caused its high absorption capacity with respect to the interstitial impurities. Therefore, a promising direction should be considered making of film cathodes by Pd deposition on metal substrates in reducing environment or in high vacuum.

When preparing compact Pd cathodes, one should be guided by the following considerations: (1) dealing with a pure metal containing minimum impurity content; (2) the annealing parameters do not play a decisive role and should be selected only from the consideration of minimizing the internal stresses in the metal arising during its rolling.

Preliminary oxidation of the cathode should be carried out in pure oxygen. The metallurgical cycle and subsequent metal treatments (rolling, etching, etc.) should be carried out in clean rooms. It would be reasonable to process Pd foils after rolling or after annealing by glow discharge plasma of the deuterium with the purpose of getting rid of lubricant residues.

Obviously, it is necessary to refuse to work with the open electrochemical cells, though they show sometimes outstanding, but highly irreproducible results with respect to AHE.

Acknowledgements

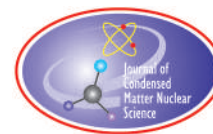
The author is grateful to Michael McKubre, Vittorio Violante, and to Graham Hubler for fruitful discussions of the problems raised here, and stimulating writing of this paper.

References

- [1] M. Fleischmann, S. Pons, M. Anderson, L. Li and M. Hawkins, Calorimetry of the palladium–deuterium–heavy water system, *J. Electroanalytical Chem.* **287** (1990) 293–350.

- [2] V. Violante, F. Sarto, E. Castagna, M. Sansovini, S. Lecci, D. L. Knies, K. S. Grabowski and G. K. Hubler, Material science on Pd–D system to study the occurrence of excess of power, *Proc. XIV Int. Conf. Condensed Matter Nucl. Sci.*, Washington DC, 10–15 August 2008, Vol. 2, pp. 429–436.
- [3] V. Violante, E. Castagna, S. Lecci, M. Sansovini, G. Hubler, D. Knies, K. Grabowski, M. McKubre, F. Tanzella, C. Sibilia, Z. Del Prete and T. Zilov, Evolution and progress in material science for studying the Fleischmann and Pons effect (FPE), *Proc. XV Int. Conf. Condensed Matter Nucl. Sci.*, Rome, Italy, 5–9 October 2009, pp. 1–4.
- [4] V. Violante, F. Sarto, E. Castagna, S. Lecci, M. Sansovini, M. McKubre and F. Tanzella, The study of the Fleischmann and Pons effect through the materials science development, *Proc. XVI Int. Conf. Condensed Matter Nucl. Sci.*, Chennai, India, 6–11 February 2011, 313–328.
- [5] V. Violante, E. Castagna, S. Lecci, F. Sarto, M. Sansovini, T. D. Makris, A. Torre, D. Knies, D. Kidwell, K. Grabowski, D. Dominguez, G. Hubler, R. Duncan, M. McKubre, A. La Gatta and L. Giorgi, Excess of power during electrochemical loading: materials, electrochemical conditions and techniques, *Proc. XVIII Int. Conf. Condensed Matter Nucl. Sci.*, Columbia, MU, USA, 20–25 July 2013, *J. Condensed Matter Nucl. Sci.* **15** (2015) 44–54.
- [6] V. Violante, E. Castagna, S. Lecci, F. Sarto, M. Sansovini, A. Torre, A. La Gatta, R. Duncan, G. Hubler, A. El Boher, O. Aziz, D. Pease, D. Knies and M. McKubre, Review of materials science for studying the Fleischmann and Pons effect, *Current Sci.* **108** (4) (2015) 540–558.
- [7] V. Violante, E. Castagna, S. Lecci, F. Sarto, M. Sansovini, T.D. Makris, A. Torre, D. Knies, D. Kidwell, K. Grabowski, D. Dominguez, G. Hubler, R. Duncan, A. El Boher, O. Azizi and M. McKubre, Excess power during electrochemical loading: materials, electrochemical conditions and techniques, *J. Condensed Matter Nucl. Sci.* **15** (2015) 44–54.
- [8] E. Castagna, C. Sibilia, S. Paoloni, V. Violante and P. Sarto, Surface plasmons and low energy nuclear reactions triggering, In A. Takahashi (Ed.), *Proc. 12th ICCF*, Yokohama, Japan, World Scientific, Singapore, 2006, 156–162.
- [9] I. Dardik, T. Zilov, H. Branover, A. El-Boher, E. Greenspan, B. Khachatorov, V. Krakov, S. Lesin and M. Tsirlin, in J.-P. Biberian (Ed.), *Proc. ICCF11*, World Scientific, Singapore, 2004, 84–102.
- [10] I. Dardik, T. Zilov, H. Branover, A. El-Boher, E. Greenspan, B. Khachaturov, V. Krakov, S. Lesin, A. Shapiro and M. Tsirlin, Report on electrolysis experiments at energetics technologies, In: Yu. Bazhutov (Ed.), *Proc. 13th Int. Conf. Cold Fusion (ICCF-13)*, Sochi, Russia, 2007, 325–347.
- [11] S.B. Ziemecki, J.A. Jones and D.S. Swartzfager, Coexistence of hydrogen and carbon solutes in the palladium lattice, *J. Less-Common. Metals* **131** (1987) 157–162.
- [12] E. Storms, Anomalous energy produced by PdD, *J. Condensed Matter Nucl. Sci.* **20** (2016) 81–99.
- [13] S. Hamm, O. Dmitrieva, D. Knies, R. Cantwell and V. McConnel, Electrochemical analysis of palladium cathodes towards the advancement of reproducibly high H/Pd loading ratios, Presented at the *ICCF 19 Conference*, April 13–17, 2015, Padua, Italy.
- [14] O. Dmitrieva, D. Knies, S. Hamm, R. Cantwell, M. McConnell, Role of dopants in deuterium loading during electrochemical experiment, Presented at the *ICCF 19 Conference*, April 13–17, 2015, Padua, Italy.
- [15] N.E. Singh-Miller and N. Marzari, Surface energies, work functions, and surface relaxations of low index metallic surfaces from first-principles, arXiv.0801.1077.v2 [cond-mat.mtrl-sci]-10 Nov, 2009, <https://arxiv.org/pdf/0801.1077.pdf>.
- [16] A. DeNinno, Dynamics in Pd–H(D) systems, *J. Condensed Matter Nucl. Sci.* **4** (2011) 291–303.
- [17] J.W. Cahn and J. E. Hilliard, *J. Chem. Phys.* **28** (1958) 258.
- [18] E. Storms, Formation of β -PdD containing high deuterium concentration using electrolysis of heavy-water, *J. Alloys Compounds* **268** (1998) 89–99.
- [19] E. Storms, Anomalous heat generated by electrolysis using a palladium cathode and heavy water, The presentation at the APS Meeting, Atlanta, GA, March 26, 1999.
- [20] J.H.W. deWit, Local potential measurements with the SKPFM on aluminium alloys, *Electrochimica Acta* **49** (2004) 2841–2850.

- [21] P. Schmutz and G. S. Frankel, Characterization of AA2024-T3 by scanning Kelvin probe force microscopy, *J. Electrochem. Soc.* **145** (7) (1998) 2285–2295.
- [22] M. Jönsson, D Thierry and N. LeBozec, Influence of microstructure on the corrosion behavior of AZ91D studied by scanning Kelvin probe force microscope and scanning Kelvin probe, *Corrosion Sci.* **5** (2006) 1193–1208.
- [23] W. Melitz, J. Shena, A.C. Kummel and S. Lee, Kelvin probe force microscopy and its application, *Surface Science Reports* **66** (2011) 1–27.
- [24] R. de Levi, Fractals and rough electrodes, *J. Electroanalytical Chem.* **281** (1990) 1–21.
- [25] M.C.H. McKubre, F. L. Tanzella, Materials Issues of Loading Deuterium Into Palladium and the Association with Excess Heat Production, *Proceedings of the 7th International Conference on Cold Fusion* (1998), Vancouver, Canada, ENECO, Inc., Salt Lake City, UT, 230.
- [26] M.C.H. McKubre, Excess Power Observations in Electrochemical Studies of the D/Pd System; the Operating Parameter Space, *Proc. 15th Int. Conf. Cold Fusion*, Rome, 5-10.



Research Article

Binuclear Atoms: A Model to Explain Low Energy Nuclear Reactions

Paolo Accomazzi*

Independent Researcher, via Pasubio 31, 28100 Novara, Italy

Abstract

In this paper we show that the helium-like hydrogen spectra obtained by Randell L. Mills and ultra-dense hydrogen obtained by Holmlid can be interpreted as experimental evidence of Binuclear Atoms. The hydrogen Binuclear Atom, a model proposed 25 years ago, is a metastable configuration in which the two nuclei are held together at a very short distance in an atom-like configuration. This should be a distinctive configuration of the hydrogen molecule where nuclei are characterized by a high kinetic energy, and nuclear motion is coupled with electronic motion. This is a completely different model from the usual Born–Oppenheimer picture of atoms and molecules we are used to, where nuclei oscillate about their equilibrium positions and electronic motion is decoupled from the nuclear one. The identification of helium-like hydrogen spectra and ultra-dense hydrogen as Binuclear Atoms has a strong impact on one of the main objections to Low Energy Nuclear Reactions (LENR): the overcoming of the Coulomb barrier thus identifying a sound mechanism for the occurrence of LENR. This work is not conclusive. The only goal of this work is to focus the attention of people interested in LENR mechanism on this subject, and encourage them to take this hypothesis more seriously.

© 2017 ISCMNS. All rights reserved. ISSN 2227-3123

Keywords: Binuclear atom, LENR, Mills hydrino, Rossi E-Cat, Ultra dense hydrogen

1. Introduction

One of the major objections to Low Energy Nuclear Reactions is the lack of a model able to explain the possibility that two nuclei might be at a short distance for a time sufficiently long to trigger nuclear reactions. The lack of a mechanism to overcome of the Coulomb barrier is an argument that dismisses any claim of nuclear reactions. For example, the Rossi–Focardi paper [1] is no exception to this objection. Discussing the nickel–hydrogen system, trying to evaluate the possibility of nuclear reactions, Rossi and Focardi calculate the tunneling probability P of the proton getting in close contact with Ni nucleus using the Gamow formula, which in Evans approximation is [2]:

$$P \approx e^{-(2\pi z Z/137\beta)}, \quad (1)$$

*E-mail: paolo.accomazzi@gmail.com.

where z and Z are the charge values for Ni ($Z = 28$) and H and $\beta = \frac{v}{c}$ is the ratio between the velocity of the incoming particle and the velocity of light. Considering that the kinetic energy can be evaluated as

$$E_c = \frac{1}{2}mv^2 = \frac{3}{2}kT,$$

where the temperature is about 1000 K, we obtain a kinetic energy of $E_c \approx 0.13$ eV. Putting these values in formula (1) we obtain an exceedingly small probability of tunneling, which is $P \approx e^{-2440} \approx 4.7 \times 10^{-1059}$, a value that does not account for the occurrence of nuclear events.

2. Binuclear Atoms

In 1991, Cerofolini [3] put forward a theory to explain some experimental results obtained with ion implantation experiments. In ion implantation experiments, ions are accelerated at various ranges of energies towards a solid target. This process gives rise to, among other things, atom–atom head-on collisions at a broad range of energies, down to the eV range when the projectile has lost most of its initial kinetic energy. We here refer in particular to papers [4,5]. In summary, various deuterated targets (as an example TiD) are bombarded with clusters of deuterated molecules (as an example D_2O), and deuteron–deuteron fusion rate is measured as a function of the impinging projectiles. The analysis of experimental data takes Cerofolini to the hypothesis of a precursor, a metastable state at about 30 eV, which should be responsible for the high fusion rate measured: the Binuclear Atom.

In an initial formulation, Binuclear atoms are defined in [6] in the following way:

Consider the head-on collision of two atoms with atomic number Z_1 and Z_2 . Particularly interesting is the situation of a kinetic energy sufficient to bring the nuclei to a distance smaller than the radius of the most bound electron. In this case the electrons can rearrange to assume, at least temporarily, a configuration that resembles that of the atom with atomic number $Z_1 + Z_2$, because this configuration has a binding energy much lower than the one of the two separate atoms. Considering only one electron, being the energy for the first orbit of the hydrogen-like atom $E(Z) = Z^2 E_0$, it follows that $E(Z_1 + Z_2) < E(Z_1) + E(Z_2)$. This excess binding energy can partially balance the internuclear Coulomb repulsion and temporarily stabilize the resulting *binuclear atom*.

After some considerations, Cerofolini concludes that the existence of Binuclear atoms is limited to a few couples of light atoms [6].

In [7], Cerofolini writes:

Binuclear atoms are metastable configurations in which two nuclei are held together by the electronic energy of the orbiting electrons in an atomic-like configuration. The hydrogen–hydrogen helium-like Binuclear atom $(H+H+)2e^-$ is explicitly predicted to exist, although the activation energy required for its formation (~ 30 eV) is extremely high for ordinary chemistry, so that it can only be formed under very special conditions such as the ones occurring inside a dense collisional cascade. The $(H+H+)2e^-$ -Binuclear atom is predicted to be metastable with a remarkably high activation energy (of several electron volts) for its dissociation. In the $(H+H+)2e^-$ -Binuclear atom, the electronic energy is not a constant of motion and is coupled with the nuclear kinetic energy, and the nuclei move with a kinetic energy on the order of 10 eV although they remain localized in a region of 0.4 to $0.5a_0$, where a_0 is the Bohr radius ($a_0 = 0.53 \times 10^{-8}$ cm) [7].

So Cerofolini's idea of Binuclear hydrogen was a short-lived kind of hydrogen, where the two protons are trapped at a very short distance and consequently electrons, orbiting in space around a more concentrated positive charge, tended to assume helium-like character. This was 1992, long before spectroscopic results of a helium-like hydrogen spectrum were obtained and brought to the attention of the scientific community.

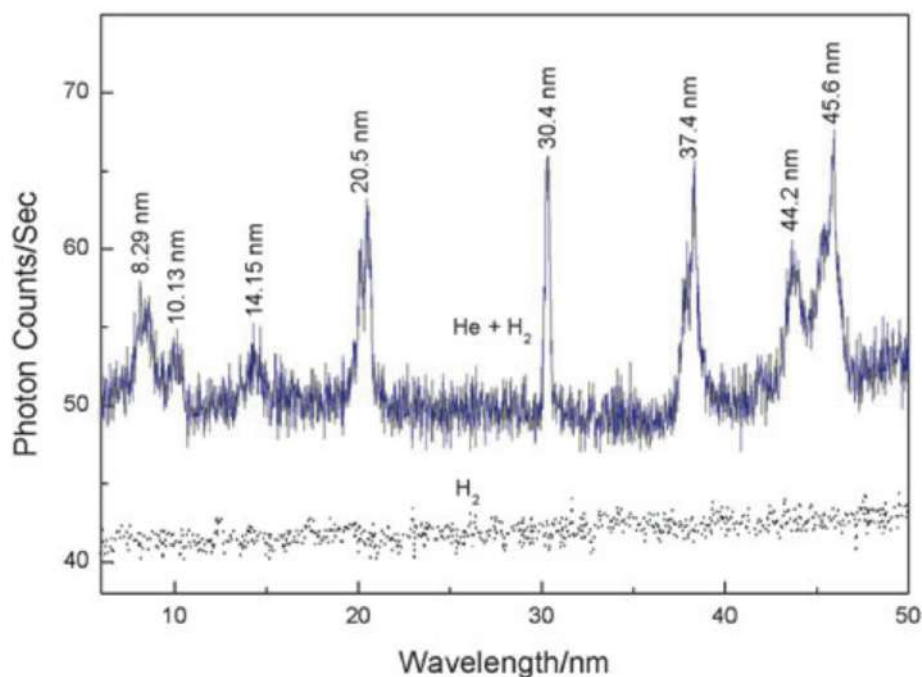


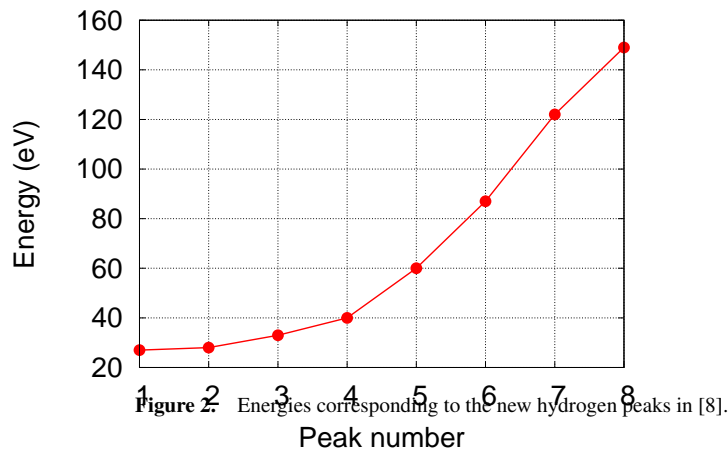
Figure 1. Figure is taken from [8]. The short wavelength EUV spectra (5–50 nm) of the microwave cell emission of the helium–hydrogen mixture (top curve) and control hydrogen (bottom curve).

3. Extreme Ultraviolet Spectroscopy of Helium–Hydrogen Plasma

Randell L. Mills, in his work *Extreme ultraviolet spectroscopy of helium-hydrogen plasma* [8], is able to show the formation of novel hydrogen emission lines (see Fig. 1) of a mixture of 98% helium and 2% hydrogen plasma at room temperatures and low pressure. The origin of the new lines cannot be easily determined: trivial explanations based on known chemical species of helium or hydrogen compounds are ruled out. The new lines appear only in helium-hydrogen mixtures, but not in helium or hydrogen alone, and not in mixtures of hydrogen with other noble gases. Experimental data have been replicated in other laboratories. Although helium seems not to be responsible for these lines, hydrogen instead shows an anomalous Doppler broadening in its atomic spectrum but at the same time it is not clear how a species of hydrogen could bound an electron at a higher energy than the first Bohr energy, which is 13.6 eV, whereas novel emission lines are at energy higher than 27.1 eV. Mills explains new emission lines with a new theory [9], the Hydrino, which should be the new fundamental state of atomic hydrogen.

Yet we can refute this interpretation if we assume a binuclear hydrogen metastable state was formed. Consider that, due to the catalytic action of helium, hydrogen Binuclear Atoms are formed in helium–hydrogen plasma. If the two hydrogen nuclei are close enough, electrons orbiting around them can rearrange taking helium characteristics, hence the origin of helium-like hydrogen spectrum.

Looking more closely at the energy diagram of the new hydrogen peaks, taken from Fig. 1, we can appreciate that the diagram formed (see Fig. 2) is similar to a parabola. Recall that the eigenvalue structure $E \approx n^2$ is characteristic of a particle in an infinite square well. This could indicate that the two protons get trapped in a potential well when their distance $r \rightarrow 0$. Since we are outside the realm of the Born–Oppenheimer approximation, what we see here should



be at the same time the electronic and nuclear eigenvalue, because electronic and nuclear motion should be strongly coupled.

Before leaving the Mills work, let us add a final important remark which we will recall later. These results have been replicated in different laboratories [10], where an anomalous broadening of hydrogen Balmer lines has been observed, and according to Mills [8] the average hydrogen atom temperature is 180–210 eV versus ≈ 3 eV for pure hydrogen (see Fig. 3 for details). An abnormal high protonic kinetic energy is a common feature that introduces us to the next experimental result: ultra dense hydrogen.

4. Ultra Dense Hydrogen

Working with Rydberg Matter, Prof. Holmlid is able to obtain in his laboratory a distinctive form of ultra dense hydrogen and deuterium with the following surprising characteristics: the two nuclei possess a kinetic energy up to 1000 eV and supposedly lie at a distance of the order of 10^{-2} Å [11]. The lower range of energies measured by Holmlid overlaps with the high range of energies found from Mills for helium-like hydrogen spectra.

Rydberg matter [12] is a state of matter formed by Rydberg atoms, which are atoms where the outermost electrons are found in excited planar circular orbits. Planar clusters of these atoms share these peripheral electrons that are loosely bound to the internal core of atoms. Rydberg electrons in the cluster are delocalized in a conduction band as in a metal.

Being in this way, normal bound distances in Rydberg matter are of the order of 10 Å and more. On the contrary, the structure of ultra dense hydrogen or deuterium appears different from ordinary Rydberg matter: the main problem is how to cope with the behavior of electrons in this structure. If nuclei are at a such short distance, how could electrons, orbiting in a very large orbit far away from nuclei, screen the nuclei Coulomb repulsion?

Needless to say, Prof. Holmlid proposes for ultra dense hydrogen a different kind of Rydberg matter based on spin (see Fig. 4). Anyway, we propose that ultra dense hydrogen is a form of Binuclear Atom, that is able to form, thanks to the interaction with the surface of Fe catalyzer used. A very interesting paper explains how a metallic surface can bring two charges of the same polarity to small distance that can be orders of magnitude smaller than the equilibrium separation of the pair potential minimum [13]. Maybe the metallic surface can have a catalytic action in both Rossi and

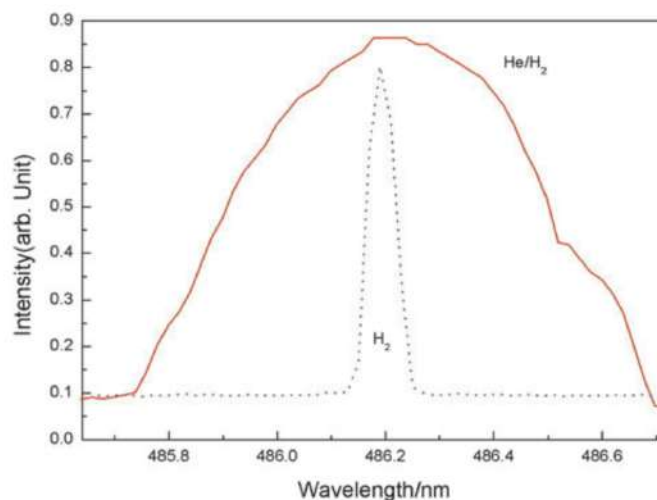


Figure 3. Figure is taken from [8]. The 656.3 nm Balmer α line width recorded with a high resolution (± 0.006 nm) visible spectrometer on helium–hydrogen (90/10%) and hydrogen microwave discharge plasmas. Significant broadening was observed from the helium–hydrogen plasma corresponding to an average hydrogen atom temperature of 180–210 eV compared to ≈ 3 eV for hydrogen alone.

Holmlid environments bringing pair of protons to small distances, where the Binuclear atom state may be triggered.

5. Discussion

Due to the lack of a known analytical formula, the solution to the equation for the hydrogen molecule has to be found numerically. Since 1964, with the work of Kolos and Wolniewicz, the wavefunction is determined solving the Schrödinger equation for the following Hamiltonian without assuming the Born–Oppenheimer approximation, i.e., treating protons and electrons on equal footing [14–19]:

$$H_0 = \sum_i \frac{p_i^2}{2m_i} + \sum_{i>j} \frac{q_i q_j}{r_{ij}}, \quad (2)$$

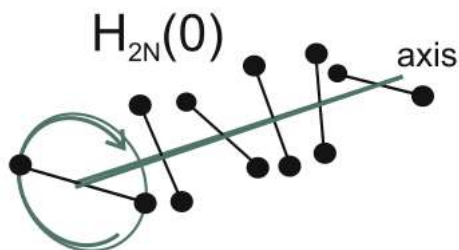


Figure 4. Ultra dense hydrogen structure proposed from Prof. Holmlid – see [9].

where indices i and j span over all four particles, \vec{r}_{ij} is the vector from particle i to particle j . We use atomic units i.e. $q = m_e = h = 1$ and the fine structure constant $\alpha^{-1} = c \approx 137$. A solution of the Schrödinger equation $H_0\psi = E\psi$ is variationally determined that, at this level, does not yet take into account spin, relativistic or QED effects. Being small, these corrections can be handled as a standard procedure using perturbation theory: the corrections are evaluated as an expectation value of the Hamiltonian describing the perturbation with the unperturbed wavefunction obtained before. Using this schema, the corrections to the energy determined using the H_0 Hamiltonian, may be ordered in terms of powers of the fine structure constant in the following way: [18,20]

$$E(\alpha) = E^{(0)} + E^{(2)} + E^{(3)} + E^{(4)} + \dots \quad (3)$$

Each $E^{(n)}$ contains the correction of the order α^n : $E^{(0)}$ is the eigenvalue of the non relativistic Schrödinger equation, H_0 , whereas $E^{(2)}$ is the expectation value of the Breit–Pauli Hamiltonian, $E^{(3)}$, $E^{(4)}$ and following are the various orders of QED contributions. For the purpose of this work it is sufficient to stop at the Breit–Pauli Hamiltonian level which is composed of several terms:

$$H_{BP} = H_{MV} + H_{DW} + H_{OO} + H_{SO} + H_{SS}, \quad (4)$$

where the various components are: H_{MV} is the mass–velocity term, H_{DW} is the Darwin term, H_{OO} the orbit–orbit interaction, H_{SO} the spin–orbit interaction, finally H_{SS} is the spin–spin interaction term.

For our goal, it is sufficient to examine in detail the corrections relative to the two protons only in the case depicted in Fig. 5. We derive our formulas from a symmetric approach to the Breit–Pauli Hamiltonian as can be found in [21] considering that for a motion around the common center of mass we have $\vec{p}_1 = -\vec{p}_2$ (see Fig. 5). Here \vec{r} is the proton–proton distance, m the proton mass, $\vec{\mu} = eg\vec{s}/(2m)$ its magnetic moment. The superscript pp means that this is the correction due to protons only.

$$H_{OO}^{pp} = -\frac{\alpha^2}{4m^2} \frac{\vec{p}_1 \cdot \vec{p}_2}{r}, \quad (5)$$

$$H_{SO}^{pp} = -\frac{g\alpha^2}{m^2} \frac{(\vec{s}_1 + \vec{s}_2) \cdot \vec{r} \times \vec{p}_1}{r^3}, \quad (6)$$

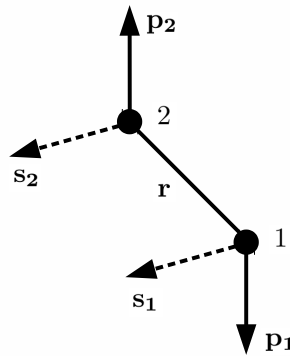


Figure 5. Two protons rotating around the common center of mass with parallel spin.

$$H_{SS}^{pp} = \frac{g^2 \alpha^2}{4m^2} \frac{\vec{s}_1 \cdot \vec{s}_2}{r^3}. \quad (7)$$

Obviously these corrections are exceedingly small if compared to the electronic ones due to the proton squared mass at the denominator, which lowers the nuclear contribution by six orders of magnitude.

But what is interesting to observe, and is the core of this paper, is the functional form of these corrections and their behavior compared to the Coulomb repulsion $1/r$ when $r \rightarrow 0$. As we can see, the three expressions H_{OO}^{pp} (5), H_{SO}^{pp} (6), H_{SS}^{pp} (7) are asymptotic to $1/r$, $1/r^2$, $1/r^3$ respectively. So, depending on how spins are mutually oriented, the sign of H_{SO}^{pp} and H_{SS}^{pp} changes consequently. Anyway, for $r \rightarrow 0$ the leading term seems to be H_{SS}^{pp} (7), that, in case of opposite protonic spin goes to $-\infty$ for $r \rightarrow 0$ as $1/r^3$. As we have said, Breit–Pauli Hamiltonian is an expression that has to be used in perturbative way, and as such it represents the first order correction to expression H_0 (2) for nuclear velocity and spin. Consequently, it is not correct to extrapolate system behavior for $r \rightarrow 0$ which is a condition very far from the Born–Oppenheimer minimum we are describing through use of H_0 Hamiltonian (2). But if we take the Breit Pauli Hamiltonian as an indication, we may speculate that the energy of the system may somehow lower for $r \rightarrow 0$, thus creating a potential well for the two protons at a smaller distance than the usual hydrogen bond length. This fact should be investigated with a stronger theoretical method such as, for instance, a suitable version of the Dirac equation.

If such a bound state exists, it should be called “Binuclear Atom” and it should present features similar to helium-like hydrogen Spectra and ultra dense hydrogen together. The reason is simple: two protons orbiting very near in space would produce an electric field similar to the one produced by the helium nucleus. Moreover, because we are not in Born–Oppenheimer conditions, the nuclear excited state directly modifies electronic eigenvalues as well, originating high energy lines of the spectrum. As far as ultra dense hydrogen is concerned, we have to recall that a Binuclear atom should be characterized by the axis of rotation of protons. This anisotropy could be at the same time cause and effect of a magnetic field and, depending on the formation mechanism, it would be possible to find several Binuclear Atoms stacked in columns as proposed by Holmlid (Fig. 4).

6. Closing Remarks

We have tried to show that the Binuclear atom model is able to explain different distinctive experimental results. The existence of helium-like hydrogen spectra, which occur only in helium–hydrogen mixed plasma, points to a formation of a metastable form of hydrogen characterized by a high protonic kinetic energy and helium-like electronic spectrum. On the other hand, the evidence of ultra dense hydrogen may be interpreted as the formation, through the assistance of a metallic surface, of another metastable hydrogen characterized by a very short proton–proton distance and a very high kinetic energy.

Last but not least, we can consider the consequences of ultra dense hydrogen in Rossi Ecat. If nickel lattice surface is able to form Binuclear atoms, we may recalculate through the Gamow formula the probability that hydrogen gets in contact with nickel nucleus. Using an energy value for protons of ≈ 1000 eV instead of $\approx 0,13$ eV [1,9], the calculated probability value becomes $P \approx 10^{-12}$. This is a rather different value than the Rossi and Focardi one, and could account for the occurrence of nuclear reactions.

The Binuclear atom model is the missing link between physics and chemistry.

Acknowledgments

The author thanks the referee for his comments, Alberto Accomazzi and Jed Rothwell for their precious editorial assistance.

References

- [1] S. Focardi and A. Rossi, A new energy source from nuclear fusion, http://www.journal-of-nuclear-physics.com/files/Rossi-Focardi_paper.pdf accessible from <http://www.journal-of-nuclear-physics.com/>, March 22, 2010.
- [2] R.D. Evans, *The Atomic Nucleus*, McGraw-Hill, New York, 1955, p. 876.
- [3] https://www.researchgate.net/publication/270633260_Editorial_In_Loving_Memory_of_GianFranco_Cerofolini.
- [4] G.F. Cerofolini, R. Dierckx, A. Foglio Para and G. Ottaviani, Deuterium–deuterium fusion by an activated precursor, *Il Nuovo Cimento* **13D** (11) (1991) 1347–1359.
- [5] G.F. Cerofolini, F. Corni, G. Ottaviani and R. Tonini, Search for nuclear reactions produced by the impact of heavy molecular ions onto LiD, *Il Nuovo Cimento* **105 A** (5) (1992) 741–750.
- [6] G.F. Cerofolini, Can binuclear atoms be formed in head-on atomic impacts at moderate energy? *J. Phy. Chem.* **96** (1992) 3298. <http://pubs.acs.org/doi/abs/10.1021/j100187a023>.
- [7] Gian Franco Cerofolini and Armando Foglio Para, Can binuclear atoms solve the cold fusion puzzle? *Fusion Sci. Technol.* **23** (1) (1993) 98–102. Abstract at http://www.ans.org/pubs/journals/fst/a_30124.
- [8] R. Mills and P. Ray, Extreme ultraviolet spectroscopy of helium-hydrogen plasma, *J. Phys. D: Appl. Phys.* **36** (2003) 1535–1542.
- [9] <http://brilliantlightpower.com/book/>.
- [10] Jonathan Phillips, Chun-Ku Chen and Toshi Shiina, Evidence of catalytic production of hot atomic hydrogen in rf generated hydrogen/helium plasmas. <https://arxiv.org/pdf/physics/0509127.pdf>.
- [11] Leif Holmlid, Excitation levels in ultra-dense hydrogen p(-1) and d(-1) clusters: Structure of spin-based Rydberg matter, *Int. J. Mass Spectrometry* **352** (2013) 1–8.
- [12] https://en.wikipedia.org/wiki/Rydberg_matter.
- [13] Nabil M. Lawandy, Interactions of charged particles on surfaces, *Appl. Phys. Lett.* **95** (2009) 234101.
- [14] S. Bubin and L. Adamowicz, Variational calculations of excited states with zero total angular momentum (vibrational spectrum) of H₂ without use of the Born–Oppenheimer approximation, *J. Chem. Phys.* **118** (2003) 3079. http://sergiybubin.org/docs/publications/bubin_jcp_118_3079_2003.pdf, <http://dx.doi.org/10.1063/1.1537719>.
- [15] D. Kedziera, M. Stanke, S. Bubin, M. Barysz and L. Adamowicz, Darwin and mass–velocity relativistic corrections in the non-Born–Oppenheimer calculations of pure vibrational states of H₂, *J. Chem. Phys.* **125** (2006) 014318. http://sergiybubin.org/docs/publications/kedziera_jcp_125_014318_2006.pdf, <http://dx.doi.org/10.1063/1.2236113>.
- [16] M. Stanke, D. Kedziera, S. Bubin, M. Molski and L. Adamowicz, Orbit–orbit relativistic corrections to the pure vibrational non-Born–Oppenheimer energies of H₂, *J. Chem. Phys.* **128** (2008) 114313. http://sergiybubin.org/docs/publications/stanke_jcp_128_114313_2008.pdf, <http://dx.doi.org/10.1103/PhysRevA.77.062509>.
- [17] S. Bubin, F. Leonarski, M. Stanke and L. Adamowicz, Non-adiabatic corrections to the energies of the pure vibrational states of H₂, *Chem. Phys. Lett.* **477** (2009) 12. http://sergiybubin.org/docs/publications/bubin_cpl_477_12_2009.pdf, <http://dx.doi.org/10.1016/j.cplett.2009.06.060>.
- [18] K. Pachucki, M. Puchalski, J. Komasa and P. Czachorowski, Complete $\alpha^6 m$ corrections to the ground state of H₂, *Phys. Rev. Lett.* (2016), in print. http://www.fuw.edu.pl/krp/papers/h2_ma6.pdf.
- [19] K. Pachucki and J. Komasa, Schrodinger equation solved for the hydrogen molecule with unprecedented accuracy, *J. Chem. Phys.* **144** (2016) 164306. <http://www.fuw.edu.pl/krp/papers/naH2.pdf>.
- [20] T. Helgaker, S. Coriani, P. Jørgensen, K. Kristensen, J. Olsen and K. Ruud, Recent advances in wave function-based methods of molecular-property calculations, *Chem. Rev.* **112** (2012) 543–631, DOI: 10.1021/cr2002239 http://folk.uio.no/helgaker/reprints/ChemRev_112_543_2012.pdf.
- [21] K. Pachucki, Theory of forbidden transitions in light atoms, *Phys. Rev. A* **67** (2003) 012504. <http://www.fuw.edu.pl/krp/papers/beryl.ps.gz>.



Research Article

The Electron and Occam's Razor

Francesco Celani*

Istituto Nazionale di Fisica Nucleare (INFN-LNF), Via E. Fermi 40, 00044 Frascati, Roma, Italy

Antonino Oscar Di Tommaso[†]

Università degli Studi di Palermo – Department of Energy, Information Engineering and Mathematical Models (DEIM), viale delle Scienze, 90128 Palermo, Italy

Giorgio Vassallo[‡]

Università degli Studi di Palermo – Department of Industrial and Digital Innovation (DIID), viale delle Scienze, 90128 Palermo, Italy

Abstract

This paper introduces a *Zitterbewegung* (ZBW) model of the electron by applying the principle of Occam's razor to Maxwell's equations and by introducing a scalar component in the electromagnetic field. The aim is to explain, by using simple and intuitive concepts, the origin of the electric charge and the electromagnetic nature of mass and inertia. A ZBW model of the electron is also proposed as the best suited theoretical framework to study the structure of Ultra-Dense Deuterium (UDD), the origin of anomalous heat in metal–hydrogen systems and the possibility of existence of “super-chemical” aggregates at Compton scale.

© 2017 ISCMNS. All rights reserved. ISSN 2227-3123

Keywords: Compton scale aggregates, Electric charge, Elementary particles, Electron structure, LENR, Lorenz gauge, Occam's razor, Space–time algebra, Ultra-dense deuterium, Vector potential, Weyl equation, Zitterbewegung

Nomenclature (see p. 77)

1. Introduction

The application of Occam's razor principle to Maxwell's equations suggests a *Zitterbewegung*^a (ZBW) interpretation of quantum mechanics [1] and a simple electromagnetic model for charge, mass and inertia. A new, particularly simple ZBW model of the electron is proposed as the best suited one to understand the structure of the Ultra-Dense Deuterium (UDD) [2,3] and the origin of Anomalous Heat in metal–hydrogen systems.

*Also at: International Society for Condensed Matter Nuclear Science (ISCMNS)-UK. E-mail: francesco.celani@lnf.infn.it.

[†]E-mail: antoninooscar.ditommaso@unipa.it.

[‡]Also at: International Society for Condensed Matter Nuclear Science (ISCMNS)-UK. E-mail: giorgio.vassallo@unipa.it.

^aGerman word for “tremble” or “shaking motion”.

Nomenclature

Symbol	Name	SI units	Natural units (NU)
A_{\square}	Electromagnetic four-potential	$V s m^{-1}$	eV
A_{Δ}	Electromag. vector potential	$V s m^{-1}$	eV
G	Electromagnetic field	$V s m^{-2}$	eV ²
F	Electromagnetic field bivector	$V s m^{-2}$	eV ²
B	Flux density field	$V s m^{-2} = T$	eV ²
E	Electric field	$V m^{-1}$	eV ²
S	Scalar field	$V s m^{-2}$	eV ²
$J_{\square e}$	Four-current density field	$A m^{-2}$	eV ³
J_{Δ}	Current density field	$A m^{-2}$	eV ³
v_{\square}	Four-velocity vector	$m s^{-1}$	1
v_{Δ}	Velocity vector	$m s^{-1}$	1
ρ	Charge density	$A s m^{-3} = C m^{-3}$	eV ³
x, y, z	Space coordinates	$m (1.97327 \times 10^{-7} m \approx 1 eV^{-1})$	eV ⁻¹
t	Time variable	$s (6.5821220 \times 10^{-16} s \approx 1 eV^{-1})$	eV ⁻¹
c	Light speed in vacuum	$2.99792458 \times 10^8 m s^{-1}$	1
\hbar	Reduced Planck constant	$1.054571726 \times 10^{-34} J s$	1
μ_0	Permeability of vacuum	$4\pi \times 10^{-7} V s A^{-1} m^{-1}$	4π
ϵ_0	Dielectric constant of vacuum	$8.854187817 \times 10^{-12} C (V m)^{-1}$	$1/4\pi$
e	Electron charge	$1.602176565 \times 10^{-19} A s$	0.085424546
m_e	Electron mass at rest	$9.109384 \times 10^{-31} kg$	$0.510998946 \times 10^6 eV$
λ_c	Electron Compton wavelength	$2.4263102389 \times 10^{-12} m$	$1.229588259 \times 10^{-5} eV^{-1}$
P_{\square}	Energy-momentum four-vector	$kg m s^{-1}$	eV
P_{Δ}	Momentum vector	$kg m s^{-1}$	eV
U, W	Energy	$J = kg m^2 s^{-2}$	eV

One of the most detailed and interesting ZBW electron models has been proposed by David Hestenes, emeritus of Arizona State University. He rewrote the Dirac equation for the electron using the four dimensional real Clifford algebra $Cl_{1,3}(\mathbb{R})$ of space–time with Minkowski signature “+ – – –”, eliminating unnecessary complexities and redundancies arising from the traditional use of matrices. The Dirac gamma matrices γ_{μ} and the associated algebra can be seen as an isomorphism of the four-basis vector of space–time geometric algebra. This simple isomorphism allows a full encoding of the geometric properties of the Dirac algebra, and a rewriting of Dirac equation that does not require complex numbers or matrix algebra. In this context the wave function ψ is characterized by the eight real values of the even grade multivectors of space–time algebra $Cl_{1,3}$ (STA). Even grade multivectors of STA can encode ordinary rotations as well as Lorentz transformations in the six planes of the space–time. Hestenes associates the rotations encoded by the wave function with an intrinsic very rapid rotation of the electron, the ZBW, that is considered at origin of the electron spin and magnetic moment. The word Zitterbewegung was originally used by Schrödinger to indicate a fast movement attributed to an hypothetical interference between “positive” and “negative” energy states. Kerson Huang later, more realistically, interpreted the ZBW as a circular motion [4].

In particular, B. Sidharth states that “*The well-known Zitterbewegung may be looked upon as a circular motion*

about the direction of the electron spin with radius equal to the Compton wavelength (divided by 2π) of the electron. The intrinsic spin of the electron may be looked upon as the orbital angular momentum of this motion. The current produced by the Zitterbewegung is seen to give rise to the intrinsic magnetic moment of the electron.” [5].

Hestenes considers the complex phase of the wave function solution of the traditional Dirac equation as the phase of the ZBW rotation, showing “the inseparable connection between quantum mechanical phase and spin” consequently rejecting the “conventional wisdom that phase is an essential feature of quantum mechanics, while spin is a mere detail that can often be ignored” [6]. Using the space–time algebra in [7] Hestenes defines the “canonical form” of the real wave function ψ :

$$\psi(x) = (\rho e^{i\beta})^{1/2} R.$$

In the above equation x is a generic space–time point, $\rho = \rho(x)$ is a scalar function interpreted as a probability density proportional to charge density, i is the spatial bivector $i = \gamma_2\gamma_1$, $\beta = \beta(x)$ is a function representing the value of a rotation phase in the plane $\gamma_2\gamma_1$ and R is a rotor valued function that encodes a Lorentz transformation. In the STA canonical form for Dirac’s wave function the imaginary unit i is replaced by a bivector that generates rotation in a well defined space-like plane and not in a generic undefined “complex plane”. This simple approach clearly reveals the geometric meaning of the imaginary numbers in the wave functions of quantum mechanics [7]. In agreement with the most common interpretations of quantum mechanics Hestenes associates the probability density function with a point-like shaped charge. In Eq. (48) of [7], by applying the relativistic time dilation to the ZBW period, Hestenes predicts a ZBW angular frequency that slows as the electron speed increase.

According to the model proposed in this paper, the electron characteristics may be explained by a massless charge distributed on the surface of sphere that rotates at the speed of light along a circumference with a radius equal to the reduced electron Compton wavelength (≈ 0.386159 pm), a value that is two times the one proposed by Hestenes in Eq. (33) of a relatively recent work [7]. The electron mass–energy, expressed in natural units, is equal to the angular speed of the ZBW rotation and to the inverse of the orbit radius (i.e. ≈ 511 keV), whereas the angular momentum is equal to the reduced Planck constant \hbar . Consequently, unlike the Hestenes prediction, our model proposes a relativistic contraction of the ZBW radius and a corresponding instantaneous ZBW angular speed that increases as the electron speed increases.

The inter-nuclear distance in UDD of ≈ 2.3 pm, found by Holmlid [2], seems to be compatible with proton–electron structures at the Compton scale [8,9] where the ZBW phases of neighbor electrons are correlated. These structures may generate unusual nuclear reactions and transmutations, considering the different sizes, time-scale and energies of these composites with respect to the dimension of the particles (such as neutrons) normally used in nuclear experiments.

By using the electromagnetic four-potential as a “*Materia Prima*” a natural connection between electromagnetic concepts and Newtonian and relativistic mechanics seems to be possible. The vector potential should not be viewed only as a pure mathematical tool to evaluate spatial electromagnetic field distributions but as a real physical entity, as suggested by the Aharonov–Bohm effect, a quantum mechanical phenomenon in which a charged particle is affected by the vector potential in regions in which the electromagnetic fields are null [10].

The present paper is structured in the following manner: Section 2 deals with a brief presentation of Maxwell’s equations that does not use Lorenz gauge; Section 3 presents a new simple ZBW model of the electron with a list of the main parameters that can be deduced by applying this model; Section 4 describes an original method to easily derive the Lorentz force law from the electromagnetic field; Section 5 consists of a short introduction to the concept of “quanta current” and it also presents the relation between the ZBW modeling and Heisenberg’s uncertainty principle; Section 6 summarizes other main models of the electron based on the concept of spinning charge distributions and, finally, Section 7 presents some preliminary hypotheses on UDD, Compton scale aggregates and the origin of anomalous heat in condensed matter.

In this paper all equations enclosed in square brackets with subscript “NU” have dimensions expressed in natural units.

2. Maxwell’s Equations in $Cl_{3,1}$

The space–time algebra is a four dimensions Clifford algebra with *Minkowski signature* $Cl_{1,3}$ (“west coast metric”) or $Cl_{3,1}$ (“east coast metric”) [11,12].

In $Cl_{3,1}$ algebra, used in this work, calling $\{\gamma_x, \gamma_y, \gamma_z, \gamma_t\}$ the four unitary vectors of an orthonormal base the following rules apply:

$$\gamma_i \gamma_j = -\gamma_j \gamma_i \quad \text{with } i \neq j \quad \text{and } i, j \in \{x, y, z, t\}, \tag{1}$$

$$\gamma_x^2 = \gamma_y^2 = \gamma_z^2 = -\gamma_t^2 = 1. \tag{2}$$

Maxwell’s equations can be rewritten considering all the derivatives of the electromagnetic four-potential \mathbf{A}_\square :

$$\mathbf{A}_\square(x, y, z, t) = \gamma_x A_x + \gamma_y A_y + \gamma_z A_z + \gamma_t A_t. \tag{3}$$

Each of the vector potential components A_x, A_y, A_z and A_t is a function of space and time coordinates and has dimension in SI units equal to $V \text{ s m}^{-1}$. \mathbf{A}_\square is a *harmonic* function [13] that can be seen as the unique source of all concepts-entities in Maxwell’s equations. Using the following definition of the operator ∂ in space–time algebra, where

$$\nabla = \gamma_x \frac{\partial}{\partial x} + \gamma_y \frac{\partial}{\partial y} + \gamma_z \frac{\partial}{\partial z} \quad \text{and} \quad c = \frac{1}{\sqrt{\epsilon_0 \mu_0}},$$

$$\partial = \gamma_x \frac{\partial}{\partial x} + \gamma_y \frac{\partial}{\partial y} + \gamma_z \frac{\partial}{\partial z} + \gamma_t \frac{1}{c} \frac{\partial}{\partial t} = \nabla + \gamma_t \frac{1}{c} \frac{\partial}{\partial t}, \tag{4}$$

the following expression can be written (see Table 1):

$$\partial \mathbf{A}_\square = \partial \cdot \mathbf{A}_\square + \partial \wedge \mathbf{A}_\square = S + \mathbf{F} = \mathbf{G}, \tag{5}$$

where

$$S = \nabla \cdot \mathbf{A}_\square - \frac{1}{c} \frac{\partial A_t}{\partial t} \tag{6}$$

is the scalar field,

$$\mathbf{F} = \frac{1}{c} \mathbf{E} \gamma_t + I \mathbf{B} \gamma_t = \frac{1}{c} (\mathbf{E} + I c \mathbf{B}) \gamma_t \tag{7}$$

the electromagnetic field and

$$I = \gamma_x \gamma_y \gamma_z \gamma_t \tag{8}$$

is the pseudoscalar unit.

Table 1. Relation between electromagnetic entities and the vector potential.

$\partial \mathbf{A}_{\square}$	$\gamma_x A_x$	$\gamma_y A_y$	$\gamma_z A_z$	$\gamma_t A_t$
$\gamma_x \frac{\partial}{\partial x}$	S_1	B_{z1}	$-B_{y1}$	$\frac{1}{c} E_{x1}$
$\gamma_y \frac{\partial}{\partial y}$	B_{z2}	S_2	B_{x1}	$\frac{1}{c} E_{y1}$
$\gamma_z \frac{\partial}{\partial z}$	$-B_{y2}$	B_{x2}	S_3	$\frac{1}{c} E_{z1}$
$\gamma_t \frac{1}{c} \frac{\partial}{\partial t}$	$\frac{1}{c} E_{x2}$	$\frac{1}{c} E_{y2}$	$\frac{1}{c} E_{z2}$	S_4

The electromagnetic field \mathbf{G} can be expressed in the following compact form

$$\mathbf{G}(x, y, z, t) = \nabla \cdot \mathbf{A}_{\Delta} - \frac{1}{c} \frac{\partial A_t}{\partial t} + \nabla A_t \gamma_t - \frac{1}{c} \frac{\partial \mathbf{A}_{\Delta}}{\partial t} \gamma_t + I \nabla \times \mathbf{A}_{\Delta} \gamma_t, \quad (9)$$

and the expression

$$\partial \mathbf{G} = \partial^2 \mathbf{A}_{\square} = 0, \quad (10)$$

represents the four Maxwell's equations.

By applying, now, the ∂ operator to the scalar field S , we obtain the expression of the four-current as

$$\frac{1}{\mu_0} \partial S = \frac{1}{\mu_0} \left(\gamma_x \frac{\partial S}{\partial x} + \gamma_y \frac{\partial S}{\partial y} + \gamma_z \frac{\partial S}{\partial z} + \gamma_t \frac{1}{c} \frac{\partial S}{\partial t} \right) = \mathbf{J}_{\square e}, \quad (11)$$

where $\mathbf{J}_{\square e} = \gamma_x J_{ex} + \gamma_y J_{ey} + \gamma_z J_{ez} - \gamma_t c \rho = \mathbf{J}_{\Delta} - \gamma_t c \rho = \rho (\mathbf{v} - \gamma_t c)$ is the four-current vector and $\mathbf{v}_{\square} = \gamma_x v_x + \gamma_y v_y + \gamma_z v_z - \gamma_t c = \mathbf{v} - \gamma_t c$ is a four-velocity vector. The ∂ operator applied to the four-current gives the charge–current conservation law

$$\frac{1}{\mu_0} \partial \cdot (\partial S) = \partial \cdot \mathbf{J}_{\square e} = \frac{\partial J_{ex}}{\partial x} + \frac{\partial J_{ey}}{\partial y} + \frac{\partial J_{ez}}{\partial z} + \frac{\partial \rho}{\partial t} = 0, \quad (12)$$

which can be written alternatively as

$$\partial \cdot (\partial S) = \partial^2 S = \frac{\partial^2 S}{\partial x^2} + \frac{\partial^2 S}{\partial y^2} + \frac{\partial^2 S}{\partial z^2} - \frac{1}{c^2} \frac{\partial^2 S}{\partial t^2} = \nabla^2 S - \frac{1}{c^2} \frac{\partial^2 S}{\partial t^2} = 0. \quad (13)$$

The charge is related to the scalar field according to

$$\frac{1}{c} \frac{\partial S}{\partial t} = \mu_0 J_{et} = -\mu_0 c \frac{\partial q}{\partial x \partial y \partial z} = -\mu_0 c \rho, \quad (14)$$

so that, by applying the time derivative to (13) and remembering (14), the wave equation of the charge density field $\rho(x, y, z, t)$ can be deduced:

$$\frac{\partial}{\partial t} (\partial^2 S) = \partial^2 \left(\frac{\partial S}{\partial t} \right) = \partial^2 (-\mu_0 c^2 \rho) = -\mu_0 c^2 \partial^2 \rho = 0, \quad (15)$$

whose last equality gives

$$\partial^2 \rho = \nabla^2 \rho - \frac{1}{c^2} \frac{\partial^2}{\partial t^2} \rho = 0. \quad (16)$$

A more detailed development of Maxwell's equations in $Cl_{3,1}$ algebra, made by the authors, can be found in *J. Condensed Matter Nucl. Sci.* **25** (2017) entitled "Maxwell's Equations and Occam's Razor".

3. Electron Zitterbewegung Model

The concept of charge that emerges from this rewriting of Maxwell's equations has a non-trivial implication: the analysis of (13) and (16) shows that the time derivative of a field S which propagates at the speed of light, must necessarily represent charges that are also moving at the speed of light.

This observation advises a pure electromagnetic model of elementary particles based on the ZBW interpretation of quantum mechanics [1,14]. According to this interpretation, the electron structure consists of a massless charge that rotates at the speed of light along a circumference equal to electron Compton wavelength λ_c [15,16]. Calling r_e the ZBW radius, ω_e the angular speed and T its period we have:

$$r_e = \frac{\lambda_c}{2\pi} \approx 3.861593 \times 10^{-13} \text{ m}, \quad (17)$$

$$\omega_e = \frac{c}{r_e} = 2\pi \frac{c}{\lambda_c} \approx 7.763440 \times 10^{20} \text{ rad s}^{-1}, \quad (18)$$

$$T = \frac{2\pi}{\omega_e} = \frac{2\pi r_e}{c} \approx 8.093300 \times 10^{-21} \text{ s}. \quad (19)$$

The value of the electron mass, expressed in SI units, can be derived from the following energy equations [1]

$$W_{\text{tot}} = m_e c^2 = \hbar \omega_e = \frac{\hbar c}{r_e}, \quad (20)$$

from which

$$m_e = \frac{\hbar \omega_e}{c^2} = \frac{\hbar}{c r_e} = \frac{h}{c \lambda_c} \approx 9.109383 \times 10^{-31} \text{ kg} \quad (21)$$

is obtained. Using natural units with $\hbar = c = 1$ the electron mass (in eV) is equal to the angular speed ω_e and to the inverse of r_e :

$$\left[m_e = \omega_e = \frac{1}{r_e} \approx 0.511 \times 10^6 \text{ eV} \right]_{\text{NU}}.$$

Recently, a connection between frequency and mass, in agreement with De Broglie's formula $f = mc^2/h$, has been experimentally demonstrated [17].

3.1. Simple electron model

A charge rotating at speed of light generates a current I_e that is equal to the ratio of the elementary charge e and its rotation period T [18]:

$$I_e = \frac{e}{T} = \frac{ec}{2\pi r_e} = \frac{e\omega_e}{2\pi} \approx 19.796331 \text{ A.} \quad (22)$$

The electron magnetic moment μ_B (Bohr magneton) is equal to the product between the current I_e and the enclosed area \mathcal{A}_e

$$\mu_B = I_e \mathcal{A}_e = \frac{e\omega_e}{2\pi} \pi r_e^2 = \frac{ec}{2} r_e = \frac{ec^2}{2\omega_e} = \frac{e\hbar}{2m_e} \approx 9.274010 \times 10^{-24} \text{ A m}^2. \quad (23)$$

Occam's razor is an effective epistemological instrument that imposes to avoid as much as possible the introduction of exceptions. Following this rule a pure electromagnetic origin of the electron's "intrinsic" angular momentum should be found.

Consequently, the canonical momentum P_t of the rotating massless charge may be seen as the cause of the intrinsic angular momentum:

$$\Omega = P_t r_e,$$

where the canonical momentum P_t of e , in presence of a vector potential A , generated by the current I_e , is

$$P_t = eA.$$

Imposing the constraint that $\Omega = \hbar$ we can compute A as function of I_e

$$\Omega = eAr_e = \frac{eAc}{\omega_e} = \frac{e^2 c A}{2\pi I_e} = \hbar, \quad (24)$$

from which it is possible to derive the expression of the vector potential seen by the spinning charge

$$A = \frac{2\pi\hbar}{e^2 c} I_e = \frac{\hbar}{er_e} = \frac{\hbar\omega_e}{ec} = \frac{m_e c}{e} \approx 1.704509 \times 10^{-3} \text{ V s m}^{-1}. \quad (25)$$

From (25) it is possible to derive the Fine Structure Constant (FSC)

$$\alpha = \frac{\mu_0}{4\pi} \frac{ce^2}{\hbar} = \frac{\mu_0}{4\pi} \frac{e\omega_e}{A} \approx 7.297352 \times 10^{-3}. \quad (26)$$

Using natural units we get these simple relations:

$$[A = 2\pi\alpha^{-1} I_e]_{\text{NU}},$$

$$[eA = \omega_e = r_e^{-1} = m_e = P_t]_{\text{NU}},$$

where α^{-1} , the inverse of the FSC, is a pure number and e is the elementary charge expressed in natural units

$$[\alpha^{-1} = e^{-2} \approx 137.035989]_{\text{NU}}.$$

3.2. Spin and intrinsic angular momentum

The intrinsic angular momentum \hbar of the electron model (see (24)) is compatible with the spin value $\hbar/2$ if we consider the electron interaction with the external flux density field \mathbf{B}_E , as in the Stern–Gerlach experiment. We can interpret the spin value $\pm\hbar/2$ as the component of the intrinsic angular momentum $\mathbf{\Omega} = \hbar$ aligned with the external flux density field \mathbf{B}_E . In this case the angle between the \mathbf{B}_E vector and the angular momentum have only two possible values, namely $\pi/3$ and $2\pi/3$ while the electron is subjected to a Larmor precession with angular frequency $\omega_p = d\vartheta_p/dt$. The Larmor precession is generated by the mechanical momentum

$$\tau = |\boldsymbol{\mu}_B \times \mathbf{B}_E| = B_E \mu_B \sin\left(\frac{\pi}{3}\right). \quad (27)$$

But

$$d\mathbf{\Omega} = \mathbf{\Omega}_\perp d\vartheta_p = \Omega \sin\left(\frac{\pi}{3}\right) d\vartheta_p,$$

where $\mathbf{\Omega}_\perp$ is the component of the intrinsic angular momentum orthogonal to \mathbf{B}_E and, therefore, it is possible to write

$$\tau = \frac{d\mathbf{\Omega}}{dt} = \Omega \sin\left(\frac{\pi}{3}\right) \frac{d\vartheta_p}{dt}. \quad (28)$$

By equating (27) and (28) we get

$$B_E \mu_B = \Omega \omega_p,$$

from which it is possible to determine the precession angular frequency

$$\omega_p = \frac{B_E \mu_B}{\Omega} = \frac{B_E \mu_B}{\hbar}. \quad (29)$$

3.3. Value of the vector potential, cyclotron resonance and flux density field

The pure electromagnetic momentum eA of the spinning charge of an electron at rest can be seen as it were the momentum of a particle of mass m_e and speed c in classical Newtonian mechanics. Considering ω_e as the cyclotron angular frequency (which is coincident with the ZBW angular speed) given by the flux density field B generated by the current I_e

$$\omega_e = \frac{eB}{m_e} = \frac{eBc^2}{\hbar\omega_e},$$

it is possible to deduce the magnetic flux density produced by the electron

$$B_e = \frac{\hbar\omega_e^2}{ec^2} \approx 4.414004 \times 10^9 \text{ V s m}^{-2}. \quad (30)$$

This very high flux density value (also known as *Landau critical value*) seems to be related to the physics of neutron stars and pulsars [19–21] or to that of superconductivity [22,23].

It is also possible to calculate the flux density at the center of the electron orbit by the following expression derived from the Biot–Savart law

$$B_0 = \frac{\mu_0 I_e}{2 r_e} \approx 32.210548 \times 10^6 \text{ V s m}^{-2}. \quad (31)$$

Considering that

$$dA = A d\vartheta \Rightarrow \frac{dA}{dt} = A\omega_e, \quad (32)$$

where $d\vartheta = \omega_e dt$ is the differential of the ZBW phase, and considering that the magnetic force F_B must be equal to the time derivative of the canonical momentum, it is possible to write

$$F_B = B_e ec = e \frac{dA}{dt} = eA \frac{d\vartheta}{dt} = eA\omega_e \approx 0.212014 \text{ N}. \quad (33)$$

Finally, by manipulating the previous equation, it is possible to recompute by another method the module of the vector potential

$$A = \frac{B_e c}{\omega_e} = \frac{\hbar\omega_e}{ec} = \frac{\hbar}{er_e}.$$

3.4. Value of magnetic and electrostatic energy, magnetic flux quantization and radius of the elementary charge

Once we obtain the expression for the vector potential it is possible to determine the magnetic flux produced by the rotating elementary charge by applying the circulation of the vector potential A :

$$\phi_e = \oint_{\lambda_e} A d\lambda = \int_0^{2\pi} \frac{\hbar}{er_e} r_e d\vartheta = 2\pi \frac{\hbar}{e} = \frac{h}{e} \approx 4.135667 \times 10^{-15} \text{ V s}, \quad (34)$$

i.e., the magnetic flux crossing the surface described by the charge trajectory is quantized (*flux quantum*). This expression has been found with a different approach with respect to [24], i.e., with the application of the vector potential. This flux quantum, though different from the value given in CODATA 2014, is compatible with $h/2e$ for the same reasons explained in Section 3.2, with reference to \hbar . Now it is possible to calculate the magnetic energy stored in the field produced by the spinning charge

$$W_m = \frac{1}{2} \phi_e I_e = \frac{1}{2} 2\pi \frac{\hbar}{e} \frac{ec}{2\pi r_e} = \frac{\hbar c}{2r_e} \approx 4.093553 \times 10^{-14} \text{ J} \quad (35)$$

which is equal to half the electron rest energy W_{tot} as can be seen from (20). The other half part can be attributed to electrostatic energy, i.e.,

$$W_{\text{tot}} - W_{\text{m}} = W_{\text{e}} = \iiint_V w_{\text{e}} dV, \quad (36)$$

where w_{e} is the electrostatic energy per unit of volume and V is the volume in which the whole energy W_{e} is stored, and whose expression is given by

$$w_{\text{e}} = \frac{1}{2} \epsilon_0 E^2 = \frac{\epsilon_0}{2} \left(\frac{1}{4\pi\epsilon_0} \frac{e}{r^2} \right)^2 = \frac{1}{32\pi^2\epsilon_0} \frac{e^2}{r^4}. \quad (37)$$

By expanding and integrating (36), with $dV = 4\pi r^2 dr$ (the generic elementary volume of a spherical thin shell centered in the middle of the electron trajectory) we obtain

$$W_{\text{e}} = \frac{e^2}{32\pi^2\epsilon_0} \int_{r_0}^{\infty} \frac{1}{r^4} 4\pi r^2 dr = \frac{e^2}{8\pi\epsilon_0} \int_{r_0}^{\infty} \frac{1}{r^2} dr = -\frac{e^2}{8\pi\epsilon_0} \frac{1}{r} \Big|_{r_0}^{\infty} = \frac{e^2}{8\pi\epsilon_0 r_0}. \quad (38)$$

Now, by taking into account that $W_{\text{e}} = W_{\text{m}}$ we get the radius

$$r_0 = \frac{e^2}{8\pi\epsilon_0 W_{\text{e}}} = \frac{e^2}{8\pi\epsilon_0 W_{\text{m}}} = \frac{e^2}{8\pi\epsilon_0} \frac{2r_{\text{e}}}{\hbar c} = \frac{e^2 r_{\text{e}}}{4\pi\epsilon_0 \hbar c} \approx 2.817940 \times 10^{-15} \text{ m}, \quad (39)$$

whose value is coincident with the classical electron radius [25]. The upper equation states that the rotating charge must have a finite dimension, in particular it may be visualized as a sphere with charge equal to e uniformly distributed over its surface. The charge cannot be concentrated in a point in order to exhibit a finite electrostatic energy. It is interesting and at the same time very important to note that the ratio r_{e}/r_0 is exactly equal to the inverse of the FSC, i.e.,

$$\frac{r_{\text{e}}}{r_0} = \frac{4\pi\epsilon_0 \hbar c}{e^2 r_{\text{e}}} r_{\text{e}} = \frac{4\pi\epsilon_0 \hbar c}{e^2} = \alpha^{-1} \approx 137.035999. \quad (40)$$

The expression of the ratio ϕ_{e}/T has in SI the dimension of a voltage:

$$V_{\text{e}} = \frac{\phi_{\text{e}}}{T} = \frac{\hbar}{e} \frac{c}{2\pi r_{\text{e}}} = \frac{\hbar c}{e r_{\text{e}}} \approx 5.109989 \times 10^5 \text{ V}, \quad (41)$$

where T is defined by (19). Now, dividing the above voltage by the current generated by the rotating charge expressed by means of (22), we find the von Klitzing constant or *quantum of resistivity*, related to the quantum Hall effect [24]

$$R_{\text{K}} = \frac{V_{\text{e}}}{I_{\text{e}}} = \frac{\hbar}{e} \frac{c}{2\pi r_{\text{e}}} \frac{2\pi r_{\text{e}}}{e c} = \frac{\hbar}{e^2} = \frac{2\pi \hbar}{e^2} \approx 25812.807 \Omega. \quad (42)$$

An alternative expression of the von Klitzing constant can be derived from the electrostatic potential φ_{e} and the current I_{e}

$$R_{\text{K}} = \frac{\varphi_{\text{e}}}{I_{\text{e}}} = \frac{1}{4\pi\epsilon_0} \frac{e}{r_0} \frac{2\pi r_{\text{e}}}{e c} = \frac{1}{2c\epsilon_0} \frac{r_{\text{e}}}{r_0} = \frac{\mu_0 c}{2\alpha} \approx 25812.807 \Omega. \quad (43)$$

Finally, it is possible to deduce the values of two interesting electrical parameters, namely the inductance L_e , the capacitance C_e of the electron and the frequency f_e . In fact

$$L_e = \frac{\phi_e}{I_e} = 4\pi^2 \frac{\hbar r_e}{e^2 c} \approx 2.089108 \times 10^{-16} \Omega \text{ s}, \quad (44)$$

$$C_e = \frac{e}{\varphi_e} = 4\pi\epsilon_0 r_0 \approx 3.135381 \times 10^{-25} \text{ F} \quad (45)$$

and

$$f_e = \frac{1}{\sqrt{L_e C_e}} \approx 1.235590 \times 10^{20} \text{ Hz}. \quad (46)$$

3.5. Electron kinematics

The finite dimension of the elementary charge imposes the constraint that all points of the surface of the spinning charged sphere must have the same instantaneous speed of light c (see Eq. (16)) and the same angular speed. In a frame rotating with the ZBW frequency the spinning charged sphere rotates around its center with opposite speed with respect to the ZBW angular frequency:

$$\omega_0 = -\omega_e. \quad (47)$$

The new (not point-like) electron model and the speed diagrams are shown in Fig. 1a. Here the charge rotates with angular speed ω_0 around the axis passing through the center of the sphere and, therefore, all points of the sphere have the same absolute speed c .

During the revolution around the origin C the charge describes a torus whose cross section is equal to πr_0^2 and having a volume equal to $2\pi^2 r_e r_0^2$. In Fig. 1b, the elementary charge is represented as a charged sphere.

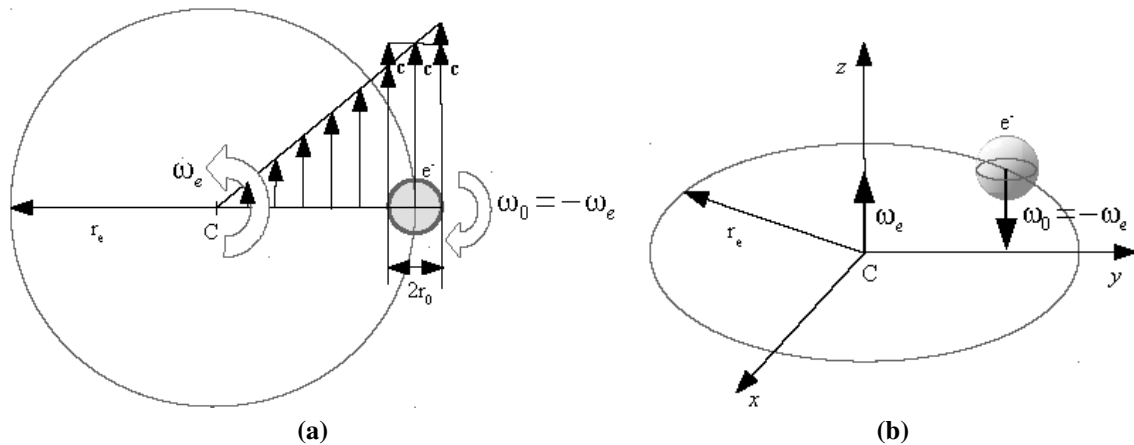


Figure 1. (a) ZBW model and speed diagrams of the electron charge (e^-). All points of the sphere have an absolute speed equal to c . (b) 3D representation. The charged sphere is rotating with the relative angular speed $\omega_0 = -\omega_e$ on the trajectory having radius r_e around the vertical axis passing through the center of the sphere.

3.6. Electron and electromagnetic Lagrangian density

From (25), (22) and (39), with the hypothesis that the electron is characterized by a uniform current density, we get the first term of the interaction part of the Lagrangian density

$$L_{\text{int1}} = \mathbf{J}_\Delta \mathbf{A}_\Delta = JA = \frac{I_e}{\pi r_0^2} \frac{m_e c}{e} \approx 1.352604 \times 10^{27} \text{ J m}^{-3}. \quad (48)$$

By integration over the volume described by the electron toroidal trajectory, it is possible to recompute its rest energy:

$$W_{\text{tot}} = \iiint_V JA \, dV = \frac{I_e}{\pi r_0^2} \frac{m_e c}{e} 2\pi^2 r_e r_0^2 \approx 8.187106 \times 10^{-14} \text{ J} = 510.998946 \text{ keV}, \quad (49)$$

which gives the same result calculated by means of (36). The same results are obtained, apart from a sign $-$, by the following relations

$$L_{\text{int2}} = -\rho\varphi_e = \frac{e}{2\pi^2 r_e r_0^2} \frac{e}{4\pi\epsilon_0 r_e} = -\frac{e^2}{8\pi^3 \epsilon_0 (r_e r_0)^2} \approx -1.352604 \times 10^{27} \text{ J m}^{-3}, \quad (50)$$

$$W_{\text{tot}} = \iiint_V |-\rho\varphi_e| \, dV = \frac{e^2 2\pi^2 r_e r_0^2}{8\pi^3 \epsilon_0 (r_e r_0)^2} = \frac{e^2}{4\pi\epsilon_0 r_e} \approx 8.187106 \times 10^{-14} \text{ J} = 510.998946 \text{ keV}. \quad (51)$$

All parameters that can be deduced by the application of the present ZBW model are resumed in Table 2, where the first three rows are referred to the model's input parameters.

3.7. ZBW and a simple derivation of the relativistic mass

With the ZBW model it is possible to show a simple, original and intuitive explanation of the relativistic mass concept. For an electron moving at constant speed v_z along the z -axis orthogonal to the rotation plane, calling v_\perp the component of the velocity of the rotating charge in the $\gamma_x\gamma_y$ plane we can find the value of the ZBW radius r of the moving electron. In fact, assuming a constant value of ω_e , we have

$$v_z^2 + v_\perp^2 = c^2, \quad (52)$$

that can be written as

$$v_z^2 + \omega_e^2 r^2 = \omega_e^2 r_e^2 = c^2.$$

Therefore

$$\frac{r^2}{r_e^2} = 1 - \frac{v_z^2}{c^2}$$

or

$$r = r_e \sqrt{1 - \frac{v_z^2}{c^2}}. \quad (53)$$

Finally, by considering that the mass is inversely proportional to r , it is possible to write the relativistic expression of the mass as

$$m = \frac{m_e}{\sqrt{1 - \frac{v_z^2}{c^2}}}, \quad (54)$$

where m_e is the electron mass at rest. Fig. 2 represents the ZBW trajectory of the spinning charge of an electron subjected to an acceleration directed along the positive z -axis. Due to the acceleration the radius reduces itself according to (53).

3.8. Dirac equation and spinor representation of motion

By using space–time algebra and following the idea of Hestenes–Dirac equation

$$i\partial\psi - m\psi = 0 \quad (55)$$

becomes the Hestenes–Dirac equation [26]

Table 2. Parameters of the *Zitterbewegung* model.

Item	Symbol	Value (SI)	Unit (SI)
Charge	e	$1.602176565 \times 10^{-19}$	C = A s
ZBW orbit radius	$r_e = \lambda_c/2\pi$	3.861593×10^{-13}	m
Intrinsic angular momentum	$\Omega = \hbar = h/2\pi$	$1.054571726 \times 10^{-34}$	J s
Spin ¹	$\hbar/2$	$0.527285863 \times 10^{-34}$	J s
Angular speed	ω_e	7.763440×10^{20}	rad s ⁻¹
Mass	m_e	9.109384×10^{-31}	kg
Current	I_e	19.796331	A
Magnetic moment (Bohr magneton)	μ_B	9.274010×10^{-24}	A m ²
Vector potential	A	1.704509×10^{-3}	V s m ⁻¹
Magnetic flux density	B_e	4.414004×10^9	V s m ⁻²
Magnetic flux	$\phi_e = h/e$	4.135667×10^{-15}	V s
Magnetic energy	W_m	4.093553×10^{-14}	J
Electrostatic energy	W_e	4.093553×10^{-14}	J
Electron energy at rest	$W_{\text{tot}} = m_e c^2$	8.187106×10^{-14}	J
Charge radius	r_0	2.817940×10^{-15}	m
Inverse of the FSC	$\alpha^{-1} = r_e/r_0$	137.035999	1
Von Klitzing constant	$R_K = h/e^2 = \mu_0 c/2\alpha$	25812.807	Ω
Inductance	$L_e = 4\pi^2 \hbar r_e / e^2 c$	2.089108×10^{-16}	Ω s
Capacitance	$C_e = 4\pi\epsilon_0 r_0$	3.135381×10^{-25}	F
1-st part of L_{int}	JA	1.352604×10^{27}	J m ⁻³
Electron energy at rest	$\iiint_V JA dV$	510.998946	keV
Electron energy at rest	$\iiint_V \rho\varphi_e dV$	510.998946	keV

¹Component of the angular momentum due to Larmor precession along the external magnetic field B_E (see (27)).

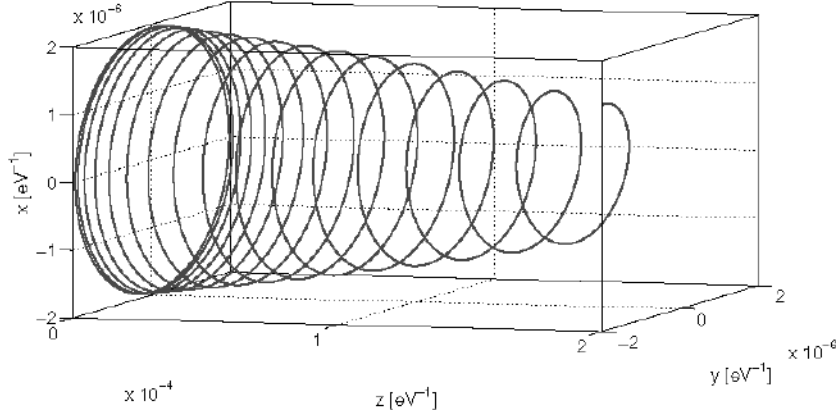


Figure 2. Zitterbewegung trajectory during an acceleration of the electron in the z -direction.

$$\partial\psi - m\psi\gamma_t\gamma_x\gamma_y = 0, \tag{56}$$

where ∂ is the same operator used in Maxwell’s equations $\partial\mathbf{G} = 0$ (see (4)), but using the space–time Minkowski signature of $Cl_{1,3}$ “+ – – –”. For a massless particle, where $m = 0$, (56) becomes the Weyl equation

$$\partial\psi = 0, \tag{57}$$

which is formally identical to (10). In all cases the solution is a *spinor* field. A spinor is a mathematical object that in space–time algebra is simply a multivector with only even grade components. The geometric product of an even number of vectors is always a spinor. A spinor that is the geometric product of two unitary vectors is a unitary rotor. The movement of a point charge that rotates in the plane $\gamma_x\gamma_y$ and at the same time moves up along the γ_z axis can be seen as the composition of an ordinary rotation in the plane $\gamma_x\gamma_y$ followed by a scaled hyperbolic rotation in the plane $\gamma_z\gamma_t$. The composition of these two rotations can be encoded with a single spinor of $Cl_{3,1}$. Therefore, if $\mathbf{r}_{e\Box 0}$ is the coordinate of the center of the charged sphere at $t = t_0$, r_e the Compton radius we have

$$\mathbf{r}_{e\Box 0} = \gamma_x r_e + \gamma_t c t_0,$$

$$[\mathbf{r}_{e\Box 0} = \gamma_x r_e + \gamma_t c t_0]_{\text{NU}}.$$

By introducing the rotor R_{xy} , that generates ordinary rotation in the $\gamma_x\gamma_y$ plane, and remembering that ω_e is the ZBW angular frequency, with

$$R_{xy}(t) = \cos\left(\frac{\omega_e t}{2}\right) + \gamma_x\gamma_y \sin\left(\frac{\omega_e t}{2}\right) = \exp\left(\gamma_x\gamma_y \frac{\omega_e t}{2}\right),$$

we obtain the instantaneous position of the center of the charged sphere:

$$\mathbf{r}_{e\Box}(t) = R_{xy}(\mathbf{r}_{e\Box 0} + \gamma_t ct) \widetilde{R}_{xy}.$$

We introduce now the rotor R_{zt} , that generates a hyperbolic rotation with rapidity φ in the $\gamma_z \gamma_t$ plane, in order to encode the motion at speed v_z along the γ_z direction

$$R_{zt} = \cosh(\varphi)^{-1/2} \left[\cosh\left(\frac{\varphi}{2}\right) - \gamma_z \gamma_t \sinh\left(\frac{\varphi}{2}\right) \right] = \cosh(\varphi)^{-1/2} \exp\left(-\gamma_z \gamma_t \frac{\varphi}{2}\right),$$

where

$$\varphi = \tanh^{-1}\left(\frac{v_z}{c}\right).$$

The instantaneous position $\mathbf{r}'_{e\Box}(t)$ of the center of the rotating and translating sphere can be obtained by applying R_{zt} :

$$\mathbf{r}'_{e\Box}(t) = R_{zt} \mathbf{r}_{e\Box} \widetilde{R}_{zt}.$$

With the definition of spinor R

$$R = R_{zt} R_{xy} = \cosh(\varphi)^{-\frac{1}{2}} \exp\left(-\gamma_z \gamma_t \frac{\varphi}{2}\right) \exp\left(\gamma_x \gamma_y \frac{\omega_c t}{2}\right),$$

we can rewrite the instantaneous position in a compact form as

$$\mathbf{r}'_{e\Box}(t) = R(\mathbf{r}_{e\Box 0} + \gamma_t ct) \widetilde{R}.$$

The instantaneous coordinate of a generic point on the surface of the charged sphere can be obtained adding a specific fixed vector $\mathbf{r}_{o\Delta}$

$$\mathbf{r}_{\text{surf}\Box}(t) = \mathbf{r}'_{e\Box}(t) + \mathbf{r}_{o\Delta}.$$

The module of vector $\mathbf{r}_{o\Delta}$ is equal to $r_{o\Delta} = \alpha r'_{e\Delta}$, a value equal to the classical radius of the electron for non relativistic speeds.

It is important to note that, according to Hestenes, the ZBW angular frequency is two times the De Broglie value $m_e c^2 / \hbar$ used in our model: “The diameter of the helix is the electron Compton wavelength $2\lambda_0 = 2c/\omega_0 = \hbar/mc$ ” [27]. The value 1.93079×10^{-13} m of the “zitter-radius” of Hestenes’ electron model is confirmed in Eq. (33) of a more recent work [7].

4. Electromagnetism, Mechanics and Lorentz force

The “pure electromagnetic” vector $e\mathbf{A}_\Box$ may be interpreted as the momentum–energy \mathbf{P}_\Box of a particle with electric charge e , momentum \mathbf{P}_Δ and energy $U = P_t c$:

$$\mathbf{P}_\Box = e\mathbf{A}_\Box, \quad (58)$$

$$\mathbf{P}_\square = \gamma_x P_x + \gamma_y P_y + \gamma_z P_z + \gamma_t \frac{U}{c} = \mathbf{P}_\Delta + \gamma_t \frac{U}{c}. \quad (59)$$

For a particle that moves with speed v along a direction z orthogonal to the ZBW rotation plane, the momentum \mathbf{P}_Δ can be decomposed in two vectors, one parallel and one orthogonal to v . The orthogonal component is a rotating vector, that indicates the component of the momentum due to the angular frequency ω_e in the spatial plane xy orthogonal to z

$$\mathbf{P}_\Delta = \mathbf{P}_\parallel + \mathbf{P}_\perp, \quad (60)$$

where

$$|\mathbf{P}_\perp| = \frac{\hbar\omega_e}{c} = m_e\omega_e r_e = m_e c,$$

$$\left[|\mathbf{P}_\perp| = \frac{1}{r_e} = \omega_e = m_e \right]_{\text{NU}}.$$

The \mathbf{P}_\parallel component can be seen as the usual three components momentum of a particle with mass at rest m_e . For simplicity of notation, from now, we will call \mathbf{P} this component, so that

$$P_\square^2 = e^2 A_\square^2 = P_\Delta^2 - \frac{U^2}{c^2} = P^2 + m_e^2 c^2 - \frac{U^2}{c^2}.$$

The relativistic mass m can be derived directly by the application of the Pythagorean theorem

$$m^2 c^2 = m_e^2 c^2 + P^2 = P_\perp^2 + P^2 = m_e^2 c^2 + m^2 v^2.$$

Consequently this electromagnetic four-momentum \mathbf{P}_\square , for electrons moving with uniform velocity, is a light-like vector:

$$P_\square^2 = m^2 c^2 - \frac{U^2}{c^2} = 0.$$

An electron that moves with velocity $v \ll c$ has an approximate momentum P given by

$$P = eA_\parallel \simeq P_\perp \frac{v}{c} = m_e v,$$

and a variation of speed

$$a = \frac{dv}{dt} \quad \text{implies a force} \quad f = \frac{dP}{dt} = e \frac{dA_\parallel}{dt} = m \frac{dv}{dt}.$$

Now recalling that the bivector part of (5) is

$$\partial \wedge \mathbf{A}_\square = \mathbf{F}$$

after multiplying both sides by the charge e , it becomes

$$e\partial \wedge \mathbf{A}_\square = \partial \wedge e\mathbf{A}_\square = e\mathbf{F}. \quad (61)$$

By considering (58) and (59) this equation can be rewritten as

$$\partial \wedge \left(\mathbf{P}_\Delta + \gamma_t \frac{U}{c} \right) = e\mathbf{F}, \quad (62)$$

or, by means of (60), as

$$\partial \wedge \left[(\mathbf{P} + \mathbf{P}_\perp) + \gamma_t \frac{U}{c} \right] = e\mathbf{F}. \quad (63)$$

The term $\partial \wedge \mathbf{P}_\perp$ can be carried out because the average value of \mathbf{P}_\perp , in a scale time much larger than the ZBW period, is zero:

$$\partial \wedge \left(\mathbf{P} + \gamma_t \frac{U}{c} \right) = e\mathbf{F}, \quad (64)$$

$$\partial \wedge \left(\mathbf{P} + \gamma_t \frac{U}{c} \right) = \frac{e}{c} \mathbf{E} \gamma_t + eI\mathbf{B} \gamma_t.$$

Equating only the components that contain bivectors with γ_t terms we obtain

$$\left(\frac{\partial \mathbf{P}}{\partial t} \right)_{\text{EU}} \gamma_t + \nabla U \gamma_t = e\mathbf{E} \gamma_t$$

or

$$\left(\frac{\partial \mathbf{P}}{\partial t} \right)_{\text{EU}} = e\mathbf{E} - \nabla U. \quad (65)$$

In (65) $(\partial \mathbf{P} / \partial t)_{\text{EU}}$ is the force acting on the charge e due both to the electric field \mathbf{E} (Coulomb force) and to the gradient of the “potential energy” U . Instead, by equating only the components that contain pure spatial bivectors we get

$$\nabla \wedge \mathbf{P} = eI\mathbf{B} \gamma_t = -eI\gamma_t \mathbf{B} = eI_\Delta \mathbf{B}, \quad (66)$$

where the term $-I\gamma_t = \gamma_x \gamma_y \gamma_z = I_\Delta$ is the unitary volume of the three dimensional space. Left-multiplying both sides of (66) by I_Δ gives

$$I_\Delta \nabla \wedge \mathbf{P} = -e\mathbf{B}, \quad (67)$$

which is equivalent to the two following equations in the ordinary algebra

$$\nabla \times \mathbf{P} = e\mathbf{B}. \quad (68)$$

Table 3. Products $\mathbf{v} \times (\nabla \times \mathbf{P} - e\mathbf{B})$.

$\mathbf{v} \times (\nabla \times \mathbf{P} - e\mathbf{B})$	$\gamma_x \left(\frac{\partial P_z}{\partial y} - \frac{\partial P_y}{\partial z} - eB_x \right)$	$\gamma_y \left(\frac{\partial P_x}{\partial z} - \frac{\partial P_z}{\partial x} - eB_y \right)$	$\gamma_z \left(\frac{\partial P_y}{\partial x} - \frac{\partial P_x}{\partial y} - eB_z \right)$
$\gamma_x v_x$	0	$\gamma_z \left(-\frac{\partial P_z}{\partial t} \Big _{xy} - ev_x B_y \right)$	$\gamma_y \left(\frac{\partial P_y}{\partial t} \Big _{xz} - ev_x B_z \right)$
$\gamma_y v_y$	$-\gamma_z \left(\frac{\partial P_z}{\partial t} \Big _{yx} - ev_y B_x \right)$	0	$\gamma_x \left(-\frac{\partial P_x}{\partial t} \Big _{yz} - ev_y B_z \right)$
$\gamma_z v_z$	$-\gamma_y \left(-\frac{\partial P_y}{\partial t} \Big _{zx} - ev_z B_x \right)$	$-\gamma_x \left(\frac{\partial P_x}{\partial t} \Big _{zy} - ev_z B_y \right)$	0

As an example, the component of the above equation along the x axis is

$$\gamma_x \left(\frac{\partial P_z}{\partial y} - \frac{\partial P_y}{\partial z} \right) = \gamma_x e B_x.$$

Now, by applying the cross product of the velocity \mathbf{v} of charge e to both terms in (68) we obtain

$$\mathbf{v} \times (\nabla \times \mathbf{P} - e\mathbf{B}) = 0. \tag{69}$$

The components of (69) are represented in Table 3 considering that

$$v_i \frac{\partial P_j}{\partial i} = \frac{\partial i}{\partial t} \frac{\partial P_j}{\partial i} = \frac{\partial P_j}{\partial t},$$

$$v_j \frac{\partial P_j}{\partial i} = \frac{\partial j}{\partial t} \frac{\partial P_j}{\partial i} = \frac{\partial j}{\partial i} \frac{\partial P_j}{\partial t} = 0 \quad \text{for } i \neq j, \quad \text{where } i, j \in \{x, y, z\}.$$

For these reasons (69) leads to the usual form of the force contribution due to the magnetic flux density field \mathbf{B}

$$\left(\frac{\partial \mathbf{P}}{\partial t} \right)_B = e\mathbf{v} \times \mathbf{B}. \tag{70}$$

Finally, we get the whole force contribution by summing up the forces

$$\frac{d\mathbf{P}}{dt} = \left(\frac{\partial \mathbf{P}}{\partial t} \right)_{EU} + \left(\frac{\partial \mathbf{P}}{\partial t} \right)_B$$

given respectively by (65) and (70)

$$\frac{d\mathbf{P}}{dt} = e(\mathbf{E} + \mathbf{v} \times \mathbf{B}) - \nabla U. \tag{71}$$

5. Energy, Momentum and Quanta Current

The nature of energy and momentum can be understood if we consider the quantum of action \hbar as a “physical object” that moves in space–time. The Planck relation $W_\varphi = \hbar\omega = 2\pi\hbar/T_\varphi$ tells us that photons with energy W_φ can transmit quanta of actions with a quanta current Q_c (number of quanta of actions per time unit)

$$Q_c = n \frac{\hbar}{T_\varphi} = n \frac{W_\varphi}{2\pi}. \quad (72)$$

The same quanta current can be obtained in a time unit by a large number of low energy photons or by a small number of high energy photons.

Calling W_H the energy of high energy photons and W_L the energy of low energy ones, and n_H and n_L their number, we observe that the same Q_c can be obtained with the same total energy following two different ways if $n_H W_H = n_L W_L$:

$$\frac{n_H \hbar}{T_\varphi} = \frac{n_H W_H}{2\pi}, \quad (73)$$

$$\frac{n_L \hbar}{T_\varphi} = \frac{n_L W_L}{2\pi}. \quad (74)$$

In the first case we have few “high speed” – high energy photons that guarantee the required current. In the latter case the same result is obtained by many “low speed” – low energy photons. An information technology analogy can be given if we consider a bus with few wires driven by a high frequency clock compared to a large bus with many wires driven by a low frequency clock. The information per unit time is the same in both case. Now, following the above considerations the equation $P_\varphi = \hbar k = 2\pi\hbar/\lambda_\varphi$, where $k = 2\pi/\lambda_\varphi$ is the wave number, should be viewed as the direction of quanta current in space. For photons the four-momentum \mathbf{P}_\square is a light-like vector

$$P_\square^2 = 0. \quad (75)$$

In this case the momentum is a vector that gives the direction of quantum of action in space and the module of momentum P_φ is the energy W_φ :

$$[P_\varphi^2 - W_\varphi^2 = 0]_{\text{NU}}.$$

5.1. ZBW and Heisenberg’s uncertainty principle

The concept of “measure” is strictly related to the quantum of action as the concept of information is related to the binary digit (bit). In natural units the quantum of action is a dimensionless (i.e., scalar) value, as it is always the ratio (measure) of two values of the same nature. For this reason the concepts of “energy”, “momentum”, “space” and “time” cannot be separated and space and time can be measured, using natural units, in eV^{-1} .

The product of the momentum P of the rotating charge and the radius r of the orbit in the proposed ZBW model is always equal to \hbar :

$$Pr = \hbar. \quad (76)$$

This expressions points out that the intrinsic momentum of a particle confined in a spherical space of radius r cannot be less than \hbar/r . Calling $t_r = T/2\pi = \omega^{-1}$ the inverse of the ZBW angular frequency, and remembering that $mc^2 = \hbar\omega$, we can observe that

$$mc^2 t_r = \hbar \omega t_r = \hbar = Pr. \quad (77)$$

This formula just states that the energy of a particle at rest (such as an electron) confined in a spherical space of radius r cannot be less than $\hbar/t_r = \hbar c/r$. Both (76) and (77) can be viewed as a particular reformulation of Heisenberg's uncertainty principle. From this point of view, energy can be seen as strictly related to the concept of quantum of action density in space–time. We remember that in quantum mechanics the concept of “particle at rest” cannot be considered as realistic, because the assumed point-like model of elementary particles implies that, due to the Heisenberg's principle, the momentum is not determined as the precision in position tends to zero.

6. Some other Spinning Charge Models

In 1915 Alfred Lauck Parson published “A Magnetron Theory of the Structure of the Atom” in the Smithsonian Miscellaneous Collection, Pub 2371 [28], where he proposed a spinning ring model of the electron. Various forms of the spinning charge model of electrons have been rediscovered by many authors. However, the incompatibility with the most widely accepted interpretations of quantum mechanics prevented them from receiving proper attention.

According to Randell L. Mills the free electron is “*is a spinning two-dimensional disk of charge. The mass and current density increase towards the center, but the angular velocity is constant. It produces an angular momentum vector perpendicular to the plane of the disk*” [29]. As in our proposed model the intrinsic angular momentum of free electron is \hbar but there is an important difference in charge distribution shape and speed. A constant angular velocity for a flat charge distribution implies that the charge speed is not always equal to the speed of light as strictly demanded by our model [30]. Mills' theory [31,32] “*assumes physical laws apply on all scales including the atomic scale*” in agreement with Occam's razor principle, is based on simple fundamental physical laws and is highly predictive.

Using geometric algebra and starting from Dirac theory, David Hestenes has proposed a ZBW model according to which “*the electron is a massless point particle executing circular motion in the rest system*” and “*with an intrinsic orbital angular momentum or spin of fixed magnitude $s = \hbar/2$* ” [1]. The phase of the probability amplitude wave function is related to the ZBW rotation phase, a concept usually hidden in the traditional mathematical formalism used in quantum mechanics based on complex numbers and matrices. However, we should remark that the concept of point-like charge in quantum mechanics should be considered unrealistic. It violates Occam's razor principle and may be used only as a first approximation. We remember also that in our model the value of intrinsic angular momentum for a free electron is \hbar and that the “spin” is interpreted as the component of the angular momentum along an external magnetic field as in Stern–Gerlach experiment (see Section 3.2). Another interesting electron model has been proposed by David L. Bergman [15,16]: according to this model the electron is a very thin, torus shaped, rotating charge distribution with intrinsic angular momentum of the electron equal to its spin value $s = \hbar/2$. The torus radius has a length $R = \hbar/mc$ and half thickness $r = 8Re^{-\pi/\alpha}$, where α is the fine structure constant.

7. Electromagnetic Composite At Compton Scale

If the electron is a current loop whose radius is equal to the reduced electron Compton wavelength, it is reasonable to assume the possibility of existence of “super chemical” structures of pico-metric ($1 \text{ pm} = 10^{-12} \text{ m}$) dimensions. These dimensions are intermediate between nuclear ($1 \text{ fm} = 10^{-15} \text{ m}$) and atomic scale ($1 \text{ \AA} = 10^{-10} \text{ m}$).

A simple ZBW model of the proton consists in a current loop generated by an elementary positive charge that rotates at the speed of light along a circumference with a length equal to the proton Compton wavelength ($\approx 1.32141 \times 10^{-15} \text{ m}$) [33]. According to this model the proton is much smaller than the electron ($r_e/r_p = m_p/m_e \approx 1836.153$). A hypothetically very simple structure formed by an electron with a proton at his center would have potential energy

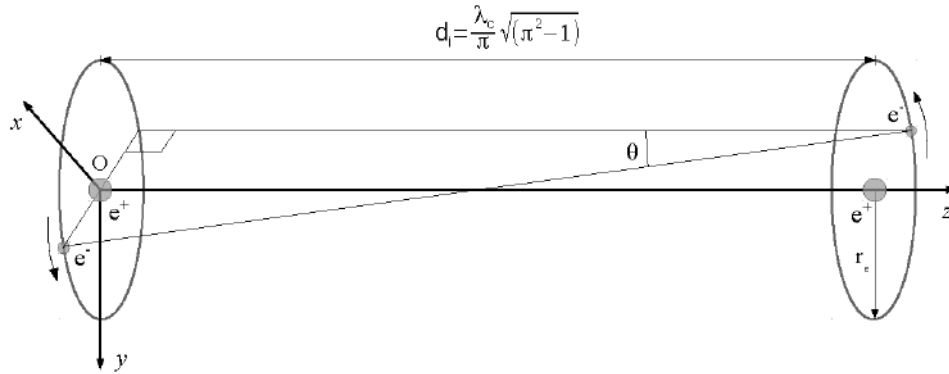


Figure 3. UDH protons distance.

of $-e^2/r_e \approx -3.728$ keV corresponding to a photon wavelength of $\lambda_\varphi \approx 3.325 \times 10^{-10}$ m. This structure may be created starting from atomic hydrogen or Rydberg State Hydrogen only in specific environments, as materials with high free electron density and with lattice constants and energy levels allowing a resonant absorption of 3.7 keV photons. A high electron density can be obtained in “swimming electron layers” formed when a metal is heated in contact with materials, such as SrO, with low work functions [34,35].

The hypothesis of existence of Compton-scale composites (CSC) has been experimentally confirmed by Holmlid [2,3,36]. The inter-nuclear distance in Ultra-Dense Deuterium (UDD) of ≈ 2.3 pm, found by Holmlid [2], seems compatible with deuteron–electron (or proton–electron in Ultra-Dense Hydrogen(UDH)) structures where the ZBW phases of adjacent electrons are correlated. Such distance may be obtained imposing, as a first step, the condition that the space–time distance d_\square between adjacent electrons rotating charges is a light-like vector:

$$d_\square^2 = d_\Delta^2 - c^2 \delta t^2 = 0, \tag{78}$$

$$[d_\square^2 = d_\Delta^2 - \delta t^2 = 0]_{\text{NU}},$$

where d_Δ is the ordinary euclidean distance in space. This condition is satisfied if d_Δ is equal to electron Compton wavelength ($d_\Delta = \lambda_c$), $\delta t = T$ is the ZBW period and the phase difference between adjacent electrons is equal to π . In this case from a direct application of the Pythagorean theorem we can find the internuclear deuteron distance d_i as shown in Fig. 3.

$$d_i = \frac{\lambda_c}{\pi} \sqrt{\pi^2 - 1} \approx 2.3 \times 10^{-12} \text{ m}, \tag{79}$$



Figure 4. UDH model.

Figure 4 shows a hypothetical chain of these deuteron–electron pairs. We must remark that the hypothesis of existence of exotic forms of hydrogen is not new and has been proposed in different ways by many authors (Mills [31], Dufour [9], Mayer and Reitz [8,37], Krasnoholovets, Zabulonov and Zolkin [38] and many others). A very interesting result has been obtained by Jan Naudts starting from the Klein–Gordon equation for the hydrogen atom. Naudts found a low-lying eigenstate in which “hydrogen” has a deep energy level $E_0 \approx -m_e c^2 \alpha \approx -3.728$ keV and a radius $r_e = \hbar/m_e c \approx 3.9 \times 10^{-13}$ m (0.0039 Å) [39].

Indirect support for these hypotheses comes also from the numerous claims of observation of anomalous heat generation in metal–hydrogen systems. We must remark that these hypothetical “Compton Scale Composites” should be electrical neutral or negatively charged objects that cannot be stopped by the Coulomb barrier. For this reason they may generate unusual nuclear reactions and transmutations, considering the different sizes, time-scales and energies of this composites with respect to the particles (such as neutrons) normally used in nuclear experiments.

Mayer and Reitz, starting from a ZBW model of the electron, propose a three body system model at the Compton scale, composed by a proton and two electrons [8]. F. Piantelli, in patent application WO 2012147045 “Method and apparatus for generating energy by nuclear reactions of hydrogen adsorbed by orbital capture on a nanocrystalline structure of a metal”, proposes an orbital capture of “H- ions” by nickel atoms in nano-clusters as a trigger for Low Energy Nuclear Reactions [40]. The orbital capture of the negatively charged structures at pico-metric scale described by Mayer and Reitz may be viewed as an alternative explanation to the capture of the much larger H- ions.

8. Conclusions

In this paper the authors want to underline that simplicity is an important and concrete value in scientific research. Connections between very different concepts in physics can be evidenced if we use the language of geometric algebra, recognizing also the fundamental role of the electromagnetic four-vector potential in physics.

The application of Occam’s Razor principle to Maxwell’s equations suggests, as a natural choice, a Zitterbewegung interpretation of quantum mechanics, similar but not identical to the one proposed by D. Hestenes. According to this framework, the electron structure consists of a massless charge distribution that rotates at the speed of light along a circumference with a length equal to electron Compton wavelength. Following this interpretation the electron mass–energy, expressed in natural units, is equal to the angular speed of the ZBW rotation and to the inverse of the orbit radius. Inertia has a pure electromagnetic origin related to the vector potential generated by the ZBW current. Moreover, in this framework the Heisenberg “uncertainty principle” derives from the relation between a particle ZBW radius and its angular momentum. The proposed model supports the ideas of some authors [3,8] that the ZBW may explain the existence of “super-chemical structures,” such as ultra-dense deuterium, at pico-metric scale. A preliminary hypothesis on the structure of Holmlid’s UDD, in which the ZBW phase of adjacent electrons are synchronized, has been presented demonstrating with good agreement Holmlid’s experimental results. Pico-chemistry reactions and composites with intermediate energy values between nuclear and chemical ones can emerge as a key concept in understanding the origin of anomalous heat and the unusual nuclear reactions seen in many metal–hydrogen systems, as already suggested by some researchers in the field of condensed matter nuclear science.

“It is a delusion to think of electrons and fields as two physically different, independent entities. Since neither can exist without the other, there is only one reality to be described, which happens to have two different aspects; and the theory ought to recognize this from the outset instead of doing things twice!” – A. Einstein, cited in [41].

“In atomic theory, we have fields and we have particles. The fields and the particles are not two different things. They are two ways of describing the same thing, two different points of view” – P.A.M. Dirac, cited in [42].

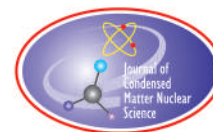
Acknowledgements

Thanks to Salvatore Mercurio, former professor of physics at the North University of China (NUC), Taiyuan, Shanxi, for interesting discussions on the nature of electric charge and on hypothesis of existence of “super-chemical” reactions. Many thanks also to the reviewers for their interesting advice and beneficial suggestions and to Jed Rothwell for the English revision of the manuscript.

References

- [1] D. Hestenes, Quantum mechanics from self-interaction, *Found. Phys.* **15**(1) (1985) 63–87.
- [2] S. Badii and P.U. Andersson and L. Holmlid. High-energy Coulomb explosions in ultra-dense deuterium: time-of-flight-mass spectrometry with variable energy and flight length, *Int. J. Mass Spectrometry* **282**(1–2) (2009) 70–76.
- [3] L. Holmlid and S. Olafsson, Spontaneous ejection of high-energy particles from ultra-dense deuterium D(0), *Int. J. Hydrogen Energy* **40**(33)(2015) 10559–10567.
- [4] K. Huang, On the zitterbewegung of the Dirac electron, *Amer. J. Phys.* **20**(8) (1952) 479–484.
- [5] B.G. Sidharth, Revisiting Zitterbewegung, *Int. J. Theoret. Phys.* **48** (2009) 497–506.
- [6] D. Hestenes, Mysteries and insights of Dirac theory, *Annales de la Fondation Louis de Broglie* **28** (2003) 3.
- [7] D. Hestenes, *Hunting for Snarks in Quantum Mechanics*, In P.M. Goggans and C.-Y. Chan (Eds.), American Institute of Phys. Conf. Series, Vol. 1193, pp. 115–131, December 2009.
- [8] F.J. Mayer and J.R. Reitz, Electromagnetic composites at the Compton scale, *Int. J. Theoret. Phys.* **51**(1) (2012) 322–330.
- [9] J. Dufour, An introduction to the pico-chemistryworking hypothesis, *J. Condensed Matter Nucl. Sci.* **10** (2013) 40–45. www.iscmns.org/CMNS/JCMNS-Vol10.pdf.
- [10] Y. Aharonov and D. Bohm, Significance of electromagnetic potentials in the quantum theory, *Phys. Rev.* **115** (1959) 485–491.
- [11] D. Hestenes, *Reforming the Mathematical Language of Physics*, Oersted Medal Lecture 2002, 2002.
- [12] D. Hestenes, Spacetime physics with geometric algebra, *Amer. J. Phys.* **71**(3) (2003) 691–714.
- [13] G. Bettini, Clifford algebra, 3- and 4-dimensional analytic functions with applications, Manuscripts of the Last Century. vixra.org, Quantum Phys.:1–63, 2011. <http://vixra.org/abs/1107.0060>.
- [14] D. Hestenes, Zitterbewegung modeling, *Found. Phys.* **23**(3) (1993) 365–387.
- [15] D.L. Bergman and J.P. Wesley, Spinning charged ring model of electron yielding anomalous magnetic moment, *Galilean Electrodynamics* **1**(5) (1990) 63–67.
- [16] D.L. Bergman and C.W. Lucas, Credibility of common sense science, *Found. Sci.*, Vol. 6, No 2 (2003) 1–17.
- [17] Shau-Yu Lan, Pei-Chen Kuan, Brian Estey, Damon English, Justin M. Brown, Michael A. Hohensee, and Holger Müller. A clock directly linking time to a particle’s mass. *Science*, January 2013. <http://science.sciencemag.org/content/early/2013/01/09/science.1230767.full.pdf>.
- [18] F. Santandrea and P. Cirilli, Unificazione elettromagnetica, concezione elettronica dello spazio, dell’energia e della materia, 2006. Atlante di numeri e lettere. <http://www.atlantedinumerielelettere.it/energia2006/labor.htm>.
- [19] R.A. Treumann, W. Baumjohann and A. Balogh, The strongest magnetic fields in the universe: how strong can they become? *Frontiers Phys.* **2** (2014) 59.
- [20] Q.-H. Peng and H. Tong, The Physics of strong magnetic fields in neutron stars, *Mon. Not. Roy. Astron. Soc.* **378** (2007) 159.
- [21] D. Dew-Hughes, The critical current of superconductors: a historical review, *Low Temperature Phys.* **27**(9) (2001) 713–722.
- [22] J. Dolbeault, M.J. Esteban and M. Loss, Relativistic hydrogenic atoms in strong magnetic fields, *Annales Henri Poincaré* **8** (2007) 749–779.
- [23] J. Dolbeault, M. J. Esteban and M. Loss, Characterization of the critical magnetic field in the Dirac–Coulomb equation. ArXiv e-prints, December 2007.
- [24] O. Consa, Helical model of the electron, *General Sci. J.* (2014) 1–14. <http://gsjournal.net/Science-Journals/Research%20Papers/View/5523>
- [25] R.P. Feynman, R.B. Leighton and M. Sands, *The Feynman Lectures on Physics: Mainly Electromagnetism and Matter*, Vol. 2, Basic Books, 2011.
- [26] D. Hestenes, Real spinor fields, *J. Math. Phys.* **8**(4) (1967) 798–808.

- [27] D. Hestenes, The Zitterbewegung interpretation of quantum mechanics, *Found. Phys.* **20**(10) (1990) 1213–1232.
- [28] A.L. Parson and Smithsonian Institution, A magneton theory of the structure of the atom (with two plates), Number v. 65 in Publication (Smithsonian Institution), Smithsonian Institution, 1915.
- [29] BlackLight Power, Periodic table of elements of the first twenty-electron-atoms solved with the grand unified theory of classical Physics. <http://www.millsian.com/images/theory/Periodic-Table-Poster-light.pdf>.
- [30] A. Rathke, A critical analysis of the hydrino model, *New J. Phys.* **7** (2005) 127.
- [31] R.L. Mills, J.J. Farrell and W.R. Good, *Unification of Spacetime, the Forces, Matter, and Energy*, Science Press, Ephrata, PA 17522, 1992.
- [32] R.L. Mills, *The Grand Unified Theory of Classical Physics*, Blacklight Power, 2008.
- [33] D.L. Bergman, The real proton, *Found. Sci.* **Vol. 3**, No 4, (2000). http://commonsensescience.org/pdf/articles/the_real_proton.pdf.
- [34] F. Celani, E. Purchi, F. Santandrea, S. Fiorilla, A. Nuvoli, M. Nakamura, P. Cirilli, A. Spallone, B. Ortenzi, S. Pella, P. Boccanera and L. Notargiacomo, Observation of macroscopic current and thermal anomalies, at high temperature, by heterostructures on thin and long Constantan wires under H₂ gas, *Int. Conf. on Condensed Matter Nucl. Sci., ICCF-19*, Padua, Italy, 13–17 April 2015.
- [35] H. Hora, G.H. Miley, J.C. Kelly and F. Osman, Shrinking of hydrogen atoms in host metals by dielectric effects and Inglis-teller depression of ionization potentials, *Proc. 9th Int. Conf. on Cold Fusion (ICCF9)*, pp. 1–6, 2002.
- [36] L. Holmlid, Excitation levels in ultra-dense hydrogen p(-1) and d(-1) clusters: structure of spin-based rydberg matter, *Int. J. Mass Spectrometry* **352**(2013) 1–8.
- [37] F.J. Mayer and J.R. Reitz, Thermal energy generation in the earth, *Nonlinear Processes GeoPhys.* **21**(2) (2014) 367–378. <http://www.nonlin-processes-geophys.net/21/367/2014/>.
- [38] V. Krasnoholovets, Y. Zabulonov and I. Zolkin, On the nuclear coupling of proton and electron, *Universal J. Phys. Appl.* **10**(3) (2016) 90–103.
- [39] J. Naudts, On the hydrino state of the relativistic hydrogen atom. ArXiv Phys. e-prints, July 2005.
- [40] F. Piantelli, Method and apparatus for generating energy by nuclear reactions of hydrogen adsorbed by orbital capture on a nanocrystalline structure of a metal, Nov. 2012. WO Patent App. PCT/IB2012/052,100.
- [41] C. Mead, *Collective Electrodynamics: Quantum Foundations of Electromagnetism*, MIT Press, Cambridge, 2000.
- [42] A. Babin and A. Figotin, Neoclassical theory of electromagnetic interactions: a single theory for macroscopic and microscopic scales, *Theoretical and Mathematical Physics*, Springer, London, 2016.



Research Article

Maxwell's Equations and Occam's Razor

Francesco Celani*

Istituto Nazionale di Fisica Nucleare (INFN-LNF), Via E. Fermi 40, 00044 Frascati, Roma, Italy

Antonino Oscar Di Tommaso[†]

Università degli Studi di Palermo – Department of Energy, Information Engineering and Mathematical Models (DEIM), viale delle Scienze, 90128 Palermo, Italy

Giorgio Vassallo[‡]

Università degli Studi di Palermo – Department of Industrial and Digital Innovation (DIID), viale delle Scienze, 90128 Palermo, Italy

Abstract

In this paper a straightforward application of Occam's razor principle to Maxwell's equation shows that only one entity, the electromagnetic four-potential, is at the origin of a plurality of concepts and entities in physics. The application of the so called "Lorenz gauge" in Maxwell's equations *denies the status of real physical entity* to a scalar field that has a gradient in space-time with clear physical meaning: the four-current density field. The mathematical formalism of space-time Clifford algebra is introduced and then used to encode Maxwell's equations starting only from the electromagnetic four-potential. This approach suggests a particular *Zitterbewegung* (ZBW) model for charged elementary particles.

© 2017 ISCMNS. All rights reserved. ISSN 2227-3123

Keywords: Coulomb gauge, Clifford algebra, Electric charge, Electron structure, Elementary particles, Maxwell's equations, Lorenz gauge, Occam's razor, Space–time algebra, Vector potential, *Zitterbewegung*

Nomenclature (see p. 101)

1. Introduction

Science is the creation and validation of models of abstract concepts and experimental data. For this reason it is important to examine the rules used to evaluate the quality of a model. Occam's razor principle emphasizes the simplicity and conciseness of the model: among different models that fit experimental data, the simplest one must

*Also at: International Society for Condensed Matter Nuclear Science (ISCMNS)-UK. E-mail: francesco.celani@inf.infn.it.

[†]E-mail: antoninooscar.ditommaso@unipa.it.

[‡]Also at: International Society for Condensed Matter Nuclear Science (ISCMNS)-UK. E-mail: giorgio.vassallo@unipa.it.

Nomenclature

Symbol	Name	SI units	Natural units (NU)
A_{\square}	Electromagnetic four-potential	$V s m^{-1}$	eV
r_{\square}	Four-position vector	m	eV^{-1}
G	Electromagnetic field	$V s m^{-2}$	eV^2
F	Electromagnetic field bivector	$V s m^{-2}$	eV^2
B	Flux density field	$V s m^{-2} = T$	eV^2
E	Electric field	$V m^{-1}$	eV^2
S	Scalar field	$V s m^{-2}$	eV^2
$J_{\square e}$	Four-current density	$A m^{-2}$	eV^3
v_{\square}	Four-velocity vector	$m s^{-1}$	1
A'	Electromagnetic eight-potential	$V s m^{-1}$	eV
P	Pseudoscalar field	$V s m^{-2}$	eV^2
$J_{\square m}$	Magnetic four-current density	$A s m^{-3}$	eV^3
ρ	Electric charge density	$A s m^{-3} = C m^{-3}$	eV^3
ρ_m	Magnetic charge density	$A m^{-2}$	eV^3
x, y, z	Space coordinates	$m^{(1)}$	eV^{-1}
t	Time variable	$s^{(2)}$	eV^{-1}
c	Light speed in vacuum	$2.99792458 \times 10^8 m s^{-1}$	1
μ_0	Permeability of vacuum	$4\pi \times 10^{-7} V s A^{-1} m^{-1}$	4π
ϵ_0	Dielectric constant of vacuum	$8.854187817 \times 10^{-12} A s (V m)^{-1}$	$1/4\pi$
P_{\square}	Electromag. four-momentum	$kg m s^{-1}$	eV
\mathfrak{S}	Generalized Poynting vector	$W m^{-2}$	eV^4
w	Specific energy	$J m^{-3}$	eV^4

⁽¹⁾ $1.9732705 \times 10^{-7} m \approx 1 eV^{-1}$;

⁽²⁾ $6.5821220 \times 10^{-16} s \approx 1 eV^{-1}$.

be preferred, i.e. the model that does not introduce concepts or entities that are not strictly necessary. The following sentences in Latin briefly illustrate this principle:

Pluralitas non est ponenda sine necessitate.

Frustra fit per plura quod potest fieri per pauciora.

Entia non sunt multiplicanda praeter necessitatem.

[1], which can be translated respectively as “plurality should not be posited without necessity”, “it is futile to do with more things that which can be done with fewer” and “entities must not be multiplied beyond necessity”.

According to this principle, the quality of a model can be measured by means of two fundamental parameters:

- (1) Good agreement of a model’s predictions with experimental data and/or with other expected results.
- (2) The simplicity of a model, a value that is inversely related to the amount of information, concepts, entities, exceptions, postulates, parameters and variables used by the model itself.

These rules are universal ones and can be applied in many contexts [2]. From this point of view, the intuitive and simple framework of Clifford algebra is a natural choice.

In this paper, we introduce and use the space–time Clifford algebra, showing that only one fundamental physical entity is sufficient to describe the origin of electromagnetic fields and charges, i.e. the electromagnetic four-potential. The vector potential should not be viewed only as a mathematical tool but as a real physical entity, as suggested by the Aharonov–Bohm effect, a quantum mechanical phenomenon in which a charged particle is affected by the vector potential in regions in which the electromagnetic fields are null [3]. Actually, many papers deal with the application of geometric algebra to Maxwell’s equation (see [4–9] and many others), but few of them deal with the concept of scalar field. Among the most interesting works we can find a paper by Bettini [5], two papers written by van Vlaenderen [10,11] and two papers of Hively [12,13].

In this paper we propose a reinterpretation of Maxwell’s equations which does not use any gauge: the unique constraint is that the electromagnetic four-potential must be represented by a *harmonic* function, as proposed by Bettini [5]. This fact gives rise to an electromagnetic field composed not only of the classical electric and magnetic flux density fields, but also by a scalar field. The scalar field will be here investigated and it will be shown that its existence produces many interesting implications and consequences on the essence of electrical charges and currents. A brief and simple but essential introduction on the main fundamental properties of Clifford algebra is given preliminarily in this paper in order to encourage a particular interpretation of Maxwell’s equations at the picometric scale.

This paper is composed of the following parts: Section 2 is a short introduction to Clifford algebra and its fundamental properties; Section 3 illustrates how Maxwell’s equations can be derived from a four dimensional vector potential without using the Lorenz gauge; Section 4 deals with the main properties of the electromagnetic field, the derivation of Maxwell’s equations from the Lagrangian density, the Lorentz force, the generalized Poynting vector, the symmetrical Maxwell’s equations and, finally, in Section 5 some essential points are summarized.

2. The Language of Scientific Knowledge

Scientific knowledge is expressed mathematically, but the importance of the optimal choice of the appropriate mathematical language is often underestimated [4–6,14]. The geometric algebra (Clifford algebra) formalism, according to Occam’s razor principle, is by far the best choice for modern physics. Clifford algebra provides a simple and unifying mathematical language for coding geometric entities and operations [8,9,15]. It integrates different mathematical concepts highlighting geometrical meanings that are often hidden in the ordinary algebra.

A particular Clifford $Cl_{p,q}$ algebra is defined in a space with $n = p + q$ dimensions with an orthonormal base of n unitary vectors. The first p vectors of this base have positive squares, whereas the remaining ones have negative squares, as shown by the following equations:

$$\gamma_i^2 = 1 \quad \text{with } 1 \leq i \leq p, \quad (1)$$

$$\gamma_i^2 = -1 \quad \text{with } p + 1 \leq i \leq p + q, \quad (2)$$

$$\gamma_i \gamma_j = -\gamma_j \gamma_i \quad \text{with } i \neq j, \quad (3)$$

where γ_i are the unitary orthogonal vectors.

The geometrical product $\gamma_i \gamma_j$ represents a “segment” of a unitary “area” of undefined shape in the plane identified by unitary vectors γ_i and γ_j . The product $\gamma_1 \gamma_2 \dots \gamma_n$ represents a unitary, n -dimensional volume segment identified by

Table 1. Blades of space–time algebra ($Cl_{3,1}$).

Blade	Bit mask	Grade	hex.
1	0000	0 (scalar)	0
γ_x	0001	1 (vector)	1
γ_y	0010	1 (vector)	2
$\gamma_x\gamma_y = \gamma_{xy}$	0011	2 (bivector)	3
γ_z	0100	1 (vector)	4
$\gamma_x\gamma_z = \gamma_{xz}$	0101	2 (bivector)	5
$\gamma_y\gamma_z = \gamma_{yz}$	0110	2 (bivector)	6
$\gamma_x\gamma_y\gamma_z = \gamma_{xyz} = I_\Delta$	0111	3 (pseudovector)	7
γ_t	1000	1 (vector)	8
$\gamma_x\gamma_t = \gamma_{xt}$	1001	2 (bivector)	9
$\gamma_y\gamma_t = \gamma_{yt}$	1010	2 (bivector)	A
$\gamma_x\gamma_y\gamma_t = \gamma_{xyt}$	1011	3 (pseudovector)	B
$\gamma_z\gamma_t = \gamma_{zt}$	1100	2 (bivector)	C
$\gamma_x\gamma_z\gamma_t = \gamma_{xzt}$	1101	3 (pseudovector)	D
$\gamma_y\gamma_z\gamma_t = \gamma_{yzt}$	1110	3 (pseudovector)	E
$\gamma_x\gamma_y\gamma_z\gamma_t = \gamma_{xyz t} = I$	1111	4 (pseudoscalar)	F

the unitary vectors $\gamma_1, \gamma_2, \dots, \gamma_n$. In the n -dimensional space no more than 2^n elementary distinct “components” exist. Each of these entities corresponds to a particular subset of the orthonormal base vectors. The “grade” of these entities (called blades) is equal to the number of base vectors which are present within the subset. The blade of grade zero (empty set) is the dimensionless scalar unit. The number of blades of k th-grade in a n -dimensional space is equal to the binomial coefficient

$$N_k = \binom{n}{k} = \frac{n!}{k!(n-k)!} \tag{4}$$

Using Clifford algebra there are two possible choices for the metric of space–time coordinates, namely $Cl_{1,3}$ and $Cl_{3,1}$. For $Cl_{1,3}$ (signature “+ – – –”) we have

$$\gamma_t^2 = -\gamma_x^2 = -\gamma_y^2 = -\gamma_z^2 = 1,$$

whereas for $Cl_{3,1}$ (signature “+ + + –”) we have

$$\gamma_x^2 = \gamma_y^2 = \gamma_z^2 = -\gamma_t^2 = 1.$$

In $Cl_{3,1}$ algebra, which is used in this work, the spatial coordinates can be viewed as the familiar Cartesian coordinates of the Euclidean space. The 2^4 components of the $Cl_{3,1}$ space–time Clifford algebra are listed in Table 1.

Each blade is associated to a real number, the blade value. The expression $a\gamma_i\gamma_j$, in which a is a real scalar, represents an area a of an undefined shape in the plane identified by vectors γ_i and γ_j .

Summing can be carried out only between coefficients of identical blades. If used for different blades the sum must be reinterpreted as a composition, in analogy with the concept of sum between real and imaginary parts of a complex number.

A multi-vector is a generic composition of one or more blades. Within an n -dimensional space a multi-vector is composed by no more than 2^n blades. The geometrical product between two blades gives a blade which is obtained from the application of the *bitwise exclusive OR* operation between the bit mask of blades to be multiplied. The value

of the resultant blade is equal to the product of the values of the operands multiplied by a sign which is a function of the two blades. For $Cl_{3,1}$ algebra the sign can be easily determined by means of Table 2, identifying the blades to be multiplied through their hexadecimal “label” taken from Table 1. In general, this product is not commutative. The sign table is obtained by the direct application of Eqs. (1)–(3).

There are other types of products in Clifford algebra, two of them are the wedge (symbol \wedge) and the scalar product (symbol \cdot). The result is computed following the same rules of geometric product, but is zero in some cases:

- (1) the wedge product is always zero if the intersection between the set of base vectors of the first operand blade and the set of base vectors of the second operand blade is not empty;
- (2) the scalar product is always zero if the blade of the first operand is different from that of the second operand.

The geometric product of two vectors in Clifford algebra can be decomposed in a scalar product and a wedge product according to the relation

$$uv = u \cdot v + u \wedge v. \tag{5}$$

It is important to note that the space–time algebra of the four γ_i vectors is isomorphic to the algebra of Majorana matrices. The Majorana matrices are the Dirac gamma matrices times the imaginary unit.

Example 2.1. Some examples of the application of products are here reported referring to $Cl_{3,1}$:

$$\gamma_x \gamma_y \gamma_x \gamma_y = -\gamma_x \gamma_x \gamma_y \gamma_y = -1,$$

$$\gamma_x \gamma_y \cdot \gamma_z \gamma_t = 0,$$

Table 2. Signs of the geometrical product in the space–time algebra $Cl_{3,1}$.
 $I = \gamma_{xyzzt} = \gamma_x \gamma_y \gamma_z \gamma_t$, $I_\Delta = \gamma_{xyz} = \gamma_x \gamma_y \gamma_z$.

Grade	0	1	1	2	1	2	2	3	1	2	2	3	2	3	3	4
hex.	0	1	2	3	4	5	6	7	8	9	A	B	C	D	E	F
Label	1	γ_x	γ_y	γ_{xy}	γ_z	γ_{xz}	γ_{yz}	I_Δ	γ_t	γ_{xt}	γ_{yt}	γ_{xyt}	γ_{zt}	γ_{xzt}	γ_{yzt}	I
1	+	+	+	+	+	+	+	+	+	+	+	+	+	+	+	+
γ_x	+	+	+	+	+	+	+	+	+	+	+	+	+	+	+	+
γ_y	+	-	+	-	+	-	+	-	+	-	+	-	+	-	+	-
γ_{xy}	+	-	+	-	+	-	+	-	+	-	+	-	+	-	+	-
γ_z	+	-	-	+	+	-	-	+	+	-	-	+	+	-	-	+
γ_{xz}	+	-	-	+	+	-	-	+	+	-	-	+	+	-	-	+
γ_{yz}	+	+	-	-	+	+	-	-	+	+	-	-	+	+	-	-
I_Δ	+	+	-	-	+	+	-	-	+	+	-	-	+	+	-	-
γ_t	+	-	-	+	-	+	+	-	-	+	+	-	+	-	-	+
γ_{xt}	+	-	-	+	-	+	+	-	-	+	+	-	+	-	-	+
γ_{yt}	+	+	-	-	-	-	+	+	-	-	+	+	+	+	-	-
γ_{xyt}	+	+	-	-	-	-	+	+	-	-	+	+	+	+	-	-
γ_{zt}	+	+	+	+	-	-	-	-	-	-	-	-	+	+	+	+
γ_{xzt}	+	+	+	+	-	-	-	-	-	-	-	-	+	+	+	+
γ_{yzt}	+	-	+	-	-	+	-	+	-	+	-	+	+	-	+	-
I	+	-	+	-	-	+	-	+	-	+	-	+	+	-	+	-

$$a\gamma_x\gamma_y \wedge b\gamma_z = ab\gamma_x\gamma_y\gamma_z,$$

$$\gamma_x\gamma_y \wedge \gamma_y = 0,$$

$$\gamma_x\gamma_y \wedge \gamma_z\gamma_t = \gamma_x\gamma_y\gamma_z\gamma_t,$$

$$\gamma_x \cdot \gamma_y = 0,$$

$$(\gamma_x + \gamma_t)^2 = (\gamma_x + \gamma_t)(\gamma_x + \gamma_t) = \gamma_x^2 + \gamma_x\gamma_t + \gamma_t\gamma_x + \gamma_t^2 = 1 + \gamma_x\gamma_t - \gamma_x\gamma_t - 1 = 0$$

(example of light-like vector, the square is 0),

$$(\gamma_x + \gamma_y)^2 = (\gamma_x + \gamma_y)(\gamma_x + \gamma_y) = \gamma_x^2 + \gamma_x\gamma_y + \gamma_y\gamma_x + \gamma_y^2 = 1 + \gamma_x\gamma_y - \gamma_x\gamma_y + 1 = 2$$

(example of space-like vector, the square is > 0),

$$(a\gamma_t)^2 = -a^2$$

(example of time-like vector, the square is < 0),

$$(a\gamma_x + b\gamma_y)^2 = (a\gamma_x + b\gamma_y)(a\gamma_x + b\gamma_y) = a^2\gamma_x^2 + ab\gamma_x\gamma_y + ba\gamma_y\gamma_x + b^2\gamma_y^2 = a^2 + ab\gamma_x\gamma_y - ab\gamma_x\gamma_y + b^2 = a^2 + b^2$$

(always a space-like vector),

$$(a\gamma_x + b\gamma_t)^2 = (a\gamma_x + b\gamma_t)(a\gamma_x + b\gamma_t) = a^2\gamma_x^2 + ab\gamma_x\gamma_t + ba\gamma_t\gamma_x + b^2\gamma_t^2 = a^2 + ab\gamma_x\gamma_t - ab\gamma_x\gamma_t - b^2 = a^2 - b^2$$

(light-like if $a = b$, time-like if $a < b$, space-like if $a > b$).

In these examples a and b are generic real scalars.

2.1. Reflection and rotation of vectors

In order to perform a mirror reflection of a vector with respect to a plane, the following formula holds in Clifford algebra:

$$\mathbf{a}' = -\mathbf{m}\mathbf{a}\mathbf{m}, \quad (6)$$

where \mathbf{m} is the unitary vector orthogonal to surface α , as shown in Fig. 1. As a matter of fact, if

$$\mathbf{a} = \mathbf{a}_\perp + \mathbf{a}_\parallel,$$

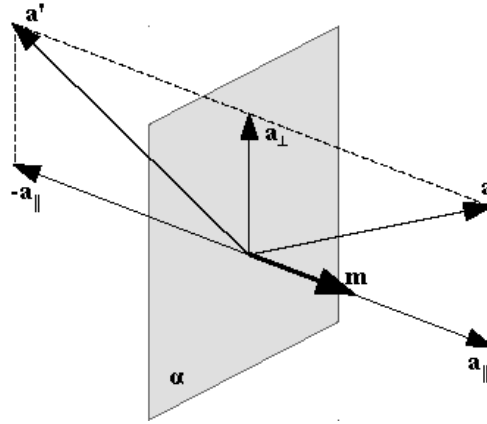


Figure 1. Reflection of a vector with respect to plane α .

where a_{\perp} and a_{\parallel} are the orthogonal and the parallel components of vector a respectively, then

$$\begin{aligned} \mathbf{a}' &= -\mathbf{m} (\mathbf{a}_{\perp} + \mathbf{a}_{\parallel}) \mathbf{m} = -\mathbf{m} \mathbf{a}_{\perp} \mathbf{m} - \mathbf{m} \mathbf{a}_{\parallel} \mathbf{m} \\ &= \mathbf{a}_{\perp} \mathbf{m}^2 - \mathbf{a}_{\parallel} \mathbf{m}^2 = \mathbf{a}_{\perp} - \mathbf{a}_{\parallel}. \end{aligned}$$

This operation is justified by the fact that the product between parallel vectors commutes, i.e.

$$\mathbf{m} \mathbf{a}_{\parallel} = \mathbf{a}_{\parallel} \mathbf{m},$$

whereas the product between orthogonal vectors anti-commutes, i.e.

$$\mathbf{m} \mathbf{a}_{\perp} = -\mathbf{a}_{\perp} \mathbf{m}.$$

If vector \mathbf{a}' is now reflected again with respect unitary vector \mathbf{n} rotated with respect to \mathbf{m} by an angle $\theta/2$ we obtain

$$\mathbf{a}'' = \mathbf{n} \mathbf{a}' \mathbf{n} = \mathbf{n} \mathbf{m} \mathbf{a} \mathbf{m} \mathbf{n}. \quad (7)$$

Vector \mathbf{a}'' is rotated, with respect to vector \mathbf{a} , by an angle θ on the common plane of the two-vector \mathbf{m} and \mathbf{n} as shown in Fig. 2.

The rotation of vector \mathbf{a} can be described also by the following formula

$$\mathbf{a}'' = \mathbf{R} \mathbf{a} \tilde{\mathbf{R}} = e^{-\mathbf{b} \frac{\theta}{2}} \mathbf{a} e^{\mathbf{b} \frac{\theta}{2}}, \quad (8)$$

where $\mathbf{R} = \mathbf{n} \mathbf{m}$, $\tilde{\mathbf{R}} = \mathbf{m} \mathbf{n}$ and the bivector $\mathbf{b} = \mathbf{m} \wedge \mathbf{n}$ is a segment of the surface on which vector \mathbf{a} is rotated.

The product of two vectors is called rotor. We remember that

$$\mathbf{R} = \mathbf{n} \mathbf{m} = \mathbf{m} \cdot \mathbf{n} - \mathbf{m} \wedge \mathbf{n}$$

and

$$\tilde{\mathbf{R}} = \mathbf{m} \mathbf{n} = \mathbf{m} \cdot \mathbf{n} + \mathbf{m} \wedge \mathbf{n}$$

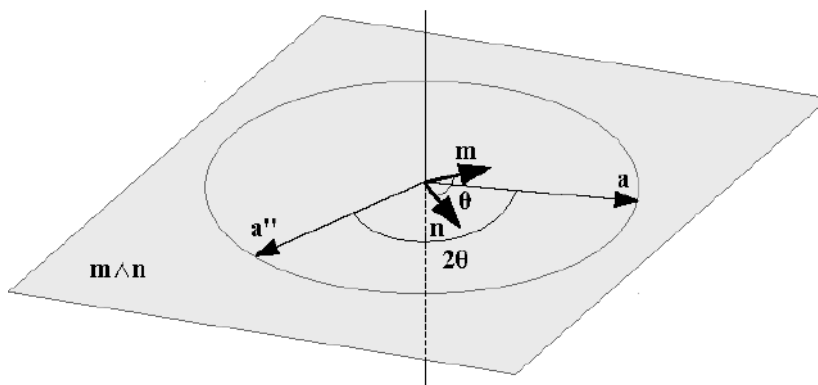


Figure 2. Rotation of vector a due to two subsequent reflections

It is important to note that these rules are independent from the signature, and for this reason they are also valid for four-vectors of the space–time algebra. In particular, rotors with pure spatial bivector parts (such as $\gamma_x\gamma_y\vartheta/2$) generate ordinary rotations, whereas rotors containing bivectors with the term γ_t (such as $\gamma_z\gamma_t\vartheta/2$) generate hyperbolic rotations. Rotors operations are a very powerful geometric tool and some hardware implementations have been attempted [16].

3. The Electromagnetic Field and the Wave Function

The behavior of electromagnetic waves was described in 1865 by James Clerk Maxwell in his work “Dynamical Theory of the Electromagnetic Field”. Maxwell’s equations are a system of partial differential equations, where different concepts are employed: electric field, flux density (or magnetic) field, charge density and current density [4–6].

In order to study the undulatory behavior of particles, the concept of wave function was introduced. Following the interpretation of Born, the square of this function represents the probability density to find a particle in a point of the space, just like the undulatory theory of light, whose intensity is given by the square of the electromagnetic wave amplitude. Now, following the principle of Occam’s razor, which suggests carefulness in the introduction of new concepts, we consider two interesting possibilities:

- (1) find a common origin of the conceptual entities used in Maxwell’s equations;
- (2) consider the wave function as a particular reformulation of concepts/entities already present in Maxwell’s equations.

3.1. The electromagnetic potential

Maxwell’s equations can be reinterpreted by means of a unique entity, namely, the vector potential with four components, as defined by the following equation:

$$\mathbf{A}_{\square}(\mathbf{r}_{\square}) = \gamma_x A_x(\mathbf{r}_{\square}) + \gamma_y A_y(\mathbf{r}_{\square}) + \gamma_z A_z(\mathbf{r}_{\square}) + \gamma_t A_t(\mathbf{r}_{\square}), \tag{9}$$

where each of the vector potential components A_x, A_y, A_z and A_t are functions of the space–time coordinates and $\mathbf{r}_{\square}(x, y, z, t) = \gamma_x x + \gamma_y y + \gamma_z z - \gamma_t ct = \mathbf{r}_{\Delta} - \gamma_t ct$ is the position vector in space–time. From now on in the four-

potential and in other field quantities the variable r_{\square} will be omitted for simplicity. The four-potential has dimension in SI units equal to $V \text{ s m}^{-1}$. Two basic assumptions are made:

- (1) the vector potential field \mathbf{A}_{\square} is represented by a *harmonic* function;
- (2) the space is homogeneous, linear and isotropic.

Therefore, we assume a function that links a vector of four components to each point of the space–time as the unique source of Maxwell’s equations entities.

We use the following definition of the operator ∂ in space–time algebra

$$\partial = \gamma_x \frac{\partial}{\partial x} + \gamma_y \frac{\partial}{\partial y} + \gamma_z \frac{\partial}{\partial z} + \gamma_t \frac{1}{c} \frac{\partial}{\partial t} = \nabla + \gamma_t \frac{1}{c} \frac{\partial}{\partial t}, \quad (10)$$

where

$$\nabla = \gamma_x \frac{\partial}{\partial x} + \gamma_y \frac{\partial}{\partial y} + \gamma_z \frac{\partial}{\partial z} \quad \text{and} \quad c = \frac{1}{\sqrt{\epsilon_0 \mu_0}}.$$

If \mathbf{A}_{\square} is the vector potential defined by (9) the following expression can be written:

$$\partial \mathbf{A}_{\square} = \partial \cdot \mathbf{A}_{\square} + \partial \wedge \mathbf{A}_{\square} = S + \mathbf{F} = \mathbf{G}, \quad (11)$$

where

$$\mathbf{G}(x, y, z, t) = S + \gamma_x \gamma_t F_{xt} + \gamma_y \gamma_t F_{yt} + \gamma_z \gamma_t F_{zt} + \gamma_y \gamma_z F_{yz} + \gamma_x \gamma_z F_{xz} + \gamma_x \gamma_y F_{xy}. \quad (12)$$

Expanding (11), by considering the products as shown in Table 3 and by collecting all terms with the same blade, the following set of equations is found:

$$\partial \cdot \mathbf{A}_{\square} = S = \frac{\partial A_x}{\partial x} + \frac{\partial A_y}{\partial y} + \frac{\partial A_z}{\partial z} - \frac{1}{c} \frac{\partial A_t}{\partial t}, \quad (13)$$

$$\gamma_x \gamma_t F_{xt} = \gamma_x \gamma_t \frac{1}{c} E_x = \gamma_x \gamma_t \left(\frac{\partial A_t}{\partial x} - \frac{1}{c} \frac{\partial A_x}{\partial t} \right), \quad (14)$$

$$\gamma_y \gamma_t F_{yt} = \gamma_y \gamma_t \frac{1}{c} E_y = \gamma_y \gamma_t \left(\frac{\partial A_t}{\partial y} - \frac{1}{c} \frac{\partial A_y}{\partial t} \right), \quad (15)$$

$$\gamma_z \gamma_t F_{zt} = \gamma_z \gamma_t \frac{1}{c} E_z = \gamma_z \gamma_t \left(\frac{\partial A_t}{\partial z} - \frac{1}{c} \frac{\partial A_z}{\partial t} \right), \quad (16)$$

$$\gamma_y \gamma_z F_{yz} = \gamma_y \gamma_z B_x = \gamma_y \gamma_z \left(\frac{\partial A_z}{\partial y} - \frac{\partial A_y}{\partial z} \right), \quad (17)$$

$$\gamma_x \gamma_z F_{xz} = -\gamma_x \gamma_z B_y = \gamma_x \gamma_z \left(\frac{\partial A_z}{\partial x} - \frac{\partial A_x}{\partial z} \right), \quad (18)$$

Table 3. Products $\partial \mathbf{A}_\square$.

$\partial \mathbf{A}_\square$	$\gamma_x A_x$	$\gamma_y A_y$	$\gamma_z A_z$	$\gamma_t A_t$
$\gamma_x \frac{\partial}{\partial x}$	$\frac{\partial A_x}{\partial x}$	$\gamma_x \gamma_y \frac{\partial A_y}{\partial x}$	$\gamma_x \gamma_z \frac{\partial A_z}{\partial x}$	$\gamma_x \gamma_t \frac{\partial A_t}{\partial x}$
$\gamma_y \frac{\partial}{\partial y}$	$-\gamma_x \gamma_y \frac{\partial A_x}{\partial y}$	$\frac{\partial A_y}{\partial y}$	$\gamma_y \gamma_z \frac{\partial A_z}{\partial y}$	$\gamma_y \gamma_t \frac{\partial A_t}{\partial y}$
$\gamma_z \frac{\partial}{\partial z}$	$-\gamma_x \gamma_z \frac{\partial A_x}{\partial z}$	$-\gamma_y \gamma_z \frac{\partial A_y}{\partial z}$	$\frac{\partial A_z}{\partial z}$	$\gamma_z \gamma_t \frac{\partial A_t}{\partial z}$
$\gamma_t \frac{1}{c} \frac{\partial}{\partial t}$	$-\gamma_x \gamma_t \frac{1}{c} \frac{\partial A_x}{\partial t}$	$-\gamma_y \gamma_t \frac{1}{c} \frac{\partial A_y}{\partial t}$	$-\gamma_z \gamma_t \frac{1}{c} \frac{\partial A_z}{\partial t}$	$-\frac{1}{c} \frac{\partial A_t}{\partial t}$

$$\gamma_x \gamma_y F_{xy} = \gamma_x \gamma_y B_z = \gamma_x \gamma_y \left(\frac{\partial A_y}{\partial x} - \frac{\partial A_x}{\partial y} \right), \tag{19}$$

where $S = S_1 + S_2 + S_3 + S_4$ is a scalar field, whose meaning will be clarified later. It is to be noted that equating (13) to zero, i.e. $S = 0$, gives an expression that takes the form of the ‘‘Lorenz gauge’’ condition if $A_t = -\varphi/c$, where φ is the scalar potential of the electric field [4,8,10,17].

Equation (13) can be rewritten as

$$S = \nabla \cdot \mathbf{A}_\Delta - \frac{1}{c} \frac{\partial A_t}{\partial t}, \tag{20}$$

where $\mathbf{A}_\Delta = \gamma_x A_x + \gamma_y A_y + \gamma_z A_z$ is the usual three-component vector potential.

Using the so-called ‘‘Lorenz gauge’’ the scalar field S is considered zero everywhere, *denying its status of a real physical entity* [5]. Same consideration can be done for the ‘‘Coulomb gauge’’ that assign zero value to each addendum S_i . We simply do not apply any ‘‘gauge’’, apart from defining \mathbf{A}_\square as a harmonic function. According to our point of view, both Lorenz and Coulomb ‘‘gauges’’ should be considered just as boundary conditions and the scalar field S , although not directly observable, has a gradient in space–time with a clear physical meaning. Similar considerations are normally presented in electromagnetism to introduce the concept of vector potential, that is a not directly measurable field. The components of the geometric product $\partial \mathbf{A}_\square$ are shown in Table 3. An electromagnetic field \mathbf{G} with seven components emerges, composed by one scalar and six bivectors.

Table 4 represents the relation between the fundamental electromagnetic entities and the space–time components of the vector potential \mathbf{A}_\square .

Table 4. Relation between electromagnetic entities and the vector potential \mathbf{A}_\square .

$\partial \mathbf{A}_\square$	$\gamma_x A_x$	$\gamma_y A_y$	$\gamma_z A_z$	$\gamma_t A_t$
$\gamma_x \frac{\partial}{\partial x}$	S_1	B_{z1}	$-B_{y1}$	$\frac{1}{c} E_{x1}$
$\gamma_y \frac{\partial}{\partial y}$	B_{z2}	S_2	B_{x1}	$\frac{1}{c} E_{y1}$
$\gamma_z \frac{\partial}{\partial z}$	$-B_{y2}$	B_{x2}	S_3	$\frac{1}{c} E_{z1}$
$\gamma_t \frac{1}{c} \frac{\partial}{\partial t}$	$\frac{1}{c} E_{x2}$	$\frac{1}{c} E_{y2}$	$\frac{1}{c} E_{z2}$	S_4

The set of equations from (14) to (19) can be rewritten also in the following way:

$$E_x = c \frac{\partial A_t}{\partial x} - \frac{\partial A_x}{\partial t} \quad (21)$$

$$E_y = c \frac{\partial A_t}{\partial y} - \frac{\partial A_y}{\partial t} \quad (22)$$

$$E_z = c \frac{\partial A_t}{\partial z} - \frac{\partial A_z}{\partial t} \quad (23)$$

$$B_x = \frac{\partial A_z}{\partial y} - \frac{\partial A_y}{\partial z} \quad (24)$$

$$B_y = -\frac{\partial A_z}{\partial x} + \frac{\partial A_x}{\partial z} \quad (25)$$

$$B_z = \frac{\partial A_y}{\partial x} - \frac{\partial A_x}{\partial y}, \quad (26)$$

where

$$\mathbf{E} = \gamma_x E_x + \gamma_y E_y + \gamma_z E_z = c \nabla A_t - \frac{\partial \mathbf{A}_\Delta}{\partial t}, \quad (27)$$

$$\mathbf{B} = \gamma_x B_x + \gamma_y B_y + \gamma_z B_z = \nabla \times \mathbf{A}_\Delta. \quad (28)$$

The sum of all diagonal elements in Table 3 represents the scalar product

$$S = \partial \cdot \mathbf{A}_\square, \quad (29)$$

whereas the sum of all extra-diagonal elements gives the six components of electromagnetic bivector \mathbf{F}

$$\mathbf{F} = \partial \wedge \mathbf{A}_\square. \quad (30)$$

Referring to the function \mathbf{G} , it is possible to note that the “electromagnetic field” is characterized by seven values: three for the electric field, three for the flux density field and one for the scalar field S .

With reference to Table 4 the electromagnetic field \mathbf{G} can also be expressed as

$$\begin{aligned} \mathbf{G}(x, y, z, t) &= S + \mathbf{F} = S + \gamma_x \gamma_t \frac{E_x}{c} + \gamma_y \gamma_t \frac{E_y}{c} + \gamma_z \gamma_t \frac{E_z}{c} + \gamma_y \gamma_z B_x - \gamma_x \gamma_z B_y + \gamma_x \gamma_y B_z \\ &= S + \frac{1}{c} \mathbf{E} \gamma_t + \mathbf{I} \mathbf{B} \gamma_t = S + \frac{1}{c} (\mathbf{E} + \mathbf{I} c \mathbf{B}) \gamma_t, \end{aligned} \quad (31)$$

where

$$I = \gamma_x \gamma_y \gamma_z \gamma_t \tag{32}$$

is the unitary pseudoscalar and

$$\mathbf{F} = \frac{1}{c} \mathbf{E} \gamma_t + I \mathbf{B} \gamma_t = \frac{1}{c} (\mathbf{E} + I c \mathbf{B}) \gamma_t. \tag{33}$$

On the other hand, with reference to Table 3, the electromagnetic field \mathbf{G} can be expressed in the following compact form

$$\mathbf{G}(x, y, z, t) = \nabla \cdot \mathbf{A}_\Delta - \frac{1}{c} \frac{\partial A_t}{\partial t} + \nabla A_t \gamma_t - \frac{1}{c} \frac{\partial \mathbf{A}_\Delta}{\partial t} \gamma_t + I \nabla \times \mathbf{A}_\Delta \gamma_t, \tag{34}$$

which again results in Eqs. (20), (27) and (28) by taking (31) into account.

3.2. Maxwell’s equations

Now, by applying the operator ∂ to the multivector \mathbf{G} (11) and equating it to zero, a new expression is found, i.e.

$$\partial \mathbf{G} = \partial^2 \mathbf{A}_\square = 0, \tag{35}$$

whose components are shown in Table 5. The equation $\partial \mathbf{G} = 0$ can be seen as an extension in four dimensions of the Cauchy-Riemann conditions for analytic functions of a complex (two dimensional) variable [15,18]. In [18] Hestenes writes: “Members of this audience will recognize $\square \psi_0 = 0$ as a generalization of the Cauchy–Riemann equations to space–time, so we can expect it to have a rich variety of solutions. The problem is to pick out those solutions with physical significance.”. In fact, if \mathbf{A}_\square is harmonic then

$$\partial^2 \mathbf{A}_\square = \nabla^2 \mathbf{A}_\square - \frac{1}{c^2} \frac{\partial^2 \mathbf{A}_\square}{\partial t^2} = 0, \tag{36}$$

which represents the wave equation of the four-potential and where

$$\partial^2 = \frac{\partial^2}{\partial x^2} + \frac{\partial^2}{\partial y^2} + \frac{\partial^2}{\partial z^2} - \frac{1}{c^2} \frac{\partial^2}{\partial t^2} = \nabla^2 - \frac{1}{c^2} \frac{\partial^2}{\partial t^2}.$$

It should be noted that in our case, considering the scalar field $S \neq 0$ and \mathbf{A}_\square harmonic, (36) is always homogeneous.

By collecting all common factors contained in Table 5 the following equations are derived:

$$\gamma_x \left(\frac{\partial S}{\partial x} - \frac{\partial B_z}{\partial y} + \frac{\partial B_y}{\partial z} + \frac{1}{c^2} \frac{\partial E_x}{\partial t} \right) = 0, \tag{37}$$

$$\gamma_y \left(\frac{\partial B_z}{\partial x} + \frac{\partial S}{\partial y} - \frac{\partial B_x}{\partial z} + \frac{1}{c^2} \frac{\partial E_y}{\partial t} \right) = 0, \tag{38}$$

$$\gamma_z \left(-\frac{\partial B_y}{\partial x} + \frac{\partial B_x}{\partial y} + \frac{\partial S}{\partial z} + \frac{1}{c^2} \frac{\partial E_z}{\partial t} \right) = 0, \tag{39}$$

Table 5. Products $\partial \mathbf{G} = \partial (\partial \mathbf{A}_{\square}) \cdot \gamma_{ij} = \gamma_i \gamma_j$, $\gamma_{ijk} = \gamma_i \gamma_j \gamma_k$.

$\partial^2 \mathbf{A}_{\square}$	S	$\gamma_{xt} \frac{1}{c} E_x$	$\gamma_{yt} \frac{1}{c} E_y$	$\gamma_{zt} \frac{1}{c} E_z$	$\gamma_{yz} B_x$	$-\gamma_{xz} B_y$	$\gamma_{xy} B_z$
$\gamma_x \frac{\partial}{\partial x}$	$\gamma_x \frac{\partial S}{\partial x}$	$\gamma_t \frac{1}{c} \frac{\partial E_x}{\partial x}$	$\gamma_{xyt} \frac{1}{c} \frac{\partial E_y}{\partial x}$	$\gamma_{xzt} \frac{1}{c} \frac{\partial E_z}{\partial x}$	$\gamma_{xyz} \frac{\partial B_x}{\partial x}$	$-\gamma_z \frac{\partial B_y}{\partial x}$	$\gamma_y \frac{\partial B_z}{\partial x}$
$\gamma_y \frac{\partial}{\partial y}$	$\gamma_y \frac{\partial S}{\partial y}$	$-\gamma_{xyt} \frac{1}{c} \frac{\partial E_x}{\partial y}$	$\gamma_t \frac{1}{c} \frac{\partial E_y}{\partial y}$	$\gamma_{yzt} \frac{1}{c} \frac{\partial E_z}{\partial y}$	$\gamma_z \frac{\partial B_x}{\partial y}$	$\gamma_{xyz} \frac{\partial B_y}{\partial x}$	$-\gamma_x \frac{\partial B_z}{\partial y}$
$\gamma_z \frac{\partial}{\partial z}$	$\gamma_z \frac{\partial S}{\partial z}$	$-\gamma_{xzt} \frac{1}{c} \frac{\partial E_x}{\partial z}$	$-\gamma_{yzt} \frac{1}{c} \frac{\partial E_y}{\partial z}$	$\gamma_t \frac{1}{c} \frac{\partial E_z}{\partial z}$	$-\gamma_y \frac{\partial B_x}{\partial z}$	$\gamma_x \frac{\partial B_y}{\partial z}$	$\gamma_{xyz} \frac{\partial B_z}{\partial z}$
$\gamma_t \frac{1}{c} \frac{\partial}{\partial t}$	$\gamma_t \frac{1}{c} \frac{\partial S}{\partial t}$	$\gamma_x \frac{1}{c^2} \frac{\partial E_x}{\partial t}$	$\gamma_y \frac{1}{c^2} \frac{\partial E_y}{\partial t}$	$\gamma_z \frac{1}{c^2} \frac{\partial E_z}{\partial t}$	$\gamma_{yzt} \frac{1}{c} \frac{\partial B_x}{\partial t}$	$-\gamma_{xzt} \frac{1}{c} \frac{\partial B_y}{\partial t}$	$\gamma_{xyt} \frac{1}{c} \frac{\partial B_z}{\partial t}$

$$\gamma_t \frac{1}{c} \left(\frac{\partial E_x}{\partial x} + \frac{\partial E_y}{\partial y} + \frac{\partial E_z}{\partial z} + \frac{\partial S}{\partial t} \right) = 0, \quad (40)$$

$$\gamma_y \gamma_z \gamma_t \frac{1}{c} \left(\frac{\partial E_z}{\partial y} - \frac{\partial E_y}{\partial z} + \frac{\partial B_x}{\partial t} \right) = 0, \quad (41)$$

$$\gamma_x \gamma_z \gamma_t \frac{1}{c} \left(\frac{\partial E_z}{\partial x} - \frac{\partial E_x}{\partial z} - \frac{\partial B_y}{\partial t} \right) = 0, \quad (42)$$

$$\gamma_x \gamma_y \gamma_t \frac{1}{c} \left(\frac{\partial E_y}{\partial x} - \frac{\partial E_x}{\partial y} + \frac{\partial B_z}{\partial t} \right) = 0, \quad (43)$$

$$\gamma_x \gamma_y \gamma_z \left(\frac{\partial B_x}{\partial x} + \frac{\partial B_y}{\partial y} + \frac{\partial B_z}{\partial z} \right) = 0. \quad (44)$$

Rearranging all equations from (37) to (44) the following are derived:

$$\frac{\partial B_z}{\partial y} - \frac{\partial B_y}{\partial z} = \frac{\partial S}{\partial x} + \frac{1}{c^2} \frac{\partial E_x}{\partial t}, \quad (45)$$

$$\frac{\partial B_x}{\partial z} - \frac{\partial B_z}{\partial x} = \frac{\partial S}{\partial y} + \frac{1}{c^2} \frac{\partial E_y}{\partial t}, \quad (46)$$

$$\frac{\partial B_y}{\partial x} - \frac{\partial B_x}{\partial y} = \frac{\partial S}{\partial z} + \frac{1}{c^2} \frac{\partial E_z}{\partial t}, \quad (47)$$

$$\frac{\partial E_x}{\partial x} + \frac{\partial E_y}{\partial y} + \frac{\partial E_z}{\partial z} = -\frac{\partial S}{\partial t}, \quad (48)$$

$$\frac{\partial E_z}{\partial y} - \frac{\partial E_y}{\partial z} = -\frac{\partial B_x}{\partial t}, \quad (49)$$

$$\frac{\partial E_x}{\partial z} - \frac{\partial E_z}{\partial x} = -\frac{\partial B_y}{\partial t}, \quad (50)$$

$$\frac{\partial E_y}{\partial x} - \frac{\partial E_x}{\partial y} = -\frac{\partial B_z}{\partial t}, \quad (51)$$

$$\frac{\partial B_x}{\partial x} + \frac{\partial B_y}{\partial y} + \frac{\partial B_z}{\partial z} = 0, \quad (52)$$

which are coincident with Maxwell's equations if

$$\frac{\partial S}{\partial x} = \mu_0 J_{ex} = \mu_0 \frac{\partial q}{\partial y \partial z \partial t} = \mu_0 \frac{\partial q \partial x}{\partial x \partial y \partial z \partial t} = \mu_0 \rho v_x, \quad (53)$$

$$\frac{\partial S}{\partial y} = \mu_0 J_{ey} = \mu_0 \frac{\partial q}{\partial x \partial z \partial t} = \mu_0 \frac{\partial q \partial y}{\partial x \partial y \partial z \partial t} = \mu_0 \rho v_y, \quad (54)$$

$$\frac{\partial S}{\partial z} = \mu_0 J_{ez} = \mu_0 \frac{\partial q}{\partial x \partial y \partial t} = \mu_0 \frac{\partial q \partial z}{\partial x \partial y \partial z \partial t} = \mu_0 \rho v_z, \quad (55)$$

$$\frac{1}{c} \frac{\partial S}{\partial t} = \mu_0 J_{et} = -\mu_0 c \frac{\partial q}{\partial x \partial y \partial z} = -\mu_0 c \rho, \quad (56)$$

where ∂q is the differential of a generic charge [4,17]. Equation (56) can be also written as

$$\frac{\partial S}{\partial t} = c \mu_0 J_{et} = -\mu_0 c^2 \frac{\partial q}{\partial x \partial y \partial z} = -\mu_0 c^2 \rho = -\frac{\rho}{\epsilon_0}. \quad (57)$$

By taking into account (53)–(56), the following relation holds for the current density field,

$$\frac{1}{\mu_0} \boldsymbol{\partial} S = \frac{1}{\mu_0} \left(\gamma_x \frac{\partial S}{\partial x} + \gamma_y \frac{\partial S}{\partial y} + \gamma_z \frac{\partial S}{\partial z} + \gamma_t \frac{1}{c} \frac{\partial S}{\partial t} \right) = \mathbf{J}_{\square e}, \quad (58)$$

where

$$\begin{aligned} \mathbf{J}_{\square e} &= \gamma_x J_{ex} + \gamma_y J_{ey} + \gamma_z J_{ez} + \gamma_t J_{et} = \gamma_x J_{ex} + \gamma_y J_{ey} + \gamma_z J_{ez} - \gamma_t c \rho \\ &= \mathbf{J}_{\Delta} - \gamma_t c \rho = \rho (\mathbf{v}_{\Delta} - \gamma_t \mathbf{c}) \end{aligned} \quad (59)$$

is the four-current vector,

$$\mathbf{v}_{\square} = \gamma_x v_x + \gamma_y v_y + \gamma_z v_z - \gamma_t \mathbf{c} = \mathbf{v}_{\Delta} - \gamma_t \mathbf{c} \quad (60)$$

is a four-velocity vector and \mathbf{v}_{Δ} is the speed in the ordinary space.

In this formulation the partial derivatives of the scalar field S with respect to time and space coordinates can be interpreted as charge density and current density, respectively. As a matter of fact (45)–(47) represent the spatial components of the Faraday–Neumann–Maxwell–Lenz law, i.e.

$$\nabla \times \mathbf{B} = \mu_0 \mathbf{J}_\Delta + \frac{1}{c^2} \frac{\partial \mathbf{E}}{\partial t}, \quad (61)$$

where $\mathbf{J}_\Delta = \gamma_x J_{ex} + \gamma_y J_{ey} + \gamma_z J_{ez}$ is the three-component vector of current density, (48) is the Gauss's law for the electric field

$$\nabla \cdot \mathbf{E} = \frac{\rho}{\epsilon_0}, \quad (62)$$

(49)–(51) represent the spatial components of Ampere's law

$$\nabla \times \mathbf{E} = -\frac{\partial \mathbf{B}}{\partial t} \quad (63)$$

and (52) the Gauss's law for the flux density field

$$\nabla \cdot \mathbf{B} = 0. \quad (64)$$

Finally, by applying the $\partial \cdot$ operator to (58) and setting the result to zero, the equation representing the law of electric charge conservation is obtained

$$\frac{1}{\mu_0} \partial \cdot (\partial S) = \partial \cdot \mathbf{J}_{\square e} = \frac{\partial J_{ex}}{\partial x} + \frac{\partial J_{ey}}{\partial y} + \frac{\partial J_{ez}}{\partial z} + \frac{\partial \rho}{\partial t} = 0. \quad (65)$$

It is important to note that the wave equation of the scalar field S can be deduced from the charge–current conservation law:

$$\partial \cdot (\partial S) = \partial^2 S = \frac{\partial^2 S}{\partial x^2} + \frac{\partial^2 S}{\partial y^2} + \frac{\partial^2 S}{\partial z^2} - \frac{1}{c^2} \frac{\partial^2 S}{\partial t^2} = \nabla^2 S - \frac{1}{c^2} \frac{\partial^2 S}{\partial t^2} = 0. \quad (66)$$

Now, by applying the time derivative to (66) and remembering (57), the wave equation of the charge field $\rho(r_\square)$ can also be deduced, i.e.

$$\frac{\partial}{\partial t} (\partial^2 S) = \partial^2 \left(\frac{\partial S}{\partial t} \right) = \partial^2 (-\mu_0 c^2 \rho) = -\mu_0 c^2 \partial^2 \rho = 0, \quad (67)$$

which gives

$$\partial^2 \rho = \nabla^2 \rho - \frac{1}{c^2} \frac{\partial^2 \rho}{\partial t^2} = 0. \quad (68)$$

Clearly, both (66) and (68) represent, respectively, fields (S and ρ) that must necessarily propagate at the speed of light [17,19]. Equation (58) means also that the 4-vector current density field can be derived directly from the scalar field S . The hypothesis of existence of scalar waves has been recently explored at the Oak Ridge laboratories: “*The new theory predicts a new charge-fluctuation-driven scalar wave, having energy but not momentum for zero magnetic and electric fields. The scalar wave can co-exist with a longitudinal-electric wave, having energy and momentum. The new theory in 4-vector form is relativistically covariant. New experimental tests are needed to confirm this theory.*” [13].

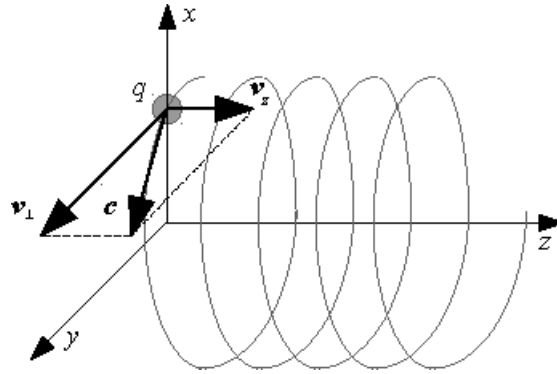


Figure 3. Helical motion of an elementary charge q moving at the speed of light, with $v_z^2 + v_{\perp}^2 = c^2$.

The proposed reinterpretation of Maxwell’s equations in this paper is in agreement with the principle of Occam’s razor: the concepts of charge and current density are not inserted “ad hoc” but are deduced from a single more fundamental entity, the four dimensional vector potential field $\mathbf{A}_{\square}(\mathbf{r}_{\square}) = \mathbf{A}_{\square}(x, y, z, t)$.

Equation (68) imposes a precise condition on charge dynamics, describing only distributions of charge density moving in vacuum at the speed of light c . At first glance, this result seems to be incompatible with experimental observations, with the usual concepts of charge and current and with the traditional way of working with Maxwell’s equations. In fact, with reference to this perspective, a big advantage in using Maxwell’s equations is the ability to simply specify both current density and charge density distributions and then see what fields result. Nevertheless, in the model proposed in this paper, the added constraint on the charge and current density seems to imply that one is no longer free to specify charge and current density distributions at will, because this information is indeed included within the electromagnetic four potential \mathbf{A}_{\square} .

As will be shown later, we can interpret (68) as a constraint for the definition of models of elementary charges (or particles). This constraint, however, can be removed when considering macroscopic electromagnetic systems or even the dynamics of a single elementary charge at a spatial scale greater than the particle Compton wavelength λ_c and at a time scale greater than the Compton period λ_c/c . In this case static elementary charges can be seen as charge density distributions moving at the speed of light on a closed trajectory but with a zero average speed (this generalization would be consistent with static charge densities, electrets, dielectrics), whereas currents can be considered as an ordered motion of charge density distributions moving with an absolute velocity equal to the speed of light but with an arbitrary average speed lower than c .

As an example, referring to Fig. 3, the electromagnetic effects generated by an elementary charge q , moving at instantaneous speed c in a helical motion of radius $\leq \lambda_c/2\pi$ with average velocity v_z along the helix axis z and tangential velocity v_{\perp} , can be approximated, on a spatial scale $\gg \lambda_c$ and a temporal scale $\gg \lambda_c/c$, to those produced by the same elementary charge q moving at uniform velocity v_z , creating the current density

$$\mathbf{J}_z = J_z \gamma_z \approx \frac{q}{\delta x \delta y \delta z} \frac{dz}{dt} \gamma_z = \frac{q}{\delta V} \frac{dz}{dt} \gamma_z = \rho v_z \gamma_z = \rho \mathbf{v}_z, \tag{69}$$

where $\delta V = \delta x \delta y \delta z \approx \lambda_c^3$. In this view and at a macroscopic level the here proposed new interpretation of Maxwell’s equations remains compatible with the traditional way of working with them, i.e. by assigning the sources and determining, as a consequence, both the electric and the flux density (magnetic) field.

The new formulation of Maxwell’s equations expressed by (35) is quite similar to the Dirac–Hestenes equation for

$m = 0$ (Weyl equation). In all cases the solution is a *spinor* field. A spinor is a mathematical object that in space–time algebra is simply a multivector of even grade components. The motion of a massless charge that moves at speed of light can be described using a composition of a rotation in the $\gamma_x\gamma_y$ plane followed by a scaled hyperbolic rotation in the $\gamma_z\gamma_t$ plane and can be encoded in $Cl_{3,1}$ with a single spinor.

At this point the Authors are encouraged by an interesting sentence of P.A.M. Dirac. In fact, in his Nobel lecture [20], held in 1933, Dirac proposed an electron model in which a charge moves at the speed of light: “*It is found that an electron which seems to us to be moving slowly, must actually have a very high frequency oscillatory motion of small amplitude superposed on the regular motion which appears to us. As a result of this oscillatory motion, the velocity of the electron at any time equals the velocity of light.*”

4. Properties of the Electromagnetic Field

In this section, the main properties of the electromagnetic field will be presented and discussed by means of $Cl_{3,1}$ Clifford algebra.

4.1. Lorentz force

A very compact and elegant form for the expression of the Lorentz force can be achieved in $Cl_{3,1}$, in terms of a generic charge q moving at a generic speed $\mathbf{v}_\square = \mathbf{v}_\Delta - \gamma_t c$, extracting from the expression $q\mathbf{G}\mathbf{v}_\square$ the blades of degree 1, and considering the four-momentum \mathbf{P}_\square , i.e.

$$\begin{aligned} \left(\frac{d\mathbf{P}_\square}{dt}\right)_q &= \langle q\mathbf{G}\mathbf{v}_\square \rangle_1 = q \left(\mathbf{E} - I_\Delta \mathbf{v}_\Delta \wedge \mathbf{B} - \gamma_t \frac{1}{c} \mathbf{v}_\Delta \cdot \mathbf{E} + S\mathbf{v}_\Delta - \gamma_t cS \right) \\ &= q \left(\mathbf{E} + \mathbf{v}_\Delta \times \mathbf{B} + S\mathbf{v}_\Delta \right) - \gamma_t q \left(\frac{1}{c} \mathbf{v}_\Delta \cdot \mathbf{E} + cS \right), \end{aligned} \quad (70)$$

where $I_\Delta = \gamma_x\gamma_y\gamma_z = -I\gamma_t$ is the unitary volume of the three dimensional space. In the last member of (70) the first term represents the Lorentz force acting on the charge q plus a force acting on the same charge but depending on the scalar field and on the speed and directed along the motion, whereas the last term in γ_t represents the work carried out by the electric and scalar fields in moving the charge along a unitary distance.

In terms of force density (in N m^{-3}) the above expression becomes

$$\begin{aligned} \frac{d\mathbf{P}_{\square V}}{dt} &= \langle \rho\mathbf{G}\mathbf{v}_\square \rangle_1 = \rho\mathbf{E} - I_\Delta \mathbf{J}_\Delta \wedge \mathbf{B} - \gamma_t \frac{1}{c} \mathbf{J}_\Delta \cdot \mathbf{E} - \gamma_t \rho cS \\ &= \rho\mathbf{E} + \mathbf{J}_\Delta \times \mathbf{B} + S\mathbf{J}_\Delta - \gamma_t \left(\frac{1}{c} \mathbf{J}_\Delta \cdot \mathbf{E} + \rho cS \right), \end{aligned} \quad (71)$$

where $\mathbf{P}_{\square V}$ is the four-momentum spatial density, \mathbf{J}_Δ is the generic 3-D current density and ρ the spatial charge density. The term $S\mathbf{J}_\Delta$ is the contribution, in terms of force per volume, due to the scalar field; this force density has the same direction of the 3-D current density. The last term in (71), with the unitary vector γ_t , represents the work density produced by the electric and scalar fields when moving the spatial charge density ρ along a unitary distance.

4.2. Derivation of Maxwell’s equations from Lagrangian density

Maxwell’s equations can be derived considering the following Lagrangian density, in form of a composition of a scalar and a pseudoscalar part:

$$\begin{aligned} \mathbf{L} &= \frac{1}{2\mu_0} \partial \mathbf{A}_\square \widetilde{\partial \mathbf{A}}_\square = \frac{1}{2\mu_0} \mathbf{G} \widetilde{\mathbf{G}} = \frac{1}{2\mu_0} \|\mathbf{G}\|^2 = \frac{1}{2\mu_0} (S + \mathbf{F})(S - \mathbf{F}) = \frac{1}{2\mu_0} (S^2 - \mathbf{F}^2) \\ &= \frac{1}{2\mu_0} \left(-\frac{E^2}{c^2} + B^2 + S^2 - \frac{2}{c} \mathbf{I} \mathbf{E} \cdot \mathbf{B} \right), \end{aligned} \quad (72)$$

where, bearing (33) in mind,

$$\mathbf{F} = \frac{1}{c} \mathbf{E} \gamma_t + \mathbf{I} \mathbf{B} \gamma_t = \frac{1}{c} (\mathbf{E} + \mathbf{I} c \mathbf{B}) \gamma_t \quad (73)$$

is the bivector part of the electromagnetic field and $\widetilde{}$ represents the conjugation operator. Expanding (72), and taking equations from (20) to (26) into account, we obtain the Lagrangian density as a function of the derivatives of the electromagnetic four-potential components, i.e.

$$\begin{aligned} \mathbf{L} &= \frac{1}{2\mu_0} \left\{ -\left(\frac{\partial A_t}{\partial x} - \frac{1}{c} \frac{\partial A_x}{\partial t} \right)^2 - \left(\frac{\partial A_t}{\partial y} - \frac{1}{c} \frac{\partial A_y}{\partial t} \right)^2 - \left(\frac{\partial A_t}{\partial z} - \frac{1}{c} \frac{\partial A_z}{\partial t} \right)^2 \right. \\ &\quad + \left(\frac{\partial A_z}{\partial y} - \frac{\partial A_y}{\partial z} \right)^2 + \left(\frac{\partial A_x}{\partial z} - \frac{\partial A_z}{\partial x} \right)^2 + \left(\frac{\partial A_y}{\partial x} - \frac{\partial A_x}{\partial y} \right)^2 \\ &\quad + \left(\frac{\partial A_x}{\partial x} + \frac{\partial A_y}{\partial y} + \frac{\partial A_z}{\partial z} - \frac{1}{c} \frac{\partial A_t}{\partial t} \right)^2 \\ &\quad - 2I \left[\left(\frac{\partial A_t}{\partial x} - \frac{1}{c} \frac{\partial A_x}{\partial t} \right) \left(\frac{\partial A_z}{\partial y} - \frac{\partial A_y}{\partial z} \right) + \left(\frac{\partial A_t}{\partial y} - \frac{1}{c} \frac{\partial A_y}{\partial t} \right) \left(\frac{\partial A_x}{\partial z} - \frac{\partial A_z}{\partial x} \right) \right. \\ &\quad \left. \left. + \left(\frac{\partial A_t}{\partial z} - \frac{1}{c} \frac{\partial A_z}{\partial t} \right) \left(\frac{\partial A_y}{\partial x} - \frac{\partial A_x}{\partial y} \right) \right] \right\}. \end{aligned} \quad (74)$$

In $Cl_{3,1}$ algebra the Euler–Lagrange equations can be expressed, considering as variables the electromagnetic four-potential components $A_x(x, y, z, t)$, $A_y(x, y, z, t)$, $A_z(x, y, z, t)$ and $A_t(x, y, z, t)$, in the following way:

$$\sum_{j=x,y,z,t} \left(\sum_{i=x,y,z,t} \gamma_i \frac{\partial}{\partial i} \left(\frac{\partial \mathbf{L}}{\gamma_i \gamma_j \partial \left(\frac{\partial A_j}{\partial i} \right)} \right) - \frac{\partial \mathbf{L}}{\gamma_j \partial A_j} \right) = 0, \quad (75)$$

which reduces itself to

$$\sum_{j=x,y,z,t} \left(\sum_{i=x,y,z,t} \gamma_i \frac{\partial}{\partial i} \left(\frac{\partial \mathbf{L}}{\gamma_i \gamma_j \partial \left(\frac{\partial A_j}{\partial i} \right)} \right) \right) = 0, \quad (76)$$

considering that in this case

$$\sum_{j=x,y,z,t} \left(\frac{\partial \mathbf{L}}{\gamma_j \partial A_j} \right) = 0, \quad (77)$$

because in (74) only the derivative terms of the four-potential ($\partial A_j/\partial i$) appear. By expanding (76), for example with $j = t$, we achieve, after some trivial calculation steps,

$$\begin{aligned} -\gamma_t \frac{\partial \mathbf{L}}{\partial A_t} &= -\gamma_t \frac{\partial}{\partial x} \frac{\partial \mathbf{L}}{\partial \left(\frac{\partial A_t}{\partial x}\right)} - \gamma_t \frac{\partial}{\partial y} \frac{\partial \mathbf{L}}{\partial \left(\frac{\partial A_t}{\partial y}\right)} - \gamma_t \frac{\partial}{\partial z} \frac{\partial \mathbf{L}}{\partial \left(\frac{\partial A_t}{\partial z}\right)} - \gamma_t \frac{\partial}{\partial t} \frac{\partial \mathbf{L}}{\partial \left(\frac{\partial A_t}{\partial t}\right)} \\ &= \gamma_t \frac{1}{\mu_0} \left(\frac{1}{c} \frac{\partial E_x}{\partial x} + I \frac{\partial B_x}{\partial x} + \frac{1}{c} \frac{\partial E_y}{\partial y} + I \frac{\partial B_y}{\partial y} + \frac{1}{c} \frac{\partial E_z}{\partial z} + I \frac{\partial B_z}{\partial z} + \frac{1}{c} \frac{\partial S}{\partial t} \right) = 0, \end{aligned} \quad (78)$$

and this equation returns Gauss's laws for the electric field (see Eq. (40)) and for the flux density field (see Eq. (44)), respectively:

$$\begin{aligned} \gamma_t \frac{1}{c} \left(\frac{\partial E_x}{\partial x} + \frac{\partial E_y}{\partial y} + \frac{\partial E_z}{\partial z} + \frac{\partial S}{\partial t} \right) &= 0, \\ \gamma_x \gamma_y \gamma_z \left(\frac{\partial B_x}{\partial x} + \frac{\partial B_y}{\partial y} + \frac{\partial B_z}{\partial z} \right) &= 0. \end{aligned}$$

Now, if we expand (76) with $j = x$, we obtain

$$\begin{aligned} \gamma_x \frac{\partial \mathbf{L}}{\partial A_x} &= \gamma_x \frac{\partial}{\partial x} \frac{\partial \mathbf{L}}{\partial \left(\frac{\partial A_x}{\partial x}\right)} + \gamma_x \frac{\partial}{\partial y} \frac{\partial \mathbf{L}}{\partial \left(\frac{\partial A_x}{\partial y}\right)} + \gamma_x \frac{\partial}{\partial z} \frac{\partial \mathbf{L}}{\partial \left(\frac{\partial A_x}{\partial z}\right)} + \gamma_x \frac{\partial}{\partial t} \frac{\partial \mathbf{L}}{\partial \left(\frac{\partial A_x}{\partial t}\right)} \\ &= \gamma_x \frac{1}{\mu_0} \left(\frac{\partial S}{\partial x} - \frac{\partial B_z}{\partial y} + \frac{I}{c} \frac{\partial E_z}{\partial y} + \frac{\partial B_y}{\partial z} - \frac{I}{c} \frac{\partial E_y}{\partial z} + \frac{1}{c^2} \frac{\partial E_x}{\partial t} + \frac{I}{c} \frac{\partial B_x}{\partial t} \right) = 0. \end{aligned} \quad (79)$$

Equation (79) gives (37) and (41):

$$\begin{aligned} \gamma_x \left(\frac{\partial B_y}{\partial z} - \frac{\partial B_z}{\partial y} + \frac{\partial S}{\partial x} + \frac{1}{c^2} \frac{\partial E_x}{\partial t} \right) &= 0, \\ \gamma_y \gamma_z \gamma_t \frac{1}{c} \left(\frac{\partial E_z}{\partial y} - \frac{\partial E_y}{\partial z} + \frac{\partial B_x}{\partial t} \right) &= 0. \end{aligned}$$

If we carry on the above procedures with $j = y$ and $j = z$ the other remaining components of Maxwell's equation can be determined, i.e (38), (42), (39) and (43):

$$\begin{aligned} \gamma_y \frac{\partial \mathbf{L}}{\partial A_y} &= \gamma_y \frac{\partial}{\partial x} \frac{\partial \mathbf{L}}{\partial \left(\frac{\partial A_y}{\partial x}\right)} + \gamma_y \frac{\partial}{\partial y} \frac{\partial \mathbf{L}}{\partial \left(\frac{\partial A_y}{\partial y}\right)} + \gamma_y \frac{\partial}{\partial z} \frac{\partial \mathbf{L}}{\partial \left(\frac{\partial A_y}{\partial z}\right)} + \gamma_y \frac{\partial}{\partial t} \frac{\partial \mathbf{L}}{\partial \left(\frac{\partial A_y}{\partial t}\right)} \\ &= \gamma_y \frac{1}{\mu_0} \left(\frac{\partial B_z}{\partial x} - \frac{I}{c} \frac{\partial E_z}{\partial x} + \frac{\partial S}{\partial y} - \frac{\partial B_x}{\partial z} + \frac{I}{c} \frac{\partial E_x}{\partial z} + \frac{1}{c^2} \frac{\partial E_y}{\partial t} + \frac{I}{c} \frac{\partial B_y}{\partial t} \right) = 0, \end{aligned} \quad (80)$$

$$\begin{aligned} \gamma_z \frac{\partial \mathbf{L}}{\partial A_z} &= \gamma_z \frac{\partial}{\partial x} \frac{\partial \mathbf{L}}{\partial \left(\frac{\partial A_z}{\partial x}\right)} + \gamma_z \frac{\partial}{\partial y} \frac{\partial \mathbf{L}}{\partial \left(\frac{\partial A_z}{\partial y}\right)} + \gamma_z \frac{\partial}{\partial z} \frac{\partial \mathbf{L}}{\partial \left(\frac{\partial A_z}{\partial z}\right)} + \gamma_z \frac{\partial}{\partial t} \frac{\partial \mathbf{L}}{\partial \left(\frac{\partial A_z}{\partial t}\right)} \\ &= \gamma_z \frac{1}{\mu_0} \left(-\frac{\partial B_y}{\partial x} + \frac{I}{c} \frac{\partial E_y}{\partial x} + \frac{\partial B_x}{\partial y} - \frac{I}{c} \frac{\partial E_x}{\partial y} + \frac{\partial S}{\partial z} + \frac{1}{c^2} \frac{\partial E_z}{\partial t} + \frac{I}{c} \frac{\partial B_z}{\partial t} \right) = 0, \end{aligned} \quad (81)$$

that give, as expected, respectively

$$\gamma_y \left(\frac{\partial B_z}{\partial x} + \frac{\partial S}{\partial y} - \frac{\partial B_x}{\partial z} + \frac{1}{c^2} \frac{\partial E_y}{\partial t} \right) = 0,$$

$$\gamma_x \gamma_z \gamma_t \frac{1}{c} \left(\frac{\partial E_z}{\partial x} - \frac{\partial E_x}{\partial z} - \frac{\partial B_y}{\partial t} \right) = 0,$$

$$\gamma_z \left(\frac{\partial B_x}{\partial y} + \frac{\partial S}{\partial z} - \frac{\partial B_y}{\partial x} + \frac{1}{c^2} \frac{\partial E_z}{\partial t} \right) = 0,$$

$$\gamma_x \gamma_y \gamma_t \frac{1}{c} \left(\frac{\partial E_y}{\partial x} - \frac{\partial E_x}{\partial y} + \frac{\partial B_z}{\partial t} \right) = 0.$$

By analyzing the above-reported equations, it is possible to reach some conclusions. First of all the Lagrangian density, as defined in (72), can be divided in the sum of two parts

$$\mathbf{L} = L_{\text{field}} + L_{\text{int}}. \quad (82)$$

The first part

$$L_{\text{field}} = \frac{1}{2\mu_0} \left(-\frac{E^2}{c^2} + B^2 \right) = -\frac{1}{2\mu_0} (\mathbf{F} \cdot \mathbf{F}) \quad (83)$$

represents the “field part” of the Lagrangian density, as known in literature, and the second

$$L_{\text{int}} = \frac{1}{2\mu_0} \left(S^2 - \frac{2}{c} I \mathbf{E} \cdot \mathbf{B} \right) \quad (84)$$

represents the “interaction term” of the Lagrangian density, that takes the interaction of the electromagnetic field with the sources into account, remembering, in addition, that the derivatives of the scalar field S , with respect to the four dimensional space coordinates x, y, z and t , are bounded respectively to the sources J_{ex}, J_{ey}, J_{ez} and $J_{et} = -c\rho$ (see Eq. (58)). Indeed, by deriving only the interaction terms of the Lagrangian density with respect to the four-potential, i.e. by performing the operation $\partial L_{\text{int}}/\partial A_j$, it is possible to derive the term $\mathbf{J}_{\square e} \cdot \mathbf{A}_{\square}$. In fact, for the component along γ_t we find

$$\begin{aligned}
-\gamma_t \frac{\partial L_{\text{int}}}{\partial A_t} &= -\gamma_t \frac{\partial}{\partial x} \frac{\partial L_{\text{int}}}{\partial \left(\frac{\partial A_t}{\partial x}\right)} - \gamma_t \frac{\partial}{\partial y} \frac{\partial L_{\text{int}}}{\partial \left(\frac{\partial A_t}{\partial y}\right)} - \gamma_t \frac{\partial}{\partial z} \frac{\partial L_{\text{int}}}{\partial \left(\frac{\partial A_t}{\partial z}\right)} - \gamma_t \frac{\partial}{\partial t} \frac{\partial L_{\text{int}}}{\partial \left(\frac{\partial A_t}{\partial t}\right)} \\
&= \frac{\gamma_t}{\mu_0} \left(I \frac{\partial B_x}{\partial x} + I \frac{\partial B_y}{\partial y} + I \frac{\partial B_z}{\partial z} + \frac{1}{c} \frac{\partial S}{\partial t} \right) = \frac{\gamma_t}{\mu_0} \left(I \nabla \cdot \mathbf{B} + \frac{1}{c} \frac{\partial S}{\partial t} \right) \\
&= \frac{\gamma_t}{\mu_0 c} \frac{\partial S}{\partial t} = \gamma_t J_{et} = -\gamma_t c \rho.
\end{aligned} \tag{85}$$

Integration of (85) yields

$$L_{\text{int}}|_t = \int \frac{\partial L_{\text{int}}}{\partial A_t} dA_t = \int \frac{1}{\mu_0 c} \frac{\partial S}{\partial t} dA_t = \frac{1}{\mu_0 c} \frac{\partial S}{\partial t} A_t = -\frac{1}{\mu_0} \mu_0 c \rho A_t = -c \rho A_t = J_{et} A_t. \tag{86}$$

For the component along γ_x we find

$$\begin{aligned}
\gamma_x \frac{\partial L_{\text{int}}}{\partial A_x} &= \gamma_x \frac{\partial}{\partial x} \frac{\partial L_{\text{int}}}{\partial \left(\frac{\partial A_x}{\partial x}\right)} + \gamma_x \frac{\partial}{\partial y} \frac{\partial L_{\text{int}}}{\partial \left(\frac{\partial A_x}{\partial y}\right)} + \gamma_x \frac{\partial}{\partial z} \frac{\partial L_{\text{int}}}{\partial \left(\frac{\partial A_x}{\partial z}\right)} + \gamma_x \frac{\partial}{\partial t} \frac{\partial L_{\text{int}}}{\partial \left(\frac{\partial A_x}{\partial t}\right)} \\
&= \frac{\gamma_x}{\mu_0} \left(\frac{\partial S}{\partial x} + \frac{I}{c} \frac{\partial E_z}{\partial y} - \frac{I}{c} \frac{\partial E_y}{\partial z} + \frac{I}{c} \frac{\partial B_x}{\partial t} \right) = \frac{\gamma_x}{\mu_0} \frac{\partial S}{\partial x} = \gamma_x J_{ex}.
\end{aligned} \tag{87}$$

Integration of (87) yields

$$L_{\text{int}}|_x = \int \left(\frac{\partial L_{\text{int}}}{\partial A_x} \right) dA_x = \int \frac{1}{\mu_0} \frac{\partial S}{\partial x} dA_x = \frac{1}{\mu_0} \frac{\partial S}{\partial x} A_x = J_{ex} A_x. \tag{88}$$

The same procedure is clearly valid also for the components in γ_y and γ_z . Finally, by integration of (77), we get the Lagrangian density interaction term as

$$L_{\text{int}} = \sum_{j=x,y,z,t} \int \left(\frac{\partial L_{\text{int}}}{\partial A_j} \right) dA_j = J_{ex} A_x + J_{ey} A_y + J_{ez} A_z - c \rho A_t = \mathbf{J}_{\square e} \cdot \mathbf{A}_{\square}, \tag{89}$$

which is the usual “source” term that is added in traditional Lagrangian theory for classical electricity and magnetism in order to obtain the complete set of Maxwell’s equations [6-8,17]. The scalar product $\mathbf{J}_{\square e} \cdot \mathbf{A}_{\square}$ has a dimension of energy per volume (J m^{-3}); in particular, the contribution of the spatial components of vectors $\mathbf{J}_{\square e}$ and \mathbf{A}_{\square} (the scalar product $\mathbf{J}_{\Delta} \cdot \mathbf{A}_{\Delta}$) can be considered as the specific “kinetic” energy of the electromagnetic field, whereas the term $J_{et} A_t = -c \rho A_t$ the “potential” energy. By virtue of (84), (89) becomes

$$L_{\text{int}} = \frac{1}{2\mu_0} \left(S^2 - \frac{2}{c} I \mathbf{E} \cdot \mathbf{B} \right) = \mathbf{J}_{\square e} \cdot \mathbf{A}_{\square}. \tag{90}$$

The pseudoscalar term $2/c I \mathbf{E} \cdot \mathbf{B}$ is clearly null as the electric and the magnetic flux density fields are always orthogonal with respect to each other: indeed, this term contains information about (63). A direct consequence of (90) is, therefore, the following relation between the scalar field, the electromagnetic four-potential and the four-current density:

$$S^2 = 2\mu_0 \mathbf{J}_{\square e} \cdot \mathbf{A}_{\square}. \tag{91}$$

By inspection of (85) and (87), and generalizing, it is possible to define the four-current vector $\mathbf{J}_{\square e}$ from the interaction Lagrangian term:

$$\begin{aligned} \sum_{j=x,y,z,t} \left(\frac{\partial L_{\text{int}}}{\gamma_j \partial A_j} \right) &= \gamma_x \frac{\partial L_{\text{int}}}{\partial A_x} + \gamma_y \frac{\partial L_{\text{int}}}{\partial A_y} + \gamma_z \frac{\partial L_{\text{int}}}{\partial A_z} - \gamma_t \frac{\partial L_{\text{int}}}{\partial A_t} \\ &= \gamma_x J_{ex} + \gamma_y J_{ey} + \gamma_z J_{ez} + \gamma_t J_{et} = \mathbf{J}_{\square e}. \end{aligned} \quad (92)$$

and, again, by virtue of the Noether's theorem, the law of current and charge conservation

$$\partial \cdot \left[\sum_{j=x,y,z,t} \left(\frac{\partial L_{\text{int}}}{\gamma_j \partial A_j} \right) \right] = \partial \cdot \mathbf{J}_{\square e} = 0, \quad (93)$$

which returns, consequently, the wave equations (66) and (68), respectively.

As can be seen the definition of the electromagnetic field \mathbf{G} is complete and it includes itself the information of both action and interaction, without the need of any additional term: this is in full accordance with the principle of Occam's razor.

Thanks to the $Cl_{3,1}$ Clifford algebra the Euler–Lagrange equations can be conveniently defined in a very compact form:

$$\partial \left(\frac{\partial L}{\partial (\partial \wedge \mathbf{A}_{\square})} \right) - \frac{\partial L}{\partial \mathbf{A}_{\square}} = \partial \left(\frac{\partial L}{\partial \mathbf{F}} \right) - \frac{\partial L}{\partial \mathbf{A}_{\square}} = 0, \quad (94)$$

where, now, the scalar Lagrangian density is

$$L = L_{\text{field}} + L_{\text{int}} = -\frac{1}{2\mu_0} \mathbf{F} \cdot \mathbf{F} + \mathbf{J}_{\square e} \cdot \mathbf{A}_{\square}. \quad (95)$$

Substituting (95) in (94) one can achieve directly Maxwell's equations in $Cl_{3,1}$ in the form shown in the previous sections (see Eq. (35)), i.e.

$$\partial \left(\frac{\partial \left(-\frac{1}{2\mu_0} \mathbf{F} \cdot \mathbf{F} + \mathbf{J}_{\square e} \cdot \mathbf{A}_{\square} \right)}{\partial \mathbf{F}} \right) - \frac{\partial \left(-\frac{1}{2\mu_0} \mathbf{F} \cdot \mathbf{F} + \mathbf{J}_{\square e} \cdot \mathbf{A}_{\square} \right)}{\partial \mathbf{A}_{\square}} = -\frac{1}{\mu_0} \partial \mathbf{F} - \mathbf{J}_{\square e} = 0, \quad (96)$$

which yields

$$\partial \mathbf{F} + \mu_0 \mathbf{J}_{\square e} = \partial \mathbf{F} + \partial S = \partial (\mathbf{F} + S) = \partial \mathbf{G} = 0. \quad (97)$$

4.3. Energy of the electromagnetic field

The energy density multivector of the field \mathbf{G} is given by

$$\begin{aligned}
 \mathbf{w} &= \frac{1}{2\mu_0} \left[S + \left(\frac{\mathbf{E}}{c} + I\mathbf{B} \right) \gamma_t \right] \left[S + \left(\frac{\mathbf{E}}{c} + I\mathbf{B} \right)^\dagger \gamma_t \right] \\
 &= \frac{1}{2\mu_0} \left[S + \left(\frac{\mathbf{E}}{c} + I\mathbf{B} \right) \gamma_t \right] \left[S + \left(\frac{\mathbf{E}}{c} - I\mathbf{B} \right) \gamma_t \right] \\
 &= \frac{S^2}{2\mu_0} + \frac{\epsilon_0 \mathbf{E}^2}{2} + \frac{\mathbf{B}^2}{2\mu_0} - \frac{1}{c\mu_0} I\mathbf{E} \wedge \mathbf{B} + \frac{1}{c\mu_0} S\mathbf{E}\gamma_t \\
 &= \frac{S^2}{2\mu_0} + \frac{\epsilon_0 \mathbf{E}^2}{2} + \frac{\mathbf{B}^2}{2\mu_0} + \frac{1}{c\mu_0} (\mathbf{E} \times \mathbf{B} + S\mathbf{E}) \gamma_t \\
 &= w_s + w_e + w_m + \frac{1}{c} \cdot \mathfrak{S} \gamma_t,
 \end{aligned} \tag{98}$$

where

$$w_s = \frac{S^2}{2\mu_0} = \mathbf{J}_{\square e} \cdot \mathbf{A}_{\square}, \quad w_e = \frac{\epsilon_0 \mathbf{E}^2}{2} \quad \text{and} \quad w_m = \frac{\mathbf{B}^2}{2\mu_0}$$

are the specific energies of the scalar, the electric and the magnetic flux density fields, respectively, \dagger is the reversion operator, whereas

$$\mathfrak{S} = \frac{1}{\mu_0} (\mathbf{E} \times \mathbf{B} + S\mathbf{E}) \tag{99}$$

is the generalized Poynting vector [10,11]. Beside the usual term $\mathbf{E} \times \mathbf{B}$ here a new energy term appears, namely $S\mathbf{E}$, which is associated to a longitudinal scalar wave [11] and that is not further investigated in the present work.

4.4. Electrostatic field and vector potential

In the case of non-time-varying potential $\partial A_t / \partial t = 0$ the scalar field S becomes the divergence of the classical 3-D vector potential \mathbf{A}_{Δ} :

$$S = \nabla \cdot \mathbf{A}_{\Delta}.$$

The time derivative of both sides gives

$$\frac{\partial S}{\partial t} = \frac{\partial(\nabla \cdot \mathbf{A}_{\Delta})}{\partial t} = \nabla \cdot \frac{\partial \mathbf{A}_{\Delta}}{\partial t}.$$

Considering that $\partial \mathbf{A}_{\Delta} / \partial t = -\mathbf{E}$ (see Eqs. (21)–(23)) and that $\partial S / \partial t = -\rho / \epsilon_0$ we rediscover Gauss's law,

$$\nabla \cdot \mathbf{E} = \frac{\rho}{\epsilon_0},$$

showing that even the electrostatic field may be seen as generated from time derivatives of a vector potential field!

4.5. Electric charge, antimatter and time direction

Feynman proposed to interpret the positron (a particle which is identical to the electron but with a positive charge) as an electron traveling back in time. Such an interpretation seems to be perfectly compatible with the definition of electric charge density given in (56):

$$\frac{\partial S}{\partial t} = \frac{-\rho}{\epsilon_0}. \tag{100}$$

By multiplying both sides of (100) by -1 we obtain

$$-\frac{\partial S}{\partial t} = \frac{\rho}{\epsilon_0}$$

or, equivalently

$$\frac{\partial S}{\partial(-t)} = \frac{\rho}{\epsilon_0}. \tag{101}$$

The positron traveling back in time is represented in the annihilation reaction diagram proposed by Feynman and shown in Fig. 4 [21].

“I did not take the idea that all the electrons were the same one from him as seriously as I took the observation that positrons could simply be represented as electrons going from the future to the past in a back section of their world lines” [22].

4.6. Magnetic charges and currents

Starting from an hypothetical eight component “vector potential” that includes the four pseudovectors (trivectors) T of space–time algebra, symmetrical Maxwell’s equations emerge. This new set of equations now include the magnetic charge and magnetic current densities that are the time and spatial derivatives of a pseudoscalar field P . By considering (9) and the four pseudovectors defined as

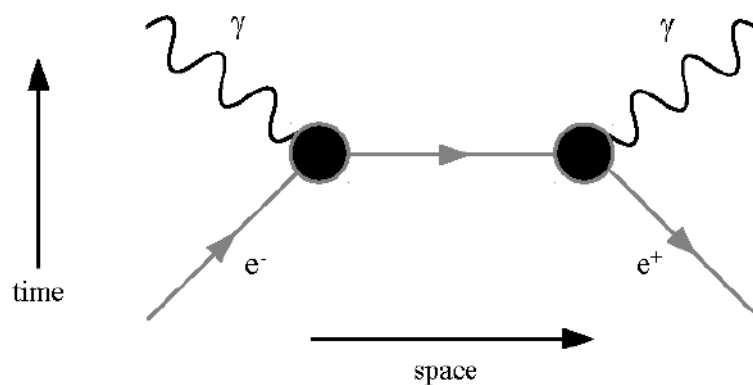


Figure 4. Feynman’s diagram of positron–electron annihilation.

$$\mathbf{T} = \gamma_y \gamma_z \gamma_t \mathbf{T}_x + \gamma_x \gamma_z \gamma_t \mathbf{T}_y + \gamma_x \gamma_y \gamma_t \mathbf{T}_z + \gamma_x \gamma_y \gamma_z \mathbf{T}_t, \quad (102)$$

a new vector potential can be defined as

$$\mathbf{A}' = \gamma_x \mathbf{A}_x + \gamma_y \mathbf{A}_y + \gamma_z \mathbf{A}_z + \gamma_t \mathbf{A}_t + \gamma_y \gamma_z \gamma_t \mathbf{T}_x + \gamma_x \gamma_z \gamma_t \mathbf{T}_y + \gamma_x \gamma_y \gamma_t \mathbf{T}_z + \gamma_x \gamma_y \gamma_z \mathbf{T}_t \quad (103)$$

from which we obtain

$$\partial(\mathbf{A}') = \partial(\mathbf{A}_\square + \mathbf{T}) = \mathbf{S} + \mathbf{F} + \mathbf{P}. \quad (104)$$

Using SI units and following the same procedure as shown in Section 3 we can write:

$$\begin{aligned} S &= \frac{\partial A_x}{\partial x} + \frac{\partial A_y}{\partial y} + \frac{\partial A_z}{\partial z} - \frac{1}{c} \frac{\partial A_t}{\partial t}, \\ \gamma_x \gamma_t \frac{1}{c} E_x &= \gamma_x \gamma_t \left(\frac{\partial A_t}{\partial x} - \frac{\partial T_z}{\partial y} - \frac{\partial T_y}{\partial z} - \frac{1}{c} \frac{\partial A_x}{\partial t} \right), \\ \gamma_y \gamma_t \frac{1}{c} E_y &= \gamma_y \gamma_t \left(\frac{\partial T_z}{\partial x} + \frac{\partial A_t}{\partial y} - \frac{\partial T_x}{\partial z} - \frac{1}{c} \frac{\partial A_y}{\partial t} \right), \\ \gamma_z \gamma_t \frac{1}{c} E_z &= \gamma_z \gamma_t \left(\frac{\partial T_y}{\partial x} + \frac{\partial T_x}{\partial y} + \frac{\partial A_t}{\partial z} - \frac{1}{c} \frac{\partial A_z}{\partial t} \right), \\ \gamma_x \gamma_y \gamma_z \gamma_t P &= \gamma_x \gamma_y \gamma_z \gamma_t \left(\frac{\partial T_x}{\partial x} - \frac{\partial T_y}{\partial y} + \frac{\partial T_z}{\partial z} - \frac{1}{c} \frac{\partial T_t}{\partial t} \right), \\ \gamma_y \gamma_z B_x &= \gamma_y \gamma_z \left(\frac{\partial T_t}{\partial x} + \frac{\partial A_z}{\partial y} - \frac{\partial A_y}{\partial z} - \frac{1}{c} \frac{\partial T_x}{\partial t} \right), \\ \gamma_x \gamma_z B_y &= \gamma_x \gamma_z \left(-\frac{\partial A_z}{\partial x} + \frac{\partial T_t}{\partial y} + \frac{\partial A_x}{\partial z} + \frac{1}{c} \frac{\partial T_y}{\partial t} \right), \\ \gamma_x \gamma_y B_z &= \gamma_x \gamma_y \left(\frac{\partial A_y}{\partial x} - \frac{\partial A_x}{\partial y} + \frac{\partial T_t}{\partial z} - \frac{1}{c} \frac{\partial T_z}{\partial t} \right). \end{aligned}$$

By applying again the ∂ operator to (104) and equating to zero:

$$\partial^2 \mathbf{A}' = \partial(\mathbf{S} + \mathbf{F} + \mathbf{P}) = \mathbf{0}. \quad (105)$$

Here

$$\partial \mathbf{F} = -\partial S - \partial P = \mu_0 \mathbf{J}_{\square e} + \frac{1}{\epsilon_0} \mathbf{J}_{\square m}, \quad (106)$$

where $\mathbf{J}_{\square e}$ is the four-current as defined in (58),

$$\mathbf{J}_{\square m} = \gamma_x J_{mx} + \gamma_y J_{my} + \gamma_z J_{mz} + \gamma_t J_{mt} = \gamma_x J_{mx} + \gamma_y J_{my} + \gamma_z J_{mz} - \gamma_t \frac{1}{c} \rho_m$$

is the magnetic four-current vector and ρ_m the magnetic charge. By carrying out all calculation in (105) the following set of equations is obtained:

$$\gamma_x \left(\frac{\partial S}{\partial x} - \frac{\partial B_z}{\partial y} + \frac{\partial B_y}{\partial z} + \frac{1}{c^2} \frac{\partial E_x}{\partial t} \right) = 0,$$

$$\gamma_y \left(\frac{\partial B_z}{\partial x} + \frac{\partial S}{\partial y} - \frac{\partial B_x}{\partial z} + \frac{1}{c^2} \frac{\partial E_y}{\partial t} \right) = 0,$$

$$\gamma_z \left(-\frac{\partial B_y}{\partial x} + \frac{\partial B_x}{\partial y} + \frac{\partial S}{\partial z} + \frac{1}{c^2} \frac{\partial E_z}{\partial t} \right) = 0,$$

$$\gamma_t \frac{1}{c} \left(\frac{\partial E_x}{\partial x} + \frac{\partial E_y}{\partial y} + \frac{\partial E_z}{\partial z} + \frac{\partial S}{\partial t} \right) = 0,$$

$$\gamma_y \gamma_z \gamma_t \frac{1}{c} \left(\frac{\partial P}{\partial x} + \frac{\partial E_z}{\partial y} - \frac{\partial E_y}{\partial z} + \frac{\partial B_x}{\partial t} \right) = 0,$$

$$\gamma_x \gamma_z \gamma_t \frac{1}{c} \left(\frac{\partial E_z}{\partial x} - \frac{\partial P}{\partial y} - \frac{\partial E_x}{\partial z} - \frac{\partial B_y}{\partial t} \right) = 0,$$

$$\gamma_x \gamma_y \gamma_t \frac{1}{c} \left(\frac{\partial E_y}{\partial x} - \frac{\partial E_x}{\partial y} + \frac{\partial P}{\partial z} + \frac{\partial B_z}{\partial t} \right) = 0,$$

$$\gamma_x \gamma_y \gamma_z \left(\frac{\partial B_x}{\partial x} + \frac{\partial B_y}{\partial y} + \frac{\partial B_z}{\partial z} + \frac{\partial P}{\partial t} \right) = 0.$$

This set of equations represents the symmetrical Maxwell's equations considering the hypothesis (never confirmed up until now by experiments) of existing magnetic currents and charges.

5. Conclusions

Simplicity is an important and concrete value in scientific research. Connections between very different concepts in physics can be evidenced if we use the language of geometric algebra. The application of Occam's Razor principle to Maxwell's equations highlights some essential concepts:

- (1) First of all, Clifford algebra is by far the most appropriate, simple and intuitive mathematical language for encoding in general the laws of physics and in particular the laws of electromagnetism.
- (2) A scalar field derives from the definition of "harmonic" electromagnetic four-potential and this scalar field becomes the source of charges and currents.
- (3) The charge density derived from the scalar field follows the wave equation with a propagation speed equal to the speed of light.
- (4) The Feynman model of the positron, seen as an electron traveling back in time, seems to be perfectly compatible with the definition of electric charge density as the time derivative of a scalar field.

In particular, the important element emerging from the present paper is that (68) imposes a precise condition on charge dynamics, describing distributions of charge density moving in vacuum at the speed of light. Indeed, van Vlaenderen found the same condition on charge dynamics but with the difference that he considers both the conditions $\mathbf{E} = 0$ and $\mathbf{B} = 0$ at the same time (no electromagnetic field) concluding that "a scalar field S can be induced by a dynamic charge/current distribution" [11].

In the model proposed here, the added constraint on the charge and current density seems to imply that one is no longer free to specify charge and current density distributions at will, because this information is indeed included within the definition of the four-potential \mathbf{A}_\square . However, this constraint can be removed when considering macroscopic electromagnetic systems or even the dynamics of a single elementary charge at a spatial scale greater than the particle Compton wavelength λ_c and at a time scale greater than the Compton period λ_c/c . In this case static elementary charges can be visualized as charge density distributions moving at the speed of light on a closed trajectory but with a zero average speed (this generalization would be consistent with static charge densities, electrets, dielectrics), whereas currents can be considered as an ordered motion of charge density distributions moving with an absolute velocity equal to the speed of light but with an arbitrary absolute average speed lower than c . This observation favors a pure electromagnetic model of elementary particles based on a particular *Zitterbewegung* interpretation of quantum mechanics [23,24]. Therefore, the free electron, and perhaps all other elementary charged particles, can be viewed as a charge distribution that rotates at the speed of light along a circumference whose length is equal to its Compton wavelength [25].

Finally, a Lagrangian density equal to the square module of the seven component electromagnetic field reveals an energy density formula for both fields and currents. Moreover, it has been demonstrated that Maxwell's equations can be explicitly derived in a simple way directly from the Lagrangian density of the electromagnetic field with the help of Clifford algebra. An interesting consequence is also that the specific energy of the scalar field is deeply connected to the interaction term of the Lagrangian density and, therefore, both to the electromagnetic four-potential and the four-current density.

It is our opinion that the *Zitterbewegung* interpretation of quantum mechanics may give an important contribution for understanding the structure of ultradense hydrogen and the origin of anomalous heat in some metal-hydrogen systems. A *Zitterbewegung* electron model and a preliminary hypothesis for the structure of ultradense deuterium will be treated more deeply in a paper written by the authors, entitled "The Electron and Occam's Razor", *J. Condensed Matter Nucl. Sci.* **25** (2017).

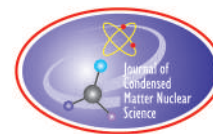
Acknowledgements

Thanks to Salvatore Mercurio, former professor of physics at the North University of China (NUC), Taiyuan, Shanxi, for interesting discussions on the nature of electric charge. Many thanks also to the reviewers for their interesting advice and beneficial suggestions and to Jed Rothwell for the English revision of the manuscript.

References

- [1] L. Bauer, *The Linguistics Student's Handbook*, Edinburgh University Press, Edinburgh, 2007.
- [2] G. Pilato and G. Vassallo, TSVD as a statistical estimator in the latent semantic analysis paradigm, *IEEE Trans. Emerging Topics Computing* **3** (2) (2015) 185–192.
- [3] Y. Aharonov and D. Bohm, Significance of electromagnetic potentials in the quantum theory, *Phy. Rev.* **115** (1959) 485–491.
- [4] J.M. Chappell, S.P. Drake, C.L. Seidel, L.J. Gunn, A. Iqbal, A. Allison and D. Abbott, Geometric algebra for electrical and electronic engineers, *Proc. IEEE* **102** (9) (2014) 1340–1363.
- [5] G. Bettini, Clifford algebra, 3- and 4-dimensional analytic functions with applications, Manuscripts of the Last Century. viXra.org, *Quantum Physics*: 1–63, 2011. <http://vixra.org/abs/1107.0060>.
- [6] J. Dressel, K.Y. Bliokh and F. Nori, Spacetime algebra as a powerful tool for electromagnetism, *Phys. Reports* **589** (2015) 1–71.
- [7] J.M. Chappell, A. Iqbal and D. Abbott, A simplified approach to electromagnetism using geometric algebra. ArXiv e-prints, oct 2010. <https://arxiv.org/pdf/1010.4947.pdf>.
- [8] W.A. Rodrigues and E.C. de Oliveira, The many faces of Maxwell, dirac and Einstein equations: a Clifford bundle approach, *Lecture Notes in Physics*, Springer, Berlin, Heidelberg, 2007.
- [9] A.M. Shaarawi, Clifford algebra formulation of an electromagnetic charge–current wave theory, *Found. Phys.* **30**(11) (2000) 1911–941.
- [10] K.J. van Vlaenderen and A. Waser, Generalization of classical electrodynamics to admit a scalar field and longitudinal waves, *Hadronic J.* **24** (2001) 609–628.
- [11] K.J. van Vlaenderen, A generalisation of classical electrodynamics for the prediction of scalar field effects, ArXiv Physics e-prints, May 2003. <https://arxiv.org/pdf/physics/0305098.pdf>.
- [12] L.M. Hively and G.C. Giakos, Toward a more complete electrodynamic theory, *Int. J. Signals Imaging Systems Eng.* **5**(1) (2012).
- [13] L.M. Hively, Implications of a new electrodynamic theory, July 2015. at <https://www.researchgate.net>.
- [14] D. Hestenes, Reforming the mathematical language of physics, *Oersted Medal Lecture*, 2002, 2002.
- [15] D. Hestenes, Spacetime physics with geometric algebra, *Amer. J. Phys.* **71**(3)(2003) 691–714.
- [16] S. Franchini, A. Gentile, F. Sorbello, G. Vassallo and S. Vitabile, Conformal ALU: a conformal geometric algebra coprocessor for medical image processing, *IEEE Trans. Computers* **64**(4) (2015) 955–970.
- [17] K. Simonyi, *Theoretische Elektrotechnik. Hochschulbücher für Physik*, VEB Deutscher Verlag der Wissenschaften, Berlin, Germany, 9 Edition, 1989.
- [18] D. Hestenes, *Clifford Algebra and the Interpretation of Quantum Mechanics*, Springer, Netherlands, Dordrecht, pp. 321–346, 1986.
- [19] A. Rathke, A critical analysis of the hydrino model, *New J. Phys.* **7** (2005) 127.
- [20] P.A.M. Dirac, Nobel lecture: theory of electrons and positrons, *Nobel Lectures, Physics 1922–1941*, 1965.
- [21] R.P. Feynman, *QED: The Strange Theory of Light and Matter*, Penguin Books, Penguin, 1990.
- [22] R.P. Feynman, Nobel lecture: the development of the space–time view of quantum electrodynamics, *Nobel Lectures, Physics 1963–1970*, 1972.
- [23] D. Hestenes, Quantum mechanics from self-interaction, *Found. Phys.* **15**(1) (1985) 63–87.
- [24] D. Hestenes, Zitterbewegung modeling, *Found. Phys.* **23**(3) (1993) 365–387.

- [25] F. Santandrea and P. Cirilli, Unificazione elettromagnetica, concezione elettronica dello spazio, dell'energia e della materia, Atlante di numeri e lettere, Laboratorio di ricerca industriale, 2006, 1–8.
<http://www.atlantedinumerielettere.it/energia2006/pdf/labor.pdf>.



Research Article

Cooperative Internal Conversion Process

Péter Kálmán*, and Tamás Keszthelyi

Budapest University of Technology and Economics, Institute of Physics, Budafoki út 8. F., H-1521 Budapest, Hungary

Abstract

This paper presents a theoretical discussion of a new phenomenon, called the ‘cooperative internal conversion process’, in which the coupling of bound-free electron and neutron (or proton) transitions due to the dipole term of their Coulomb interaction, which permits cooperation of two nuclei leading to neutron (or proton) exchange if that is allowed by energy conservation. General expressions of the cross section of the processes are reported in the case of one particle nuclear and spherical shell models as well as in the case of free atoms (e.g. noble gases). A half-life characteristic of the process is also determined. As numerical examples, the cooperative internal conversion process by neutron exchange in Ne and by proton exchange in Al are dealt with. The processes may have significance in fields of nuclear waste disposal and nuclear energy production. As a generalization, cooperative internal conversion process by heavy charged particle exchange is discussed, and as an example of it, the cooperative internal conversion process by triton exchange is also discussed.

© 2017 ISCMNS. All rights reserved. ISSN 2227-3123

Keywords: Internal conversion and extranuclear effects, Other topics of nuclear reactions: specific reactions, Other topics in nuclear engineering and nuclear power studies, Radioactive wastes, Waste disposal

1. Introduction

The issue of modifying nuclear processes by the surroundings has been a question of primary interest of nuclear physics from the very beginning. The best known and investigated process in respect of modifying nuclear processes by surroundings is the internal conversion process, in which an atomic electron around an excited nucleus takes away nuclear transition energy of an electromagnetic multipole transition which otherwise would be prohibited by angular momentum conservation [1].

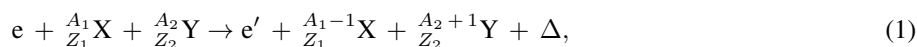
Motivated by observations of an anomalous screening effect (see e.g. [2]) we have searched for physical processes that may affect nuclear reactions in the solid state environment. We found theoretically [3,4] that the leading channel of the $p + d \rightarrow {}^3\text{He}$ reaction in the solid environment is the so-called solid state internal conversion process, an adapted version of an ordinary internal conversion process. It was shown [3,4] that if the reaction $p + d \rightarrow {}^3\text{He}$ takes place in solid material the nuclear energy is taken away by an electron of the environment instead of the emission of a γ photon.

*E-mail: kalmanpeter3@gmail.com.

In the usual internal conversion process only one nucleus is involved. However, very many pairs of nuclei can be found which may go to a state of lower energy if they could cooperate exchanging e.g. a neutron (or proton) [5]. Therefore it is worth investigating the way the electronic environment could lead to such cooperation.

Let us take two initial nuclei ${}_{Z_1}^{A_1}\text{X}$, ${}_{Z_2}^{A_2}\text{Y}$ and two final nuclei ${}_{Z_1-1}^{A_1-1}\text{X}$, ${}_{Z_2+1}^{A_2+1}\text{Y}$ which may be formed by neutron exchange. If the sum E_{0i} of the rest energies of the initial nuclei is higher than the sum E_{0f} of the rest energies of the final nuclei, i.e. if $E_{0i} - E_{0f} = \Delta > 0$, then the two nuclei (${}_{Z_1}^{A_1}\text{X}$ and ${}_{Z_2}^{A_2}\text{Y}$) are allowed to make a neutron exchange. $\Delta = \Delta_- + \Delta_+$, with $\Delta_- = \Delta_{A_1} - \Delta_{A_1-1}$ and $\Delta_+ = \Delta_{A_2} - \Delta_{A_2+1}$. Δ_{A_1} , Δ_{A_1-1} , Δ_{A_2} , Δ_{A_2+1} are the energy excesses of neutral atoms of mass numbers A_1 , $A_1 - 1$, A_2 , $A_2 + 1$, respectively [5]. As it was stated above there exist very many pairs of nuclei that fulfill the $\Delta > 0$ requirement. So it is a question of how these nuclei can realize the ${}_{Z_1}^{A_1}\text{X}$, ${}_{Z_2}^{A_2}\text{Y} \rightarrow {}_{Z_1-1}^{A_1-1}\text{X}$, ${}_{Z_2+1}^{A_2+1}\text{Y}$ neutron exchange transition.

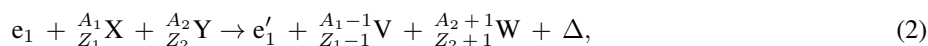
The process



that we call cooperative internal conversion process by neutron exchange (CICP-NE), will be discussed with bound-free electron transition and for atomic state only.

On the other hand, it can happen that the two final nuclei are ${}_{Z_1-1}^{A_1-1}\text{X}$, ${}_{Z_2+1}^{A_2+1}\text{Y}$ which may be formed by proton exchange from ${}_{Z_1}^{A_1}\text{X}$, ${}_{Z_2}^{A_2}\text{Y}$. If the sum E_{0i} of the rest energies of the initial nuclei is higher than the sum E_{0f} of the rest energies of the final nuclei then the two nuclei (${}_{Z_1}^{A_1}\text{X}$ and ${}_{Z_2}^{A_2}\text{Y}$) are allowed to make a proton exchange.

Proton exchange can be realized in the process



called cooperative internal conversion process by proton exchange (CICP-PE) which will be discussed theoretically in more detail too. (In processes (1) and (2) e and e' denote bound and free electrons, respectively.)

In Section 2, the transition rate (the transition probability per unit time) and in Section 3 the cross section of the cooperative internal conversion process by neutron exchange (CICP-NE) in the single electron-single nucleon model are derived. In Section 4, the cross section of CICP-NE in the spherical nuclear shell model is determined. Section 5 is devoted to cooperative internal conversion by proton exchange (CICP-PE). In Section 6, the total rate per unit volume of the sample, in Sections 7 and 8 as numerical examples the CICP-NE in Ne and CICP-PE in Al are given. In Section 9, other results and discussion and in Section 10, a summary can be found. In the Appendix the Coulomb factors $f_{2'3}$ and f_{34} , which are necessary in the case of CICP-PE, are determined.

2. Transition Rate of CICP-NE in Single Electron – Single Nucleon Model

The CICP-NE can be understood with the aid of a standard time independent second order perturbation calculation of quantum mechanics. There are two perturbations present which cause the effect and which have to be taken into account. The first is the electric dipole term $V_{\text{Cb}}^{\text{dip}}$ of the Coulomb interaction between a bound electron and a neutron of an atom of nucleus ${}_{Z_1}^{A_1}\text{X}$ in which the effective charge of the neutron $q_n = -Z_1 e/A_1$ [6].

$$V_{\text{Cb}}^{\text{dip}} = \frac{Z_1 e^2}{A_1} \frac{4\pi}{3} x_1 x_e^{-2} \sum_{m=-1}^{m=1} Y_{1m}^*(\Omega_e) Y_{1m}(\Omega_1), \quad (3)$$

where Z_1 and A_1 are charge and mass numbers of the first nucleus, e is the elementary charge, x_1 , x_e and Ω_1 , Ω_e are magnitudes and solid angles of vectors \mathbf{x}_1 , \mathbf{x}_e which are the coordinates of the neutron and the electron in the first atom, respectively and Y_{1m} denotes spherical harmonics. The second is the nuclear strong interaction potential V_{st}

of nucleus ${}_{Z_2}^{A_2}\text{Y}$. For this nuclear potential a rectangular potential well is assumed, i.e. $V_{\text{st}} = -V_0$ ($x_2 \leq R_{A_2}$) and $V_{\text{st}} = 0$ ($x_2 > R_{A_2}$) where x_2 is the magnitude of vector \mathbf{x}_2 , which is the coordinate of the neutron in the second nucleus and R_{A_2} is its radius.

The initial state, which is composed from the state of a bound electron of the atom having nucleus ${}_{Z_1}^{A_1}\text{X}$, the state of a bound neutron of the atomic nucleus ${}_{Z_1}^{A_1}\text{X}$ and the states of centers of mass motion, is changed to first order due to the perturbation $V_{\text{Cb}}^{\text{dip}}$ according to stationary perturbation calculation as

$$\psi_i = \left[\psi_i^{(0)} + \sum_k a_{\text{bb},k} \psi_{k,\text{bb}}^{(0)} + \sum_k \int a_{\text{bf},k} \psi_{k,\text{bf}}^{(0)} d\nu_k + \int a_{\text{ff},k} \psi_{k,\text{ff}}^{(0)} d\nu_k \right] e^{-\frac{iE_i t}{\hbar}}. \quad (4)$$

Here E_i is the total initial energy, which includes the sum E_{0i} of the rest energies of the initial nuclei ${}_{Z_1}^{A_1}\text{X}$, ${}_{Z_2}^{A_2}\text{Y}$. $\psi_i^{(0)}$ is the product of the unperturbed bound electron and neutron states and two plane waves ψ_{CM,A_1} and ψ_{CM,A_2} which describe the motions of the centers of mass of the atoms having ${}_{Z_1}^{A_1}\text{X}$ and ${}_{Z_2}^{A_2}\text{Y}$ nucleus, respectively. $\psi_{k,\text{bb}}^{(0)}$ is the product of other bound electron and neutron states, ψ_{CM,A_1} and ψ_{CM,A_2} . In $\psi_{k,\text{bf}}^{(0)}$ one of the electron and neutron states is bound and the other is free which are multiplied by ψ_{CM,A_1} (in case of free electron) or by ψ_{CM,A_1-1} (in case of free neutron) and ψ_{CM,A_2} , where ψ_{CM,A_1-1} describes the motion of the center of mass of the atom having ${}_{Z_1}^{A_1-1}\text{X}$ nucleus. The last term is interesting from the point of view of our process and in $\psi_{k,\text{ff}}^{(0)}$ both the electron and the neutron are free and their product is multiplied by ψ_{CM,A_1-1} and ψ_{CM,A_2} . Accordingly, the last term in Eq. (4) can be written as

$$\delta\psi_{i,\text{free}} = \int \frac{V_{\text{Cb},ki}^{\text{dip}}}{E_i - E_k} \psi_{k,\text{ff}}^{(0)} d\nu_k e^{-\frac{iE_i t}{\hbar}}. \quad (5)$$

The sum of the energy of the free electron, neutron and center of mass states is E_k , which contains the sum E_{0k} of the rest energies and the state density is $d\nu_k$ [7].

Taking into account the interaction V_{st} between a free neutron and an other nucleus ${}_{Z_2}^{A_2}\text{Y}$ the second order transition rate has the form

$$W_{\text{fi}} = \frac{2\pi}{\hbar} \int \left| \int \frac{V_{\text{st},fk} V_{\text{Cb},ki}^{\text{dip}}}{E_i - E_k} d\nu_k \right|^2 \delta(E_i - E_f) d\nu_f. \quad (6)$$

Here $V_{\text{Cb},ki}^{\text{dip}}$ and $V_{\text{st},fk}$ are matrix elements of $V_{\text{Cb}}^{\text{dip}}$ and V_{st} with states $\psi_{k,\text{ff}}^{(0)}$, $\psi_i^{(0)}$ and $\psi_f^{(0)}$, $\psi_{k,\text{ff}}^{(0)}$, respectively. $\psi_f^{(0)}$ is the product of the free electron state of the nucleus ${}_{Z_1}^{A_1-1}\text{X}$, the bound neutron state of ${}_{Z_2}^{A_2+1}\text{Y}$ and free center of mass states of the two nuclei. The quantity $d\nu_f$ is the density of the final states of sum energy E_f , which comprises the sum E_{0f} of the rest energies of the final nuclei ${}_{Z_1}^{A_1-1}\text{X}$ and ${}_{Z_2}^{A_2+1}\text{Y}$. If the free states are plane waves of wave vectors \mathbf{k}_e , \mathbf{k}_1 and \mathbf{k}_2 corresponding to the wave vectors of the free electron, the ${}_{Z_1}^{A_1-1}\text{X}$ nucleus which has lost the neutron and the nucleus ${}_{Z_2}^{A_2+1}\text{Y}$ which has taken up the neutron then

$$d\nu_f = \frac{V^3}{(2\pi)^9} d\mathbf{k}_e d\mathbf{k}_1 d\mathbf{k}_2, d\nu_k = \frac{V}{(2\pi)^3} d\mathbf{k}_n, \quad (7)$$

where \mathbf{k}_n is the wave vector of the free (intermediate) neutron, and V is the volume of normalization. The initial wave vectors of atoms having nuclei ${}_{Z_1}^{A_1}\text{X}$ and ${}_{Z_2}^{A_2}\text{Y}$ are negligible. The nuclear energy difference Δ , that is the reaction energy, is distributed between the kinetic energies of the final free electron and the two final nuclei. All told, in process (1) the nucleus ${}_{Z_1}^{A_1}\text{X}$ loses a neutron which is taken up by the nucleus ${}_{Z_2}^{A_2}\text{Y}$ forming ${}_{Z_2}^{A_2+1}\text{Y}$ in this manner.

3. Cross Section of CICP-NE in Single Electron – Single Nucleon Model

The cross section σ_{bf} of the bound-free (bf) electron transitions of CICP-NE can be determined from the transition rate by the standard method. The evaluation of the transition rate is carried out in a one particle nuclear model. The hydrogen-like state of binding energy E_{Bi} and Coulomb-factor corrected plane wave are used as initial, bound and final, free electron states. The motion of the intermediate neutron and the two final nuclei are also described by plane waves. The rest masses of the two initial nuclei of mass numbers A_1 and A_2 are $m_1 = A_1 m_0$ and $m_2 = A_2 m_0$ where $m_0 c^2 = 931.494$ MeV is the atomic energy unit.

When calculating σ_{bf} , it is reasonable to use the

$$e^{i \frac{m_e}{(A_1-1)m_0} \mathbf{k}_1 \cdot \mathbf{x}_e} = 1$$

long wavelength approximation in the electron part of the Coulomb matrix element since

$$\frac{m_e}{(A_1 - 1) m_0} \ll 1.$$

The analysis of σ_{bf} shows that those processes give an essential contribution to the cross section in which $k_e \ll k_1$ and $k_e \ll k_2$ where k_e , k_1 and k_2 are the magnitudes of the wave vectors of \mathbf{k}_e , \mathbf{k}_1 and \mathbf{k}_2 . In this case as a consequence of momentum conservation the integration over \mathbf{k}_1 can be carried out resulting the substitution $\mathbf{k}_1 = -\mathbf{k}_2$. Thus E_f , which is the sum of the kinetic energies of the free electron, particle ${}_{Z_1}^{A_1-1}\text{X}$ and particle ${}_{Z_2}^{A_2+1}\text{Y}$, (in the Dirac-delta) and $E(k_e, k_2)$, which is the sum of the kinetic energies in the intermediate state (in the energy denominator) become $E_f = \hbar^2 k_e^2 / [2m_0 a_{12}] + \hbar^2 k_e^2 / (2m_e)$ with $a_{12} = (A_1 - 1)(A_2 + 1) / (A_1 + A_2)$ and

$$E(k_e, k_2) = \frac{A_1}{A_1 - 1} \hbar^2 k_2^2 / (2m_0) + \hbar^2 k_e^2 / (2m_e),$$

respectively (the intermediate neutron has wave vector $-\mathbf{k}_2$). These simplifications result

$$\sigma_{\text{bf}} = \left(\frac{2Z_1}{3A_1} V_0 \right)^2 \frac{\alpha_f^2 \hbar c^2}{v (2\pi)^3} \int \int \int \delta(E_f - \Delta_{\text{Bi}}) \frac{\left| \sum_{m=-1}^{m=1} I_{\text{ef}}^m(\mathbf{k}_e) I_1^m(\mathbf{k}_2) \right|^2 |I_2(\mathbf{k}_2)|^2 d\mathbf{k}_e d\mathbf{k}_2}{[E(k_e, k_2) + \Delta_n - \Delta_- + E_{\text{Bi}}]^2}, \quad (8)$$

where v is the relative velocity of the two atoms, c is the velocity of light (in vacuum),

$$I_{\text{ef}}^m(\mathbf{k}_e) = \int u_i(\mathbf{x}_e) Y_{1m}^*(\Omega_e) x_e^{-2} e^{-i\mathbf{k}_e \cdot \mathbf{x}_e} d\mathbf{x}_e, \quad (9)$$

$$I_1^m(\mathbf{k}_2) = \int \phi_i(\mathbf{x}_1) x_1 Y_{1m}(\Omega_1) e^{-i\mathbf{k}_2 \frac{A_1}{(A_1-1)} \cdot \mathbf{x}_1} d\mathbf{x}_1, \quad (10)$$

and

$$I_2(\mathbf{k}_2) = \int_{\Delta V} \phi_f^*(\mathbf{x}_2) e^{i\mathbf{k}_2 \cdot \mathbf{x}_2} d\mathbf{x}_2. \quad (11)$$

Here $u_i(\mathbf{x}_e)$ and $\phi_i(\mathbf{x}_1)$ are the initial bound electron and neutron states and $\phi_f(\mathbf{x}_2)$ is the final bound neutron state. α_f denotes the fine structure constant and \hbar is the reduced Planck-constant. $\Delta_n = 8.071$ MeV is the energy excess of the neutron. Furthermore, m_e is the rest mass of the electron and $\Delta_{\text{Bi}} = \Delta - E_{\text{Bi}}$. ΔV in $I_2(\mathbf{k}_2)$ is that volume of the surface of the second nucleus (of A_2) in which direct neutron capture may be assumed [8]. It can be considered as a shell of a sphere of radius R_{A_2} and of thickness L , where L is the mean free path of the ingoing neutron in the nucleus.

4. Cross Section of CICP – NE in Spherical Nuclear Shell Model

The bound, initial electron, the initial and final nuclear states, which are used, have the form:

$$u_i(\mathbf{x}_e) = R_i(x_e) Y_{js}(\Omega_e), \quad \phi_i(\mathbf{x}_1) = \varphi_i(x_1) Y_{l_i m_i}(\Omega_1)/x_1 \quad \text{and} \quad \phi_f(\mathbf{x}_2) = \varphi_f(x_2) Y_{l_f m_f}(\Omega_2)/x_2.$$

Here j and s are orbital angular momentum and magnetic quantum numbers of the bound electron state. $\varphi_i(x_1)/x_1$ and $\varphi_f(x_2)/x_2$ are the radial parts of the one particle shell-model solutions of quantum numbers l_i, m_i and l_f, m_f . In the cases to be investigated the corresponding part $R_{0\Lambda} = b_k^{-1/2} \Gamma(\Lambda + 3/2)^{-1/2} 2^{1/2} \rho_k^{\Lambda+1} \exp(-\rho_k^2/2)$ of 0Λ one particle spherical shell model states [9] is applied as $\varphi_i(x_1)$ and $\varphi_f(x_2)$. Here

$$\rho_k = x_k/b_k, \quad b_k = \left(\frac{\hbar}{m_0 \omega_{sh,k}} \right)^{1/2} \quad \text{and} \quad \hbar \omega_{sh,k} = 41 A_k^{-1/3}$$

(in MeV units, [6]) with $k = 1, 2$ corresponding to A_1 and A_2 , and $\Gamma(x)$ is the gamma function.

Thus in the case of spherical shell model states

$$\begin{aligned} \sigma_{\text{bf,sh}} &= \frac{32}{3v} \left(\frac{Z_1}{A_1} V_0 \right)^2 (2l_f + 1) \int \left| J_2^{l_f}(k_2) \right|^2 \\ &\times \int \sum_{l,\lambda} \frac{N_{l\lambda} \left| J_1^\lambda(k_2) \right|^2 \left| J_e^l(k_e) \right|^2}{[E(k_e, k_2) + \Delta_n - \Delta_- + E_{\text{Bi}}]^2} \alpha_f^2 \hbar c^2 \delta(E_f - \Delta_{\text{Bi}}) k_e^2 dk_e k_2^2 dk_2, \end{aligned} \quad (12)$$

where in case of $0l_f$ final nuclear state

$$\left| J_2^{l_f}(k_2) \right|^2 = \frac{\pi L^2 \rho_f^{2l_f+3} e^{-\rho_f^2} J_{l_f+\frac{1}{2}}^2(k_2 R_{A_2})}{\Gamma(l_f + \frac{3}{2}) k_2} \quad (13)$$

with $\rho_f = R_{A_2}/b_2$ and $J_{l_f+\frac{1}{2}}$ is a Bessel-function of the first kind. In the case of $0l_i$ initial nuclear state

$$J_1^\lambda(k_2) = \int R_{0l_i}(x_1) j_\lambda \left(\frac{A_1}{A_1-1} k_2 x_1 \right) x_1^2 dx_1, \quad (14)$$

$$J_e^l(k_e) = F_{\text{Cb}}^{1/2}(k_e) \int R_i(x_e) j_l(k_e x_e) dx_e, \quad (15)$$

$$N_{l\lambda} = (2l+1)(2\lambda+1) \begin{pmatrix} j & l & 1 \\ 0 & 0 & 0 \end{pmatrix}^2 \begin{pmatrix} l_i & 1 & \lambda \\ 0 & 0 & 0 \end{pmatrix}^2. \quad (16)$$

The parenthesized expressions are Wigner $3j$ symbols. In Eqs. (14) and (15) j_λ and j_l are spherical Bessel-functions of the first kind. (The suffix sh of any quantity denotes that it is calculated in the one particle spherical shell model.) In (15) $F_{\text{Cb}}(k_e)$ is the Coulomb factor.

We restrict ourselves to $1s$ initial electronic state of $R_i(x_e) = 2a^{-3/2} \exp(-x_e/a)$ with $a = a_0/Z_{\text{eff}}$, where a_0 is the Bohr-radius, $Z_{\text{eff}} = \sqrt{E_{\text{Bi}}/\text{Ry}}$ and Ry is the Rydberg energy and use the $F_{\text{Cb}}(k_e) = 2\pi/(k_e a)$ approximation. Since

$$j = 0 \quad \text{and} \quad (2l+1) \begin{pmatrix} 0 & 1 & l \\ 0 & 0 & 0 \end{pmatrix}^2 = \delta_{1,l},$$

$$N_{1\lambda} = (2\lambda + 1) \begin{pmatrix} l_i & 1 & \lambda \\ 0 & 0 & 0 \end{pmatrix}^2. \quad (17)$$

Keeping the leading term of $J_e^1(k_e)$, introducing $k_2 = k_0 x$, and carrying out integration over k_e with the aid of the energy-Dirac-delta and in the case of $l_i = \text{even}$ [$l_i = 2$; $\text{Ne}(3/2^+, 0d)$] to be investigated one obtains

$$\sigma_{\text{bf,sh}} = \frac{2^{10} \pi^3}{3v} \frac{Z_1^2 V_0^2}{A_1^2 \hbar^3} \frac{b_1^5 L^2}{a_0^2} m_0 a_{12} (2l_f + 1) \frac{\rho_f^{2l_f+3} e^{-\rho_f^2}}{\Gamma(l_f + \frac{1}{2})} \sum_{\lambda=l_i \pm 1} \frac{N_{1\lambda} (k_0 b_1)^{2\lambda}}{\Gamma(\lambda + \frac{3}{2})} S_\lambda. \quad (18)$$

Here $k_0 = \sqrt{2m_0 c^2 a_{12} \Delta_{\text{Bi}}} / (\hbar c)$,

$$S_\lambda = \int_0^1 f(x) g_\lambda(x) dx, \quad \text{with } x = k_2/k_0, \quad (19)$$

$$f(x) = \frac{(1-x^2) x^{2\lambda+1} e^{-(k_0 b_1)^2 x^2} J_{l_f + \frac{1}{2}}^2(x k_0 R_{A_2})}{\left[1 + \frac{\Delta_{\text{Bi}}}{E_{\text{B}}} (1-x^2)\right]^2 \left[\frac{A_1 a_{12}}{A_1 - 1} x^2 + 1 + \xi\right]^2} \quad (20)$$

and $\xi = (\Delta_n - \Delta_- + E_{\text{Bi}}) / \Delta_{\text{Bi}}$. In Eq. (19) $g_\lambda(x) = 1$ if $\lambda = l_i + 1$ and

$$g_\lambda(x) = (2l_i + 1)^2 - 2(2l_i + 1)(k_0 b_1 x)^2 + (k_0 b_1 x)^4 \quad (21)$$

if $\lambda = l_i - 1$.

The differential cross section $d\sigma_{\text{bf,sh}}/dE_2$ of the process can be determined with the aid of

$$P(x) = \sum_{\lambda=l_i \pm 1} \frac{N_{1\lambda} (k_0 b_1)^{2\lambda}}{\Gamma(\lambda + \frac{3}{2})} \frac{f(x) g_\lambda(x)}{x} \quad (22)$$

as $d\sigma_{\text{bf,sh}}/dE_2 = K_{\text{bf}} [P(x)]_{x=\sqrt{z}} / (2E_{20})$ where $z = E_2/E_{20}$ with $E_{20} = (A_1 - 1) \Delta_{\text{Bi}} / (A_1 + A_2)$, which is the possible maximum of the kinetic energy E_2 of particle ${}_{Z_2}^{A_2+1}\text{Y}$ created in the process, K_{bf} stands for the whole factor which multiplies the sum in (18). $d\sigma_{\text{bf,sh}}/dE_2$ has accountable values near below $z = 1$, i.e. if $E_2 \sim E_{20}$.

$d\sigma_{\text{bf,sh}}/dE_e = K_{\text{bf}} [P(x)]_{x=\sqrt{1-z}} / (2\Delta_{\text{Bi}})$ can also be determined with the aid of $P(x)$ where $z = E_e/\Delta_{\text{Bi}}$, E_e is the kinetic energy of the electron and K_{bf} is defined and is given above. $d\sigma_{\text{bf,sh}}/dE_e$ has accountable values near above $z = 0$, i.e. if $E_e \sim 0$.

5. Cooperative Internal Conversion Process by Proton Exchange

Now the cooperative internal conversion process by proton exchange (CICP-PE, process (2)) will be discussed. In this process (see Fig. 1) a bound proton of an atomic nucleus $\left({}_{Z_1}^{A_1}\text{X}, \text{particle } 2\right)$ is virtually excited into a free state (particle 3) due to the dipole term $V_{\text{Cb}}^{\text{dip}}$ of its Coulomb-interaction (in electric dipole coupling the proton has effective charge $q_p = (1 - Z_1/A_1) e$ [6]) with one of the bound atomic electrons (e_1) of the atom containing the ${}_{Z_1}^{A_1}\text{X}$ nucleus while the electron becomes free (e_1'). The free, virtual proton is captured by an other nucleus ${}_{Z_2}^{A_2}\text{Y}$ (particle 4) due to its nuclear potential V_{st} (created by strong interaction) forming the nucleus ${}_{Z_2+1}^{A_2+1}\text{W}$ (particle 5) in this way. The sum of the rest energies of the initial nuclei is E_{0i} and the sum of the the rest energies of the final nuclei is E_{0f} . If $E_{0i} - E_{0f} = \Delta > 0$, i.e. if $E_{0i} > E_{0f}$, then the process is energetically allowed and proton exchange is possible. The nuclear energy difference Δ , which is the reaction energy, is shared between the kinetic energies of the final, free electron and the two final nuclei [${}_{Z_1-1}^{A_1-1}\text{V}$ (particle 2') is the nucleus which has lost the proton].

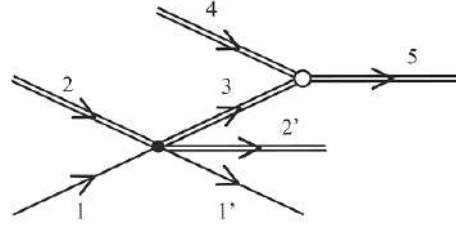


Figure 1. Graph of the cooperative internal conversion process by a heavy charged particle (e.g. proton) exchange. Particle 1 (bound) and 1' (free) are electrons, particle 2 is the nucleus which loses the heavy charged particle (e.g. proton) and becomes particle 2'. Particle 3 is the intermediate heavy charged particle (e.g. proton). Particle 4 is the nucleus which absorbs the heavy charged particle (e.g. proton) and becomes particle 5. The filled dot denotes (in case of a proton the dipole term of) the Coulomb-interaction and the open circle denotes nuclear (strong) interaction.

The transition rate and the cross section σ_{bf} of CICP-PE with bound-free (bf) electron transitions can also be determined with the aid of a standard second-order perturbation calculation of quantum mechanics. (The cross section of CICP-PE with bound-bound electron transition is neglected since it has proved to be much smaller than σ_{bf} .) The calculation of σ_{bf} is similar to the calculation of CICP-NE. The difference is the appearance of the square of the two Coulomb factors $f_{2'3}$ and f_{34} which ($f_{2'3}^2$ and f_{34}^2) multiply the cross section and Δ_n , $\frac{Z_1}{A_1}$ are changed to Δ_p , $(1 - \frac{Z_1}{A_1})$, respectively. $\Delta_p = 7.288969$ MeV is the energy excess of the proton. ($f_{2'3}$ and f_{34} are determined in the Appendix, see (A.1).) The dipole term of the Coulomb interaction reads as

$$V_{Cb}^{dip} = \left(1 - \frac{Z_1}{A_1}\right) e^2 \frac{4\pi}{3} x_1 x_e^{-2} \sum_{m=-1}^{m=1} Y_{1m}^*(\Omega_e) Y_{1m}(\Omega_1),$$

where x_1 and Ω_1 are magnitude and solid angle of vector \mathbf{x}_1 which is the coordinate of the proton in the first atom. (The order of magnitude of the cross section produced by the L -th pole coupling is $(R/r)^{2L-2}$ times smaller than the cross section produced by the dipole coupling where R and r are the nuclear and atomic radii. Therefore the leading term to the cross section is produced by the dipole coupling.) The motion of the intermediate proton and the two final nuclei are also described by plane waves.

Introducing the wave vectors \mathbf{k}_e and \mathbf{k}_1 , \mathbf{k}_2 of the free electron and particles $\frac{A_1-1}{Z_1-1}V$ (particle 2') and $\frac{A_2+1}{Z_2+1}W$ (particle 5), respectively, the analysis of σ_{bf} shows that, similarly to the CICP-NE, those processes give essential contribution to the cross section in which $k_e \ll k_1$ and $k_e \ll k_2$ where k_e , k_1 and k_2 are the magnitudes of the wave vectors of \mathbf{k}_e , \mathbf{k}_1 and \mathbf{k}_2 . (In this case as a consequence of momentum conservation $\mathbf{k}_1 = -\mathbf{k}_2$, furthermore the intermediate proton has wave vector $-\mathbf{k}_2$.)

The initial and final nuclear states are one particle shell-model solutions of quantum numbers l_i, m_i and l_f, m_f . The case of spherical shell model states of $0l_i$ initial nuclear state and of $0l_f$ final nuclear state is investigated.

Also keeping the leading term of $J_e^1(k_e)$, in the one particle spherical shell model and in the case of $l_i = \text{even}$ [$l_i = 2; A1(5/2^+, 0d)$] to be investigated one obtains

$$\sigma_{bf,sh} = \frac{2^{10}\pi^3}{3v} \left(1 - \frac{Z_1}{A_1}\right)^2 \frac{V_0^2 b_1^5 L^2}{\hbar^3 a_0^2} m_0 a_{12} (2l_f + 1) \frac{\rho_f^{2l_f+3} e^{-\rho_f^2}}{\Gamma(l_f + \frac{1}{2})} \sum_{\lambda=l_i\pm 1} \frac{N_{1\lambda} (k_0 b_1)^{2\lambda}}{\Gamma(\lambda + \frac{3}{2})} S_{\lambda 2}. \quad (23)$$

Here

$$S_{\lambda 2} = \int_0^1 f(x) g_{\lambda}(x) h_{2'3}(x) h_{34}(x) dx, \quad (24)$$

$$f(x) = \frac{(1-x^2) x^{2\lambda+1} e^{-(k_0 b_1)^2 x^2} J_{l_f + \frac{1}{2}}^2(x k_0 R_{A_2})}{\left[1 + \frac{\Delta_{\text{Bi}}}{E_{\text{B}}} (1-x^2)\right]^2 \left[\frac{A_1 \alpha_{12}}{A_1 - 1} x^2 + 1 + \xi\right]^2}, \quad (25)$$

$x = k_2/k_0$, and $\xi = (\Delta_{\text{p}} - \Delta_{-} + E_{\text{Bi}})/\Delta_{\text{Bi}}$. In (24) $h_{jk}(x) = d_{jk}(x)/[\exp(d_{jk}(x)) - 1]$, $j, k = 2', 3$ and $3, 4$ ($f_{2'3}^2$ and f_{34}^2 , see (A.1) in the Appendix) with

$$d_{2'3}(x) = 2\pi(Z_1 - 1)\alpha_f \frac{1}{x} \sqrt{\frac{(A_1 + A_2) m_0 c^2}{2A_1(A_2 + 1)\Delta_{\text{Bi}}}} \quad (26)$$

and

$$d_{34}(x) = 2\pi Z_2 \alpha_f \frac{1}{x} \sqrt{\frac{(A_1 + A_2) m_0 c^2}{2(A_1 - 1)(A_2 + 1)\Delta_{\text{Bi}}}} \quad (27)$$

(see (A.4) and (A.6) in the Appendix).

The quantities $d\sigma_{\text{bf,sh}}/dE_2$ and $d\sigma_{\text{bf,sh}}/dE_e$ can also be determined with the aid of

$$P(x) = \sum_{\lambda=l_i \pm 1} \frac{N_{1\lambda} (k_0 b_1)^{2\lambda}}{\Gamma(\lambda + \frac{3}{2})} \frac{f(x) g_{\lambda}(x) h_1(x) h_2(x)}{x} \quad (28)$$

but now K_{bf} stands for the whole factor which multiplies the sum in (23). $d\sigma_{\text{bf,sh}}/dE_2$ has accountable values if $E_2 \sim E_{20}$ and $d\sigma_{\text{bf,sh}}/dE_e$ has accountable values if $E_e \sim 0$.

6. Total Rate Per Unit Volume

The transition rate λ_1 of CICIP of one nucleus of mass number A_1 of an atomic gas of number density n created by all those isotopes of mass number A_2 for which CICIP is allowed, is expressed in the spherical shell model in the $\sigma_{\text{bf}} = \sigma_{\text{bf,sh}}$ approximation as $\lambda_1 = n \sum_{A_2} r_{A_2} v \sigma_{\text{bf,sh}}$. Here r_{A_2} is the relative natural abundance of isotope of mass number A_2 (in the cases of Ne and Al to be investigated the $A_2 = A_1$ event is only possible). Furthermore $\tau_{1/2,1} = \ln 2/\lambda_1$, which can be considered as a half-life.

The quantity $r_{A_1} n \lambda_1$ is the rate per unit volume of the sample produced by the nuclei of mass number A_1 which take part as initial nuclei in CICIP, and $r_{\text{tot}} = \sum_{A_1} r_{A_1} n \lambda_1$, which is the total rate per unit volume of the sample.

If the participating atoms are in the same solid then the cross sections are multiplied by the so-called Debye–Waller factor [10]. The analysis of (8), (12), (18) and (23) modified accordingly shows that the cross section and consequently the transition rate drastically drop due to the Debye–Waller factor and the phenomenon (CICIP) becomes unobservable. In the case of diatomic molecules the appearance of a factor $\exp(-\beta^2 r_a^2/4)$ in the cross section and the transition rate leads to the same result. (Here r_a is the distance between the two nuclei in equilibrium position and $\beta = \sqrt{\mu\omega/\hbar}$ were μ is the reduced mass of the two vibrating atoms and ω is the angular frequency of vibration.) One can draw the conclusion that the phenomenon (CICIP) is mainly related to atomic state, i.e. CICIP can have an observable rate if either of the participating atoms is in atomic state or they belong to different clusters (solids, molecules).

7. Numerical Calculation in Case of Ne (CICP-NE)

In the numerical calculation $V_0 = 50$ MeV is used [6]. In the case of Ne only the $e + {}^{21}_{10}\text{Ne} + {}^{21}_{10}\text{Ne} \rightarrow e' + {}^{20}_{10}\text{Ne} + {}^{22}_{10}\text{Ne} + \Delta$ reaction of $\Delta = 3.603$ MeV is allowed. CICP-NE does not work in Ar since all the possible channels are energetically forbidden. On the other hand in the case of Kr and Xe nuclei the applicability of the spherical shell model may be in doubt. For Ne the transition rate is estimated as $\lambda_1 > \lambda_1(K)$, which is the transition rate of the bound-free CICP-NE from the K shell of Ne. The initial and final states of ${}^{21}\text{Ne}$ and ${}^{22}\text{Ne}$ are supposed to be $0d$ spherical shell model states of $l_i = l_f = 2$, $r_{A_1} = r_{A_2} = r_{21} = 0.0027$, and $\Delta_- = 1.310$ MeV. The electron binding energy in the K shell is $E_{\text{Bi}} = 870.1$ eV. ($2E_{20} = 3.26$ MeV and $K_{\text{bf}}/(2E_{20}) = 4.77 \times 10^{-25} \text{ cm}^3\text{s}^{-1}\text{MeV}^{-1}/v$). $v\sigma_{\text{bf,sh}}(K) = 2.48 \times 10^{-34} \text{ cm}^3\text{s}^{-1}$ is obtained in the case of bound-free CICP-NE from the K shell of Ne. Taking this, the $\lambda_1 > 1.8 \times 10^{-17} \text{ s}^{-1}$ and $\tau_{1/2,1} < 3.8 \times 10^{16} \text{ s}$ ($1.2 \times 10^9 \text{ y}$) and $r_{\text{tot}} > 1.25 \text{ cm}^{-3}\text{s}^{-1}$ for a gas of normal state ($n = 2.652 \times 10^{19} \text{ cm}^{-3}$). The estimated half life is so long that the decay through CICP-NE does not alter natural abundance of Ne in observable measure. However, the rate is high enough to be measurable. ${}^{20}_{10}\text{Ne}$ and ${}^{22}_{10}\text{Ne}$ are mostly formed with energy near below

$$E_{10} = \frac{A_1 + 1}{A_1 + A_2} \Delta_{\text{Bi}} = 1.97 \text{ MeV} \quad \text{and} \quad E_{20} = \frac{A_1 - 1}{A_1 + A_2} \Delta_{\text{Bi}} = 1.63 \text{ MeV}$$

and with wave vectors of opposite direction. Therefore, it is plausible to observe their creation in coincidence measurement.

8. Numerical Calculation in Case of Al (CICP-PE)

It is a special case of process (2) when the two initial nuclei are identical. In this case the CICP-PE reads as

$$e_1 + \frac{A_1}{Z_1}X + \frac{A_1}{Z_1}X \rightarrow e'_1 + \frac{A_1-1}{Z_1-1}V + \frac{A_1+1}{Z_1+1}W + \Delta. \quad (29)$$

For example of such a case the reaction $e + {}^{27}_{13}\text{Al} + {}^{27}_{13}\text{Al} \rightarrow e' + {}^{26}_{12}\text{Mg} + {}^{28}_{14}\text{Si} + \Delta$ is considered when the reaction starts from the K shell. The initial and final nuclear states are supposed to be $0d$ spherical shell model states of $l_i = l_f = 2$, $\Delta = 3.31362$ MeV. The electron binding energy in the K shell is $E_{\text{Bi}} = 1.5596$ keV and $\Delta_- = -0.98235$ MeV. In this case $v\sigma_{\text{bf,sh}}(K) = 7.23 \times 10^{-36} \text{ cm}^3\text{s}^{-1}$ is obtained in the case of bound-free CICP-PE from the K shell of Al. If one compares this result with $v\sigma_{\text{bf,sh}}(K) = 2.48 \times 10^{-34} \text{ cm}^3\text{s}^{-1}$ obtained in the case of CICP-NE in Ne one can recognize that the ratio of the two cross sections is only 0.029. At first sight it seems to be larger than expected since two Coulomb factors appear in the cross section. But as it was said earlier the intermediate proton has wave vector $-\mathbf{k}_2$ and thus its energy $E_3 = \hbar^2\mathbf{k}_2^2/(2m_0)$ with $\hbar k_2 = \hbar k_0 x = x\sqrt{2m_0\Delta_{\text{Bi}}a_{12}}$. It gives $E_3 = x^2\Delta_{\text{Bi}}A_1/2$ since $a_{12} = A_1/2$ if $A_1 = A_2$ and near below $x = 1$ the value of E_3 is large enough to result moderately small Coulomb factors.

For a gas of atomic Al and of number density n the rate $\lambda_1 = n \sum_{A_2} r_{A_2} v\sigma_{\text{bf,sh}} = nv\sigma_{\text{bf,sh}}$ since the relative natural abundance r_{A_2} of the initial ${}^{27}_{13}\text{Al}$ isotope equals unity. λ_1 is estimated as $\lambda_1 > \lambda_1(K)$, which is the transition rate of the bound-free CICP-PE from the K shell of Al ($\lambda_1(K) = nv\sigma_{\text{bf,sh}}(K)$), resulting $\lambda_1 > 1.92 \times 10^{-16} \text{ s}^{-1}$ and $r_{\text{tot}} > 5.08 \times 10^3 \text{ cm}^{-3}\text{s}^{-1}$ for a gas of normal state ($n = 2.652 \times 10^{19} \text{ cm}^{-3}$ and $r_{\text{tot}} = n\lambda_1$, which is the total rate per unit volume of the sample, in this case since $r_{A_1} = 1$).

9. Other Results and Discussion

Although the λ_1 obtained for Ne and Al is rather small, the Weisskopf-estimation of the cross section indicates that it, and consequently λ_1 , may be increased very much with the increase of the atomic number. Moreover, the magnitudes of σ_{bf} and λ_1 are very sensitive to the model applied, e.g. if neutron or proton capture of the nucleus of A_2 is not

Table 1. Data for cooperative internal conversion process by neutron exchange of long lived nuclear fission products. (Data to reaction (1).) $A - 1$ and $A + 1$ are the mass numbers of the two final isotopes, τ is the half-life of the fission product in year units. For the definition of Δ_- and Δ_+ see the text.

Isotope	τ (year)	$A - 1, A + 1$	Δ_- (MeV)	Δ_+ (MeV)
^{113m}Cd	14.1	112, 114	1.795	1.235
^{121m}Sn	55	120, 122	1.907	0.749
^{151}Sm	90	150, 152	2.475	0.186
^{79}Se	6.5×10^4	78, 80	1.108	1.842
^{93}Zr	1.53×10^6	92, 94	1.337	0.149
^{107}Pd	6.5×10^6	106, 108	1.533	1.149

restricted to the direct reaction then the integral in $I_2(\mathbf{k}_2)$ must be carried out over the whole volume of the nucleus. In this case $\sigma_{\text{bf,sh}}$ and λ_1 are increased by a factor of about 240 for Ne. Furthermore, λ_1 can essentially increase e.g. with the increase of n . Therefore, contrary to the smallness of the value of λ_1 obtained in the cases of Ne and Al, CICP-NE and CICP-PE could play a role in the problem of nuclear waste disposal.

In Tables 1 and 2 some long lived fission products are listed which can take part in CICP-NE and CICP-PE, respectively. The values of Δ_- and Δ_+ indicate that each pair of isotopes chosen from either of the two tables can produce CICP-NE or CICP-PE since $\Delta_- + \Delta_+ = \Delta > 0$ in every case. Consequently, it seems there may be a practical chance to accelerate the decay of the listed isotopes if they are collected in appropriately high concentration and density in atomic state. This is, however, a great technical challenge.

A special family of CICP-NE reactions – the $e + d + \frac{A}{Z}\text{X} \rightarrow e' + p + \frac{A}{Z}^{+1}\text{X} + \Delta$ reaction family – is worth mentioning. The quantity $\Delta_-(\text{dp}) = \Delta_d - \Delta_p = 5.846$ MeV, which is characteristic of neutron loss of the deuteron. Here Δ_d and Δ_p are mass excesses of d and p. The energy of the reaction is $\Delta = \Delta_-(\text{dp}) + \Delta_+$ and some specific reactions together with their Δ_+ and Δ values are listed in Table 3. (This is not a complete list.) Chances are that these reactions may open new perspectives in the field of nuclear energy production.

In Table 4. the Δ_- , Δ_+ and Δ data of some cooperative internal conversion processes by proton exchange (data to reaction (2)) can be found. In the first column the initial stable isotope of relative natural abundance unity and in the second column the reaction products are listed.

There are other possibilities to realize CICP, when a charged heavy particle (such as d, t, ^3_2He and ^4_2He) is exchanged instead of proton exchange. The process is called cooperative internal conversion process by heavy charged particle exchange (CICP-HCPE) and it can be visualized with the aid of Fig.1 too. Denoting the intermediate particle (particle 3 in Fig. 1) by $^{A_3}_{z_3}\text{w}$, which is exchanged, the cooperative internal conversion process by heavy charged particle exchange reads as

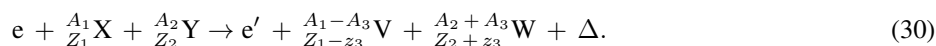


Table 2. Data for the cooperative internal conversion process by proton exchange of long lived nuclear fission products. (Data to reaction (2).) Products are the two stable final isotopes, τ is the half-life of the fission product in year units. For the definition of Δ_- and Δ_+ see the text.

Isotope	τ (year)	Products	Δ_- (MeV)	Δ_+ (MeV)
^{99}Tc	2.11×10^5	$^{98}\text{Mo}, ^{100}\text{Ru}$	0.789	1.896
^{129}I	1.57×10^7	$^{128}\text{Te}, ^{130}\text{Xe}$	0.491	1.378
^{135}Cs	2.3×10^6	$^{134}\text{Xe}, ^{136}\text{Ba}$	0.538	1.305
^{137}Cs	30.07	$^{136}\text{Xe}, ^{138}\text{Ba}$	-0.126	1.716
^{155}Eu	4.7611	$^{154}\text{Sm}, ^{156}\text{Gd}$	0.637	0.717

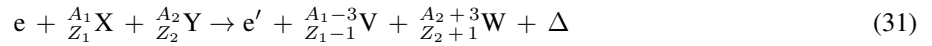
Table 3. The values of the quantities $\Delta_+(A)$ and $\Delta = \Delta_-(dp) + \Delta_+(A)$ of the $e + d + {}^A_ZX \rightarrow e' + p + {}^{A+1}_ZX + \Delta$ reaction. r_A is the natural abundance of the isotope. $\Delta_-(dp) = \Delta_d - \Delta_p = 5.846$ MeV, Δ_d and Δ_p are mass excesses of d and p.

Isotope	r_A	$\Delta_+(A)$ (MeV)	Δ (MeV)
${}^9_4\text{Be}$	1.0	-1.259	4.587
${}^{10}_5\text{B}$	0.199	3.382	9.228
${}^{11}_5\text{B}$	0.812	-4.701	1.145
${}^{12}_6\text{C}$	0.989	-3.125	2.721
${}^{13}_6\text{C}$	0.011	0.105	5.951
${}^{14}_7\text{N}$	0.99634	2.762	8.608
${}^{15}_7\text{N}$	0.00366	-5.581	0.265
${}^{16}_8\text{O}$	0.99762	-3.928	1.918
${}^{17}_8\text{O}$	0.00038	-0.027	5.819

Here e and e' denote bound and free electron and Δ is the energy of the reaction, i.e. the difference between the rest energies of initial $\left({}^{A_1}_{Z_1}X + {}^{A_2}_{Z_2}Y\right)$ and final $\left({}^{A_1-A_3}_{Z_1-z_3}V + {}^{A_2+A_3}_{Z_2+z_3}W\right)$ states. $\Delta = \Delta_- + \Delta_+$, with $\Delta_- = \Delta_{Z_1}^{A_1} - \Delta_{Z_1-z_3}^{A_1-A_3}$ and $\Delta_+ = \Delta_{Z_2}^{A_2} - \Delta_{Z_2+z_3}^{A_2+A_3}$. $\Delta_{Z_1}^{A_1}$, $\Delta_{Z_1-z_3}^{A_1-A_3}$, $\Delta_{Z_2}^{A_2}$, $\Delta_{Z_2+z_3}^{A_2+A_3}$ are the energy excesses of neutral atoms of mass number–charge number pairs A_1, Z_1 ; $A_1 - A_3, Z_1 - z_3$; A_2, Z_2 ; $A_2 + A_3, Z_2 + z_3$, respectively [5].

In process (30) the initial bound electron (particle 1) Coulomb interacts with the nucleus ${}^{A_1}_{Z_1}X$ (particle 2). A free electron (particle 1'), the intermediate particle ${}^{A_3}_{z_3}w$ (particle 3) and the nucleus ${}^{A_1-A_3}_{Z_1-z_3}V$ (particle 2') are created due to this interaction. The intermediate particle ${}^{A_3}_{z_3}w$ (particle 3) is captured due to the strong interaction by the nucleus ${}^{A_2}_{Z_2}Y$ (particle 4) forming the nucleus ${}^{A_2+A_3}_{Z_2+z_3}W$ (particle 5) in this manner. So in process (30) the nucleus ${}^{A_1}_{Z_1}X$ (particle 2) loses a particle ${}^{A_3}_{z_3}w$ which is taken up by the nucleus ${}^{A_2}_{Z_2}Y$ (particle 4). The process is energetically forbidden if $\Delta < 0$.

As an example we deal with the



reaction in which a triton is exchanged. It is called CICIP by triton exchange (CICIP-TE). A special type of reaction (31) is

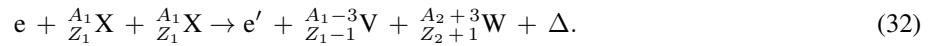


Table 4. Data for cooperative internal conversion process by proton exchange. (Data for reaction (2).) In the first column the initial stable isotope and in the second column the reaction products can be found. For the definition of Δ_- , Δ_+ and Δ see the text.

Isotope	Products	Δ_- (MeV)	Δ_+ (MeV)	Δ (MeV)
${}^{19}\text{F}$	${}^{18}\text{O}, {}^{20}\text{Ne}$	-0.705	5.555	4.850
${}^{23}\text{Na}$	${}^{22}\text{Ne}, {}^{24}\text{Mg}$	-1.505	4.404	2.899
${}^{27}\text{Al}$	${}^{26}\text{Mg}, {}^{28}\text{Si}$	-0.982	4.296	3.314
${}^{31}\text{P}$	${}^{30}\text{Si}, {}^{32}\text{S}$	-0.008	1.575	1.567
${}^{45}\text{Sc}$	${}^{44}\text{Ca}, {}^{46}\text{Ti}$	0.400	3.056	3.456
${}^{55}\text{Mn}$	${}^{54}\text{Cr}, {}^{56}\text{Fe}$	-0.778	2.895	2.117
${}^{59}\text{Co}$	${}^{58}\text{Fe}, {}^{60}\text{Ni}$	-0.075	2.245	2.170
${}^{103}\text{Rh}$	${}^{102}\text{Ru}, {}^{104}\text{Pd}$	1.076	1.369	2.445
${}^{127}\text{I}$	${}^{126}\text{Te}, {}^{128}\text{Xe}$	1.083	0.873	1.956
${}^{133}\text{Cs}$	${}^{132}\text{Xe}, {}^{134}\text{Ba}$	1.204	0.879	2.083

Table 5. Data for the cooperative internal conversion process by triton exchange. (Data to reaction (32).) In the first column the initial stable isotope and in the second column the reaction products can be found. For the definition of Δ_- , Δ_+ and Δ see the text.

Isotope	Products	Δ_- (MeV)	Δ_+ (MeV)	Δ (MeV)
^{19}F	$^{16}\text{O}, ^{22}\text{Ne}$	3.250	6.537	9.787
^{23}Na	$^{20}\text{Ne}, ^{26}\text{Mg}$	-2.488	6.685	4.197
^{27}Al	$^{24}\text{Mg}, ^{30}\text{Si}$	-3.263	7.236	3.973
^{31}P	$^{28}\text{Si}, ^{34}\text{S}$	-2.948	5.491	2.543
^{45}Sc	$^{42}\text{Ca}, ^{48}\text{Ti}$	-2.522	7.418	4.896
^{55}Mn	$^{52}\text{Cr}, ^{58}\text{Fe}$	-2.294	4.443	2.149
^{59}Co	$^{56}\text{Fe}, ^{62}\text{Ni}$	-1.623	4.519	2.896
^{103}Rh	$^{100}\text{Ru}, ^{106}\text{Pd}$	1.197	1.882	3.079
^{127}I	$^{124}\text{Te}, ^{130}\text{Xe}$	1.536	0.893	2.429
^{133}Cs	$^{130}\text{Xe}, ^{136}\text{Ba}$	1.806	0.816	2.622

In Table 5, the Δ_- , Δ_+ and Δ data of some cooperative internal conversion processes by triton exchange (data to reaction (32)) can be found.

10. Summary

In this paper the cooperative internal conversion process (CICP) is discussed. It is shown that the Coulomb interaction between bound electrons and the nucleons of a nucleus may lead to exchange of one or more nucleons between two nuclei which are located in different atoms. The cross sections of CICP with neutron and proton exchange are calculated and the qualitatively extended mechanism also shows the possibility of many nucleon (such as d, t, ^3_2He and ^4_2He) exchange. There is a chance that CICP may accelerate the decay of long lived isotopes, e.g. long-lived nuclear fission products. Moreover, it was found that special types of CICP with neutron exchange of deuterons with other nuclei may open new perspectives in the field of nuclear energy production. In conclusion, the results indicate that CICP seems to be able to significantly modify nuclear processes.

Appendix A. Square of Coulomb Factors ($f_{2'3}^2$ and f_{34}^2)

Since particles 2', 3 and 4 all have positive charge, and furthermore they are all heavy, the square of the two essential Coulomb factors $f_{2'3}$ and f_{34} appears in the cross section. Since $f_{2'3}^2$ and f_{34}^2 determine the order of magnitude of the cross section of the process (as it is proportional to $f_{2'3}^2 f_{34}^2$) we treat them in more detail in the case of CICP-PE in the following.

The wave function $\varphi(\mathbf{r})$ of a free particle of charge number z_j in a repulsive Coulomb field of charge number z_k [11] (called Coulomb solution) has the following property: $\varphi(\mathbf{r}) \sim e^{-\pi\eta_{jk}/2}\Gamma(1 + i\eta_{jk})$, where Γ is the Gamma function. The quantity

$$\left| e^{-\pi\eta_{jk}/2}\Gamma(1 + i\eta_{jk}) \right| = \sqrt{\frac{2\pi\eta_{jk}(E)}{\exp[2\pi\eta_{jk}(E)] - 1}} = f_{jk}(E) \quad (\text{A.1})$$

is the Coulomb factor. Here

$$\eta_{jk}(E) = z_j z_k \alpha_f \sqrt{a_{jk} \frac{m_0 c^2}{2E}} \quad (\text{A.2})$$

is the Sommerfeld parameter.

$$a_{jk} = \frac{A_j A_k}{A_j + A_k} \quad (\text{A.3})$$

is the reduced mass number of particles j and k of mass numbers A_j , A_k and E is taken in the center of mass (CM) coordinate system.

If initial particles have negligible initial momentum then in the final state $\mathbf{k}_1 = -\mathbf{k}_2$ ($\mathbf{k}_{\text{particle},2'} = -\mathbf{k}_{\text{particle},5}$) because of momentum conservation. (We have determined that the process has an accountable cross section if the momentum of the final electron can be neglected.) In this case the momentum and energy of the virtual particle 3 (e.g. proton) are $\mathbf{k}_{\text{particle},3} = -\mathbf{k}_{\text{particle},2'} = \mathbf{k}_{\text{particle},5} \equiv \mathbf{k}_2$ and $E_3 = \hbar^2 \mathbf{k}_2^2 / (2m_3)$, where \hbar is the reduced Planck-constant. Calculating the Coulomb factor $f_{2'3}$ (see (A.1)) between particles 2' and 3 the energy E_3 is given in their CM coordinate system (since $\mathbf{k}_{\text{particle},3} = -\mathbf{k}_{\text{particle},2'}$) thus E_3 can be substituted directly in (A.2) producing

$$\eta_{2'3} = (Z_1 - 1) \alpha_f \frac{1}{x} \sqrt{\frac{(A_1 + A_2) m_0 c^2}{2A_1 (A_2 + 1) \Delta_{\text{Bi}}}} \quad (\text{A.4})$$

in case of proton exchange. Here the $k_2 = k_0 x$ substitution is also used. Calculating f_{34} , the energy E_3 of particle 3 is now given in the laboratory frame of reference since particle 4 is at rest. In the CM system of particles 3 and 4 the energy $E_3(\text{CM})$ is

$$E_3(\text{CM}) = \frac{A_{\text{particle},4}}{(A_{\text{particle},3} + A_{\text{particle},4})} E_3. \quad (\text{A.5})$$

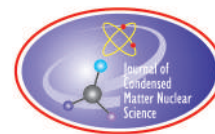
Substituting it into (A.2)

$$\eta_{34} = Z_2 \alpha_f \frac{1}{x} \sqrt{\frac{(A_1 + A_2) m_0 c^2}{2(A_1 - 1)(A_2 + 1) \Delta_{\text{Bi}}}} \quad (\text{A.6})$$

in case of proton exchange.

References

- [1] J. H. Hamilton, *Internal Conversion Processes*, Academic Press, New York, 1966.
- [2] A. Huke, K. Czerski, P. Heide, G. Ruprecht, N. Targosz and W. Zebrowski, *Phys. Rev. C* **78** (2008) 015803.
- [3] P. Kálmán and T. Keszthelyi, *Phys. Rev. C* **69** (2004) 031606(R).
- [4] P. Kálmán and T. Keszthelyi, *Phys. Rev. C* **79** (2009) 031602(R).
- [5] R.B. Firestone and V.S. Shirly, *Tables of Isotopes*, 8th Edn., Wiley, New York, 1996.
- [6] W. Greiner and J.A. Maruhn, *Nuclear Models*, Springer, Berlin-Heidelberg, 1996.
- [7] L.D. Landau and E.M. Lifsic, *Quantum Mechanics, Non-relativistic Theory*, 3rd Edn., in *Course of Theoretical Physics*, Vol. 3, Chapter 43, Pergamon Press, Oxford, 1977.
- [8] J.M. Blatt and V.F. Weisskopf, *Theoretical Nuclear Physics*, Wiley, New York, 1952.
- [9] M.K. Pal, *Theory of Nuclear Structure*, Scientific and Academic, New York, 1983.
- [10] C. Kittel, *Quantum Theory of Solids*, 2nd Edn., Ch. 19, Wiley, New York, 1964.
- [11] K. Alder, A. Bohr, T. Huus, B. Mottelson and A. Winther, *Rev. Mod. Phys.* **28** (1956) 432–542.



Research Article

Recoil Assisted Low Energy Nuclear Reactions

Péter Kálmán*, and Tamás Keszthelyi

Budapest University of Technology and Economics, Institute of Physics, Budafoki út 8. F., H-1521 Budapest, Hungary

Abstract

Low energy nuclear processes, which are strongly hindered by Coulomb repulsion between the reacting nuclei, are investigated in solid environment. It is shown that this hindering effect may be essentially weakened (it practically disappears) if one takes into account the Coulomb interaction of one of the reacting particles with the surroundings. It is obtained that if the modification of the wave function due to Coulomb interaction with charged constituents of the environment is taken into account applying standard perturbation calculation of quantum mechanics then waves of high momentum with small amplitude are mixed to the initial wave of small momentum. This may be interpreted as the slow, quasi-free heavy particle of positive charge pushes a heavy particle of the environment and they can obtain (virtually) such a great magnitude of momentum (of opposite direction) in the intermediate state in that the probability of nuclear reaction with another positively charged, slow, heavy particle significantly increases. This magnitude of (virtual) momentum is determined by energy and momentum conservation between initial and final states. The mechanism (called recoil assistance) opens the door to a great variety of nuclear processes that are now thought to have negligible rate at low energies. The recoil assisted nuclear *pd* reaction is investigated like a sample reaction numerically. A partial overview of low energy nuclear reactions allowed by recoil assistance and leading to nuclear transmmutations is presented. A critical analysis of Fleischmann–Pons type low energy nuclear reaction experiments is also presented.

© 2017 ISCMNS. All rights reserved. ISSN 2227-3123

Keywords: Fusion and fusion–fission reactions, ^2H -induced nuclear reactions, Nucleon induced reactions

1. Introduction

Since the publication of “cold fusion” by Fleischmann and Pons in 1989 [1] a new field of experimental physics has emerged. Although even the possibility of the phenomenon of nuclear fusion at low energies is in doubt in mainstream physics, the quest for low-energy nuclear reactions (LENR) is on and hundreds of publications (mostly experimental) have been devoted to various aspects of the problem. (For a summary of experimental observations, theoretical efforts and background events, see e.g. [2–4].)

The main reasons for revulsion against the topic according to standard nuclear physics have been: (a) due to the Coulomb repulsion no nuclear reaction should take place at energies corresponding to room temperature, (b) the observed excess heat attributed to nuclear reactions is not accompanied by the nuclear end products expected from hot

*E-mail: kalmanpeter3@gmail.com.

fusion, (c) traces of nuclear transmutations were also observed. Considering the repulsive Coulomb interaction, that is an even more inexplicable fact at these energies. It also bodes against acceptance of the phenomenon that (d) its reproduction seems to be uncertain. It is evident that these serious questions must be at least qualitatively answered in order to transfer the field back into proper science.

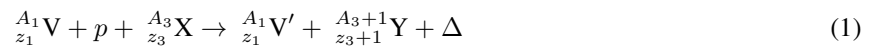
Moreover, the phenomenon is strongly associated with the hope for a practical source of energy for society. People who deal with the phenomenon have often said their aim is to construct practical generators with cold fusion. This association is disturbing. (Although the theoretical ground of hot fusion is clear the technical realization of a power supply based on hot fusion has been pushed back and delayed for about 70 years.)

On the other hand, in the last two decades, investigations into astrophysical factors of nuclear reactions at low atomic numbers, which have great importance in nuclear astrophysics [5] have been made. In the cross section of measurements of the dd reactions in deuterated metal targets, extraordinary observations, called “anomalous screening”, were made in low energy accelerator physics ([6] and references there in). Several years ago a systematic survey of the experimental methods applied in these investigations, and the theoretical efforts for the explanation of the anomalous screening effect was made [6] from which one can conclude that the full theoretical explanation of the effect is still missing.

The observations in the above two fields motivate us to search for physical phenomena that may have modifying effect on nuclear reactions in solid state environment. Earlier we found that theoretically [7] if the reaction $p+d \rightarrow {}^3\text{He}$ takes place in a solid material, then the nuclear energy is mostly taken away by an electron in the environment instead of by the emission of a γ photon, a result that calls the attention to the possible role of the presence of charged particles of the surroundings.

The cross section of direct (first order in terms of perturbation calculation) nuclear reactions has strongly and nonlinearly decreasing energy dependence due to the repulsive Coulomb potential in the low energy range (as will be seen in Section 2). In the second order processes this huge decrease of the cross section may disappear. Therefore, the cross section of a not direct (second order) reaction may be essentially higher than the cross section of the direct reaction. In this paper, we attempt to demonstrate this effect.

We investigate the



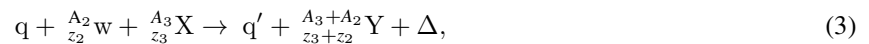
process which we are going to call recoil assisted proton capture. The solid is a metal ${}_{z_1}^{A_1}\text{V}$ (e.g. Pd) which is irradiated with low energy free protons, while free ions or atoms of nuclei ${}_{z_3}^{A_3}\text{X}$ (e.g. deuterons) are also present. The particles ${}_{z_1}^{A_1}\text{V}$ interact with the ingoing free protons via Coulomb interaction and push them (virtually) into an intermediate state of large momentum. These protons are captured by the nuclei ${}_{z_3}^{A_3}\text{X}$ due to strong interaction and a nucleus ${}_{z_3+1}^{A_3+1}\text{Y}$ is created in this manner. The particles ${}_{z_1}^{A_1}\text{V}$ (initial) and ${}_{z_1}^{A_1}\text{V}'$ (final) assist the process only. Δ is the energy of the reaction.

The recoil assisted $p+d \rightarrow {}^3\text{He}$ reaction



is discussed in more detail. Here $\Delta = 5.493$ MeV.

The reaction



a generalization of (1), is also dealt with. Here q is any charged particle of the environment.

In Section 2, the decreasing energy dependence of the cross section in the low energy range is connected to the hindering role of Coulomb repulsion and the Coulomb factor. In Section 3, the basic ideas are expounded. Sections 4 and 5 are devoted to the deduction of transition probability per unit time and cross section of recoil assisted $p+d \rightarrow$

^3He reaction, which is the simplest recoil assisted proton capture reaction, in a very simple model of the recoil assisted reaction. Section 6 is an overview of some other recoil assisted low energy nuclear reactions, which may lead to nuclear transmutations. Sections 7 and 8 are devoted to critical analysis of electrolysis experiments and summary. Some correspondences and identities applied in the calculation can be found in the Appendix.

2. Hindering Role of Coulomb Repulsion

It is standard in nuclear physics that heavy particles j and k of like positive charge need considerable amount of relative kinetic energy E determined by the height of the Coulomb barrier in order to enhance the probability of their nuclear interaction to a significant value.

The cross section of such a process can be derived applying the Coulomb solution $\varphi(\mathbf{r})$,

$$\varphi(\mathbf{r}) = e^{i\mathbf{k}\cdot\mathbf{r}} f(\mathbf{k}, \mathbf{r}) / \sqrt{V}, \quad (4)$$

which is the wave function of a free particle of charge number z_j in a repulsive Coulomb field of charge number z_k [8], in the description of relative motion of projectile and target. In (4) V denotes the volume of normalization, \mathbf{r} is the relative coordinate of the two particles, \mathbf{k} is the wave number vector in their relative motion and $f(\mathbf{k}, \mathbf{r}) = e^{-\pi\eta_{jk}/2} \times \Gamma(1 + i\eta_{jk}) \times {}_1F_1(-i\eta_{jk}, 1; i[kr - \mathbf{k} \cdot \mathbf{r}])$, where ${}_1F_1$ is the confluent hypergeometric function and Γ is the Gamma function. $\varphi(\mathbf{r}) \sim e^{-\pi\eta_{jk}/2} \Gamma(1 + i\eta_{jk})$ and

$$\left| e^{-\pi\eta_{jk}/2} \Gamma(1 + i\eta_{jk}) \right| = \sqrt{\frac{2\pi\eta_{jk}(E)}{\exp[2\pi\eta_{jk}(E)] - 1}} = f_{jk}(E), \quad (5)$$

which is the so-called Coulomb factor. Here

$$\eta_{jk}(E) = z_j z_k \alpha_f \sqrt{a_{jk} \frac{m_0 c^2}{2E}} \quad (6)$$

is the Sommerfeld parameter.

$$a_{jk} = \frac{A_j A_k}{A_j + A_k} \quad (7)$$

is the reduced mass number of colliding particles j and k of mass numbers A_j and A_k and rest masses $m_j = A_j m_0$, $m_k = A_k m_0$. $m_0 c^2 = 931.494$ MeV is the atomic energy unit, α_f is the fine structure constant and E is taken in the center of mass (CM) coordinate system.

The cross section of the process is proportional to $f_{jk}^2(E)$ thus the rate of the nuclear reaction of heavy, charged particles of like positive charge becomes very small at low energies as a consequence of $f_{jk}^2(E)$ being very small. Mathematically it appears in the energy dependence of the cross section (σ) of the charged-particle induced reactions as

$$\sigma(E) = S(E) \exp[-2\pi\eta_{jk}(E)] / E, \quad (8)$$

where $S(E)$ is the astrophysical factor, which can be written as $S(E) = S(0) + S_1 E + S_2 E^2$, [5].

It is the consequence of energy dependence (8) of the cross section that to this day it is a commonplace that the rate of any nuclear reaction between heavy, charged particles of positive charge is unobservable at low energies. The aim of this paper is to show that in solids, contrary to the above assumption, there can exist nuclear processes with observable rates at low energies.

It will be shown that the huge increment in the Coulomb factor due to recoil makes it possible for the cross section of recoil assisted nuclear reactions to reach an observable magnitude even in the very low energy case. Since the actual

Coulomb factors are the clue to the recoil assisted nuclear reactions we focus our attention on to them, especially concerning the Coulomb factors of heavy charged particles.

3. General Considerations

It is thought that the state of one participant of the nuclear process is changed by Coulomb interaction with a charged particle of the environment (e.g. solid material, a metal) before the nuclear process takes place. As an example, which will be considered in more detail, let us consider the $p + {}^{A_3}_{z_3}X \rightarrow {}^{A_4}_{z_4}Y$ (especially the $p+d \rightarrow {}^3_2\text{He}$) model-process ($A_4 = A_3 + 1, z_4 = z_3 + 1$). In this reaction, slow initial protons enter the solid (e.g. Pd) while quasi-free ${}^{A_3}_{z_3}X$ particles (e.g. deuterons) are also present. The graphs of the process can be seen in Fig. 1. In this case, one of the slow protons (as particle 2) can enter into Coulomb interaction with a heavy constituent (Pd atom) of the solid (as particle 1) knocking out it from the lattice before the nuclear reaction with an ${}^{A_3}_{z_3}X$ particle (e.g. a deuteron). The Coulomb interaction is followed by strong interaction, that induces a nuclear process, e.g. a nuclear capture process, in which the energy Δ of the nuclear reaction is divided between the heavy constituent (Pd atom) and the heavy nuclear product ${}^{A_4}_{z_4}Y$ (e.g. ${}^3_2\text{He}$). This process is a second order process in terms of standard perturbation theory (see Fig. 1(a)). The rest masses of the participants are: $m_1 = A_1 m_0, m_2 = m_0, m_3 = A_3 m_0$ (e.g. $m_3 = 2m_0$) and $m_4 = A_4 m_0$ (e.g. $m_4 = 3m_0$) corresponding to the heavy constituent, the proton, the other nucleus (e.g. deuteron) and the nuclear product ${}^{A_4}_{z_4}Y$ (e.g. ${}^3_2\text{He}$), respectively. The states of the heavy constituent, the proton, the other nucleus and the nuclear product must fulfill energy and momentum conservation in the initial and final states. If initially (before the Coulomb interaction) protons and ${}^{A_3}_{z_3}X$ particles (e.g. deuterons) move slowly and the heavy constituent has only vibration of thermal origin then their initial momenta can be neglected and the initial total momentum can be taken to be zero. Therefore in the final state $\mathbf{p}_{1'} + \mathbf{p}_4 = 0$, where $\mathbf{p}_{1'}$ and \mathbf{p}_4 are the momenta of the heavy constituent, knocked out from the lattice, and the nuclear product resulting $\mathbf{p}_{1'} = -\mathbf{p}_4 (= \mathbf{p})$. From energy conservation it follows that $\mathbf{p}^2 / (2m_1) + \mathbf{p}^2 / (2m_4) = \Delta$ which determines $p = |\mathbf{p}| = \sqrt{2m_0 a_{14} \Delta}$. (If $m_1 > m_4$ then the nuclear product (particle 4) will take away the larger part of the total nuclear reaction energy Δ .) If the Coulomb interaction preserves the momentum (as will be shown later) then the Coulomb scattered proton (particle 2') has momentum $\mathbf{p}_{2'} = \mathbf{p}_4 = -\mathbf{p}$

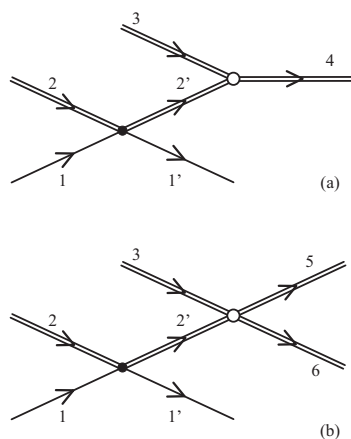


Figure 1. The graphs of recoil assisted nuclear reactions. The single lines represent (initial localized (1) and final free(1')) heavy constituent of the solid. The double lines represent free, heavy, charged initial (2) particles (such as p, d), their intermediate state (2'), target nuclei (3) and reaction products (4)–(6). The filled dot denotes Coulomb-interaction and the open circle denotes nuclear (strong) interaction. Fig. 1(a) is a capture process and Fig. 1(b) is a reaction with two fragments.

too. It means that its energy

$$E_{2'} = \frac{p^2}{2m_2} = a_{14}\Delta/A_2 \quad \left(\text{e.g. } E_{2'} = \frac{3A_1}{A_1 + 3}\Delta \text{ in the case of } p + d \rightarrow {}^3_2\text{He reaction} \right)$$

in the intermediate state. (A_1 is the nucleon number of the heavy constituent (Pd atom) and $A_2 = 1$ in the case of proton capture discussed.) The Coulomb factor must be calculated in the CM system. $E_{2'}(\text{lab}) = a_{14}\Delta/A_2$ is valid in the laboratory frame of reference (lab). Thus

$$E_{2'}(\text{CM}) = \frac{m_3}{m_2 + m_3} E_{2'}(\text{lab}) = \frac{A_3}{A_2(A_2 + A_3)} a_{14}\Delta$$

must be substituted in (6) that results

$$\eta_{2'3} = z_2 z_3 \alpha_f A_2 \sqrt{\frac{m_0 c^2}{2a_{14}\Delta}} \quad (9)$$

and which gives $\eta_{2'3} = z_3 \alpha_f \sqrt{m_0 c^2 / (2a_{14}\Delta)}$ with $z_2 = 1$ and $A_2 = 1$ corresponding to proton capture. In the case of $p+d \rightarrow {}^3_2\text{He}$ reaction $\Delta = 5.493$ MeV [9], which is the reaction energy and if $A_1 = 106$ corresponding to one of the Pd isotopes then $2a_{14}\Delta = 32.05$ MeV, $\eta_{2'3} = 0.039$ and $f_{2'3}^2 = 0.88$.

Moreover, in a proton capture process with particle 3 of mass number A_3 the mass number of particle 4 becomes $A_4 = A_3 + 1$ and the reduced mass number $a_{14} = A_1(A_3 + 1) / (A_1 + A_3 + 1)$. If $A_1 \simeq A_3 = \hat{A}$ then $a_{14} = \hat{A}/2$ and $2a_{14}\Delta = \hat{A}\Delta = 572$ MeV at $\hat{A} = 100$ and with a typical (averaged) value of $\Delta = 5.72$ MeV (see Table 1). If $z_3 = 46$ then $\eta_{2'3} = 0.428$ and $f_{2'3}^2 = 0.196$.

Thus, the Coulomb scattered proton will have (virtual) momentum (virtual kinetic energy) in the intermediate state that is large enough to make a drastic increase of the Coulomb factor $f_{2'3}$ as has been demonstrated above in the two numerical examples. As a conclusion, the state of an ingoing heavy, charged particle may be changed by a solid environment in such a way that must not be neglected in rate calculations of nuclear processes.

4. Model of Recoil Assisted Nuclear Reactions in d-filled Metals

The reaction of heavy charged particles induced by a solid-state environment (deuterized metals in a proton flux from an accelerator) is modeled in the following way. Let us take two independent systems A and B, where A is a solid and B is an ensemble of free, heavy charged particles (e.g. free protons) with the corresponding Hamiltonians H_A and H_B . It is supposed that their eigenvalue problems are solved, and the complete set of the eigenvectors of the two independent systems are known.

In the processes investigated, the Coulomb and the strong interactions play crucial roles. The interaction Hamiltonian H_I comprises the Coulomb interaction potential V_{Cb} with the charged constituents of surroundings (solid) and the interaction potential V_{St} of the strong interaction:

$$H_I(\mathbf{x}_{AB}) = V_{Cb}(\mathbf{x}_{AB}) + V_{St}(\mathbf{x}_{AB}). \quad (10)$$

Therefore, the charged particle assisted nuclear reactions are at least of second order in terms of standard perturbation calculation. The interaction $H_I(\mathbf{x}_{AB})$ between them is switched on adiabatically, the suffixes A and B in the argument symbolize that one party of the interaction comes from system A and the other from system B.

According to (10), the lowest order of S-matrix element of a charged particle assisted nuclear reaction has two terms. However, the contribution by the term, in which V_{St} according to chronological order precedes V_{Cb} , is negligible because of the smallness of the Coulomb factor which is appearing in the matrix element of V_{St} in this case (as discussed

above). In the following we only deal with the dominant term. (In the nuclear matrix element, the Coulomb interaction between the charged participants is taken into account using an appropriate approximate form (21) of (4).)

Thus in the process investigated, first a heavy, charged particle of system B takes part in a Coulomb scattering with any charged particle of system A and it is followed by a strong interaction $V_{St}(\mathbf{x}_{aB})$ with some nucleus of system A that leads to their final bound states. Particles 1, 3 belonging to system A are heavy constituents (e.g. atoms, ions (particle 1) and quasi-free deuterons (particle 3)) of the solid. Ingoing particles 2 belong to the system B, that are charged, heavy particles (e.g. protons (p)), and it is supposed that they move freely at the surface of the solid (e.g. metal). The sub-lattice of the solid is filled partly with particles 3, which are deuterons further on, i.e. the number of filled lattice points of the d sub-lattice is $N_1\xi$, where N_1 is the number of possible lattice sites. It is supposed that only quasi-free deuterons take part in the process and they are produced by thermal activation. The number N_3 of quasi-free deuterons has strong temperature dependence.

$$N_3(T) = N_1\xi e^{-\frac{U}{kT}} e^{-\frac{\varepsilon}{kT}}, \quad (11)$$

where U is the activation energy of the deuteron necessary for it to be quasi-free in the host lattice and ε is its quasi-kinetic energy. So $N_3(T)$ gives the number of those deuterons which are bound in the lattice but are delocalized, move quasi-free in it and take part in the process discussed.

Since the aim of this paper is to show the fundamentals of the main effect, the problem, that there may be identical, indistinguishable particles in systems A and B is not considered. The simplest description and the simplest process (the p capture reaction) is chosen.

For atomic potential we use screened Coulomb interaction potential of charge number z_1 with screening parameter $\lambda = z_1/a_0$ that results $V_{Cb}(\mathbf{r})$ of form

$$V_{Cb}(\mathbf{r}) = \frac{z_1 z_2}{2\pi^2} e^2 \int \frac{\exp(i\mathbf{q}\mathbf{r})}{q^2 + \lambda^2} d\mathbf{q} \quad (12)$$

and coupling strength $e^2 = \alpha_f \hbar c$. \hbar is the reduced Planck-constant, c is the velocity of light in vacuum and a_0 is the Bohr radius. Here z_2 is the charge number of the ingoing heavy charge particle (particle 2).

For the strong interaction the interaction potential

$$V_{St}(\mathbf{x}) = -V_0 \quad \text{if } |\mathbf{x}| \leq b \quad \text{and} \quad V_{St}(\mathbf{x}) = 0 \quad \text{if } |\mathbf{x}| > b \quad (13)$$

is applied, where the choice for $V_0 = 25$ MeV and $b = 2 \times 10^{-13}$ cm seem to be reasonable in the case of deuteron like target particle [10].

According to standard perturbation theory of quantum mechanics the transition probability per unit time ($W_{fi}^{(2)}$) of the process can be written as

$$W_{fi}^{(2)} = \frac{2\pi}{\hbar} \sum_f |T_{fi}^{(2)}|^2 \delta(E_f - \Delta) \quad (14)$$

with

$$T_{fi}^{(2)} = \sum_{2'} \frac{V_{St,f2'} V_{Cb,2'i}}{E_{2'} - E_i}, \quad (15)$$

where E_i , $E_{2'}$ and E_f are the kinetic energies in the initial, intermediate and final states, respectively, Δ is the reaction energy, i.e. the difference between the rest energies of the initial (E_{i0}) and final (E_{f0}) states ($\Delta = E_{i0} - E_{f0}$). $V_{Cb,2'i}$ is the matrix element of the Coulomb potential between the initial and intermediate states and $V_{St,f2'}$ is the matrix

element of the potential of the strong interaction between intermediate and final states. Only capture processes are dealt with. The initial momenta and kinetic energies of particles 1–3 are neglected ($E_i = 0$).

$$E_f = \frac{\hbar^2 \mathbf{k}_{1'}^2}{2m_1} + \frac{\hbar^2 \mathbf{k}_4^2}{2m_4}, \quad (16)$$

$$E_{2'} = \frac{\hbar^2 \mathbf{k}_{2'}^2}{2m_2} + \frac{\hbar^2 \mathbf{k}_{1'}^2}{2m_1} \quad (17)$$

are the kinetic energies in the final and intermediate states. $\mathbf{k}_{1'}$, $\mathbf{k}_{2'}$ and \mathbf{k}_4 are wave vectors of particle 1', 2' and 4, respectively (see Fig. 1a).

5. Cross Section of Recoil Assisted Nuclear Reaction in d-filled Metals

The initial states of heavy constituents (e.g. atom or ion of the host lattice, particle 1 of rest mass m_1), that is localized around all of the lattice points, are described by a Bloch-function of the form [11]

$$\varphi_{\mathbf{k}_{1,i}}(\mathbf{r}_1) = \frac{1}{\sqrt{N_1}} \sum_{\mathbf{L}} e^{i\mathbf{k}_{1,i} \cdot \mathbf{L}} a(\mathbf{r}_1 - \mathbf{L}), \quad (18)$$

where \mathbf{r}_1 is the coordinate, $\mathbf{k}_{1,i}$ is wave vector of the first Brillouin zone (BZ) of the reciprocal lattice, $a(\mathbf{r}_1 - \mathbf{L})$ is Wannier-function, which is independent of $\mathbf{k}_{1,i}$ within the BZ and is well localized around lattice site \mathbf{L} . N_1 is the number of lattice points of the lattice of particles 1. (The Coulomb-interaction between the incoming free particles and the crystal may change the energy distribution of the states of form (18).)

$$a(\mathbf{x}) = \left(\frac{\beta^2}{\pi}\right)^{3/4} e^{-\frac{\beta^2}{2}x^2}, \quad (19)$$

that is the wave function of the ground state of a 3-dimensional harmonic oscillator of angular frequency ω with $\beta = \sqrt{m_1 \omega / \hbar}$ [12].

For particles 2 (ingoing heavy particles, in our case protons) taking part in Coulomb interaction with the heavy constituent of the solid (with particle 1) we use plane waves before and after scattering as well. The final state of heavy constituent which comes from the solid (particle 1') is also a plane wave.

Using the states defined above for Coulomb matrix element we have

$$\begin{aligned} V_{\text{Cb},2'i} &= \frac{z_1 z_2}{2\pi^2} e^2 \left(\frac{\beta^2}{\pi}\right)^{3/4} \frac{\delta(\mathbf{k}_{2'} + \mathbf{k}_{1'})}{\mathbf{k}_{1'}^2 + \lambda^2} \\ &\times \frac{(2\pi)^6}{V^{3/2}} \frac{1}{\sqrt{N_1}} \sum_{\mathbf{L}} \exp(i\mathbf{k}_{1,i} \cdot \mathbf{L}). \end{aligned} \quad (20)$$

Here the approximation $\tilde{a}(\mathbf{k}) = 8\pi^{9/4} \beta^{3/2} \delta(\mathbf{k})$ in the case of $\beta \ll k$ is used where

$$\tilde{a}(\mathbf{k}) = \int e^{-i\mathbf{k} \cdot \mathbf{x}} a(\mathbf{x}) d^3x$$

is the Fourier transform of (19) which is

$$\tilde{a}(\mathbf{k}) = 2^{3/2} \pi^{3/4} \beta^{-3/2} \exp\left(-\frac{k^2}{2\beta^2}\right)$$

that allows this approximation since $\beta \ll |\mathbf{k}_{1'}|, |\mathbf{k}_{2'}|$ and $|\mathbf{k}_4|$ as will be seen later. Furthermore $\mathbf{k}_{1,i}$ is neglected in the argument of the Dirac-delta since $|\mathbf{k}_{1,i}| \ll |\mathbf{k}_{1'}|$ (see later too).

Particle 3 is also supposed to be free, therefore its state may also be considered to be a plane wave. When calculating the matrix element of the strong interaction potential between particles 2' and 3 we use an approximate form $\varphi_{2'3,Cb}(\mathbf{r})$ of the Coulomb solution

$$\varphi_{2'3,Cb}(\mathbf{r}) = e^{i\mathbf{k}_{2'} \cdot \mathbf{r}} f_{2'3}(k_{2'}) / \sqrt{V}, \quad (21)$$

namely a plane wave corrected by the appropriate Coulomb factor $f_{2'3}(k_{2'})$ corresponding to the particles 2' and 3, that take part in strong interaction. Here $\mathbf{r} = \mathbf{r}_{2'} - \mathbf{r}_3$ is their relative coordinate. (The approximation of the Coulomb solution of form (21) is valid in the range of the nucleus only.) The wave function of particles 2' and 3 can be written as the function of \mathbf{r} and \mathbf{R} , which is the center of mass coordinate of particles 2' and 3, as

$$\varphi_{2'3}(\mathbf{R}, \mathbf{r}) = e^{i\mathbf{k}_{2'} \cdot (\mathbf{R} + \mathbf{r})} f_{2'3}(k_{2'}) / V. \quad (22)$$

The final state has the form

$$\varphi_4(\mathbf{R}, \mathbf{r}) = e^{i\mathbf{k}_4 \cdot \mathbf{R}} \Phi_f(\mathbf{r}) / \sqrt{V}, \quad (23)$$

where $\Phi_f(\mathbf{r})$ is the final nuclear state of the proton (particle 2') in particle 4. In the nuclear part of the model the Weisskopf-approximation is used, i.e. for the final nuclear state of the proton we take

$$\Phi_{fW}(\mathbf{r}) = \sqrt{\frac{3}{4\pi R_0^3}} \quad (24)$$

if $r \leq R_0$, where R_0 is the nuclear radius, and $\Phi_{fW}(\mathbf{r}) = 0$ for $r > R_0$. Since $\Phi_{fW}(\mathbf{r})$ and $V_{St}(\mathbf{r})$ both have spherical symmetry the spherical term $\sin(k_{2'} r) / (k_{2'} r)$ remains from $e^{i\mathbf{k}_{2'} \cdot \mathbf{r}}$ in the nuclear matrix-element. With the aid of the above wave function and $b = R_0$ assumption

$$V_{St,f2'}^W = -V_0 \frac{\sqrt{12\pi b}}{k_{2'}} f_{2'3}(k_{2'}) H(k_{2'}) \frac{(2\pi)^3}{V^{3/2}} \delta(\mathbf{k}_{2'} - \mathbf{k}_4), \quad (25)$$

where

$$H(k_{2'}) = \int_0^1 \sin(k_{2'} b x) x \, dx. \quad (26)$$

Collecting everything obtained above, applying correspondence (71) in (15) and integrating over $\mathbf{k}_{2'}$

$$\begin{aligned} T_{fi}^{(2)} = & - \frac{(3\beta^3 b)^{1/2}}{\pi^{9/4}} \frac{(2\pi)^6}{|\mathbf{k}_{1'}| V^2} \frac{\delta(\mathbf{k}_4 + \mathbf{k}_{1'})}{(|\mathbf{k}_{1'}|^2 + \lambda^2)} \\ & \times \frac{f_{2'3}(k_{1'}) H(k_{1'})}{\frac{\hbar^2 |\mathbf{k}_{1'}|^2}{2m_0 a_{12}}} \frac{z_1 z_2 e^2 V_0}{\sqrt{N_1}} \sum_{\mathbf{L}} \exp(i\mathbf{k}_{1,i} \cdot \mathbf{L}). \end{aligned} \quad (27)$$

Substituting (27) into (14), the following correspondence and identities are used: (72) – (75). Carrying out integration over $\mathbf{k}_{1'}$ with the aid of $\delta(\mathbf{k}_4 + \mathbf{k}_{1'})$, applying the relations (76) and (77), neglecting λ since $\lambda \ll |k_0|$, taking $z_2 = 1, A_2 = 1$ (particle 2 is a proton), integrating over \mathbf{k}_4 and dividing by v/V which is the flux of ingoing particles 2 of velocity v one can obtain the cross section σ_{RANR} of the process as

$$\sigma_{RANR} = \frac{S}{\sqrt{E_{2i}}}, \quad (28)$$

where

$$S = 24\sqrt{\pi}\beta^3 b \frac{(z_1 z_2 \alpha_f V_0)^2 (\hbar c)^4}{\Delta^{9/2} (m_0 c^2)} \frac{a_{12}^2}{a_{14}^{7/2}} f_{2'3}^2(\Delta) H^2(k_0). \quad (29)$$

(The subscript RANR refers to the abbreviation of recoil assisted nuclear reaction.) Now it may be checked that the supposed $\beta \ll |\mathbf{k}_{1'}|, |\mathbf{k}_{2'}|, |\mathbf{k}_4|$ and $|\mathbf{k}_{1,i}| \ll |\mathbf{k}_{1'}|$ conditions are fulfilled since $|\mathbf{k}_{1'}| = |\mathbf{k}_{2'}| = |\mathbf{k}_4| = k_0$, ($k_0 = \hbar^{-1} \sqrt{2m_0 a_{14} \Delta}$).

In a deuterized Pd the ground state of the oscillator which describes the vibration of particles 1 is $E_0 = 72$ meV leading to $\hbar\omega = 48$ meV [13] and $\beta = 3.4 \times 10^8 \times A_1^{1/2} \text{ cm}^{-1}$. Applying this and taking $A_1 = 106$ as a characteristic Pd atomic number, $b\beta^3 = 8.58 \times 10^{15} \text{ cm}^{-2}$. In the case of Pd assisted p + d \rightarrow ^3He reaction $z_1 = 46$ and the $a_{12} = 1$ and $a_{14} = 3$ approximations may be applied. Furthermore, with $\Delta = 5.493$ MeV, $H(k_0 b) = 0.43$ and $f_{2'3}^2 = 0.88$ the cross-section results $\sigma_{\text{RANR}} = 6.67 \times E_{2i}^{-1/2} \mu\text{b}$ (i.e. $S = 6.67 \text{ eV}^{1/2} \mu\text{b}$, and E_{2i} is measured in eV).

Based on the above results, one can estimate that energy range of astrophysical factor measurements where recoil assisted nuclear reactions have to be taken account. It is determined by the following relation $\sigma_{\text{RANR}} \exp[-U/(kT)] \gtrsim \sigma(E)$ where $\sigma(E)$ is determined by (8). This relation can be converted to the condition

$$\ln \left(\frac{S}{S(0)} \sqrt{E_{2i,\text{lab}}} \right) - \frac{U}{kT} \gtrsim -2\pi\alpha_f \sqrt{\frac{m_0 c^2}{E_{2i,\text{lab}}}}, \quad (30)$$

which is valid in the laboratory frame of reference. Here $E_{2i,\text{lab}}$ is the initial energy of particle 2, i.e. the beam energy, and it is also supposed that the S value of the recoil assisted dd reactions may be estimated by the S value obtained above. If one takes $U = 0.23$ eV [14] and $kT = 0.025$ eV which corresponds to room temperature then $U/(kT) = 9.2$. Moreover, $S(0) = 5.5 \times 10^4 \text{ eVb}$ and $5.6 \times 10^4 \text{ eVb}$ of the d + d \rightarrow $^3\text{He} + \text{n}$ and d + d \rightarrow p + t reactions [5]. Applying these numbers in (30) one obtains that near and below $E_{2i,\text{lab}} = 8$ keV the recoil assisted reactions have to be taken into account when evaluating astrophysical measurements of dd reactions. This result fits in with observations [6].

It is worth mentioning, that usual nuclear experiments, in which nuclear reactions of heavy charged particles are investigated, are usually devised taking into account the hindering effect of Coulomb repulsion. Consequently, the beam energy is taken to be appropriately high to reach the energy domain where the cross section of the processes becomes appropriately large. Therefore, in an ordinary nuclear experiment, the role of recoil assisted reactions is not generally essential.

6. Low Energy Nuclear Reactions Allowed by Recoil Assistance – Possibility of Nuclear Transmutations

In order to get more information on the capability of the recoil mechanism discussed, some cases of the recoil assisted proton captures (see (1)) are investigated. Particle 1 is a heavy particle, which assists the nuclear reaction and particle 2 is proton. Particles 3 and 4 have mass and charge numbers A_3, z_3 and $A_3 + 1, z_3 + 1$, respectively (see Fig. 1). The reaction energy Δ may be calculated using mass excess data [9]. Δ is the difference between the sum of the initial and final mass excesses, i.e. $\Delta = \Delta_p + \Delta_{A_3, z_3} - \Delta_{A_3+1, z_3+1}$, where $\Delta_p, \Delta_{A_3, z_3}$ and Δ_{A_3+1, z_3+1} are mass excesses of proton, ${}_{z_3}^{A_3}\text{X}$ and ${}_{z_3+1}^{A_3+1}\text{Y}$, respectively. Investigating the mass excess data [9] one can recognize that the process is energetically allowed in the case of great number of nuclei and, consequently, may lead to nuclear transmutations [3].

Considering experiments using Pd cathode during electrolysis an important family of the recoil assisted proton capture reads as

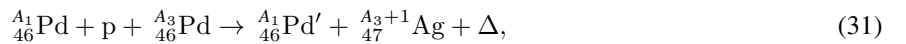


Table 1. Numerical data of the ${}_{46}^{A_1}\text{Pd} + p + {}_{46}^{A_3}\text{Pd} \rightarrow {}_{46}^{A_1}\text{Pd}' + {}_{47}^{A_3+1}\text{Ag} + \Delta$ reactions. r_A is the relative natural abundance. Δ is the energy of the reaction.

A_3	102	104	105	106	108	110
$\Delta(\text{MeV})$	4.155	4.966	5.814	5.789	6.487	7.156
r_{A_3}	0.0102	0.1114	0.2233	0.2733	0.2646	0.1172

where the recoil assisted proton capture is mainly followed by the

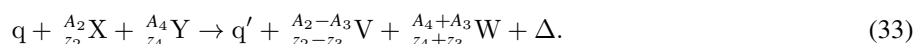


reaction. (The relevant data can be found in Table 1, the estimated $f_{2'3}^2 = 0.196$, which may be attached to the reactions, is determined in Section 3, the nuclear data of Table 1 are taken from [9].)

The processes (31) may produce stable ${}_{47}^{107}\text{Ag}$ and ${}_{47}^{109}\text{Ag}$ isotopes whose recoil assisted proton capture reaction may give rise to a chain of nuclear transmutations.

Moreover, the capture reaction may be extended to the recoil assisted capture of heavy particles ${}_{z_2}^{A_2}w$ (see reaction (3)), e.g. the capture of deuteron (d), triton (t), ${}^3\text{He}$, ${}^4\text{He}$, etc. The number of energetically allowed reactions of that type is also very large, their detectability is limited by the actual value of the factor $f_{2'3}^2$. The reactions of type (3) are also the sources of nuclear transmutations [3].

Another family of recoil assisted reactions, which is worth mentioning, is the family of exchange reactions. In recent works [15] the cooperative internal conversion processes by neutron and proton exchange were investigated. The cooperative exchange processes may be generally written in the form



Here q stands for any charged particle (initially a free or bound electron and any nucleus of charge number z_1) which assists the reaction in which a heavy particle ${}_{z_3}^{A_3}w$ (n, p, d, t, ${}^3\text{He}$, ${}^4\text{He}$, etc.) is exchanged between the initial nuclei ${}_{z_2}^{A_2}\text{X}$ and ${}_{z_4}^{A_4}\text{Y}$ resulting the final particles ${}_{z_2-z_3}^{A_2-A_3}\text{V}$ and ${}_{z_4+z_3}^{A_4+A_3}\text{W}$ (see Fig. 2). These reactions lead to nuclear transmutations too [3] and the number of energetically allowed reactions of that type is also very large. In exchange reactions, the reaction energy Δ is divided between particles q' , ${}_{z_2-z_3}^{A_2-A_3}\text{V}$ and ${}_{z_4+z_3}^{A_4+A_3}\text{W}$. It was shown in [15] that in the case of electron assistance the electrons take off minor parts of Δ .

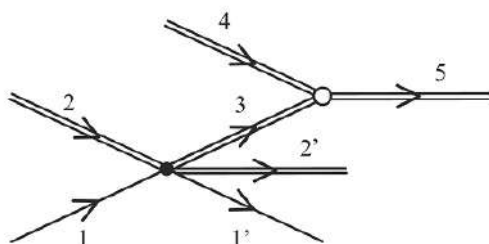
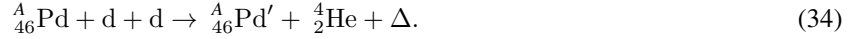


Figure 2. The graph of cooperative exchange process by heavy particle (e.g. neutron, proton, etc.) exchange. Particle 1 and 1' are any charged particle which assist the reaction, particle 2 is the nucleus which loses the heavy particle (e.g. neutron, proton, etc.) and becomes particle 2'. Particle 3 is the intermediate heavy particle (e.g. neutron, proton, etc.). Particle 4 is the nucleus which absorbs the heavy particle (e.g. neutron, proton, etc.) and becomes particle 5. The filled dot denotes (in the case of neutron the dipole term of) the Coulomb-interaction and the open circle denotes nuclear (*strong*) interaction.

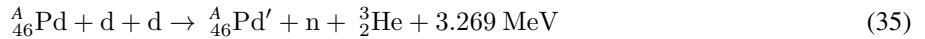
7. Critical Analysis of Experiments of Fleischmann–Pons Type

In the experiment of [1] Pd was filled with deuterons during electrolysis. The electrolyte had LiOD content too. The most straightforward Pd assisted d capture reaction is



In this reaction $\Delta = 23.847$ MeV and it is carried by the particles ${}^A_{46}\text{Pd}'$ and ${}^4_2\text{He}$ which have momentum of equal magnitude but opposite direction. Since both particles are charged and heavy they lose their kinetic energy in a very short range and so they convert the reaction energy into heat.

However, it is also possible that the two deuterons take part in the



and



reactions. Obviously, any other charged particle q of the environment may assist the above three reactions. The following qualitative consideration suggests that the rate of (34) is expected to be larger than that of (35) and (36). In the case of (34) $\mathbf{p}_4 = \mathbf{p}_{2'} (= -\mathbf{p}_{1'})$ and in the case of (35) and (36) $\mathbf{p}_5 + \mathbf{p}_6 = \mathbf{p}_{2'} (= -\mathbf{p}_{1'})$. ($\mathbf{p}_{1'}$, \mathbf{p}_4 , \mathbf{p}_5 and \mathbf{p}_6 are the momenta of particles 1, 2', 4, 5 and 6, see Fig. 1.) Thus in the later case the effective momentum transfer to particle 2' is limited if $\mathbf{p}_5 - \mathbf{p}_6$ is large and this limit decreases the effective phase space where large momentum transfer to particle 2' happens. Large momentum transfer is necessary for the large value of $f_{2'3}^2$.

7.1. Rate and power of sample in electrolysis

The above model (see Sections 4 and 5) of recoil assisted nuclear reactions in d -filled metals will be applied. Although this is a very rough model of electrolysis it shows some parameters which are crucial from the point of view of the phenomenon. Using the cross-section result obtained ((28) and (29)) and estimating S with the numerical value of S of the recoil assisted $\text{p} + \text{d} \rightarrow {}^3\text{He}$ reaction, we can estimate the rate and the generated power during electrolysis. In this naive model, it is supposed that reaction (34) is the only one, which assumption is not correct as will be seen later.

Supposing a surface effect, the rate of the process can be written as

$$\frac{dN}{dt} = N_1 N_3 \sigma_{\text{RANR}} \Phi, \quad (37)$$

where Φ is the flux of particles 2 (Φ is now the deuteron flux).

In a numerical example it is supposed that deuterons are very slow, e.g. of energy $E_{1i} = 1$ eV. The deuteron current is $I_p = \eta I$, where I is the total current, and the surface of the electrode is F (in cm^2) resulting $\Phi = \eta I / (eF) = \eta j / e$ where $e = 1.602 \times 10^{-19}$ As is the elementary charge and j is the current density in Acm^{-2} . The parameter η may be connected to the pH value of the electrolyte. The very slow deuterons may interact only with first Pd atomic plane of volume Fd which contains $N_1 = Fd/v_{\text{cell}} = 4F/d^2$ number of lattice points of the Pd lattice. v_{cell} is the volume of the elementary cell of the solid ($v_{\text{cell}} = d^3/4 = 1.47 \times 10^{-23}$ cm^3 with $d = 3.89 \times 10^{-8}$ cm which is the lattice parameter of the Pd lattice).

Using (11) the rate of the process in the sample can be estimated as

$$\begin{aligned} \frac{dN}{dt} &\simeq \frac{16jF^2}{ed^4} \xi \eta \sigma_{\text{RANR}} e^{-\frac{U}{kT}} \\ &= 2.9 \times 10^{20} \times jF^2 \xi \eta e^{-\frac{U}{kT}}. \end{aligned} \quad (38)$$

Taking $U = 0.23$ eV [14] and $kT = 0.025$ eV (room temperature) as done above $e^{-\frac{U}{kT}} = 1.01 \times 10^{-4}$ which results $dN/dt = 2.9 \times 10^{16} \times jF^2\xi\eta$. In this case the power $P = \Delta (dN/dt) = 1.1 \times 10^5 \times jF^2\xi\eta$ in W, which results $P = 1$ W at $\xi = 1$, $F = 1$ cm², $j = 1$ Acm⁻² and with $\eta = 9.1 \times 10^{-6}$.

We conclude, that the current density j of electrolysis, the effective surface F of the Pd cathode, the deuteron concentration ξ in Pd, the pH value (connected to η) the Li concentration and the temperature T both at the surface of the Pd cathode are crucial quantities from the point of view of the created power by recoil assisted nuclear reaction at the surface. Unfortunately, the published observations are generally incomplete, the pH value is usually missing, which may be the reason that the generated power reported seems to be sometimes on and sometimes off. The different kinds of cathode surface (e.g. smooth or cauliflower like) may be the reason that the result of some seemingly same experiments differ, since it is very hard to estimate the effective surface of, e.g. a cauliflower like surface.

Naturally the recoil assisted $p + d \rightarrow {}^3\text{He}$ reaction may also take place if there is some normal H concentration present.

7.2. Other recoil assisted nuclear reactions in experiments of Fleischmann–Pons type

Moreover, charged particle (q) assisted d capture reactions may take place with ${}^6\text{Li}$ and ${}^7\text{Li}$ isotopes



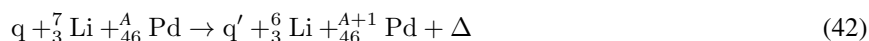
and



We now deal with neutron exchange reactions (see (33) and Fig. 2). Two types of charged particle (q) assisted neutron exchange processes with Pd nuclei are also possible:



with $\Delta = \Delta_-(d) + \Delta_+(A)$ and



with $\Delta = \Delta_-(Li) + \Delta_+(A)$ (the $\Delta_+(A)$ values can be found in Table 2). $\Delta_-(d) = \Delta_d - \Delta_p = 5.847$ MeV and $\Delta_-(Li) = \Delta({}^7_3\text{Li}) - \Delta({}^6_3\text{Li}) = 0.821$ MeV are the energies of neutron loss of d and ${}^7_3\text{Li}$, where Δ_d , Δ_p , $\Delta({}^7_3\text{Li})$ and $\Delta({}^6_3\text{Li})$ are the mass excesses of deuteron, proton, ${}^7_3\text{Li}$ and ${}^6_3\text{Li}$, respectively. In reactions (41) and (42) q denotes any charged particle (e.g. electron of the metal, Pd) and it is particle 1, d and ${}^7_3\text{Li}$ are particle 2, respectively, and ${}^A_{46}\text{Pd}$ appears as particle 4 (see Fig. 2). Reaction (41) is energetically allowed for all the natural isotopes of Pd since $\Delta = \Delta_-(d) + \Delta_+(A) > 0$ for each A (see the $\Delta_+(A)$ values of Table 2).

In the case of reaction (42) the $\Delta = \Delta_-(Li) + \Delta_+(A) > 0$ condition holds at $A = 102$ and $A = 105$ resulting $\Delta = 0.375$ MeV and $\Delta = 2.312$ MeV, respectively.

Table 2. Numerical data of reactions (41) and (42). The reaction is energetically allowed if $\Delta = \Delta_-(d) + \Delta_+(A) > 0$ (in the case of (41)) and $\Delta = \Delta_-(Li) + \Delta_+(A) > 0$ (in the case of (42)). A is the mass number, r_A is the relative natural abundance, For $\Delta_-(d) = 5.847$ MeV and $\Delta_-(Li) = 0.821$ MeV. $\Delta_+(A) = \Delta_A - \Delta_{A+1}$ are given in MeV units. Δ_A and Δ_{A+1} are the mass excess data of isotopes of mass numbers A and $A + 1$.

A	102	104	105	106	108	110
Δ_+	-0.446	-0.978	1.491	-1.533	-1.918	-2.320
r_A	0.0102	0.1114	0.2233	0.2733	0.2646	0.1172

However, at the Pd surface other types of charged particle assisted neutron and proton exchange processes (see (33) and Fig. 2) with d and Li nuclei of the electrolyte and d solved in Pd are possible:



and



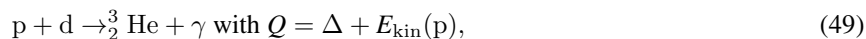
which is promptly followed by the decay ${}^8_4\text{Be} \rightarrow 2{}^4_2\text{He}$ (with $\Gamma_\alpha = 6.8$ eV). In reactions (43)–(47) d is particle 2 (see Fig. 2). The



reaction is also a charged particle (q) assisted neutron exchange reaction (here ${}^7_3\text{Li}$ is particle 2, see Fig. 2.) (This list of reactions is incomplete.)

7.3. Possibility of usual nuclear reactions

In reaction (41) protons of energy up to 7.269 MeV and in reaction (42) ${}^6_3\text{Li}$ particles of maximum energy 2.189 MeV are created. These energetic particles may enter into usual nuclear reactions with the nuclei of deuteron loaded Pd and electrolyte. The reactions are (without completeness):

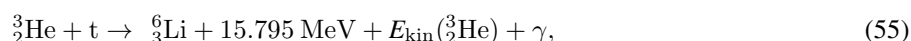


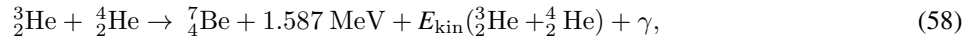
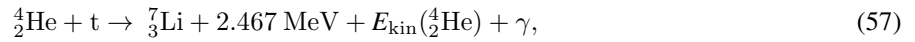
In (50) and (51) the emitted ${}^4_2\text{He}$ has energy $E_{4\text{He}} > 8.674$ MeV and $E_{4\text{He}} > 11.186$ MeV, and in (52) the created p and ${}^7_3\text{Li}$ have energy $E_p > 4.397$ MeV and $E_{7\text{Li}} > 0.628$ MeV, respectively. It can be seen that in (50) and (51) ${}^4_2\text{He}$ is produced. The ${}^7_3\text{Li}$ particles may enter into reaction



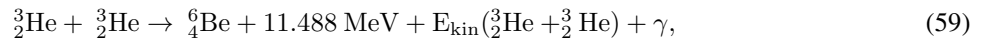
that contributes to ${}^4_2\text{He}$ production too. Here and above $E_{\text{kin}}(p)$ and $E_{\text{kin}}(\text{Li})$ are the kinetic energies of the initial protons, ${}^6_3\text{Li}$ and ${}^7_3\text{Li}$ isotopes. In reactions (41) – (53) heavy, charged particles of kinetic energy lying in the MeV range are created which are able to assist nuclear reactions too.

The energetic ${}^3_2\text{He}$ and ${}^4_2\text{He}$ particles may enter in the following reactions:



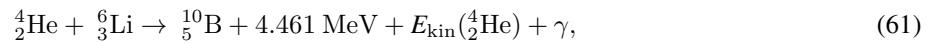
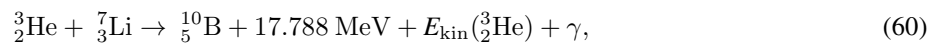


which decays with $\tau = 53.29 \text{ d}$ into ${}^7_3\text{Li}$ by electron capture (EC) and

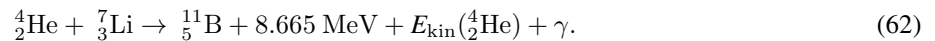


which decays with $\Gamma = 92 \text{ keV}$ into $2\text{p} + \alpha$.

Moreover the following normal reactions may also take place



and



The nuclei ${}^{10}_5\text{B}$ and ${}^{11}_5\text{B}$ are stable.

From the above one can see that many types of reactions exist which are capable of energy production and in many of them energy production is accompanied by ${}^4_2\text{He}$ production. In the majority of the above reactions, heavy charged particles are created with short range, so they lose their energy in the matter of the experimental apparatus mainly in the electrode (cathode) and the electrolyte, therefore directly observing them is difficult. It is mainly heat production, which is a consequence of deceleration in the matter of the apparatus, that can be observed. About the third of the processes, mainly the secondary processes are the sources of neutron emission. X- and γ -rays may be originated mainly from bremsstrahlung. The above reasoning tallies with experimental observations [3].

One can obtain the possible recoil assisted reactions if in reactions q is replaced by heavy charged particles (p , t , ${}^3_2\text{He}$, ${}^4_2\text{He}$, ${}^6_3\text{Li}$, ${}^7_3\text{Li}$, ${}^8_4\text{Be}$ and ${}^{A+1}_{46}\text{Pd}$ with $A = 102, 104-106, 108, 110$) some of them are created also in normal reactions. Consequently, it is a rather great theoretical challenge and task to determine precisely the relative rates and their couplings of all the accountable reactions, a work which is, nevertheless, necessary to the accurate quantitative analysis of experiments.

The relative rates of coupled reactions of many types depend significantly on the geometry, the kind of matter and other parameters of the experimental apparatus and on some further variables, which may be associated to the specific experiment. This situation may also be responsible for the diversity of the results of experiments, which are thought to have been carried out in seemingly similar circumstances.

7.4. Further nuclear transmutations

If there are deuterons present in the experiment then the most plausible process is the

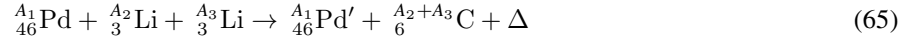


recoil assisted d capture process. This type of reaction may cause nuclear transmutations explained by supposing successive d capture reported recently [16].

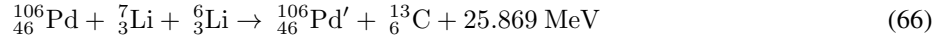
If there is Li present then



recoil assisted Li capture reactions may also lead to nuclear transmutations (and energy production). As an example, let us examine the Pd assisted

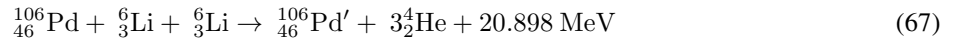


Li capture reactions. Using (9) with $z_2 = z_3 = 3$, $A_2 = 7$, $A_2 + A_3 = A_4 = 13$ and $A_1 = 106$, which corresponds to the



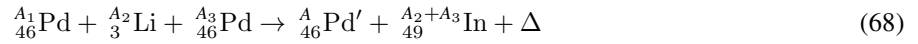
reaction, $\eta_{2'3} = 0.573$ and $f_{2'3}^2 = 0.101$.

The reaction



may have importance too.

It seems to be surprising, but the Pd assisted



recoil assisted Li capture reactions in Pd has small, but not negligible rate. As a numerical example let us take $z_2 = 3$, $z_3 = 46$, $A_2 = 7$, $A_3 = 106$, $A_4 = 113$ and $A_1 = 106$ in (9) resulting $\eta_{2'3} = 5.42$ and $f_{2'3}^2 = 5.3 \times 10^{-14}$ with $\Delta = 14.369 \text{ MeV}$, which is the reaction energy of the



recoil assisted Li capture reaction. In reactions (68) stable and unstable In isotopes may appear with the later decaying into Cd and Sn isotopes by electron capture and β^- emission.

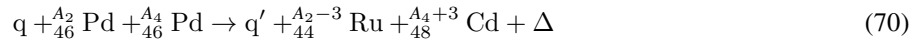
Next let us see the possibility of normal reactions. For instance in a Fleischmann-type experiment ${}^6_3\text{Li}$ particles of energy up to 2.189 MeV are created in reaction (42) so the reaction



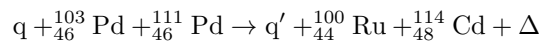
may have minor, but measurable probability. Here $Q = 28.17 \text{ MeV} + E_{\text{kin}}(\text{Li})$.

The Coulomb factor of reaction (69) is $f_{\text{Li,Li}}^2 = 1.71 \times 10^{-3}$ at 2.189 MeV kinetic energy of ${}^6_3\text{Li}$ particles. The magnitude of the factor $f_{\text{Li,Li}}^2$ indicates that the rate of reaction (69) may be large enough to be able to produce carbon traces in observable quantity too.

Moreover, in reactions (41) and (42) free ${}_{46}^A\text{Pd}$ particles are created offering, e.g. the possibility of the



charged particle assisted ${}^3_2\text{He}$ exchange process (see (33) and Fig. 2). The particle q and the other Pd particle are in the solid. Analyzing mass excess data [9] it was found that, e.g. the



${}^3_2\text{He}$ exchange process has reaction energy $\Delta = 5.7305 \text{ MeV}$. ${}_{46}^{103}\text{Pd}$ and ${}_{46}^{111}\text{Pd}$ are produced in reaction (41).

Calculating the $f_{2'3}^2 = f_{34}^2$ factors taking $A_2 = A_4 = 100$, $z_2 = z_4 = 46$, $A_3 = 3$, $z_3 = 2$ (see (33) and Fig. 2) in the calculation one gets $f_{2'3}^2 f_{34}^2 = 2.5 \times 10^{-12}$ which seems to be large enough to produce Cd and Ru traces in an experiment of time of many days long.

The above reactions are only examples and may offer starting point to the full explanation of nuclear transmutations arising in the experiment [3].

8. Summary

We have determined that, contrary to the commonly accepted opinion, nuclear reactions can occur between heavy, charged particles of like (positive) charge at low initial energy due to the assistance of other charged particles present. It is recognized, that one of the participant particles of a nuclear reaction of low initial energy may pick up great momentum in a Coulomb scattering process on a third particle of the surroundings. The virtually acquired great momentum, that is determined by the energy of the reaction, can help to overcome the hindering Coulomb barrier and can highly increase the rate of the nuclear reaction even in cases when the rate would be otherwise negligible. It is found that the recoil assisted $p + d \rightarrow {}^3\text{He}$ process may have a cross section of accountable magnitude at low energies.

There may be many fields of physics where the traces of the proposed mechanism may have previously appeared. It is not the aim of this work to give a systematic overview of these fields. Here, we only dealt with two of them that are thought to be partly related or explained by the proposed processes. The first is the so called anomalous screening effect observed in low energy accelerator physics investigating astrophysical factors of nuclear reactions of low atomic numbers [6]. The second is the family of low energy nuclear fusion processes. The physical background, discussed in the Introduction and in Section 2, was questioned by the two-decade old announcement [1] on excess heat generation at deuterized Pd cathodes during electrolysis at near room temperature. The mechanisms discussed here can explain the main problems raised in connection of the phenomenon (listed as points (a)–(d) in Section 1). (a) The mechanisms proposed here make low energy fusion reactions and (c) nuclear transmutations possible. (b) The processes discussed explain the lack of the normally expected reaction products. (d) The reason replication remains difficult is also made clear.

Appendix

In the calculation the following correspondences and relations applied:

$$\sum_{2'} \rightarrow \int [V/(2\pi)^3] d\mathbf{k}_{2'}, \quad (71)$$

$$\sum_f \rightarrow \int [V/(2\pi)^3] d\mathbf{k}_4 \times \int [V/(2\pi)^3] d\mathbf{k}_{1'}, \quad (72)$$

$$\frac{1}{N_1} \sum_{\mathbf{L}, \mathbf{L}'} \frac{1}{N_1} \sum_{\mathbf{k}_{1,i} \in BZ} \exp i\mathbf{k}_{1,i} (\mathbf{L} - \mathbf{L}') = 1, \quad (73)$$

$$[\delta(\mathbf{k}_4 + \mathbf{k}_{1'})]^2 = \delta(\mathbf{k}_4 + \mathbf{k}_{1'}) \delta(\mathbf{0}), \quad (74)$$

$$\delta(\mathbf{0}) = (2\pi)^{-3} V, \quad (75)$$

$$\delta(E_f - \Delta) = \delta(k_4 - k_0) m_0 a_{14} \hbar^{-2} k_0^{-1} \quad (76)$$

with

$$k_0 = \hbar^{-1} \sqrt{2m_0 a_{14} \Delta}. \quad (77)$$

References

- [1] M. Fleishmann and S. Pons, *J. Electroanal. Chem.* **261** (1989) 301–308.
- [2] S.B. Krivit and J. Marwan, *J. Environ. Monit.* **11** (2009) 1731–1746.
- [3] E. Storms, *Naturwissenschaften* **97** (2010) 861–881.
- [4] E. Storms, *Current Sci.* **108** (2015) 535.
- [5] C. Angulo, M. Arnould, M. Rayet, P. Descouvemont, D. Baye, C. Leclercq-Willain, A. Coc, S. Barhoumi, P. Aguer, C. Rolfs, R. Kunz, J.W. Hammer, A. Mayer, T. Paradellis, S. Kossionides, C. Chronidou, K. Spyrou, S. Degl'Innocenti, G. Fiorentini, B. Ricci, S. Zavatarelli, C. Providencia, H. Wolters, J. Soares, C. Grama, J. Rahighi, A. Shotter and M. Laméhi Rachti, *Nucl.Phys. A* **656** (1999) 3–183.
- [6] A. Huke, K. Czerski, P. Heide, G. Ruprecht, N. Targosz and W. Zebrowski, *Phys. Rev. C* **78** (2008) 015803.
- [7] P. Kálmán and T. Keszthelyi, *Phys. Rev. C* **69** (2004) 031606(R); *Phys. Rev. C* **79** (2009) 031602(R).
- [8] K. Alder, A. Bohr, T. Huus, B. Mottelson and A. Winther, *Rev. Mod. Phys.* **28** (1956) 432–542.
- [9] R.B. Firestone and V.S. Shirley, *Tables of Isotopes*, 8th Edn., Wiley, New York, 1996.
- [10] J.M. Blatt, and V.F. Weisskopf, *Theoretical Nuclear Physics*, Wiley, New York, 1952.
- [11] J.M. Ziman, *Principles of the Theory of Solids*, University Press, Cambridge, 1964.
- [12] C. Cohen-Tannoudji, B. Diu and F. Lalöe, *Quantum Mechanics*, Vol. 1, Wiley, New York/English version/Hermann, Paris, 1977.
- [13] E. Wicke, H. Brodowsky and H. Züchner, *Hydrogen in Palladium and Palladium Alloys*, in *Hydrogen in Metals*, G. Alefeld and Völkl (Eds.), Vol. 2, Chapter 3, Springer, Heidelberg, 1978, Fig. 3.7, p. 88.
- [14] S. Ichimaru, *Rev. Mod. Phys.* **65** (1993) 255–293.
- [15] P. Kálmán and T. Keszthelyi, arXiv 1511.07164, arXiv. 1602.05774.
- [16] Y. Iwamura, T. Itoh and S. Tsuruga, *Current Sci.* **108** (2015) 628–632.



Research Article

Exothermic Reactions in the Partially Molten Li–Ni–Cu Alloy

Andras Kovacs*, David Brown and Fredrik Ek

Fiskarsin Voima oy, Nordanvik 142, 02580 Sjundeå, Finland

Abstract

Experiments with Li–Ni–Cu alloy, as a novel energy source, are described. The experiments are performed in the 1200–1300°C temperature range, using welded metallic containers and also in open tube under inert gas flow. The measured reaction energy is too high to be explained by chemical origin. The initial experiments elucidate the properties of this reaction, while the last experiment demonstrates its continuous operation.

© 2017 ISCMNS. All rights reserved. ISSN 2227-3123

Keywords: Continuous operation, High power rate, Lithium–nickel–copper fuel, Nuclear reaction, Temperature cycling

1. Introduction

An energy generating reaction arising within a metallic alloy has great potential utility. The aim of this study has been to investigate the possible reaction between Lithium and Nickel at elevated temperature. The theoretical possibility of $^{58}\text{Ni} + 2e^- \rightarrow ^{58}\text{Fe}$ double electron capture reaction, which liberates nearly 2 MeV energy, provides motivation to explore its practical realization, and we suspect Lithium to play a role in enabling such reaction. However, it is also known that having only a molten alloy of Lithium and Nickel is not yet sufficient for initiating an exothermic reaction [1]. We, instead, propose a Li–Ni–Cu system to initiate a reaction. The simplicity of the Li–Ni–Cu system is, in general, particularly useful for the development and validation of corresponding theoretical models, and the selected experimental setup is, in particular, relatively easy to reproduce and commercially scale.

2. Experimental Setup

The precursor metals were placed in a metallic container made of APM material (composition: 72% Fe, 22% Cr, 6% Al, m.p.: 1500°C, good oxidation resistance), and TIG-welded to ensure airtight sealing and significant overpressure tolerance even at high temperatures. The enclosed air volume was about 1 cm³ per container in the initial four experiments. The employed furnace heated the sample from three directions, to achieve good temperature uniformity. The heating filaments were made of Kanthal wire (m.p. 1500°C, high oxidation resistance), having 1 mm diameter

*E-mail: andras.kovacs@broadbit.com

and 22 m length. S-type and N-type thermocouples were used for temperature sensing. The heating was controlled by temperature threshold triggered on/off switching in all cases, except the second and third experiments where thyristor electronics was used for precise heating power control. Figure 1 shows the reactor schematics.

3. Solid-state Li-Ni Alloying

An amount of 0.5 g Ni powder and 0.1 g Li was enclosed in the metallic container, and heat treated by being held for approximately 1 h at 1200°C. There was no excess heat detected during the heat treatment. After cooling and opening the container, an air-stable material was found inside, with metallic appearance. All the powders were sintered into a single solid. No free Li metal was observed. In summary, this experiment demonstrated that Li even up to 20 wt.% helps for the sintering of Ni powder, and diffuses well into the solid state metal.

4. First Experiment with the High Temperature Li-Ni-Cu Alloy

An amount of 2 g of Constantan wires (55% Cu + 45% Ni alloy, purchased from Conrad) and 0.06 g Li was loaded into a metallic container, and sealed by welding. Figure 2 shows the Cu-Ni alloy's phase diagram.

The sample was held at 1200°C, then the temperature was increased to 1300°C. After 10–15 min at 1300°C, an event occurred, which breached the metallic container wall (about 2 mm thick at thinnest part) and melted the heating wires above the sample, as well as the ceramic tube around which the wires are coiled. No detected sound accompanied this event. Figure 3 shows the damaged reactor and resulting appearance of the sample.

It can be observed in Fig. 3 that the container has bulged out along the drilled shaft (about 3/4 of the container length from the left), which indicates significant internal pressure and/or high temperature. While the originally enclosed O₂

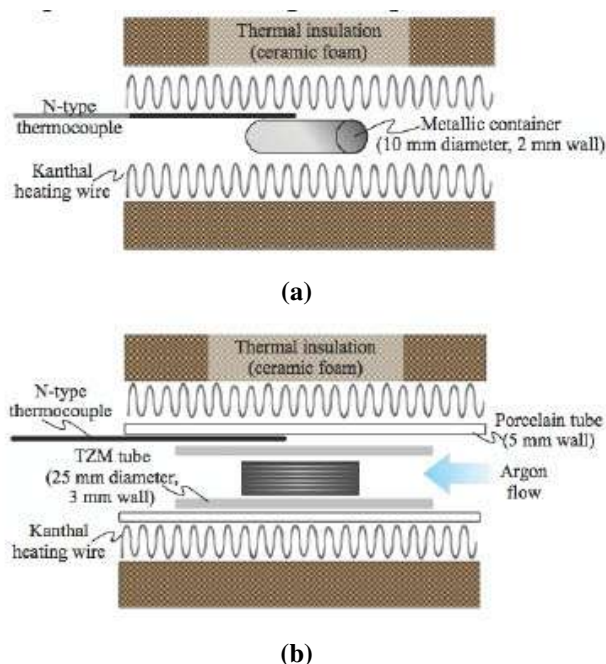


Figure 1. Reactor schematics for the container (*top*) and flow (*bottom*) experiment setups.

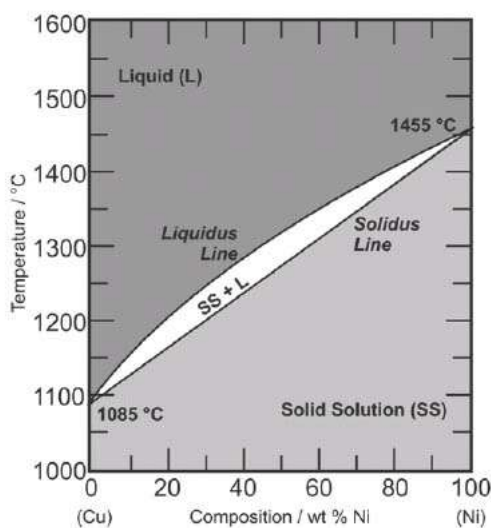


Figure 2. Cu–Ni phase diagram [2].

and N_2 gases react with molten Li already at the early phase of the heat treatment, Li_3N is known to decompose already below $1300^\circ C$. As the temperature approaches $1300^\circ C$, the estimated overpressure inside the container is 3 bar. Since the previously described Li–Ni alloying experiment showed no similar signs of bulging or container failure, some reaction process generated a higher internal pressure and/or a wall-softening higher internal temperature.

The leftover contents have the appearance of Ni_3O_4 and CuO material. Such thorough and complete burning of the sample indicates a significantly elevated temperature at the time of the container wall failure. The damage to the reactor material indicates that the ejected molten metal had a temperature well above $1500^\circ C$. This damage cannot be explained by Li vapor burning, because even a sideways flying molten metal droplet has melted the Kanthal wires, as can be seen on the upper tube in Fig. 3. Also, the complete breaching of the APM wall is consistent with a structural damage caused by very high internal temperature. Therefore, it appears that a sudden localized event has increased the internal temperature well above $1500^\circ C$ in certain parts of the container, and then caused the ejection of molten metal. A gamma-ray detector showed no signs of radioactivity in the resulting sample.

5. Instrumented Observation of a Single Reaction Event in the Li–Ni–Cu Alloy

The molten Li–Ni–Cu alloy experiment was repeated with an improved setup, employing more precise computer control and temperature logging, and thicker walls of the APM container. Constantan wires of 2 g and 0.06 g of Li were again loaded into the metallic container. An N-type thermocouple was in direct contact with the container's outer wall for precise temperature logging.

Figure 4 shows the temperature logged during the experiment, from the point of exceeding $1200^\circ C$. The vertical axis shows the temperature and the horizontal axis shows the number of elapsed seconds from the start of heating. After reaching $1280^\circ C$, the heating program has been set to maintain a temperature of $1250^\circ C$. Approximately 1 kW of power was required to maintain the temperature of this reactor at $1250^\circ C$. An exothermic reaction apparently started at 1540 s, i.e. 9 min after exceeding $1200^\circ C$.

It can be seen in Fig. 4 that the control electronics gradually reduced the heating power as the temperature rose

**(a)****(b)****(c)**

Figure 3. View of the damaged reactor with breached container (a), zoom onto the melted part of the reactor (b), and the remainders of the container and sample material inside (c).

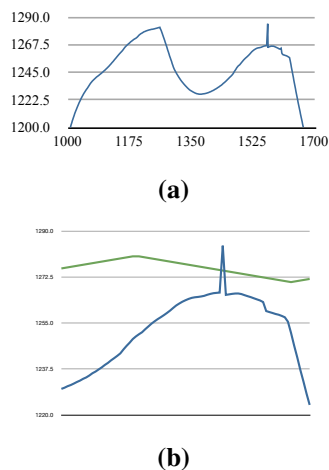


Figure 4. The temperature log of the experiment, with the green line showing heater voltage overlay (arbitrary scale).

above 1250°C. At about 1550 s time the thermocouple registered a sudden 20°C spike in temperature. We believe that this apparent spike is a signature of an X-ray emission burst, which was directly heating the thermocouple junction. The frequency of such radiative bursts is analyzed in more detail in a later section. Concurrently, a ‘metal geyser’ erupts from the container, once again melting through the heating filaments and ceramic tube above the container. Subsequently, all heating power is lost. As in the previous experiment, no sound was detected accompanying this event. Figure 6 shows the resulting view of the container after cooling. As detailed below, this reaction onset seems to be directly preceded by some melting of the Li–Ni–Cu alloy.

Note the observation of multiple similar upward spikes in subsequent experiments, such as shown in Fig. 12. The heating wires have not been broken in these follow-on experiments

Figure 5 shows details of the temperature history around the reaction event. The color coding of Fig. 5 shows our interpretation of the signal data. The yellow shading indicates either melting events or some other endothermic process inside the container, characterized by temporary slowing of the temperature rise. The radiative emission burst is a signature of the reaction event. Since the heating power is lost as a consequence of the reaction, the green shaded region indicates a temperature rise caused by the reaction itself. This interpretation is consistent with the effect of

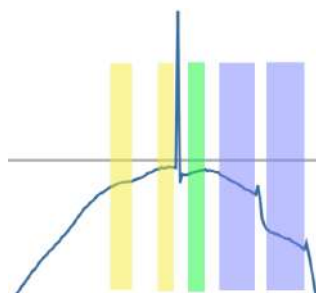


Figure 5. Temperature curve around the reaction event, the shading highlights the reaction related events.

spatial separation between the thermocouple (placed in the middle of the container) and the reaction hotspot (eruption is near the container end). A number of observations combine to indicate the localized hot-spot nature of the reaction:

- It was observed in the previous experiment that the ejected molten metal's temperature is above 1500°C, yet the thermocouple registers only a small temperature rise at the external container surface.
- While the radiative burst lasts for less than a second, the corresponding temperature rise is spread over several seconds and arrives with some delay, as the heat had to diffuse from the reaction site to the thermocouple to be detected.
- The small temperature rise registered at the top of container and a few centimeters from the molten metal burst location indicates a highly localized reaction hot-spot.

The radiative burst indicates the actual timing of the run-away reaction; there is a small subsequent local cooling due to lost heating power, followed by a gradual temperature rise from the propagated reaction heat, and finally followed by the cooling phase. In the cooling phase the slower cooling blue shaded regions indicate either the partial freezing of the container content or an ongoing exothermic process. Signatures of minor radiative bursts can be seen at the edge of the shaded regions.

After cooling, the container was opened. Its cross section is shown in Fig. 7. The 'metal geyser' apparently only transferred materials out of the container and then resealed itself, without any resulting hole in the container. Thus, apparently no external air entered the container. Consequently, Fig. 7 shows metallic surfaces across the container's interior, indicating that the exothermic reaction indeed happened within the Li–Ni–Cu alloy and was not due to oxidation with air. The melting of the ceramic tube and heating wires indicates that the internal reaction temperature was well above 1500°C at certain spots.

As can be seen in Fig. 7, a reddish shade appears at some spotty locations of the inner surface, while the bulk of the reaction material remains metallic gray. This indicates a copper accumulation on the metal surface, which might be caused by a segregation mechanism during solidification. It is also possible that an immiscibility gap appeared that was responsible for the separation of a Cu-rich liquid phase. The relationship between this behavior and the exothermic reaction is not clear at this stage but should deserve more investigation.



Figure 6. The container at the end of the experiment, with the view of the frozen metal geyser.



Figure 7. The cross-section view of the opened-up container, showing non-oxidized metallic surfaces along its interior.

A gamma-ray detector showed no signs of radioactivity in the resulting sample. Altogether, the above observations indicate that the observed reaction is of a localized run-away reaction type. To confirm this hypothesis, in subsequent experiments we expect to see radiative bursts of varying magnitude and temperature jumps of various magnitude/steepness. The spread of these quantities is expected to vary with the reaction-sensor distance and with the hot-spot reaction energy.

6. Exploring the Effect of Phase Change Events

A third molten Li–Ni–Cu alloy experiment was carried out with the following setup: the welded APM container was embedded into an approximately 0.5 cm thick ceramic encasement to prevent the spilling of bursting metal and to slow the thermal heating/cooling of the sample inside. Constantan wires of 4 g (Alfa Aesar) and 0.12 g Li were loaded into the metallic container. An N-type thermocouple was placed in direct contact with the ceramic encasement.

The temperature was raised in a stepwise fashion to different target temperatures, and at each target temperature to cycle $\pm 1^\circ\text{C}$ around the target. This methodology allows precise detection of phase changes and radiative noise. Figure 8 shows the observed temperature plots.

The normal ‘eventless’ operation would be a smooth temperature cycling curve within the $\pm 1^\circ\text{C}$ target tolerance limits. Every chart of Fig. 8 shows the time segment just after reaching the new target temperature from the previous lower temperature.

At every tested temperature, the temperature plot is initially a smooth cycle, then, after phase-change events, it becomes noisy for some minutes, and subsequently becomes smooth again. Based on the previous experiment, the observed noise is interpreted as the reaction’s radiative noise signature. The noise amplitude is smaller in this test than in the previous one, which is in line with the thermocouple being further away from the sample due to the ceramic encasement. This observed pattern supports our previous assumption that the reaction takes place at the solid metal surface; i.e. the reaction spontaneously initiates whenever a fresh new solid surface is generated. It also points to the transient or self-limiting nature of the observed phenomenon; the reaction appears to last for 2–3 min only in each case.

The intensity of the observed events does not seem to depend on the temperature. Figure 9 shows the temperature plot at 1310°C , which is essentially eventless. At this temperature the Li–Ni–Cu alloy is assumed to be completely

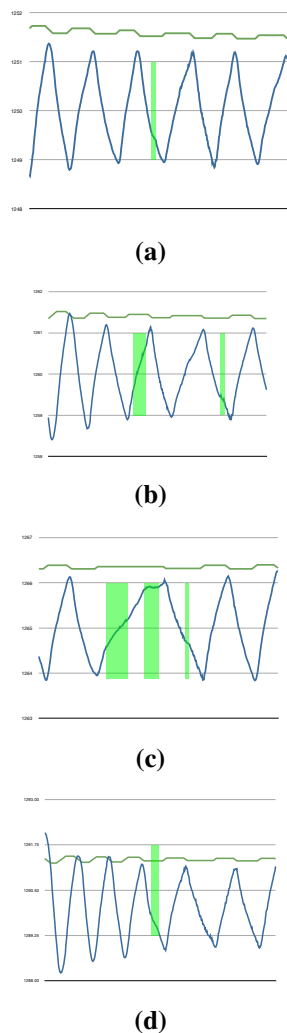


Figure 8. The temperature vs. time plot (*blue line*) at various reactor temperatures. The light green shading highlights either phase changes or some other endothermic/exothermic process. Each plot shows a 6–8 min time segment. The upper green curve shows the heater control voltage.

molten (Fig. 1). This observation supports our hypothesis that the reaction takes place at the surface of the solid phase and not in the molten phase.

After the conclusion of the experiment, it was noticed that some metal erupted from the container during the experiment, and flowed along the inner surface of the ceramic layer. The ceramic surface along the metal flow became shiny, indicating its local melting, which requires a temperature higher than 1500°C . The inside content of the APM container appears to have remained unexposed to air, as in the previous test.

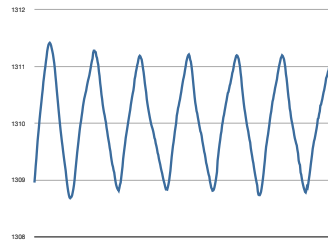


Figure 9. Temperature vs time plot at 1310°C (8 min segment).

7. Reaction Surface Cycling and Detection Of Reaction Heat Events

Since the observed reaction appears to terminate after a few minutes at a given temperature and since it appears to be triggered by a phase change, the question arises as to whether a stable reaction can be achieved through temperature cycling. The investigation of such temperature cycling was the aim of the fourth test. A further aim was to collect more heat signature data from the burst reaction events.

This experiment was carried out with the following setup: nine welded APM containers were embedded into an approximately 0.5 cm thick porcelain encasement. Constantan wires of 2 g and 0.06 g of Li were loaded into each container. As shown in Fig. 10, the N-type thermocouple was placed in the middle of the container cluster. The main purpose of the porcelain encasement in this improved setup was to ensure a uniform temperature of the containers. Since the thermocouple was embedded within this porcelain encasement, the measured temperature values in this setup correspond precisely to the container temperature at its given location. The containers are placed sideways from the heating wires, as there was not enough space to put them in the center.

After the experiment, some containers remained apparently un-breached while others breached. Figure 11 shows post-test views of some containers. In line with previous test observations, a bloating of the intact container can be observed and a dramatic damage on the breached container is observed. As the temperature control stayed below the Li boiling point throughout this experiment, and far below the APM melting point, this extensive container damage is an indication of the highly exothermic runaway nature of the observed reaction.

During this experiment the reactor temperature was cycled in an approximately $\pm 10^\circ\text{C}$ range. Low level radiative bursts were persistent during this cycling experiment, demonstrating the feasibility of extending the reaction lifetime.



Figure 10. Photo of the container setup in this experiment. The N-type thermocouple is embedded under the porcelain encasement, and the S-type thermocouple measures the temperature between the heating spirals.



Figure 11. Post-test views of an apparently intact (slightly bloated) container and a completely breached container.

Figure 12 shows the temperature plot during one part of the temperature cycling process; the radiative bursts are seen to become periodically weaker and stronger during the cycling. This data confirms the few-minute lasting self-limiting reaction events, which were similarly observed in the previous experiment, and gives further evidence to the idea that the reaction takes place on the solid alloy surface. Based on this data, it is proposed that the reaction can be nearly continuous when temperature cycling has periodicity on the order of minutes. With slower temperature cycling periodicity, e.g. on the order of an hour, the reaction would be expected to persist for only a small fraction of the time.

The most notable direct reaction heat events are shown in Fig. 13. As expected, all events showed an abrupt temperature jump. The strongest one is in the first example, showing a 10°C jump followed by cooling towards the preceding temperature. This data indicates the reaction takes place through run-away events in strongly localized hot-spots.

The second example in Fig. 13 shows that the initial reaction heat event was detected already slightly below 1200°C, when there was no molten phase yet, indicating a minimum temperature for this reaction at the solid alloy surface.

Since more temperature jumps were observed than the number of breached containers (Fig. 13 shows only the most pronounced ones), and since similar temperature jumps were observed also in a later experiment under Ar-flow (e.g. the green curve of Fig. 17 shows a 6°C jump at 60 s time), these temperature jumps cannot be explained as sudden oxidation events.

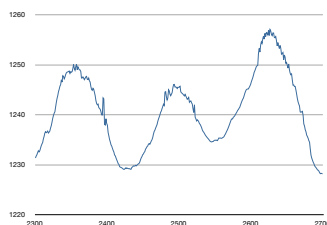
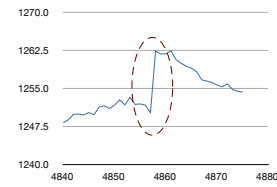
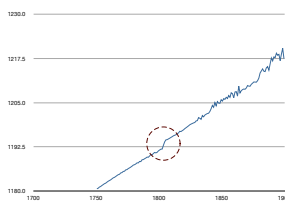


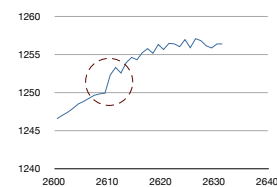
Figure 12. Temperature log of the temperature cycling process. The horizontal axis indicates the experiment time (seconds).



(a)



(b)



(c)



(d)

Figure 13. Highlights of the most pronounced temperature jump events. The horizontal axis indicates the experiment time (seconds).

Figure 14 shows the post-mortem metallic surfaces of the Li–Ni–Cu alloy. The round objects are ejected alloy metal pieces originating from some of the containers. The previously noted copper accumulation is even more clearly seen on these surfaces. As the copper concentration grows, the surface takes on a yellowish color, and then becomes copper-red in the spots where the copper is highly concentrated.

8. Peak Reaction Power Measurement

A fifth molten Li–Ni–Cu alloy experiment was carried out with an Ar-flow based setup: 15 g Constantan foils (Schlenk) and 0.5 g Li wires were loaded into an open TZM (99.4% Mo, 0.5% Ti, 0.1% Zr) metal tube. The TZM tube was placed



(a)



(b)



(c)

Figure 14. Apparent copper accumulation on the surfaces of the samples.

into a ceramic tube flooded with an Ar flow. An N-type thermocouple was placed between the TZM and ceramic tubes. The heating voltage and current were measured by a Voltcraft EL 4000 device.

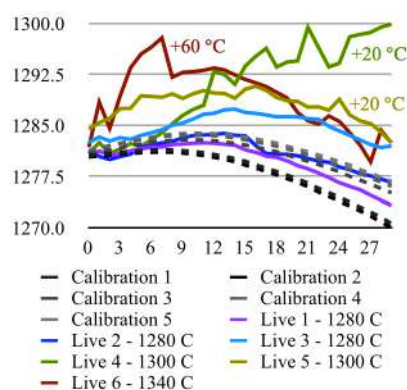


Figure 15. Post-heating temperature charts, showing 30 s evolution after heating stop.

This experiment was aimed at quantifying the reaction power and validating heat production. A calibration test was performed on the empty reactor, using the following temperature cycling program: constant power heating was used from 1200 to 1280°C, heating was turned off at the 1280°C upper temperature threshold, and then constant power heating was turned back on at the 1200°C lower temperature threshold. The employed heating power was approximately 1.5 kW. The dashed lines of Fig. 15 show 30 second segments of temperature evolution, starting from the moment when heating was turned off. The cooling rate was slightly decreasing in subsequent cycles as the insulating outer reactor walls heated up.

The live test run was started from the same room temperature initial condition as the calibration run, and upon reaching 1200°C the initial three cycles used the same heating program cycling between 1200°C and 1280°C thresholds. The purple-blue lines of Fig. 15 show the temperature evolution in these initial cycles, starting from the moment when heating was turned off. The shape and trend of these curves gradually diverges from corresponding calibration curves, indicating a start-up of the reaction. An exothermic reaction signature is noticeable in each temperature cycle.

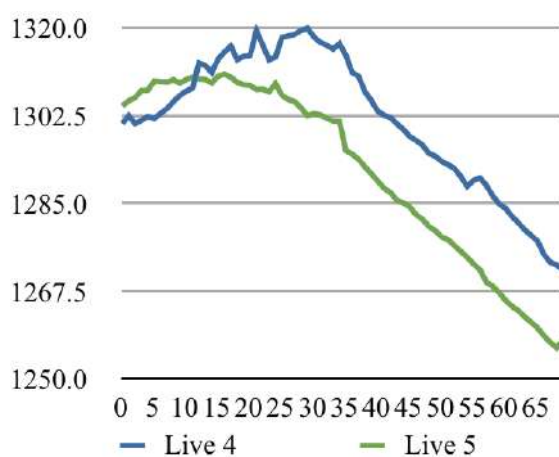


Figure 16. Comparison of live run's cycle 4 vs. 5 cooling phase temperature charts, showing 70 s duration post-heating segment.

In the third cycle, the temperature was rising for 14 s after turning off the heating, and stayed above 1280°C even 30 s after turning off the heating.

In the next two temperature cycles the upper threshold limit was adjusted to 1300°C. For the sake of comparison, Fig. 15 shows the corresponding temperature evolution (green curves) with a –20°C offset. It is noted that while Figs. 8 and 9 show the container in almost thermal equilibrium, Fig. 15 shows the temperature evolution just after a heating rate of 20°C/min. The strongest self-heating event has been observed in cycle 4; it is therefore used for the peak power rate estimation. The repeated cycle at 1300°C showed much smaller self-heating power, essentially maintaining temperature for over 30 s. Finally, the last cycle, where heating remained turned on up to the 1340°C temperature threshold, showed very fast initial self-heating which extinguished after 7 s. This is consistent with the eventless over-1300°C behavior shown in Fig. 9.

To estimate the peak power rate, Fig. 16 compares cycle 4 to cycle 5 cooling just after the heating was switched off. As a conservative estimate, we neglect any reaction heat which cycle 5 has produced during this time. The exothermic reaction of cycle 4 caused self-heating within the 6–26 s time segment, i.e. about 20 s duration. The subsequent time-wise separation of the cooling curves was 13 s. Considering that the 1.5 kW heating was turned on 69% of the time during calibration, it took 1 kW average heating power to maintain the reactor temperature. Therefore self-heating rate of cycle 4 shown in Fig. 15 was at least 650 W, in order to have generated the 13 s time-wise separation^a. This corresponds to a peak power rate of 42 W/g with respect to the mass of reaction materials.

A longer time view of the temperature evolution is shown in Fig. 17, where the vertical line indicates the time when the electric heating was turned off. This figure uses same color coding as Fig. 15, but without any temperature offsets.

It is seen also from Fig. 17 that while all calibration temperature curves are very smooth, the live test runs are increasingly erratic. The first two calibration runs have significantly lower slope than the other calibrations or the first two live runs. Their lower slope might have been caused by some transitory effect relating to the warm-up or initial usage of this flow reactor.

Energy-producing time periods can be visually gauged as those segments where the slope of temperature change significantly deviates from the calibration slopes. Qualitatively, the most noteworthy heat-producing time periods are:

- 120–150 s of cycle 4; pure self-heating causes continuous temperature rise,
- 0–120 s of cycle 5; rise gradient was noticeably higher than during calibration,
- 72–130 s of cycle 6; rise gradient had an inflection point and transitioned to higher value.

In summary, the exothermic reaction was observed to produce heat at a peak rate of 42 W/g with respect to the mass of reaction materials; this power rate lasted for 20 s. With the above-described temperature cycling program, several heat-producing time periods were observed during the 40 min experiment run.

Considering all the previous experimental observations, we propose that the exothermic reaction raises the reaction hot-spots' temperature well above the Li boiling point. The evaporating Li causes a significant pressure rise, and the bulging and bursting of the APM containers. In this experiment run, we observed that the evaporated Li was evacuated from the reactor by the Ar flow. Figure 18 shows the blackened inner surface of the ceramic tube downstream, onto which Li condensed out. No discoloration of the tube was observed upstream. This hypothesis implies that the observed exothermic reaction might be sustained for a longer time with the combined use of temperature cycling and a leak-free container.

Figure 19 shows the post-experiment view of the reaction tube. Parts of the metal foils retained their original shape, parts were melted around the tube walls, and parts clumped together, e.g. the piece seen in the middle of the image. The de-alloying of copper is again clearly observable along the walls. Although the metals were not physically

^aThat is $13 \times 1000/20$ W.

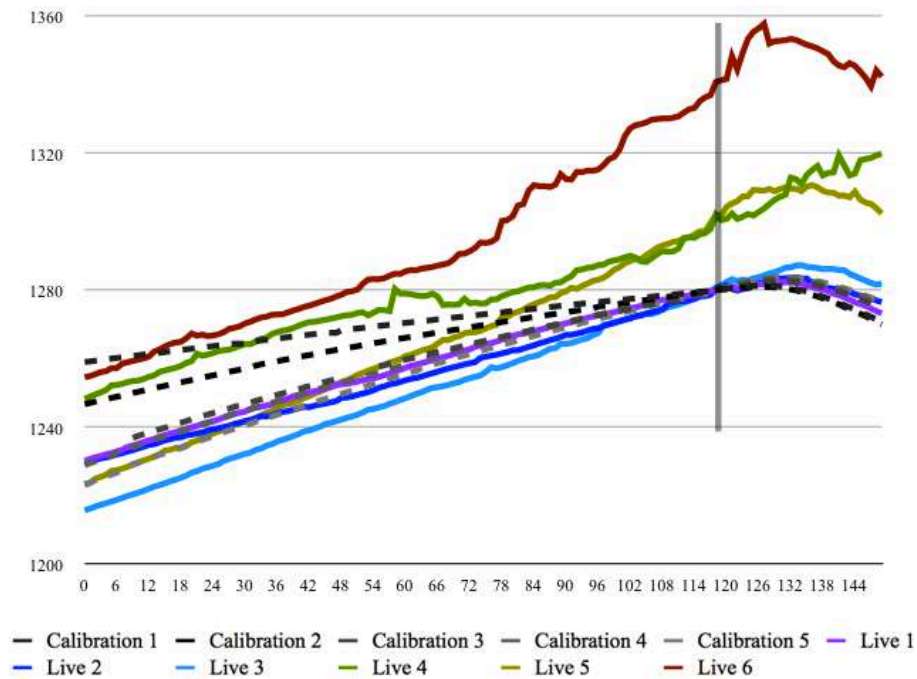


Figure 17. Temperature evolution during the last 2 min of heating, and the sub-sequent 30 s without external heating.

confined in the tube, they did not flow out because the tube has been sufficiently long to retain the molten metals inside, as seen in Fig. 19.

9. Average Reaction Power Measurement

A sixth molten Li–Ni–Cu alloy experiment was carried out with a N_2 -flow based setup: 9.52 g Constantan foils (Schlenk) and 0.28 g Li pieces were loaded into a steel tube, and sealed by welding. This steel container was then



Figure 18. Post-experiment view of the downstream ceramic tube surface.



Figure 19. Post-experiment view of the reaction materials inside the TZM tube.

placed into a TZM (99.4% Mo, 0.5% Ti, 0.1% Zr) metal tube, and sealed by welding. The schematics of this reactor setup is shown in Fig. 20.

This choice of container materials was motivated by the consideration of Li alloying/corrosion issues. While Li is known to be corrosive to most metals [3–5], especially at high temperatures, the employed container must be inert with respect to molten Li. Fe and Mo are suitable materials for containing high temperature molten Li, and most importantly Mo has a high melting point of 2600°C. By welding the TZM container, we have achieved a container with both high strength and high melting point, which is suitable for long term testing. The reactor was equipped with two thermocouples; the first one above the TZM container, and the second one approximately above the N₂-flow inlet. The N₂ sheath flow exited the reactor through small fissures at the top of the reactor chamber. The first thermocouple was used for the heating control feedback. Consequent to the above-described reactor structure, during the experiment the temperature at the second thermocouple was somewhat lower than the temperature at the first one.

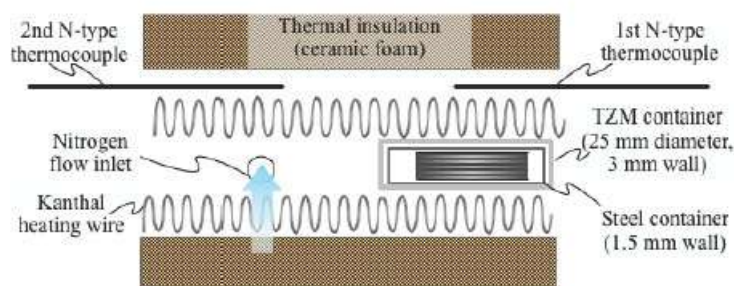


Figure 20. Reactor schematics for the TZM container based experiment setup.

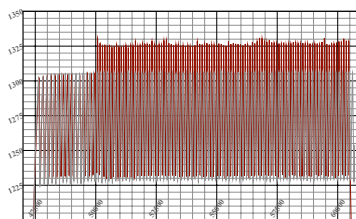


Figure 21. Temperature evolution of the first thermocouple during calibration (*gray*) and live experiment run (*red*).

A calibration run was first performed for measuring the baseline power consumption, followed by the live experiment run. Both runs used the same temperature program, the only difference was the absence of the TZM container in the calibration run. The temperature program consisted of ramping up the reactor temperature to its operational range over 13 h, followed by the temperature cycling program: constant power heating was used from 1240 to 1300°C, the heating was turned off at the 1300°C upper temperature threshold, and then the constant power heating was turned back on at the 1240°C lower temperature threshold. The employed heating power was approximately 1.2 kW.

The goal of this experiment run was to perform average reaction power measurement over an extended time period. The thermocouples were Kanthal sheathed for continuous operation in this high temperature range. The previously performed peak power measurement, radiative emission detection, or heat burst detection were not in the scope of this experiment; the thicker container walls and the employed thermocouple sheathing allow only averaged reaction power measurement.

Figure 21 shows the comparative temperature evolution of the first thermocouple during calibration (*gray* curve) and live run (*red* curve). The vertical axis shows the temperature, and the horizontal axis shows the number of seconds since the start of the temperature program. The 47 500 s value corresponds to the starting time of temperature cycling in the 1240–1300°C operating range. The very similar initial periodicity of the two curves indicates that the heating and cooling powers are nearly the same at the start. The 60 500 s value corresponds to the breaking of the heating wire during the live run; the subsequent drop in temperature is seen at the right. We believe this wire failure was caused by the wire temperature being too close to its melting point near the end of heating cycles.

It can be seen in Fig. 21 that the calibration run proceeded as expected through this time window. During the initial half hour, the temperature evolution of the live run corresponded closely to the temperature evolution during the calibration. About 30 min into the temperature cycling, the abrupt rise of the maximum live temperature to 1325°C indicated the start-up of the exothermic reaction. Over the subsequent three hours, the very consistent temperature peak values indicated the continuous operation of this reaction. Such continuous operation and good controllability are essential for any industrial applicability of this new energy source.

Figure 22 shows the comparative temperature evolution of the first thermocouple (*red* curve) and second thermocouple (*blue* curve) during the live run. The vertical axis shows the temperature, and the horizontal axis shows the number of seconds since the start of the temperature program.

Initially, the temperature at the second thermocouple cycled in the 1185–1270°C temperature range. As discussed above, this lower temperature range is caused by the N₂-flow cooling effect. At the same time when the starting-up exothermic reaction caused a temperature rise at the first thermocouple, the second thermocouple showed a remarkable drop in its temperature range. This range shift was the consequence of its sensitivity to the reduced electric heating. The produced reaction heat caused the first thermocouple to reach the shut-off temperature threshold faster and to reach the next turn-on temperature threshold later, which reduced the ratio of time when the electric heating was on. As the second thermocouple was closer to the heating wires than to the TZM container, and since it was cooled to a

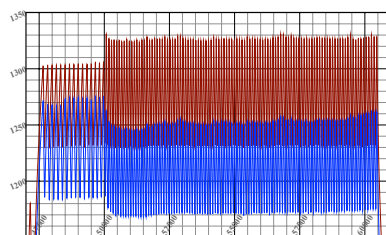


Figure 22. Temperature evolution of the first (*red*) and second (*blue*) thermocouple during the live experiment run.

larger extent by the N_2 -flow, the net result was a temperature range downshift at this location. Altogether, the data of Figs. 21 and 22 are very consistent with the hypothesis of continuous energy production during the last three hours of the live experiment run.

Quantitatively, the average reaction power was measured from the time ratio of electric heating-on times, summarized in Table 1. During the initial half-hour of the temperature cycling, the calibration and live run heating-on time ratios are very similar. The average grid voltage during calibration is 234 V, while the average grid voltage during live run is 232 V; i.e. the electric heating power is 1.7% higher during calibration. Altogether, the electric power input is measured to be 5% higher during calibration. At least part of this power mismatch may be caused by some initial bursts of the exothermic reaction.

During the last three hours of the experiment, the mismatch between the heating-on time ratios was 0.25. This means that the reaction power was equivalent to having electric heating on 25% of the time. Since the electric heating power was 1.2 kW, the average reaction power was 300 W. This corresponds to 30 W/g average reaction power with respect to the fuel mass.

The cumulative reaction energy over these last three hours was over 3 MJ. This amount of reaction energy is larger than any possible chemical reaction. The airtight TZM container has remained intact by the end of the experiment run.

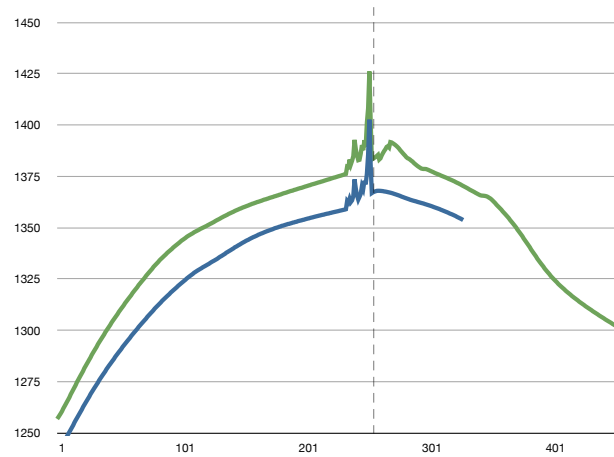
10. Radiation Analysis

The objective of the next experiment is to analyze the radiation emitted during the exothermic reaction. The same experimental setup was used as in the previous experiment, except that a flow of Ar was used instead of a flow of N_2 . The low end of the emitted radiation spectrum was monitored by an oscilloscope capable of up to 10 MHz spectroscopy. The high end of the emitted radiation spectrum was monitored by a Geiger counter, which was placed about 40 cm from the fuel container.

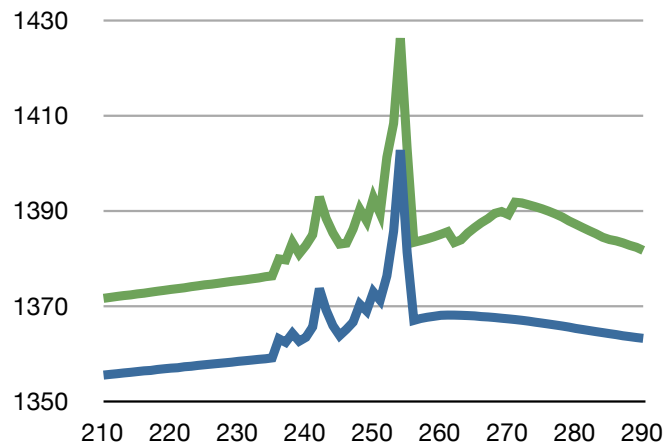
To get a clear reaction signal, a simple heating program was used, to trigger a single runaway reaction event. The temperature evolution of the experiment is shown in Fig. 23. After thermal reactor stabilization at about 1260°C, constant-power heating was started, using about 1.2 kW heating power. This heating was maintained until the heating wire was broken by the intense heat. This event is indicated by the dashed line in Fig. 23 at ~255 s. The horizontal axis shows the number of seconds from the start of constant-power heating. The onset of the reaction event is clearly

Table 1. Ratio of electric heating ON times

	Calibration	Live run
47 800–49 800 s	0.63	0.61
50 200–60 200 s	0.58	0.33



(a)



(b)

Figure 23. Temperature evolution measured by the first (*blue*) and second (*green*) thermocouple. The dashed line indicates loss of heating due to wire breaking.

seen in Fig. 23 at ~ 235 s, and it is also noticeable that the reaction hotspot was close to the second thermocouple because only this thermocouple detects the continued temperature rise after heating stops.

The Geiger counter indicated an elevated radiation level for only 4–5 s duration, approximately coinciding with the largest peak seen in Fig. 23. The counting level was normal before and after this brief event. During this elevated

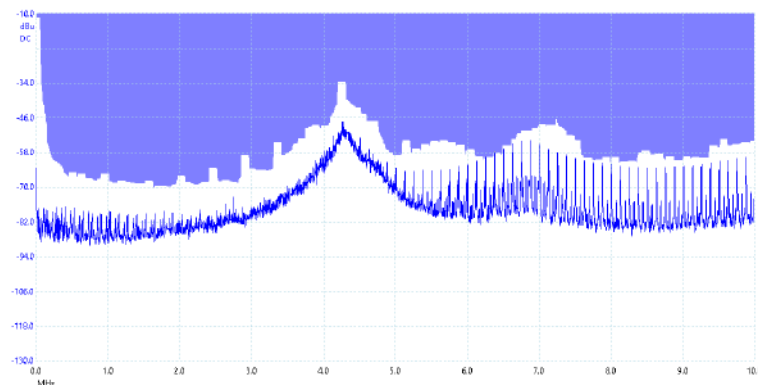


Figure 24. The background RF spectrum.

Geiger counter reading, a buzzing sound was heard from the reactor, similar to the sound of electric arcing.

The 235–255 s time segment of the thermocouple signal in Fig. 23 shows synchronized peaks between the two thermocouples, indicating radiative signal detection. Since the peaks are always in the positive direction only, and since the largest peaks have a measurable upwards and downwards slope, this signal is interpreted not as noise caused by an RF signal, but as radiative heating of the thermocouple junction. As discussed above, the reaction spot is close to the second thermocouple, and yet both thermocouples measure radiative heating peaks to have approximately the same magnitude. This observation indicates that the detected radiation frequency is strongly scattered by the metallic container; since both thermocouples are placed at equal distances from the metallic container, they detect scattered signals having approximately equal magnitude. Altogether, this thermocouple data indicates the radiative emission of X-rays. The frequency of detectable X-rays is constrained by the following requirements: high enough frequency to partially escape the metallic container, strong scattering by the metallic container, and strong enough interaction with the thermocouple junction to cause local heating of the thermocouple.

According to the minute-by-minute Geiger counter record shown in Table 2, an excess of 84 counts was produced over the 30 background counts during that reaction minute. As this excess count was concentrated in 4–5 s, it indicates about 40 times stronger radioactivity than the background signal.

Figure 24 shows the background RF spectrum measured before the experiment. The apparent peak near 4.2 MHz is caused by the increased sensitivity of the antenna geometry around that frequency; i.e., it is not a physical signal. The shaded region is the mask definition for log capture.

Figure 25 shows consecutive snapshots of RF spectrum captured during the reaction. The produced RF signal is approximately 20 dB above the background and is equally spread over the 1–10 MHz frequency range, which cannot

Table 2. One-minute resolution Geiger statistics relative to the reaction time.

	-5	-4	-3	-2	-1	0	1	2	3	4	5
Hits	31	33	17	40	31	114	34	34	23	29	33

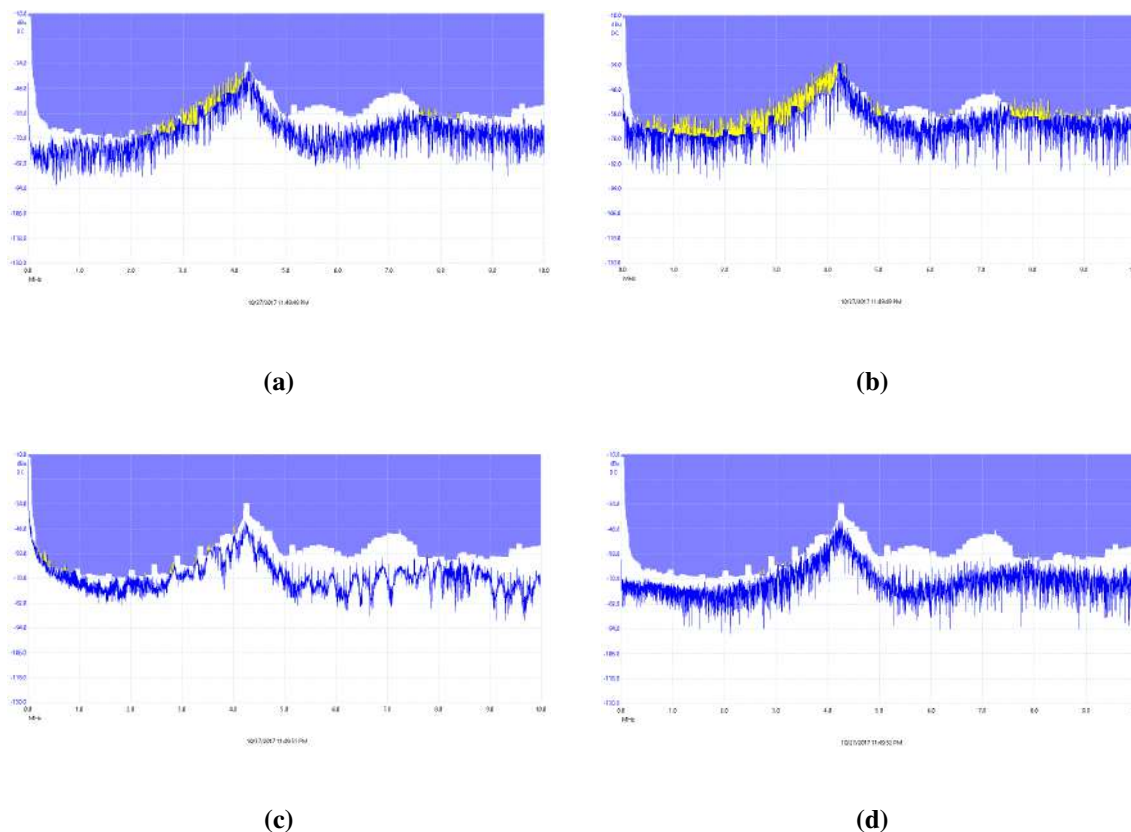


Figure 25. The RF spectrum evolution during the reaction event.

be produced by a chemical reaction or by arcing at the employed voltage. The consecutive snapshots show the rise and fading of this signal.

The third snapshot shows a stronger low-frequency component of the signal. This low-frequency component's shape and frequency range are characteristic of RF emission from electric arcing discharge. Therefore, this component is interpreted to be the signature of the electric arcing between the wires, whose presence was also detected from its sound. Since this signal is generated by ionized argon, it is not coming from the reaction itself; it is however an additional indicator of ionizing radiation.

Altogether, this electromagnetic emission analysis indicates a broad spectrum radiative emission spanning the RF, X-ray, and gamma frequency ranges. This data provides insights into the reaction signature and dynamics.

11. Conclusions

An exothermic reaction has been found to be spontaneously initiated in the Li–Ni–Cu alloy in the 1200–1300°C temperature range. The reaction is fully reproducible, with a 100% reproduction rate over the course of six test events. The reaction appears to be a series of localized run-away bursts at the Li–Ni–Cu alloy's solid surface, and is accompanied

by simultaneous broad spectrum radiative emission. The reaction self-extinguishes after a few minutes at constant temperature, but can be restarted via molten-solid phase cycling of the alloy surface. With a temperature cycling program, we have been able to sustain the reaction for about 3 h. The reaction is likely to be extendable to longer time scales. The average reaction power was approximately 30 W/g, while the peak power rate was approximately 40 W/g. With such power levels, this newly discovered reaction is industrially relevant. The described experimental setup facilitates further study and elucidation of the nature of this reaction. The planned scope of further experiments includes achieving longer experiment runs, and post-experiment isotope analysis of the reaction fuel.

Acknowledgements

The authors are grateful to Dr. Pekka Janhunen for the insightful consultation and advising, and to Pertti Heikkinen for the TZM material welding.

References

- [1] US patent 3383204.
- [2] http://www.spaceflight.esa.int/impress/text/education/Solidification/Phase_Diagrams.html.
- [3] W.D. Manly, *Fundamentals of Liquid Metal Corrosion*, Oak Ridge National Laboratory, 1956.
- [4] E.E. Hoffman and W.D. Manly, *Corrosion Resistance of Metals and Alloys to Sodium and Lithium*, Oak Ridge National Laboratory, 1957.
- [5] G. DeVries, The corrosion of metals by molten lithium, in J.E. Draley and J.R. Weeks (Eds.), *Corrosion by Liquid Metals*, Springer, Boston, MA, 1970.



Research Article

Hydrogen-lithium Low Energy Resonant Electron-capture and Bethe's Solar Energy Model

Xing Z. Li*, Zhan M. Dong, Chang L. Liang, Yun P. Fu, Bin Liu and Gui S. Huang

Department of Physics, Tsinghua University, Beijing 100084, China

Shu X. Zheng and Si Chen

Department of Engineering Physics, Tsinghua University, Beijing 100084, China

Abstract

Bethe's solar energy model is applied to the case of $(p+{}^6\text{Li})$ low energy resonance near 50 eV. The cross-section would be greatly enhanced to meet the experimental observations in Ni-H(LiAlH₄) systems and in "Hydrogen-lithium fusion devices." The width of the resonance does not prevent low energy resonance from contributing to the cross-section.

© 2017 ISCMNS. All rights reserved. ISSN 2227-3123

Keywords: Bethe's solar energy model, Huizenga's three puzzles, LiAlH₄, $(p+{}^6\text{Li})$ Low energy resonance, New formula for fusion cross-section with three parameters, Resonant electron capture, Width of resonance peak

1. Introduction

A combination of strong interactions and weak interactions is the essence of Bethe's solar energy model, in which a nuclear potential of a strong interaction was used to calculate the elastic scattering of $(p+p)$, and a nuclear transmutation of a weak interaction was used to calculate the probability of a transition from $(p+p)$ continuum to $(n+p)$ discrete energy level (deuteron) [1]. This model gave the correct fusion rate of $p + p \rightarrow D + e^+ + \text{neutrino}$, and made a good prediction of the solar temperature. In Bethe's model there was no low energy resonance between $(p+p)$, and the positron emission was the dominant weak interaction process. The same model might be applied to $(p+{}^6\text{Li})$ low energy resonance if the effect of $(p+{}^6\text{Li})$ low energy resonance is fully included, and if the orbital electron capture of the beryllium excited state (${}^7\text{Be}^*$) is introduced. The reaction rate is compared with the "excess power" in the Ni-H gas-loading experiments with LiAlH₄ as an additive [2–5], and is compared with Lipinski's measurement of the helium ion emission rate from low temperature $(p+{}^6\text{Li})$ plasma [6]. Both comparisons lead to a $(p+{}^6\text{Li})$ low energy resonance near 50 eV. This is consistent with $(p+{}^6\text{Li})$ low energy fusion cross-section as well [7].

*E-mail: lxz-dmp@tsinghua.edu.cn.

2. Bethe's Solar Energy Model and its Application to (p+⁶Li) Low Energy Resonance

Bethe assumed that the formation of deuterons through (p+p) fusion reaction is an elastic scattering of (p+p) followed by a positron emission. The cross-section of this reaction may be written as:

$$\sigma(E) = \frac{gF(W_e)}{v} \left| \int \psi_f \psi_i d\tau \right|^2. \quad (1)$$

Here, g is the coupling constant of weak interaction, and $F(W_e)$ is a factor different for the case of K-capture or positron emission. $\left| \int \psi_f \psi_i d\tau \right|^2$ is the probability of transition from a mother state, ψ_i , to a daughter state, ψ_f . The overlapping of these two wave functions determines the amplitude of this transition. For (p+⁶Li) low energy resonance, ψ_i is the wave function of (p+⁶Li) relative motion. At large distance between p and ⁶Li, ψ_i approaches to a plane wave, e^{ikz} , normalized to a unit density (where k is the wave number of relative motion in the z -direction in the center of mass system). Thus the current density of probability is ν , and ν is the speed of relative motion. At low energy, only the S-partial wave is important for the interaction; hence, in the Coulomb interaction region, the wave function may be written as:

$$\Psi_i = \frac{1}{kr} e^{i\delta} (\cos[\delta]F_0[r] + \sin[\delta]G_0[r]) \quad (r > r_0). \quad (2)$$

Here, r is the distance between p and ⁶Li; δ is the phase shift of the S-partial wave due to the strong nuclear interaction. F_0 and G_0 are the regular and irregular Coulomb wave function for S-partial wave, respectively. r_0 is the radius of the nuclear interaction region. Inside the nuclear interaction region, the wave function is

$$\Psi_i = \frac{1}{kr} e^{i\delta} (\cos[\delta]F_0[r_0] + \sin[\delta]G_0[r_0]) \frac{\sin[k_1 r]}{\sin[k_1 r_0]} \quad (r < r_0), \quad (3)$$

$$k = \sqrt{\frac{2\mu E}{\hbar^2}}, \quad k_1 = \sqrt{\frac{2\mu(E - U_{pp})}{\hbar^2}}.$$

k and k_1 are the wave numbers in the Coulomb field and inside the nuclear potential well U_{pp} , respectively. \hbar is the Planck constant divided by 2π . ψ_f is the final state of the electron-capture process:



⁷Li* may be assumed as a confined state of a neutron in the potential well of ⁶Li* (similar to neutron halo of Lithium we may call it neutron skin of ⁶Li* in the case of the electron-capture in (p+⁶Li) low energy resonance):

$$\psi_f = \frac{1}{\sqrt{2\pi b(1 + \frac{r_0}{b})(1 + \frac{\beta^2}{k_2^2})}} \frac{1}{r} e^{-\beta(r-r_0)}, \quad \beta = \sqrt{\frac{2\mu E_b}{\hbar^2}}, \quad b = \frac{1}{\beta} \quad (r > r_0), \quad (5)$$

$$\psi_f = \frac{1}{\sqrt{2\pi b(1 + \frac{r_0}{b})(1 + \frac{\beta^2}{k_2^2})}} \frac{1}{r} \frac{\sin[k_2 r]}{\sin[k_2 r_0]}, \quad k_2 = \sqrt{\frac{2\mu(-U - E_b)}{\hbar^2}} \quad (r < r_0). \quad (6)$$

Here, E_b is the binding energy of the neutron in the nuclear potential of excited ⁶Li*, U is the depth of this nuclear potential. r_0 is the radius of this potential, b is the range of the extension of neutron wave function outside this nuclear interaction region. The coefficients in ψ_f normalize the final state in its confined region. ψ_f is a rapidly

decrease function with r outside the nuclear interaction region. The overlapping between ψ_i and ψ_f is maximized when the shape of ψ_i is very similar to ψ_f , and the amplitude of ψ_i is greatly enhanced at the nuclear boundary. Hence, we are looking for the case where G_0 is dominant in the wave function in Eq. (2), because G_0 is a rapidly decrease function with r outside the nuclear interaction region and G_0 is greatly enhanced at the nuclear boundary as well (F_0 behaves in an opposite way). In order to make G_0 dominant in the wave function ψ_i , the coefficient of G_0 in Eq. (2), $\sin[\delta]$, should be enhanced. $\sin[\delta]$ is determined by the nuclear boundary condition at $r = r_0$, i.e.

$$\cot[\delta] = \left[-\left(\frac{G_0}{F_0}\right) \left(\frac{D_L - \frac{k}{G_0} \frac{\partial G_0}{\partial \rho}}{D_L - \frac{k}{F_0} \frac{\partial F_0}{\partial \rho}} \right) \right]_{r=r_0}. \quad (7)$$

Here, D_L is the logarithmic derivative of the wave function at the boundary between nuclear interaction region and the Coulomb field. $\rho \equiv kr$. Usually, $\cot[\delta]$ is a very large number, because (G_0/F_0) is a very large number. At the very low energy,

$$\begin{aligned} F_0 &= C_0 \rho \Phi[y], & G_0 &= C_0^{-1} \Theta[y], \\ C_0 &= \sqrt{\frac{2\pi\eta}{e^{2\pi\eta} - 1}}, & \eta &= \frac{1}{ka_c}, \\ a_c &= \frac{4\pi\epsilon_0 \hbar^2}{z_a z_b \mu e^2}, \end{aligned} \quad (8)$$

$$\Phi[y] \equiv \frac{1}{\sqrt{y}} I_1[2\sqrt{y}], \quad (9)$$

$$\Theta[y] \equiv 2\sqrt{y} K_1[2\sqrt{y}]. \quad (10)$$

Here, $y = 2r/a_c$, $I_1[2\sqrt{y}]$ is the modified Bessel Function of first kind, and $K_1[2\sqrt{y}]$ is the modified Bessel Function of second kind. a_c is the length of Coulomb unit, ϵ_0 is the dielectric constant in vacuum, z_a and z_b are charge number of colliding particles, respectively; e is the charge of a proton. At low energy, $k \rightarrow 0$, η is very large; then, C_0 is a very small number. $\Phi[2r/a_c]$ and $\Theta[2r/a_c]$ are slow varying functions and equal to 1 when $r \rightarrow 0$. Therefore,

$$\left(\frac{G_0}{F_0}\right) = \frac{\Theta}{C_0^2 \rho \Phi} \rightarrow \frac{e^{2\pi\eta} - 1}{2\pi\eta\rho} \Big|_{r=r_0} = \frac{e^{2\pi\eta} - 1}{2\pi} \frac{a_c}{r_0} \equiv \frac{a_c}{r_0} \theta[E]^2. \quad (11)$$

The ratio (G_0/F_0) in Eq. (7) should be an exponentially increase number at low energy. Consequently,

$$\sin[\delta] = \sqrt{\frac{1}{1 + \cot[\delta]^2}} \rightarrow 0.$$

This makes F_0 dominant instead of G_0 dominant. However, there is a way to make G_0 dominant. Notice that at low energy three of logarithmic derivatives at the nuclear boundary condition in Eq. (7) approach to three constants [8].

$$\frac{k}{G_0} \frac{\partial G_0}{\partial \rho} \rightarrow -\sqrt{\frac{2}{a_c r_0}}; \quad (12)$$

$$\frac{k}{F_0} \frac{\partial F_0}{\partial \rho} \rightarrow \sqrt{\frac{2}{a_c r_0}}; \quad (13)$$

$$D_L = k_1 \cot[k_1 r_0] \rightarrow \sqrt{\frac{2\mu(-U_{pp})}{\hbar^2}} \cot \left[\sqrt{\frac{2\mu(-U_{pp})}{\hbar^2}} r_0 \right]. \quad (14)$$

For a certain specific nuclear potential, U_{pp} , it is possible to make the difference of two logarithmic derivatives in numerator of Eq. (7) as small as needed for a resonance to appear: e.g.

$$\frac{D_L - \frac{k}{G_0} \frac{\partial G_0}{\partial \rho}}{D_L - \frac{k}{F_0} \frac{\partial F_0}{\partial \rho}} \rightarrow \frac{r_0}{\theta[E_0]^2 a_c} \ll 1. \quad (15)$$

Then, for

$$E > E_0, \quad |\cot[\delta]| \sim \frac{\theta[E]^2}{\theta[E_0]^2} \ll 1 \quad \text{and} \quad \sin[\delta] = \sqrt{\frac{1}{1 + \cot[\delta]^2}} \rightarrow 1.$$

Thus G_0 is dominant. It should be noticed that $\theta^2(E)$ defined in Eq. (11) is different from $\frac{1}{C_0^2}$ in Eq. (8). When $E \rightarrow \infty$, $\theta^2(E) \rightarrow 0$, but $1/C_0^2 \rightarrow 1$. The question remaining is: Is there really a nuclear boundary which makes $|\cot[\delta]| \ll 1$?

3. Search for the Low Energy Resonance use (p+⁶Li) Fusion Reaction

We can use the (p+⁶Li) fusion reaction data [9] to investigate if there is a low energy resonance, because we have derived a tool to extract information about $\cot[\delta]$ from the fusion cross-section data. That is a new formula for light nuclei fusion cross-section, $\sigma_0[E]$, at low energy [10–15].

$$\sigma_0[E] = \frac{\pi}{k^2} \left(1 - |e^{i2\delta}|^2 \right) \equiv \frac{\pi}{k^2} \frac{(-4W_i)}{W_r^2 + (W_i - 1)^2}. \quad (16)$$

Here, $W \equiv \cot[\delta] = W_r + iW_i$, which determines the coefficient in front of $G_0[r]$ in Eq. (2). We may calculate W_r based on experimental data $\sigma_0[E]$ if W_i is assumed:

$$W_r^2 = \frac{\pi}{k^2} \frac{(-4W_i)}{\sigma_0[E]} - (W_i - 1)^2. \quad (17)$$

According to Eqs. (7) and (11), we may extract the fast varying part in W and define $(w_r + iw_i)$ as

$$W = \left[- \left(\frac{a_c}{r_0} \theta[E]^2 \right) \left(\frac{D_L - \frac{k}{G_0} \frac{\partial G_0}{\partial \rho}}{D_L - \frac{k}{F_0} \frac{\partial F_0}{\partial \rho}} \right) \right]_{r=r_0} \equiv \theta[E]^2 (w_r + iw_i). \quad (18)$$

At very low energy, $(w_r + iw_i)$ is a slowly varying function of energy; particularly, w_i is almost a constant because it is proportional to the ratio of flight-time to life-time $\tau_{\text{flight}}/\tau_{\text{life}}$ [12]. Here, τ_{flight} is the flight time of proton inside the nuclear interaction region; τ_{life} is the life-time of the composite nuclear state, (p+⁶Li). Use Eq. (18), we have w_r^2 as a function of energy E :

$$w_r^2 = \frac{\pi}{k^2} \frac{(-4w_i)}{\theta[E]^2 \sigma_0[E]} - \left(w_i - \frac{1}{\theta[E]^2} \right)^2 \quad (19)$$

There are three features in Eq. (19): (1) w_r^2 is a positive number by definition; (2) w_i must be a negative number to keep $w_r^2 > 0$; (3) we may adjust w_i to keep the minimum of w_r^2 equal to zero. This zero point of w_r^2 is just the

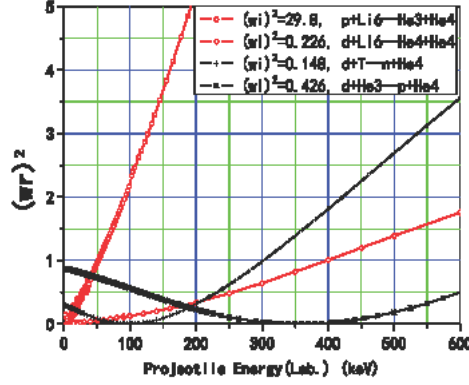


Figure 1. The minimum of w_r^2 approaches zero for four pairs of fusion reactions when w_i is assigned a specific number (data points are from ENDF/B-VII.1(2011)[9]).

resonance point, E_0 . Figure 1 shows a slow varying w_r^2 when w_i is assumed as a constant for four pairs of nuclear reactions.

Even though the data near the low energy limit might be not very accurate, it is enough to judge qualitatively whether there is a resonance; i.e. whether $w_r^2 = 0$ or $w_r^2 \ll 1$ is below or above the lower limit of the experimental data for energy. Figure 1 demonstrates that there are resonances, $w_r^2 = 0$, at $E_0 \sim 95$ keV and $E_0 \sim 375$ keV for d+T and d+He3 (+ and x signs), respectively. These are the famous resonances in hot fusion reactions. On the other hand, Fig. 1 reveals also that there are possible resonances near zero energy for (p+⁶Li) and (d+⁶Li) fusion reactions as well (open squares and circles). These are very important to understand the “anomalous heat effect” in early heavy water electrolysis experiments with lithium ions in electrolyte [16–24], and “anomalous heat effect” in Ni–H gas-loading systems with LiAlH₄ as an additive [2–5]. Recently, the publication of Lipinski patent [6], entitled as “Hydrogen-lithium fusion device,” strongly suggested that lithium is just the fuel per se.

4. Average over Maxwell Velocity Distribution

In order to compare with the experimental data of anomalous heat effect (e.g. [2–6]), we have to average the cross-section over Maxwell velocity distribution of temperature T . Use Eq. (1), we have the average reaction rate

$$\begin{aligned}
 \langle \sigma[E] v \rangle &= \left(\frac{\mu}{2\pi T} \right)^{3/2} \int_0^\infty gF(W) \left| \int \Psi_f \Psi_i d\tau \right|^2 \exp \left[-\frac{\mu v^2}{2T} \right] 4\pi v^2 dv \\
 &= \left(\frac{\mu}{2\pi T} \right)^{3/2} gF[W] \frac{(4\pi b^2)^2}{2\pi b} \Lambda^2 \int_0^\infty \cos[\delta]^2 C_0^2 \exp \left[-\frac{\mu v^2}{2T} \right] 4\pi v^2 dv \\
 &= \frac{32\pi^2 \hbar}{\sqrt{\mu}} \left(\frac{1}{2\pi T} \right)^{3/2} \frac{gF[W]}{a_c} b^3 (w_r)^2 \Lambda^2 \int_0^\infty \frac{\theta[E]^2}{1 + (w_r \theta[E])^2} \exp \left[-\frac{E}{T} \right] dE,
 \end{aligned} \tag{20}$$

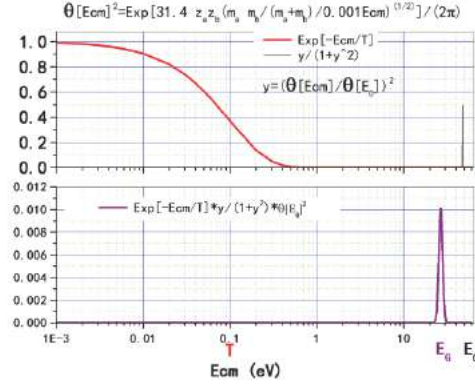


Figure 2. A Gamow peak is formed at E_G between T and E_0 .

$$\Lambda = \frac{\Lambda_1 + \Lambda_2 + \Lambda_3}{\sqrt{\left(1 + \frac{r_0}{b}\right) \left(1 + \frac{\beta^2}{k_2^2}\right)}}, \quad (21)$$

$$\Lambda_1 = \frac{\frac{1}{2}x_0^2 \left(\Phi \left[\frac{2r_0}{a_c} \right] + \frac{a_c}{r_0 w_r} \Theta \left[\frac{2r_0}{a_c} \right] \right)}{\sin \left[\frac{k_1}{\beta} x_0 \right] \sin \left[\frac{k_2}{\beta} x_0 \right]} \int_0^{x_0} \sin \left[\frac{k_1}{\beta} x \right] \sin \left[\frac{k_2}{\beta} x \right] dx,$$

$$\Lambda_2 = \int_{x_0}^{\infty} x \exp[-(x - x_0)] \Phi \left[\frac{2bx}{a_c} \right] dx, \quad (22)$$

$$\Lambda_3 = \frac{a_c}{r_0 w_r} x_0 \int_{x_0}^{\infty} \exp[-(x - x_0)] \Theta \left[\frac{2bx}{a_c} \right] dx.$$

In the case of low energy resonance, w_r is very small (see Eqs. (15) and (18)); therefore, only the terms with $1/w_r$ in Λ_1 and Λ_3 need to be kept in Λ^2 . Thus

$$(w_r)^2 \Lambda^2 \approx \frac{1}{\left(1 + \frac{r_0}{b}\right) \left(1 + \frac{\beta^2}{k_2^2}\right)} \left\{ \frac{\frac{1}{2}x_0^2 \left(\frac{a_c}{r_0} \Theta \left[\frac{2r_0}{a_c} \right] \right)}{\sin \left[\frac{k_1}{\beta} x_0 \right] \sin \left[\frac{k_2}{\beta} x_0 \right]} \left(\frac{\sin \left[\left(\frac{k_1}{\beta} - \frac{k_2}{\beta} \right) x_0 \right]}{\frac{k_1}{\beta} - \frac{k_2}{\beta}} - \frac{\sin \left[\left(\frac{k_1}{\beta} + \frac{k_2}{\beta} \right) x_0 \right]}{\frac{k_1}{\beta} + \frac{k_2}{\beta}} \right) + \frac{a_c}{r_0} x_0 \int_{x_0}^{\infty} \exp[-(x - x_0)] \Theta \left[\frac{2bx}{a_c} \right] dx \right\}^2. \quad (23)$$

The integrand of integral

$$\int_0^{\infty} \frac{\theta[E]^2}{1 + (w_r \theta[E])^2} \exp \left[-\frac{E}{T} \right] dE$$

has two factors competing with each other: $\exp[-\frac{E}{T}]$ decreases rapidly with E , when E is greater than T . On the other hand,

$$\frac{\theta[E]^2}{1 + (w_r\theta[E]^2)^2}$$

increases rapidly with E , before its peak at E_0 (if we assume $w_r = \frac{1}{\theta[E_0]^2}$). Because the “excess heat” in experiments is always increase with temperature, E_0 should be greater than T . As a result, Gamow peak is formed between T and E_0 . In Fig. 2 upper plot, the thick line (red) shows that the $\exp[-\frac{E}{T}]$ decreases rapidly with E when $E > T$, and the thin line (black) shows a sharp peak of function,

$$\frac{y}{1 + y^2}, \quad \text{where } y \equiv \theta[E]^2 w_r.$$

The integrand

$$\frac{\theta[E]^2}{1 + (w_r\theta[E]^2)^2} \exp\left[-\frac{E}{T}\right] = \frac{1}{w_r} \frac{y^2}{1 + y^2} \exp\left[-\frac{E}{T}\right]$$

would have a new peak at E_G shown in Fig. 2 lower plot. Therefore, this integral may be estimated by the steepest descent method.

$$\begin{aligned} \langle \sigma v \rangle = & \frac{32\pi^2 \hbar}{\sqrt{\mu}} \left(\frac{1}{2\pi T} \right)^{3/2} \frac{gF[W]}{a_c} b^3 \frac{1}{(1 + \frac{r_0}{b}) \left(1 + \frac{\beta^2}{k_2^2}\right)} \left\{ \frac{\frac{1}{2} x_0^2 \left(\frac{a_c}{r_0} \Theta \left[\frac{2r_0}{a_c}\right]\right)}{\sin\left[\frac{k_1}{\beta} x_0\right] \sin\left[\frac{k_2}{\beta} x_0\right]} \right. \\ & \times \left(\frac{\sin\left[\left(\frac{k_1}{\beta} - \frac{k_2}{\beta}\right) x_0\right]}{\frac{k_1}{\beta} - \frac{k_2}{\beta}} - \frac{\sin\left[\left(\frac{k_1}{\beta} + \frac{k_2}{\beta}\right) x_0\right]}{\frac{k_1}{\beta} + \frac{k_2}{\beta}} \right) \\ & \left. + \frac{a_c}{r_0} x_0 \int_{x_0}^{\infty} \exp[-(x - x_0)] \Theta\left[\frac{2bx}{a_c}\right] dx \right\}^2 \frac{1}{w_r^2 \theta[E_G]^2} \exp\left[-\frac{E_G}{T}\right] \sqrt{\frac{4E_G^2 \sqrt{2\mu E_G a_c}}{3\hbar}}. \quad (24) \end{aligned}$$

Here,

$$E_G = \left(\frac{\hbar T}{2\sqrt{2\mu a_c}} \right)^{2/3}$$

is the Gamow peak energy and $\hbar = 2\pi\hbar$. We notice that the position of Gamow peak is determined by temperature T only, and the height of the Gamow peak is greatly enhanced by $\frac{1}{w_r} = \theta[E_0]^2$.

For the case of $p + {}^6\text{Li}^* + e^- \rightarrow T + {}^4\text{He} + \text{neutrino} + 4 \text{ MeV}$, $m_a = 1$, $m_b = 6$, $z_a = 1$, $z_b = 3$, $gF(W) \approx 0.9 \times 10^{-4} \text{ s}^{-1}$. The radius of nuclear potential is assumed same for both ($p + {}^6\text{Li}$) and for ($n + {}^6\text{Li}^*$); then, $r_0 = 1.746 \times 10^{-15} (m_a^{1/3} + m_b^{1/3}) = 4.9 \times 10^{-15} \text{ m}$. The depth of the nuclear potential between ($p + {}^6\text{Li}$), $-U_{pp}$, is assumed to keep the resonance condition: Eqs. (14) and (15). Thus, for ($p + {}^6\text{Li}$) $k_1 = 4.08 \times 10^{14} \text{ m}^{-1}$. The depth of the nuclear potential between ($n + {}^6\text{Li}^*$), $-U$, is assumed to have the binding energy $E_b = 782 \text{ keV}$ which is the necessary condition for turning a free proton into a bound neutron. Thus, $k_2 = 4.04 \times 10^{14} \text{ m}^{-1}$. Then, $\beta = 1.80 \times 10^{14} \text{ m}^{-1}$, $b = 5.56 \times 10^{-15} \text{ m}$, and $x_0 = 0.884$.

For H. Zhang's Ni-H (LiAlH_4) system [5], $T = 1000^\circ\text{C} = 1273 \times 1.38 \times 10^{-23} \text{ J}$,

$$E_G = \left(\frac{hT}{2\sqrt{2}\mu a_c} \right)^{2/3} = 4.55 \times 10^{-18} \text{J} = 28.4 \text{eV} \quad (25)$$

$$w_r^2 = \frac{1.61 \times 10^{-20}}{\langle \sigma v \rangle} \left(\frac{1}{T} \right)^{2/3} \exp \left[-\frac{8416}{T^{1/3}} \right] \quad (T \text{ is in units of Kelvin}). \quad (26)$$

When

$$w_r \equiv \frac{1}{\theta[E_0]^2}$$

is assumed, $E_0 = 48 \text{ eV}$. This value is very close to the lower limit of the proton beam energy, 50 eV, in Lipinski's patent [6]. After seven years of effort with 25 runs of experiments, Lipinski claimed that he was able to detect the helium when a low energy proton beam was injected into the lithium vapor. The lower limit of proton beam energy was 50 eV.

5. The Width of the Low Energy Resonance

The rapid decrease factor, $\exp[-\frac{E}{T}]$ and the rapid increase factor,

$$\frac{\theta[E]^2}{1 + (w_r \theta[E]^2)^2},$$

solved the problem of the width of the low energy resonance. The down-hill slope meets the up-hill slope at $E = E_G$, where the first derivative of the product of

$$\exp \left[-\frac{E}{T} \right] \times \left(\frac{\theta[E]^2}{1 + (w_r \theta[E]^2)^2} \right)$$

reaches zero. The width of this Gamow peak is determined by its second derivative, i.e.

$$\Delta E = 2 \sqrt{\frac{2 \log[2]}{f''[E_G]}}, \quad f = -\frac{E}{1.38 \times 10^{-23} T} - 31.4 z_a z_b \sqrt{\frac{m_a m_b}{0.625 \times 10^{16} (m_a + m_b) E}}. \quad (27)$$

Here, E is in units of Joules, and T is in units of Kelvin. $\Delta E = 3.4 \text{ eV}$ is a function of T only. Therefore it is independent of the resonance energy E_0 . Thus we need not worry about the width of Gamow peak while resonance energy E_0 approaches zero as long as $E_0 \gg E_G$.

Even if the width of resonance peak itself is not very small as we might see from Fig. 2 upper plot, because the resonance peak of

$$\frac{y}{1 + y^2} \text{ is at } y = 1,$$

and the width of this resonance peak is determined by the equation $y = 2 \pm \sqrt{3}$. Therefore the width of resonance peak approaches zero like

$$\left(\frac{1}{\log[E_0]} \right)^2$$

as we discussed in ICCF-17 [25].

There was a mistake that the width of resonance peak would approach zero like $\frac{1}{\theta[E]^2}$, because it was assumed that the position of resonance peak is determined by $W_r^2 = 0$ in Eq. (16), and the width of resonance peak is assumed to be determined by the equation of $W_r^2 \approx 1$. In most of the literature, $W_r^2 = \theta[E]^2 w_r$ is used to be expanded as

$$W_r = \theta[E_0]^2 \left(w_r[E_0] + \frac{\partial w_r}{\partial E} \Big|_{E=E_0} (E - E_0) \right) = \theta[E_0]^2 \frac{\partial w_r}{\partial E} \Big|_{E=E_0} (E - E_0); \quad (28)$$

therefore, the width of resonance peak would be:

$$\Delta E = \frac{2}{\theta[E_0]^2 \frac{\partial w_r}{\partial E} \Big|_{E=E_0}} \propto O \left[\frac{1}{\theta[E_0]^2} \right].$$

It should be noted that $w_r[E_0] = 0$ is assumed in Eq. (16) instead of

$$w_r[E_0] = \frac{1}{\theta[E_0]^2}.$$

Numerically, there is no big difference between these two different assumptions; however, they are very different at very low energy where $w_r[E_0]$ approaches a constant according to Eqs. (12)–(14). At very low energy, $\theta[E]^2$ varies much faster than w_r does; therefore, the assumption in Eq. (28) is no longer valid. The width of resonance should be determined by the fast variation of $\theta[E]^2$ instead of the very slow variation of w_r .

The width of resonance blocked the resonance approach in the early days of condensed matter nuclear science. Now we understand that at very low energy this block was just a mistake. The behavior of $\theta[E]^2$ at 100 keV ($\sim 10^9$ K) is not supposed to be the same as the behavior of $\theta[E]^2$ near 0.1 eV (~ 1000 K). The resonance contribution to the reaction rate does not diminish when the resonance approaches zero energy, because the resonance peak height is increase much faster than the resonance width is shrinking.

6. The Energy Carried away by Neutrino

If during the resonant electron-capture-process, the daughter state, Ψ_f , is the ground state of ${}^7\text{Li}$ instead of the excited state ${}^7\text{Li}^*$; then the neutrino might have carried away most of the reaction energy in the process of electron-capture: $p + {}^6\text{Li} + e^- \rightarrow {}^7\text{Li} + \text{neutrino} + 4.001 \text{ MeV}$.

Consequently, the “anomalous heat effect” would have not been detected. However, during the resonant electron-capture the mother state, Ψ_i , is dominant by G_0 because it is formed in a low energy resonant process. The transition probability,

$$\left| \int \Psi_f \Psi_i d\tau \right|^2,$$

requires that the daughter state Ψ_f should be very similar to the mother state, Ψ_i : i.e. the wave function, Ψ_f , should be extended to outside the nuclear core, and decrease quickly. Hence, Ψ_f should be a state very similar to neutron halo instead of the ground state of ${}^7\text{Li}$. Fortunately, lithium is a famous halo nuclide. ${}^9\text{Li}$ and ${}^{11}\text{Li}$ may have a halo state [26] with one or two neutrons away from the nuclear core. Thus, the excited ${}^7\text{Li}^*$ may just have a neutron skin as a daughter state, Ψ_f , of the resonant electron-capture process. As a result, the neutrino carries away just a little reaction energy and ${}^7\text{Li}^*$ keeps most of the reaction energy in its excited state. When ${}^7\text{Li}^*$ decays into ${}^3\text{T} + {}^4\text{He}$, both of the charged products carry away the reaction energy and transfer the kinetic energy to the surrounding electrons while they are slowing down. The energy carried by ${}^7\text{Li}^*$ is then detected as the anomalous heat effect.

7. The Analytical Property of the Elastic Scattering Amplitude Determined by Inelastic Scattering

In the discussion above, we used the inelastic fusion process to determine the low energy resonance of elastic scattering. This is based on the analytical property of scattering amplitude on the complex energy E -plane. According to Landau [27], the scattering amplitude might be extended to the complex energy plane as an analytical function. Its property is determined by its poles and the residues of these poles. Indeed, the positions of these poles determine the resonance energy, and the residues of these poles determine the life-time of these resonance states. The elastic scattering and inelastic scattering share the same scattering amplitude at resonance energy. Therefore, we may use the inelastic fusion process to determine the pole of elastic scattering.

8. Concluding Remarks

The 3-parameter equation for low energy fusion cross-section, Eq. (16), reveals a way to overcome the Coulomb barrier suppression. Provided that there is a low energy level to keep $W_r = \theta[E]^2 w_r \leq 1$, and a tiny interaction to keep $|W_i| = |\theta[E]^2 w_i| \leq 1$; then the Gamow factor would disappear in the formula of fusion cross-section. This has led us to an elastic process followed by a weak interaction. The formula for a low energy elastic scattering cross-section is

$$\sigma_{\text{elastic}} = \frac{\pi}{k^2} \frac{4}{W_r^2 + 1}. \quad (29)$$

Provided that there is a low energy level to keep $W_r = \theta[E]^2 w_r \leq 1$, σ_{elastic} would be free of Coulomb barrier suppression, because there would be no Gamow factor in the expression of σ_{elastic} . It is not necessary to require $W_r = \theta[E]^2 w_r = 0$, in order to overcome the Coulomb barrier, although $W_r = 0$ does make the cross-section maximized.

It is also interesting to note that the accompanied weak interaction—electron capture introduces an additional favorable factor $\theta[E]^2$ from G_0 ; then,

$$\frac{\theta[E]^2}{1 + (w_r \theta[E]^2)^2}$$

would have a resonance peak at E_0 where $W_r = \theta[E_0]^2 w_r = 1$, and the peak height would be enhanced a factor of $1/w_r$, which is a very large number in the case of resonance.

Although this new resonance peak would appear at the phase shift $\delta_0 = \frac{\pi}{4}$: i.e. $\cot[\delta_0] = W_r = \theta[E]^2 w_r = 1$, the Gamow peak still appears at some phase shift $\delta \ll \delta_0$ after averaging over a Maxwell distribution of velocity, because usually the temperature T is still too low to compare with the resonance energy, E_0 . However, the enhancement factor $1/w_r$ is enhancing the integrand in Eq. (20) over the whole energy region (including the Gamow peak E_G), even if $\delta \ll \delta_0$.

The reaction rate after averaging is heavily dependent on the temperature, T :

$$\langle \sigma v \rangle = \frac{1.61 \times 10^{-20}}{w_r^2} \left(\frac{1}{T} \right)^{2/3} \exp \left[-\frac{8416}{T^{1/3}} \right] \quad (30)$$

(T in Kelvin, $\langle \sigma v \rangle$ in m^3/s). It quickly increases with temperature. This would have a positive feedback effect as an exothermic process in experiments. The micro-melting spots in a palladium cathode with heavy water electrolysis [28] are exactly the kind of evidence we would expect for this positive feedback effect.

In conclusion, the combination of a selective resonant tunneling model and the weak interaction has answered Huizenga's three puzzles, and the anomalous heat effect may be achieved without commensurate neutron and gamma radiation.

Acknowledgements

This work is supported by The Ministry of Education (#20091770437), The Ministry of Science and Technology (Fundamental Research Division, #2009CB226113), Natural Science Foundation of China (#10475045 & #21153003) and Tsehua University (Basic Research Fund (985-III)).

References

- [1] H.A. Bethe and C.L. Critchfield, The formation of deuterons by proton combination, *Phys. Rev.* **54**(1938) 248.
- [2] G. Levi et al., Observation of abundant heat production from a reactor device and of isotopic changes in fuel (Lugano report 2014).
- [3] A.G. Parkhomov, *Int. J. Unconventional Sci.* **7**(3) (2015) 68–72.
- [4] Songsheng Jiang et al. <http://www.e-catworld.com/2015/07/31/low-energy-nuclear-reaction-occurring-in-hydrogen-loaded-nickel-wire-songsheng-jiang/>.
- [5] H. Zhang, Anomalous heat effect in Ni–H (LiAlH₄) systems, Sept. 28–30, 2016, Xiamen, China, will be presented in *SSICCF-20*,
- [6] S.A. Lipinski and H.M. Lipinski, Hydrogen-Lithium Fusion Device, WO2014/189799 A9 (27 November, 2014).
- [7] X.Z. Li, Z.M. Dong and C.L. Liang, Studies on p+⁶Li fusion reaction use 3-parameter model, *J. Fusion Energy* **31** (2012) 432.
- [8] M. Abramowitz and I.A. Stegun, *Handbook of Mathematical Functions*, 10th Printing, December, 1972, p.542.
- [9] National Nuclear Data Center, Brookhaven National Laboratory, ENDF/B-VII.1(2011) is available on Internet <http://www.nndc.bnl.gov>.
- [10] X.Z. Li, A new approach towards fusion energy with no strong nuclear radiation, *Nuclear Fusion and Plasma Physics* (in Chinese), **16**(2) (1996) 1–8 (see also *J. New Energy* **1** (1996) 44–54 (4):in English).
- [11] X.Z. Li, J. Tian, M.Y. Mei and C.X. Li, Sub-barrier fusion and selective resonant tunneling, *Phys. Rev. C* **61** (2000) 024610.
- [12] X.Z. Li, Nuclear physics for nuclear fusion, *Fusion Sci. Technol.* **41** (2002) 63.
- [13] X.Z. Li, B. Liu, S. Chen, Q.M. Wei and H. Hora, Fusion cross sections for inertial fusion energy, *Laser Part Beams*, **22** (2004) 469.
- [14] X.Z. Li, Q.M. Wei and B. Liu, A new simple formula for fusion cross-sections of light nuclei, *Nucl. Fusion* **48** (2008) 125003.
- [15] M. Kikuchi, *Frontiers in Fusion Research – Physics and Fusion*, Springer, London, 2011, p. 31.
- [16] M. Fleischmann, S. Pons, M.W. Anderson, L.J. Li and M. Hawkins, Calorimetry of the palladium–deuterium–heavy water system, *J. Electroanal. Chem.* **287** (1990) 293–348.
- [17] M.H. Miles, Correlation of excess enthalpy and helium-4 production: a review, *Proc. ICCF-10*, 2003, MIT, Cambridge, USA.
- [18] M.C.H. McKubre, F. Tanzella1, P. Tripodi and P. Hagelstein, The Emergence of a Coherent explanation for Anomalies Observed in D/Pd and H/Pd System: Evidence for 4He and 3He production, in *8th Int. Conf. on Cold Fusion*, May, 2000, Lerici (La Spezia), Italy: Italian Physical Society, Bologna (ISBN 88-7794-256-8), pp. 3–10.
- [19] Edmund Storms, Excess power production from platinum cathodes use the Pons–Fleischmann effect, in *8th Int. Conf. on Cold Fusion*, 2000, Lerici (La Spezia), Italy: Italian Physical Society, Bologna, Italy.
- [20] I. Dardik, T. Zilov, H. Branover, A. El-Boher, E. Greenspan, B. Khachatorov, V. Krakov, S. Lesin and M. Tsirlin, Excess heat in electrolysis experiments at energetics technologies, In *Condensed Matter Nuclear Science*, Proc. 11th Int. Conf. on Cold Fusion, Marseilles, France, 31 Oct. 5 Nov. 2004, pp. 84–101.
- [21] De Ninno, A. Frattolillo, A. Rizzo and E. Del Giudice, Experimental evidence of 4He production in a cold fusion experiment, 2002, ENEA – Unita Tecnico Scientifica Fusione Centro Ricerche Frascati, Roma, *ICCF-10 Proc.*, 2003.
- [22] D. Gozzi, F. Cellucci, P.L. Cignini, G. Gigli, M. Tomellini, E. Cisbani, S. Frullani and G.M. Urciuoli, X-ray, heat excess and 4He in the D/Pd system, *J. Electroanal. Chem.* **452** (1998) 251.
- [23] F.G. Will, K. Cedzyska and D.C. Linton, Reproducible tritium generation in electrochemical cells employing palladium cathodes with high deuterium loading, *J. Electroanal. Chem.* **360** (1993) 161.

- [24] J. Ó. M. Bockris, G.H. Lin, R.C. Kainthla, N.J.C. Packham and O. Velev, Does tritium form at electrodes by nuclear reactions? in *The First Ann. Conf. on Cold Fusion*, 1990, University of Utah Research Park, Salt Lake City, Utah: National Cold Fusion Institute.
- [25] X.Z. Li, Z.M. Dong and C.L. Liang, Excess heat in Ni–H systems and selective resonant tunneling, *J. Condensed Matter Nucl. Sci.* **13** (2014) 299–310.
- [26] X.Z. Li, Z.M. Dong and C.L. Liang, Recent experimental progress in nuclear halo structure studies, *Progr. Particle and Nucl. Phys.* **68** (2013) 215–313.
- [27] L.D. Landau and E.M. Lifshitz, *Quantum Mechanics, Non-relativistic Theory*, Pergamon, Oxford, 1958, p. 526.
- [28] R. Duncan, An outsider’s view of the Fleischmann–Pons effect (PowerPoint slides), in *15th Int. Conf. on Condensed Matter Nucl. Sci.*, 2009. Rome, Italy, ENEA.